Modeling water availability for smallholder farming in inland valleys under climate and land use / land cover change in Dano, Burkina Faso

Dissertation

zur

Erlangung des Doktorgrades (Dr. rer. nat.)

der

Mathematisch-Naturwissenschaftlichen Fakultät

der

Rheinischen Friedrich-Wilhelms-Universität Bonn

vorgelegt von

Mouhamed Idrissou

aus

Abrewankor, Togo

Bonn, Januar 2020

Angefertigt mit Genehmigung der Mathematisch-Naturwissenschaftlichen Fakultät
der Rheinischen Friedrich-Wilhelms-Universität Bonn

1. Gutachter: Prof. Dr. Bernd Diekkrüger
2. Gutachter: PD. Dr. Gerd Welp
Tag der mündlichen Prüfung: 21.04.2020
Erscheinungsjahr: 2020

I wish to dedicate this work to the memory of my mother Fousséna Alassane who passed away in March 2017. Her love and sacrifices have inspired this work. May she rest in peace.

This work is also dedicated to my wife Adissétou, our sons Mansour and Abdoulaziz for their support and their sacrifice during the long years of my absence at home for this work.

ACKNOWLEDGEMENT

I would like to express my deep gratitude to my supervisor, Prof. Dr. Bernd Diekkrüger, for his wise guidance, advice, and encouragement throughout this work. He has been more than a supervisor to me. His professional and human qualities have inspired and shaped this work tremendously. In my moments of challenge, his words and behavior helped to build my trust in my capabilities and to keep things up. Words cannot express my gratitude for all his never-ending supports. I am also very grateful to PD Dr. Gerd Welp, Prof. Dr. Christian Borgemeister, and Prof. Dr. Mariele Evers for accepting to be part of the doctoral committee.

Furthermore, I would like to thank ZEF directors Prof. Dr. C. Borgemeister, Prof. Dr. J. von Braun, Prof. Dr. S. Gerke, and PD Dr. E. Youkhana for creating the perfect working environment that allowed this work to be possible. Special thanks to Dr. G. Manske, Maike Retat-Amin, Sabine Aengenendt-Baer, Ludger Hammer, Volker Merx, Sarah Verleysdonk, Antonio Rogmann for their help and kindness. I would also want to say sincere thanks to my tutor Dr. Bernhard Tischbein for his tireless support and his availability for me. Thanks to Dr. M. Denich, Dr. J. Lamers, Dr. D. Wisser, and Dr. D. Callo-Concha for their support. I would like to express my profound gratitude to Dr. T. Poméon and his wife Amélie for their endless and unconditional support to me in many different ways. Many thanks to Gero Steup and his family Alex, Mattis, and Aenne for their tremendous support and kindness. Throughout this research, I have been lucky to work with very wonderful colleagues and friends. I appreciate very much every second spent together. Each of them has supported this work in various ways. In no specific order, they are: Dr. W. Okumu, Nicolas Moret, Aline Pereira, Marcos Jiménez, Dr. F. Akhtar, Dr. J. Räp Wenceslas Somda, Claudia Schepp, Kristian Näschen, Alexander Ahring, Emmanuel Nkundimana, Dr. F. Op de Hipt, Dr. Y. Yira, Dr. G. Gabiri, Dr. I. Rabbel, Dr. C. Leemhuis, Dr. C. Gaba, Dr. S. Giertz, Dr. L. Taft, Dr. B. Höllermann, Dörte Schultz, Dr. M. Mensah.

Thanks to Dr. B. Ibrahim, Dr. A. Y. Bossa, Hermann Hien, Hamadou Barro, Salif Some, and Koumbassolo Dabire for their precious assistance during my field research in Dano. Thanks to Prof. L. M. Bawa, Dr. S. Tairou, Dr. M. Gnazou, Prof. K. Koba, Victor Doni, Dr. F. N. Diop, Prof. S. Faye, Marius Nambo, Affo B. Adjama, Raouf Akakpo, Hervé Allain, Anastasie Allain, Afefa Allain, Soumanou Sagbo, Benjamin Sangnan, Dr. G. Katawa for their support and encouragement.

This research has been funded by the German Ministry of Education and Research (BMBF) under the project West African Science Service Center on Climate Change and Adapted Land Use (WASCAL, Grant No.01LG1202A) and by the Islamic Development Bank through the Merit scholarship program (Grant No. 600029612). I am very grateful to them.

ABSTRACT

Effective water management in inland valley catchments is crucial for adaptation to the adverse impact of climate change and land use and land cover change (LULCC) on smallholder farming systems, poverty reduction, attaining food security, and ecosystem preservations in the West African region.

An intensive hydrological instrumentation of four sparse data catchments (Bankandi-Loffing, Mebar, Moutori, and Fafo in Dano, Burkina Faso) has been undertaken in order to better understand hydrological processes which control water availability, to calibrate and validate the physically-based and spatially distributed water balance simulation model WaSiM, to assess the impact of climate and land use and land cover change on water resources, and subsequently to derive strategies for improving the capacity of smallholder farmers to cope with water scarcity and climate variabilities.

The instrumentation of the catchment helped to achieve three years (2014-2016) of high temporal and spatial resolution data. The temporal resolutions of meteorological and stream flow data were 5 min to 10 min, six hours to a week for piezometric data, and 30 min to a week for soil moisture data.

Five rain recorders, seven stream gauges, 64 piezometers in shallow groundwater (< 5 m deep), and 64 soil moisture measurements at three different depths (5 cm, 30 cm, and 50 cm) were installed and operated in the four catchments (total area: 65 km²). Additionally, the groundwater tables of three relatively deep wells (6 m, 16 m, and 25 m deep) were monitored.

The analyses of hydrographs and the flow duration curves (FDC) using observed discharge show less discharge in the headwater sub-catchments compared to the downstream sub-catchments. This is due to the low contribution of base flow in the headwater sub-catchments. The decomposition of total runoff using observed hydrographs and stream electric conductivity suggests that interflow is the major contributor to total discharge.

The calibration and validation of the Bankandi-Loffing catchment achieved a good model performance using the coefficient of determination (R^2), the Nash-Sutcliffe efficiency (NSE), the Kling-Gupta efficiency (KGE), and the percent bias (Pbias). The R^2 ranges from 0.47 to 0.95, NSE from 0.40 to 0.95, and KGE from 0.57 to 0.84 between the observed and simulated discharge. The numerical performance for soil moisture modeling is 0.70 for both R^2 and NSE, and 0.80 for KGE while for the groundwater table modeling the results are 0.30, 0.20, and 0.5 for R^2, NSE, and KGE, respectively. The fact that the transfer of the parameter set from Bankandi-Loffing to Mebar catchment without recalibration resulted in a good model performance (R^2: 0.93, NSE: 0.92, and KGE: 0.84 in 2014-2015; R^2: 0.65, NSE: 0.64, and KGE: 0.59) suggests the strong robustness of WaSiM in the investigated area.

The resulting water balance shows that evapotranspiration is quantitatively the most important hydrological process, physical evaporation dominates the evapotranspiration, and 14% of rainfall runs out of the catchment as discharge. Interflow dominates runoff at the headwater sub-catchments whereas base flow is the major runoff component in the downstream area where the inland valley bottoms are located.

The conversion of savanna to cropland leads to an increase of surface runoff. This is potentially associated with an exacerbation of soil erosion and soil fertility loss. Therefore, supplementing the current erosion technique (stone-belt) with agroforestry and/or mulching will reduce the negative effects of land cover change.

Two scenarios were considered during the impact assessment. The first scenario evaluated exclusively the climate change impact by utilizing five regional climate models (RCMs) using land use and land cover (LULC) of the year 2013 for both the reference period (1971-2000) and the projection period (2021-2050). Each RCM is composed of the representative concentration pathways (RCPs) 4.5 and 8.5. The results indicate large uncertainty in the discharge projection for the future. Three RCMs predict an increase of total runoff for the projection period compared to the reference period. The mean total runoff increase is +61% (standard deviation Std= 31%) compared to the reference period. However, two RCMs project a decrease of total runoff. The mean total runoff decrease is -34% (Std= 10%) compared to the reference period.

The second scenario utilizes the five RCMs and LULC 2013 for the reference period and LULC 2030 for the projection period in order to assess the combined impact of climate change and LULCC. The results suggest that LULCC exacerbates the increase of total runoff in combination with the three RCMs with a mean increase in total runoff by +108% (Std= 38%) compared to the reference period (versus mean= +61% in the first scenario). However, for the two RCMs predicting a decrease of total runoff, LULCC reduces the decrease of total runoff. The mean decrease is -20% (Std= 10%) compared to the reference period (versus mean= -34% in the first scenario).

The results of this study can be used as input to water management models in order to derive strategies to cope with present and future water scarcities for smallholder farming in the investigated area.

ZUSAMMENFASSUNG

Modellierung der Wasserverfügbarkeit für die kleinbäuerliche Landwirtschaft in Talgrund-Feuchtgebieten unter Berücksichtigung von Klima- und Landnutzungswandel in Dano, Burkina Faso

Eine effektive Wasserbewirtschaftung in den Einzugsgebieten von Talgrund-Feuchtgebieten ist essentiell, um die negativen Auswirkungen des Klimawandels und der Landnutzungs- und der Landbedeckungssänderung (LULCC) auf die kleinbäuerlichen Anbausysteme, die Armutsbekämpfung, die Ernährungssicherheit und den Erhalt der Ökosysteme in Westafrika zu minimieren.

Eine intensive hydrologische Instrumentierung von vier datenarmen Einzugsgebieten (Bankandi-Loffing, Mebar, Moutori und Fafo in Dano, Burkina Faso) wurde durchgeführt, um hydrologische Prozesse, die die Wasserverfügbarkeit steuern, besser zu verstehen, das physikalisch-basierte und räumlich gegliederte Wasserhaushaltssimulationsmodell WaSiM zu kalibrieren und zu validieren, die Auswirkungen von Klimawandel und LULCC auf die Wasserressourcen zu bewerten und anschließend Strategien zur Verbesserung der Kapazität von Kleinbauern mit Wasserknappheit und Klimaschwankungen umzugehen zu unterstützen.

Die Instrumentierung des Einzugsgebiets trug dazu bei, dass Daten für drei Jahre (2014-2016) mit hoher zeitlicher und räumlicher Auflösung zur Verfügung stehen. Die zeitliche Auflösung der meteorologischen Daten und der Abflussdaten lag bei 5 min bis 10 min, bei piezometrischen Daten bei sechs Stunden bis zu einer Woche und bei Bodenfeuchtigkeitsdaten bei 30 min bis zu einer Woche.

Fünf Niederschlagsschreiber, sieben Abflussmessstationen, 64 Piezometer im flachen Grundwasser (< 5 m tief) sowie 64 Bodenfeuchtemessungen in drei verschiedenen Tiefen (5 cm, 30 cm und 50 cm) wurden in den vier Einzugsgebieten (Gesamtfläche: 65 km²) installiert und in Betrieb genommen. Zusätzlich wurde der Grundwasserspiegel von drei tiefen Brunnen (6 m, 16 m und 25 m tief) überwacht.

Die Analyse der Abflussganglinien und der Durchflussdauerlinien (FDC) mit beobachteten Abflüssen zeigen geringe Abflüsse in den Teileinzugsgebieten der Oberläufe im Vergleich zu den stromabwärts gelegenen Teileinzugsgebieten. Dies ist auf den geringeren Beitrag des Grundwasserzuflusses in den Oberläufen zurückzuführen. Die Dekonstruktion des Gesamtabflusses unter Verwendung von beobachteten Ganglinien und der elektrischen Leitfähigkeit des Abflusses deutet darauf hin, dass der Zwischenabfluss die wichtigste Komponente für den Gesamtabfluss ist.

Die Kalibrierung und Validierung des Bankandi-Loffing-Einzugsgebiets ergab im Allgemeinen eine gute Modellgüte unter Verwendung des Bestimmtheitsmaßes (R^2), der

Nash-Sutcliffe Efficiency (NSE), der *Kling-Gupta Efficiency* (KGE) und der prozentualen Abweichung (*Pbias*). R^2 reicht von 0,47 bis 0,95, NSE von 0,40 bis 0,95 und KGE von 0,57 bis 0,84 beim Vergleich des beobachteten und simulierten Abflusses. Die Modellgüte für die Bodenfeuchtemodellierung beträgt 0,70 für R^2 und NSE und 0,80 für KGE. Die Modellierung des Grundwasserspiegels zeigt Ergebnisse von 0,30, 0,20 und 0,5 für R^2, NSE und KGE. Die Tatsache, dass die Übertragung des Parametersatzes vom Bankandi-Loffing zum Mebar-Einzugsgebiet ohne Rekalibrierung zu einer guten Modellleistung führte (R^2: 0,93, NSE: 0,92 und KGE: 0,84 in 2014-2015; R^2: 0,65, NSE: 0,64 und KGE: 0,59) deutet auf die Robustheit von WaSiM in der Region hin.

Die Berechnung der Wasserbilanz zeigt, dass die Evapotranspiration quantitativ der wichtigste hydrologische Prozess ist, die physikalische Evaporation dominiert die Evapotranspiration, und 14% der Niederschläge verlassen als Abfluss das Einzugsgebiet. Der Zwischenabfluss dominiert den Abfluss in den Quellgebieten, während der Grundwasserabfluss die wichtigste Abflusskomponente im stromabwärts gelegenen Bereich ist, in dem sich die Talgrund-Feuchtgebiete befinden.

Die Umwandlung von Savanne in Ackerland führt zu einer Zunahme der Oberflächenabflüsse. Dies ist potenziell mit einer Verschärfung der Bodenerosion und des Verlusts der Bodenfruchtbarkeit verbunden. Daher könnte eine Ergänzung der derzeitigen Erosionsschutzmaßnahmen (Steinbänder) durch Agroforstwirtschaft und/oder Mulchen die negativen Auswirkungen des Landnutzungswandels reduzieren.

Bei der Folgenabschätzung wurden zwei Szenarien berücksichtigt. Das erste Szenario bewertete ausschließlich die Auswirkungen des Klimawandels, indem es fünf regionale Klimamodelle (RCMs) und die gleiche Landnutzung und Landbedeckung (LULC) des Jahres 2013 sowohl für den Bezugszeitraum (1971-2000) als auch für den Vorhersagezeitraum (2021-2050) verwendete. Für jedes RCM wurden zwei verschiedene repräsentative Konzentrationspfade (RCPs) 4.5 und 8.5 simuliert. Die Ergebnisse deuten auf eine große Unsicherheit für die Zukunft hin. Drei RCMs prognostizieren einen Anstieg des Gesamtabflusses für den Vorhersagezeitraum im Vergleich zum Referenzzeitraum. Der mittlere Anstieg der Abflüsse beträgt +61% (Standardabweichung = 31%) gegenüber de

m Referenzzeitraum. Zwei RCMs gehen jedoch von einer Verringerung des Abflusses aus. Die mittlere Abnahme der Abflüsse beträgt für diese -34% (Standardabweichung= 10%) im Vergleich zum Referenzzeitraum.

Das zweite Szenario verwendete die fünf RCMs und LULC 2013 für den Bezugszeitraum und LULC 2030 für den vorhergesagten Zeitraum, um die kombinierten Auswirkungen von Klimawandel und LULCC zu bewerten. Die Ergebnisse zeigen, dass LULCC die Zunahme des Gesamtabflusses im Vergleich zum ersten Szenario in Kombination mit den drei RCMs mit zunehmendem Abfluss verstärkt. Die mittlere

Zunahme der Abflüsse beträgt im Mittel +108% (Standardabweichung= 38%) gegenüber dem Referenzzeitraum (Mittelwert= +61% im ersten Szenario). Für die beiden RCMs, die eine Abnahme des Abflusses voraussagen, reduziert LULCC jedoch die Abnahme des Gesamtabflusses. Der mittlere Rückgang beträgt -20% (Standardabweichung= 10%) gegenüber dem Referenzzeitraum (gegenüber -34% im ersten Szenario).

Die Ergebnisse dieser Studie können als Basis für wasserwirtschaftliche Modelle genutzt werden, um Strategien zur Bewältigung der gegenwärtigen und zukünftigen Wasserprobleme abzuleiten.

RESUME

Modélisation de la disponibilité de l'eau pour les petites exploitations agricoles des bas-fonds sous l'influence du changement climatique, d'utilisation des sols / couverture végétale à Dano, Burkina Faso

La gestion efficiente des ressources en eau dans les bassins versants des bas-fonds est indispensable non seulement pour l'adaptation aux impacts néfastes du changement climatique, utilisation sols / couverture végétale sur les petites exploitations agricoles, mais aussi pour réduire la pauvreté, l'insécurité alimentaire et préserver les écosystèmes en Afrique de l'Ouest.

Une instrumentation hydrologique intensive de quatre (04) bassins versants pourvus de très peu de données (Bankandi-Loffing, Mebar, Moutori et Fafo situés à Dano, Burkina Faso) a été entreprise afin de mieux comprendre les processus hydrologiques qui contrôlent la disponibilité en ressources hydrologiques. Le modèle WaSiM (modèle à base physique distribué) a été utilisé, pour évaluer les impacts du changement climatique, d'utilisation des sols et de couverture végétale sur les ressources en eau. Cette étude pourra aider à développer des stratégies d'amélioration de la capacité des petits exploitants agricoles à surmonter les problèmes de manque d'eau et de variabilités climatiques.

L'équipement hydrologique des bassins versants a permis d'obtenir durant trois (03) années (2014-2016) de données de hautes précisions temporelles et spatiales. Les précisions temporelles des données météorologiques et des données de débit des cours d'eau étaient de 5 à 10 minutes. Ces précisions étaient de 6 heures à une semaine pour les données piézométriques et de 30 minutes et une semaine pour les données sur l'humidité du sol.

Cinq (05) pluviomètres, sept (07) station limnimétriques, soixante-quatre (64) piézomètres captant la nappe phréatique (< 5 m de profondeur), soixante-quatre (64) points de mesures de l'humidité du sol à trois profondeurs (5 cm, 30 cm et 50 cm) ont été installés et rendus opérationnels sur les quatre bassins versants (leur superficie total est d'environ 65 km²). De plus, le niveau de la nappe phréatique a été régulièrement mesuré dans trois puits relativement profonds (6 m, 16 m et 25 m de profondeurs respectivement).

Les analyses des hydrogrammes et des courbes de débits classés à partir des débits observés révèlent des débits plus faibles dans les sous-bassins en amont par rapport aux sous-bassins en aval. Cela s'explique en partie par la faible contribution des écoulements de base dans les sous-bassins en amont. La décomposition de l'écoulement à l'aide des hydrogrammes de débits observés et de la conductivité électrique des cours

d'eau suggère que l'écoulement hypodermique est le principal contributeur des écoulements.

La calibration et la validation de WaSiM pour le bassin versant de Bankandi-Loffing ont permis d'obtenir une bonne performance du modèle en utilisant le coefficient de détermination (R^2), l'efficacité de Nash-Sutcliffe (NSE), l'efficacité de Kling-Gupta (KGE), et le pourcentage de biais (Pbias). R^2 varie de 0,47 à 0,95, NSE de 0,40 à 0,95 et KGE de 0,57 à 0,84 entre les débits observés et les débits simulés. La performance numérique pour la modélisation de l'humidité du sol est de 0,70 pour les deux paramètres de performance R^2 et NSE, et de 0,80 pour KGE. Concernant la modélisation du niveau de la nappe phréatique, les résultats sont de 0,30, 0,20 et 0,5 pour R^2, NSE et KGE, respectivement. Le fait que le transfert du jeu de paramètres de Bankandi-Loffing au bassin versant de Mebar sans recalibration ait donné lieu à une bonne performance du modèle (R^2: 0,93, NSE: 0,92, et KGE: 0,84 en 2014-2015 ; R^2: 0,65, NSE: 0,64, et KGE: 0,59 en 2016) dénote une forte robustesse du modèle WaSiM pour la zone d'étude.

Le bilan hydrique qui résulte de la modélisation montre que l'évapotranspiration est le processus hydrique le plus important quantitativement. L'évaporation physique est plus importante que la transpiration et 14% des précipitations s'écoulent du bassin versant sous forme d'écoulement de surface. Le ruissellement de surface domine les écoulements dans les sous-bassins en amont, tandis que l'écoulement de base est la principale composante des écoulements dans les sous-bassins en aval où se situent les bas-fonds.

La conversion des savanes en terres cultivées entraîne une augmentation du ruissellement de surface. Ceci est potentiellement associé à une exacerbation de l'érosion et à la perte de fertilité des sols. Par conséquent, il serait envisageable de compléter les techniques anti-érosives actuelles (ceinture de pierres) par de l'agroforesterie et/ou du paillage.

Deux scénarii ont été considérés lors de l'étude d'impact. Le premier scénario a évalué uniquement l'impact du changement climatique en se servant de cinq (05) modèles climatiques régionaux (RCMs) et de la carte d'utilisation des sols / couverture végétale de l'année 2013 (LULC 2013) pour la période de référence (1971-2000) et pour les projections futures (2021-2050). Chaque RCM est composé de profils représentatifs d'évolution des concentrations (RCPs) 4.5 et 8.5. Les résultats indiquent une grande incertitude des projections de débits d'écoulement pour l'avenir. Trois RCMs prévoient une augmentation moyenne annuelle de débits de +61% (écart-type Std = 31%) par rapport à la période de référence. En revanche deux RCMs prévoient une diminution des débits de -34% (Std = 10%) en moyenne par rapport à la période de référence.

Le deuxième scénario a utilisé les cinq RCMs et le LULC 2013 pour la période de référence et le LULC 2030 pour le futur afin d'évaluer l'impact combiné du

changement climatique et de le LULCC. Les résultats suggèrent que le LULCC accentue l'augmentation des débits quand il est combiné avec les trois modèles prévoyant l'augmentation des débits. L'augmentation moyenne des débits est de +108% (Std = 38%) par rapport à la période de référence (contre +61% en moyenne dans le premier scénario). Cependant, pour les deux RCMs qui prévoient une diminution des débits, le LULCC attenue le changement de débit. La diminution moyenne de débit est de -20% (Std = 10%) par rapport à la période de référence (contre –34% en moyenne dans le premier scénario).

Les résultats de cette étude pourront servir de données d'entrée aux modèles de gestion des ressources en eau afin d'élaborer des stratégies pour faire face aux pénuries d'eau actuelles et futures pour les petites exploitations agricoles dans la zone d'étude.

TABLE OF CONTENTS

LIST OF FIGURES

LIST OF TABLES

LIST OF ABREVIATIONS

ADC	*Acoustic Digital Current meter*
BaLof	*Bankandi-Loffing*
BMBF	*German Ministry of Education and Research*
BUMIGEB	*National Department of Mining and Geology of Burkina Faso*
BUNASOL	*Bureau National des Sols*
CORDEX	*Coordinated Regional Climate Downscaling Experiment*
CPCS	*Commission de Pédologie et de la Cartographie des Sols*
DEM	*Digital elevation model*
DGPS	*Differential global positioning system*
EC	*Electric conductivity of water*
ECOWAS	*Economic Community West African States*
EIP	*Interception evaporation*
EP	*Evaporation from the bare soil*
ERT	*Electrical resistivity tomographie*
ETa	*Actual evapotranspiration*
ETp	*Potential evapotranspiration*
FDC	*Flow duration curve*
FDR	*Frequency Domain Reflectometry*
GCMs	*Global climate models*
GDP	*Gross domestic product*
IMF	*International Monetary Funds*
KGE	*Kling-Gupta efficiency*
Ks	*Hydraulic conductivity*
LAI	*Leaf area index*
LCM	*Land Change Modeler*
LULC	*Land use and land cover*
LULCC	Land use and land cover change
Meb	*Mebar*
mHM	*Mesoscale Hydrological Model*
NSE	*Nash-Sutcliffe efficiency*
PAW	*Plant-available water*
Pbias	*Percent bias*
QB	*Base flow*
QD	*Surface flow or overland flow*
QI	*Interflow*
R^2	*Coefficient of determination*
RCMs	*Regional climate models*
RCP	*Representative concentration pathways*
r_s	*Bulk surface resistance*
$r_{s.day}$	*Bright day surface resistance*
$r_{s.night}$	*Night surface resistance*
r_{sc}	*Canopy surface resistance*

r_{se}	*Evaporation surface resistance*
r_{si}	*Interception surface resistance*
SimLab	*Simulation Environment for uncertainty and sensitivity analysis*
SPEI	*Standardized Precipitation Evaporation index*
SPI	*Standardized Precipitation Index*
SRTM	*Shuttle Radar Topography Mission*
SWAT	*Soil & Water Assessment Tool*
Ta	*Actual transpiration*
TP	*Potential transpiration from plant leaves*
TP_{day}	*Bright day potential transpiration*
TP_{night}	*Night potential transpiration*
USGS	*United States Geological Survey*
vcf	*Vegetation cover fraction*
WASCAL	*West African Service Center on Climate Change and Adapted Land Use*
WaSiM	*Water balance simulation model*
WHC	*Soil water holding capacity*
WMO	*World Meteorological Organization*
WRB	*World Reference Base*

1 GENERAL INTRODUCTION

1.1 Problem statement

Water resources availability for smallholder farmers in West Africa is a major concern for poverty alleviation, economic development and food security as the majority of the population practice rainfed agriculture (Denis et al., 2012). Agriculture contributes approximately 25% of the gross domestic product (GDP) of the Economic Community of West African States (ECOWAS) and account for more than a quarter of the region's GDP growth (African Development Bank, 2019). The major part of the active labor force (60%) works in in agriculture (Jalloh et al., 2013). Smallholder farming is a mainstay of the agricultural economy and the main source of food production in the region (Denis et al., 2012). However, the majority of people (approximately 57%) live below the poverty line (INSD, 2014).

Smallholder farmers are the most vulnerable to climate variabilities in West Africa due to the fact that they have a limited adaptation capacity to climate change impacts (Makate et al., 2017; Traore et al., 2015). The region experienced high variability of rainfall during the last five decades and is expected to be the most impacted worldwide by climate change in the twenty first century (Descroix et al., 2009; Frappart et al., 2009; Ibrahim et al., 2013a; Lebel et al., 2009; Lebel and Ali, 2009; Mougin et al., 2009; Niang et al., 2014; Oguntunde et al., 2017).

Inland valleys are estimated to cover 22-52 million ha in West Africa (Windmeijer and Andriesse, 1993). Due to the relatively wet characteristic of inland valleys and in order to cope with water scarcity, many development projects have focused on runoff in inland valleys by building small reservoirs, whereas basic information on groundwater resources is scarce (Eguavoen and McCartney, 2013; Sparacino, 2011).

An implementation of efficient water management strategies is crucial for coping with adverse impacts of climate change and to preserve the ecosystems which contribute to the stability of the climate system (Baldocchi and Penuelas, 2019; Hessen et al., 2004; Lal, 2004). However, no management strategies can be developed without a robust observation network and the region has only limited *in situ* data (Poméon, 2019). Therefore, one of the main objectives of the West African Service Center on Climate Change and Adapted Land Use (WASCAL, www.wascal.org) project is to improve in situ observation in the region through intensive instrumentation of experimental catchments. The three experimental catchments selected for this purpose include Dassari, Benin; Vea, Ghana; and Dano, Burkina Faso. The latter catchment is the focus of this study.

Physically-based and spatially distributed hydrological modeling constitutes a challenge in the region because of limited availability of spatially distributed and time

series data. The data limitation can be reduced with an appropriate instrumentation network (Cornelissen, 2016; Danvi et al., 2017; Op de Hipt, 2017; Yira, 2016). The Water balance Simulation Model (WaSiM) (Schulla, 2015) has been successfully applied in the region (Cornelissen et al., 2013; Kasei, 2010; Yira et al., 2016). Therefore, WaSiM was selected to compute hydrological processes and estimate the water balance in the study area.

Regional climate models (RCMs) have increasingly been utilized to assess the hydrological impact of climate change due to their relatively high spatial resolutions (0.11° to 0.44°) compared to global climate models (GCMs) (Gutiérrez et al., 2019). Although it is shown that these climate models fairly represent the West African monsoon, a lot of uncertainties still exist in terms of the direction of future rainfall signals (Cook and Vizy, 2006; Dosio et al., 2015; Gbobaniyi et al., 2014; Paeth et al., 2011; Yira et al., 2017).

Muerth et al. (2012) highlighted three major sources of uncertainties in climate modeling: imperfect climate models, uncertainties regarding future greenhouse gas emissions, and uncertainties about the natural variability of the climate system.

RCMs are imperfect and need to be improved regarding process description, parameterization, and their boundary conditions that are defined using GCMs. Dosio et al. (2015) showed that the use of GCMs as boundary conditions for RCMs strongly influences RCMs seasonal precipitation projections. Moreover, Déqué et al. (2007) looked into the different sources of the uncertainties in climate model projections in the European spatial domain. They found that the uncertainty stemming from GCMs is larger than the other sources of uncertainties (greenhouse gas emission and natural variability of the climate systems).

The uncertainty related to future greenhouse gas emissions is due to the fact that the future emission scenarios (such as representative concentration pathways, RCPs) are based on assumptions. This is because they might considerably change in the future depending on many factors including policies and technologies. Furthermore, the uncertainties originating from greenhouse gas emissions can be attributed to the fact that climate models have to make predictions based on greenhouse gas emissions which have never been recorded in the past.

Natural climate variability in the West African region has been remarkable during the last few decades. There has been a succession of very wet years (1950-1970) and severe drought years (1970-1990) (Frappart et al., 2009; Le Barbé et al., 2002; Mahé, 2009; Nicholson, 1980; Stanzel et al., 2018). The current period (since the 1990s) is said to be a recovery period from the drought (Lebel and Ali, 2009; Maidment et al., 2015). Additionally, rainfall variabilities were spatially highly distributed in the region and resulted in various spatial hydrological responses (Ali and Lebel, 2009; Lebel and Ali,

2009). Some sub-regions were experiencing decrease in surface and groundwater (e.g. Sudan Guinea zone of West Africa), while others were experiencing an increase in water resources (e.g. Sahelian zone)(Leduc et al., 2001; Mahé, 2009).

In addition to the aforementioned sources of uncertainties, bias correction of climate variables, choice of the hydrological model, historical measured data availability, and the complexity of the West African monsoon contribute to the overall uncertainty of the impact of climate change on the hydrology in the region (Cornforth, 2011; Dosio et al., 2015; Klein et al., 2015; Muerth et al., 2012). Ensembles of hydrological models including lumped or distributed models and conceptual or physically-based models are often applied to account for uncertainties related to the hydrological model (Block et al., 2009; Cornelissen et al., 2013; Muerth et al., 2012; Seiller et al., 2012; Velázquez et al., 2013).

In order to account for the large uncertainties in climate projections, it has been recommended to apply ensembles of multiple models and multiple runs (Bormann et al., 2009; Laux et al., 2017; Stanzel et al., 2018).

Several studies have attempted to assess the impact of climate change on water resources in the region (Aich et al., 2014; Bossa et al., 2014; Kasei, 2010). However, few studies investigated impacts of climate change on hydrology at the local scale (Cornelissen et al., 2013; Op de Hipt et al., 2018; Yira et al., 2017). Apart from climate change impact studies land use and land cover change (LULCC) has been proven to significantly influence the hydrology of the region (Giertz et al., 2005; Yira et al., 2016). Therefore, hydrological impact assessment studies might lack significant processes if LULCC are not included in the analyses. Moreover, local studies that combine impacts of climate change and LULCC change on hydrology with a focus on inland valleys are very rare in the West African region (Op de Hipt et al., 2019).

1.2 Objectives

This study aims at:

- Understanding the hydrology of the inland valley system.
- Supporting strategies for efficient management of surface and groundwater resources at local scale for smallholder farming in inland valleys in the Dano catchment.
- Improving adaptation capacities of smallholder farmers to future potential climate change.
- Reducing poverty, improve food security, and preserve ecosystems.

1.3 Research questions

The following research questions have been addressed in order to achieve the objectives:

1) To what extent can an intensive instrumentation combined with fundamental hydrological methods effectively improve the understanding of hydrological processes in four inland valley catchments?

The instrumentation includes the installation and operationalization of five rainfall recorders, seven stream gauges, 64 piezometers in the shallow groundwater (<5 m deep), three points of relatively deep (6, 16, and 25 m) aquifer monitoring, and 64 points of soil moisture measurement at three different depths (5, 30 and 50 cm). The field research has been undertaken in four local catchments within the Dano catchment for three consecutive years. Additionally, rigorous field surveys such as slug tests, sub-surface electrical resistivity, shallow groundwater use in agriculture, and ground surface leveling using a differential global positioning system (DGPS) have been conducted.

The utilized analytical methods include, among others, flow duration curve (FDC), two different approaches of total runoff decomposition (hydrograph based and water electrical conductivity based), spatial and temporal representation of soil water and groundwater variations.

2) How can a physically-based and a spatially distributed hydrological model be applied in a data limited environment to improve the understanding of hydrological processes in an inland valley catchment?

The hydrological model WaSiM was parameterized, calibrated, and validated for the Bankandi-Loffing catchment in Dano. The model was calibrated in 2014-2015 and validated in 2016 preceded by a four-year warmup period. The multi-criteria approach

was utilized for model performance evaluation. WaSiM was chosen because it is mainly based on the quantification of physical hydrological processes at the catchment scale. Consequently, WaSiM may help to understand hydrological processes better than a conceptual model. Moreover, WaSiM is a grid based spatial discretization model, therefore it is adapted to small scale modeling. The model can be used without any financial charge and has already been successfully applied in West Africa.

3) How will the performance of WaSiM develop when the resulting parameter set from calibration and validation of a catchment is applied without recalibration to another catchment in the study area?

The parameter set stemming from the optimization of the Bankandi-Loffing model was directly transferred without recalibration to the Mebar catchment and the model performance was evaluated using multiple criteria. Although the Bankandi-Loffing and Mebar catchments are located in the same climate zone (Sudan Sahelian zone) and the model was evaluated for the same period (2014 to 2016), the successful transfer of the parameters without recalibration will show a hint on the robustness of the physically-based WaSiM model to adequately describe hydrological processes in the study area.

4) What is the impact of climate change and LULCC on water resources in an inland valley catchment? What are the implications of climate change on adaptation strategies?

Five RCMs originating from the Coordinated Regional Climate Downscaling Experiment (CORDEX-Africa, www.cordex.org) project and four historical and three future predicted land use and land cover (LULC) data sets provided by Op de Hipt(2017) were utilized for this purpose. Annual and seasonal change in water balance components were scrutinized. The implications of the future potential climate change on water management strategies were explored in order to set the base for policy oriented decision making.

1.4 Structure of the thesis

The study is divided in eight chapters from the general introduction to the general conclusion.

After the general introduction in chapter 1, chapter 2 describes the physical aspects of the study area including the geomorphology of the investigated catchments and characteristics of inland valleys, the climate and the vegetation, characteristics of the soil, the geology, hydrogeology and groundwater use in agriculture. The WaSiM hydrological modeling approaches including numerical descriptions of the hydrological processes and the evaluation of the model performance are laid out in chapter 3. Chapter 4 is dedicated to the instrumentation of the selected catchments. The number and locations of the measurement devices, the measurement principles and the quality and the limitation of the measurements are illustrated in this chapter. Chapter 5 characterizes runoff, groundwater and soil water using fundamental hydrological methods in order to set the base of the hydrological process understanding for further sophisticated analysis. Chapter 6 presents the hydrological modeling of an inland valley catchment (Bankandi-Loffing) using WaSiM and the transfer of a parameter set from the calibrated Bankandi-Loffing catchment to the uncalibrated Mebar catchment without recalibration. Chapter 7 deals with the hydrological impacts of climate change and LULCC and the implications of these changes for water resource management in the area. Finally, chapter 8 provides the overall conclusion of the study.

2 STUDY AREA

2.1 Overview

The Dano catchment is located in the south-west of Burkina Faso in West Africa (Fig. 2-1). Except for the western border, made up of the Ioba Mountains, the majority of the catchment is flat with a mean slope of 2° to 3° allowing the formation of inland valleys. The province of Dano consists of 22 villages and the town of Dano, with the province being home to around 55,000 people with 63% living in rural areas (Commune de Dano, 2013). Approximately 80% of the population are small-scale farmers who mainly practice rainfed subsistence agriculture (Pale and Da, 2013). The livelihood of farmers is jeopardized by the unstable climate potentially causing yield losses as a consequence of droughts or inundations. The last two decades have seen investments in building many small reservoirs in order to cope the impacts of climate variability on poor rural population. However, the efforts are far from meeting the necessary water demand for irrigation and especially for future challenges. Two reservoirs were built in the catchment, namely in Fafo in 1987, located in the northern part, and in Moutori in 2002, located in the southern area of the catchment. Additionally, some initiatives have promoted shallow groundwater use for vegetable cultivation in the dry seasons. However, basic information on the shallow groundwater is insufficient or lacking (Eguavoen and McCartney, 2013).

Hydrographically, Dano is drained by intermittent streams which are tributaries of the Black Volta or Mouhoun River. Black Volta is a transboundary river between three countries namely Burkina Faso, Côte d'Ivoire and Ghana.

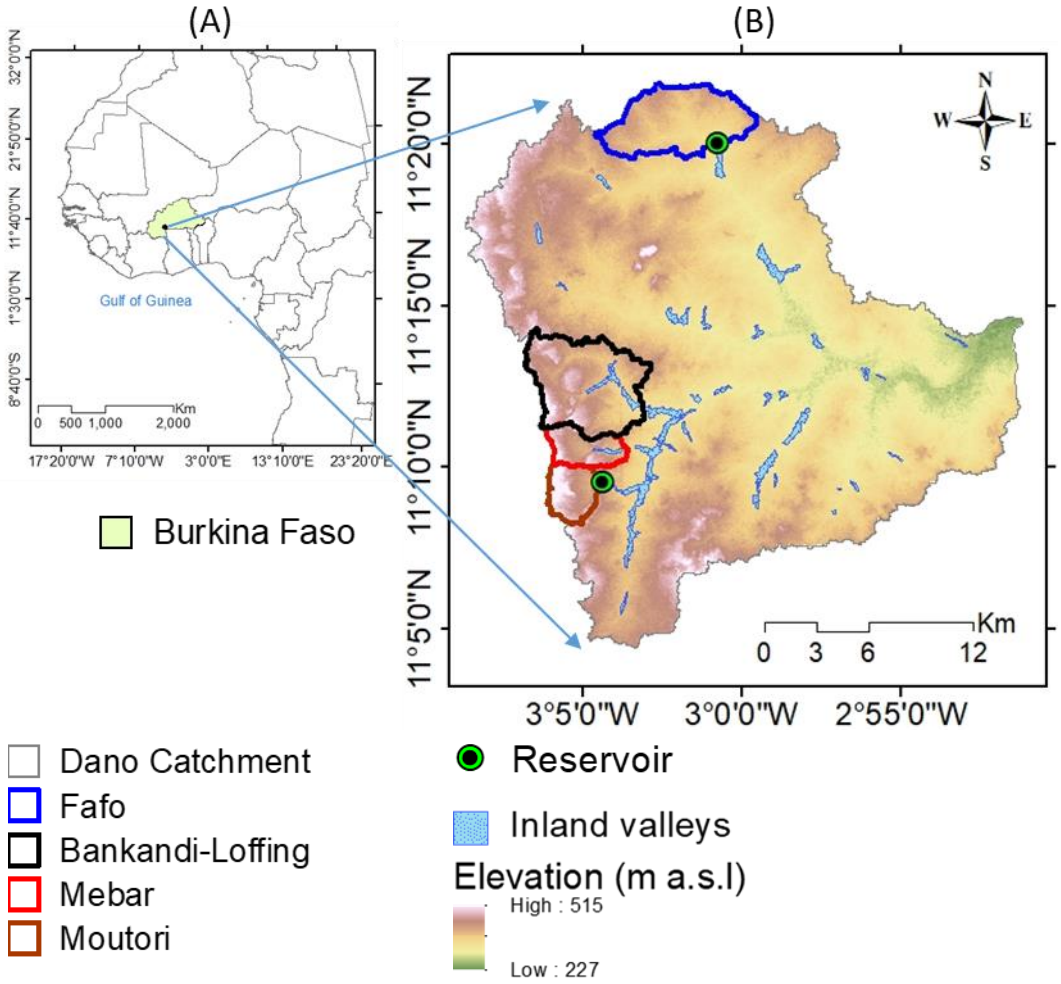

Fig. 2-1. Location of the Dano catchment (A) with the investigated small catchments and the inland valleys (B) (data on inland valleys provided within the WASCAL project).

This study focuses on four small catchments (Fig. 2-1), namely Bankandi-Loffing, which covers an area of 30 km^2, followed in size by Fafo (24 km^2), Mebar (8 km^2) and Moutori (8 km^2). They were selected based on the management options already in place and the representative spatial distribution in Dano. On the one hand, Fafo and Moutori are reservoir based catchments. Therefore, they are characterized by a high water availability which enables cropping during the dry season. The farmers of these catchments have access to technical support and agricultural inputs including fertilizer. On the other hand, Mebar is a traditional used agricultural catchment. It is characterized by a completely rainfed cropping system which has low access to the agricultural inputs and uses local traditional knowledge. Consequently, there is no cropping during the dry season and productivity is lower compared to the other catchments. The third catchment is qualified as mixed management scheme and is represented by the Bankandi-Loffing catchment. In Bankandi-Loffing, traditional agriculture is practiced in

the upstream areas, while improved agricultural activities are observed in the downstream areas. For instance, some small concrete flumes were installed in order to control runoff, water distribution into the fields and drainage from the fields. These three management schemes are representative of agriculture practices in the region.

2.2 Inland valleys

Inland valleys are wetlands located at the upper reaches of main river systems (Windmeijer and Andriesse, 1993) with a significant contribution of groundwater to soil water (Mitsch and Gosselink, 2015). They include the valley bottoms and their hydromorphic fringes which may be submerged in the rainy seasons and some part of the dry season (Andriesse et al., 1994). More water, nutrients, and organic matter are available in the valley bottoms and hydromorphic fringes compared to the adjacent uplands. The low slopes of inland valleys reduce outflow from the valley bottoms, therefore increase infiltration when the conditions of soil allow it, and in turn increase groundwater recharge. In return, groundwater can supply inland valleys temporarily or during the complete dry season depending on the groundwater storage and extent. Inland valleys are estimated to cover 22-52 million ha in West Africa (Windmeijer and Andriesse, 1993) and approximately 1200 ha in the Dano catchment (Fig. 2-1).

Longitudinally, inland valleys can be subdivided in three parts: the valley head, the midstream part, and the downstream part of the valley. The valley head, which is located at the upstream part of the valley, is characterized by a concave profile, an absent stream channel, and a soil dominated by colluvial processes. The midstream part is wider than the valley head and has an almost flat valley bottom, a shallow stream channel, and it is located at the central part of the valley. Finally, the downstream part of the valley is characterized by an alluvial soil, low slopes, and a flooding during high flows. These downstream areas are gradually converted to floodplains (Raunet, 1985). Kiepe (2006) defines a *floodplain* as a relatively flat and dry area made of recent alluvial deposits along a stream or a river undergoing periodic inundations.

Inland valley soils are unique in the way that they are saturated during at least a few months in the wet season. They accumulate partially decayed plants and nutrients washed away from the adjacent uplands (Mitsch and Gosselink, 2015). Although the West African inland valleys soils are less fertile than the paddy soils in tropical Asia (Abe et al., 2010), an appropriate water management in combination with selection of adapted crops could help small hold farmers to reach food security (Carsky et al., 1993; Ogban and Babalola, 2003).

2.3 Climate

The climate is of Sudan Sahelian type with an annual rainfall of 800-1200 mm concentrated in a unimodal rainy season starting in May and ending in October (Fig. 2-2a). The mean annual rainfall from 1970 to 2013 is 886 mm. More than 77% of annual rainfall occurs from June to September with August recording the highest rainfall (225 mm or 25% of annual rainfall). The average daily minimum and maximum temperatures are 21°C and 32°C respectively with an overall daily mean temperature of 28°C from 1970 to 2013. However, the West-African rainfall regime has been one of the most affected by climate variability and climate change during the last five decades with disastrous droughts (Sahel drought) in the 1970s and 1980s (Lebel and Ali, 2009). The Standardized Precipitation Index (SPI) (Hayes et al., 1999) and the Standardized Precipitation Evaporation index (SPEI) (Beguería et al., 2014; Vicente-Serrano et al., 2010) were calculated for twelve month intervals (Fig. 2-2b) using monthly precipitation and temperature data from 1970 to 2016. The results show that the area experienced frequent occurrence of droughts ranging from a moderately dry (SPI – SPEI of -1.49 to -1) to extremely dry climate (SPI-SPEI less than -2) conditions according to categorizations of Hayes et al. (1999) and Yu et al. (2014).

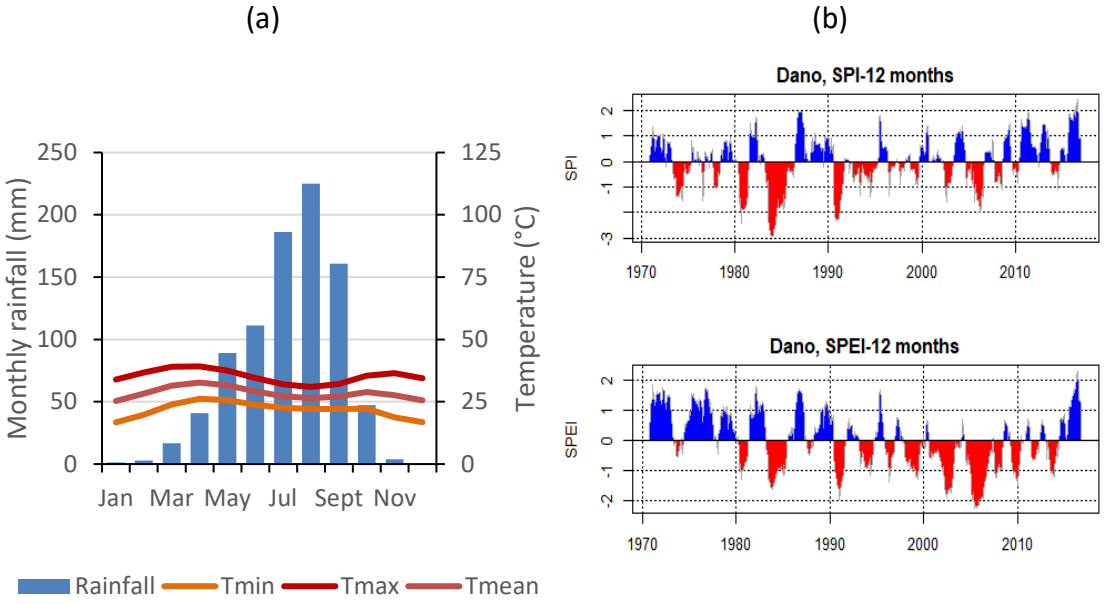

Fig. 2-2. Climate characteristics in the region: (**a**) mean monthly rainfall, minimum, maximum and mean temperature for 1970-2016, (**b**) 12 months Standardized Precipitation Index (SPI) and Standardized Precipitation Evaporation Index (SPEI) for the period 1970-2016. Rainfall data were measured in Dano and temperature data in Boromo (a town located approximately 70km north of Dano). Data source: DGM (Direction Nationale de la Météorologie du Burkina Faso).

2.4 Geology and hydrogeology

The geology of Burkina Faso consists of Precambrian formations which are part of the West-African craton. The paleoproteozoic basement, which is covered by sedimentary formations, is made of Birimian green stone belts (2238 to 2170 million years old), volcano-sedimentary and plutonic sequences (Giorgis et al., 2014). In West-Africa, including Burkina Faso, Mali, and Ghana, the Birimian formations are known as the major source of gold and diamond deposits (Henry et al., 2004). In Dano, the Ante-Birimian granites are found at the upstream areas of Bankandi-Loffing, Mebar, and Fafo (western area). Whereas, at the downstream areas (eastern area), the Birimian shists can be observed at Bankandi-Loffing and Mebar while green rocks at found at Fafo. Moutori is exclusively underlain of Ante-Birimian granite (Fig. 2-3).

The regional geology is made of a crystalline type of rocks and therefore groundwater is mainly available in fractures or in the weathered rock layers called saprolites. The selected catchments are located in an area where the weathered aquifer is 10-30 m thick. The weathered aquifer is often saturated (Fig. 2-3). The geological transect shown in III-A‘ (Fig. 2-4) is located approximately 60 km north of Dano in the area of almost the same geological characteristics as in the Dano catchment. It shows

granites in the basement covered by the weathered profile whose thickness varies in the space with the maximum thickness reached around the major fractures and lowland areas. It highlights the role of water in accentuating the weathering process of rocks. Moreover, an overlain alluvial aquifer can be found in the valley bottoms of inland valleys. According to the information collected during the digging of the piezometers, the alluvial aquifers are made of loamy sand to sandy clay materials.

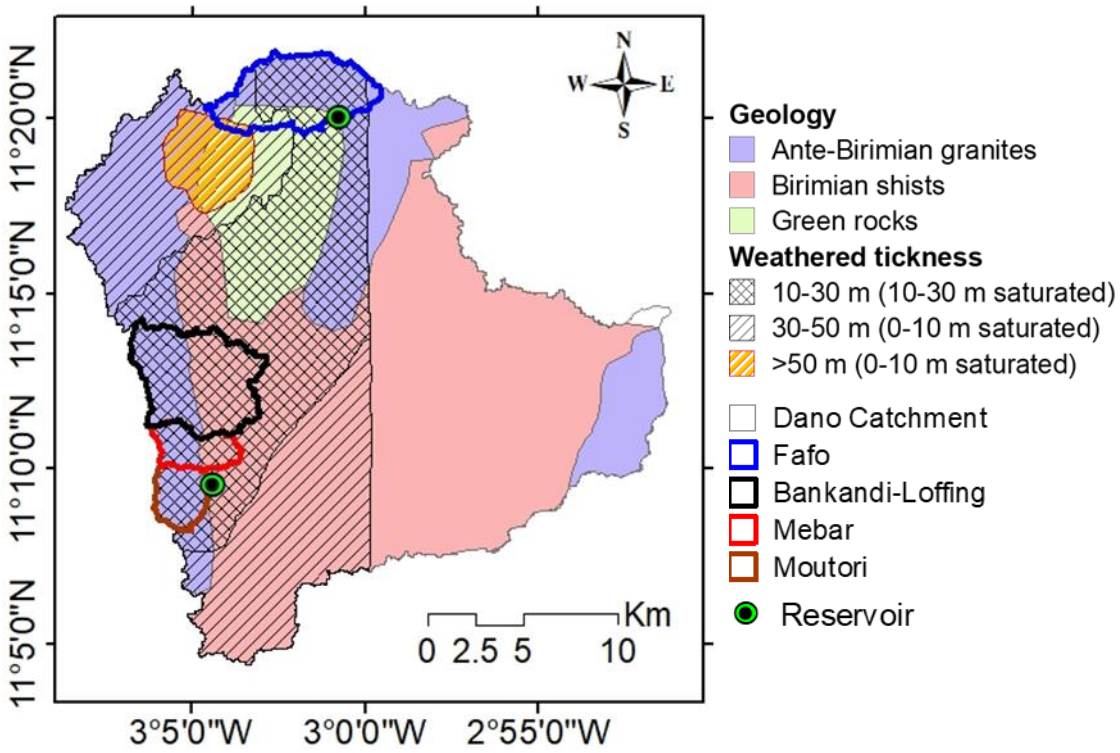

Fig. 2-3. Geology and hydrogeology of Dano catchment; thickness of the weathered horizon data only cover the eastern area of the catchment (Data set: IWACO, 1993).

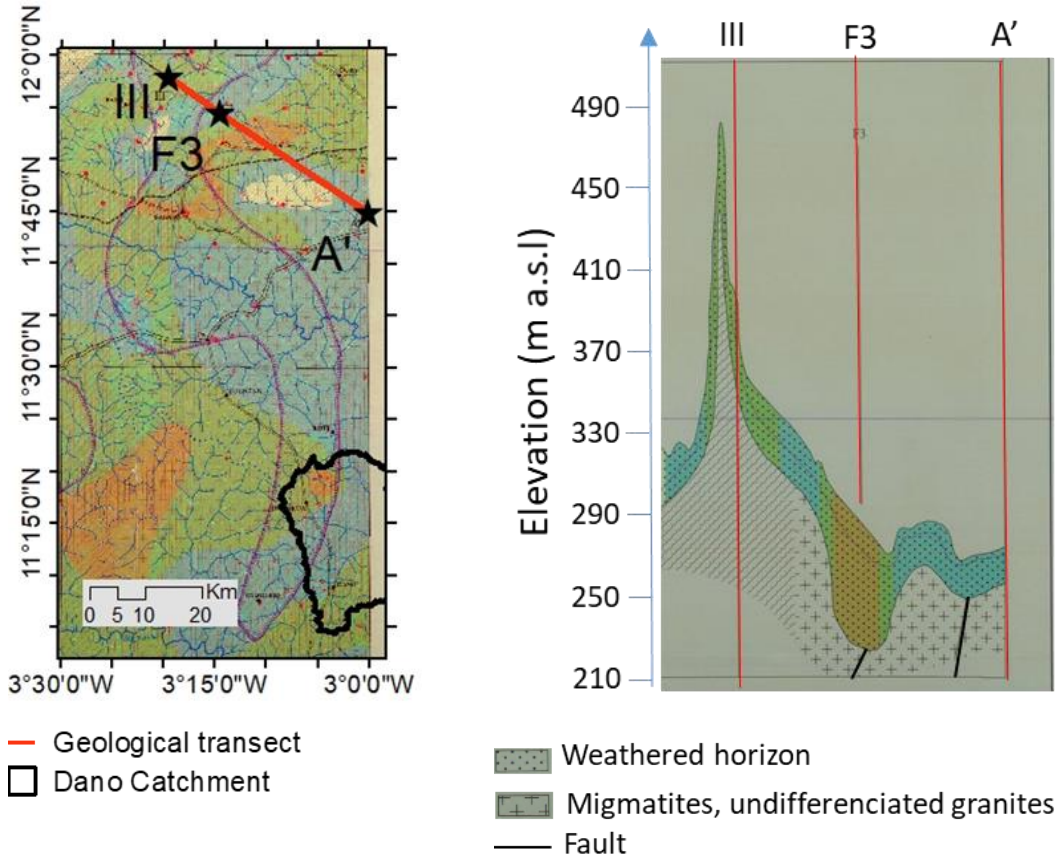

Fig. 2-4. Geological transect III-A' 60 km north of the Dano catchment (source: Bureau des Mines et de la Géologie du Burkina Faso).

2.5 Soil characteristics

The soil map (Fig. 2-5) was initially created in the French CPCS (Commission de Pédologie et de la Cartographie des Sols) system by BUNASOL (Bureau National des Sols)- Burkina Faso. It was then converted to the closest possible equivalence in the WRB (World Reference Base) system (WRB, 2006). Hence, the Umbric Gleysol (sol hydromorphe peu humifère à pseudogley de surface) is the major soil type in the valley bottoms whereas the Vertic Cambisol (sol brun eutrophe hydromorphe vertique) is dominant at the slopes in Moutori, Mebar, and Bankandi-Loffing. Concerning Fafo, the Plinthic Lixisol (sol ferrugineux tropical lessivé à tache et à concretion) is mainly found on the slopes instead. It has to be noted that this soil map was created at the country scale. Uncertainties are therefore high when the map is utilized for local scale analysis. A more accurate map after Hounkpatin (2017) in the WRB system was utilized for the southern catchments (Bankandi-Loffing, Mebar, and Moutori).

A soil survey carried out by Hounkpatin (2017) was based on composite sampling per horizon down to 1m depth. In total, 1177 points were described in the Dano

catchment. The results show a similarity in terms of soil depth between the Plinthosols and the Cambisols. The average depth was 0.5 m for the Plinthosols and 0.58 m for the Cambisol. Gleysols and Lixisols are shallower in comparison to the previous soil types. Their average depths are 0.4 m for Gleysols and 0.45 m for Lixisols. Due to fast land use change, the soils are affected by erosion with soil organic matter loss (Op de Hipt et al., 2017; Schmengler, 2011). Moreover, high coarse particle content was observed especially in Plinthosols (62% of total soil weight).

The saturated volumetric soil water which was measured at the WASCAL laboratory in Dano by Yira (2016) proved that the Cambisols have the highest saturated soil water with an average of 46% and a maximum of 55%. The mean saturated soil water contents were 40%, 38%, and 37% for the Gleysols, Plinthosols, and Lixisols respectively. The mean measured saturated hydraulic conductivity for Plinthosols and Cambisols (approximately 10^{-4} m s^{-1}) are higher than those recorded in Gleysols and Lixisols (10^{-5} m s^{-1}) because of the higher clay (32% to 33%) and silt (50% to 57%) contents in Gleysols and Lixisols. Moreover, the mean bulk density was higher in Plinthosols (1.6 g cm^{-3}) than in Gleysols (1.4 g cm^{-3}), the Cambisols, and Lixisols (1.3 g cm^{-3}). However, the average organic carbon content is almost equally low at 1% for the investigated soils (Yira 2016).

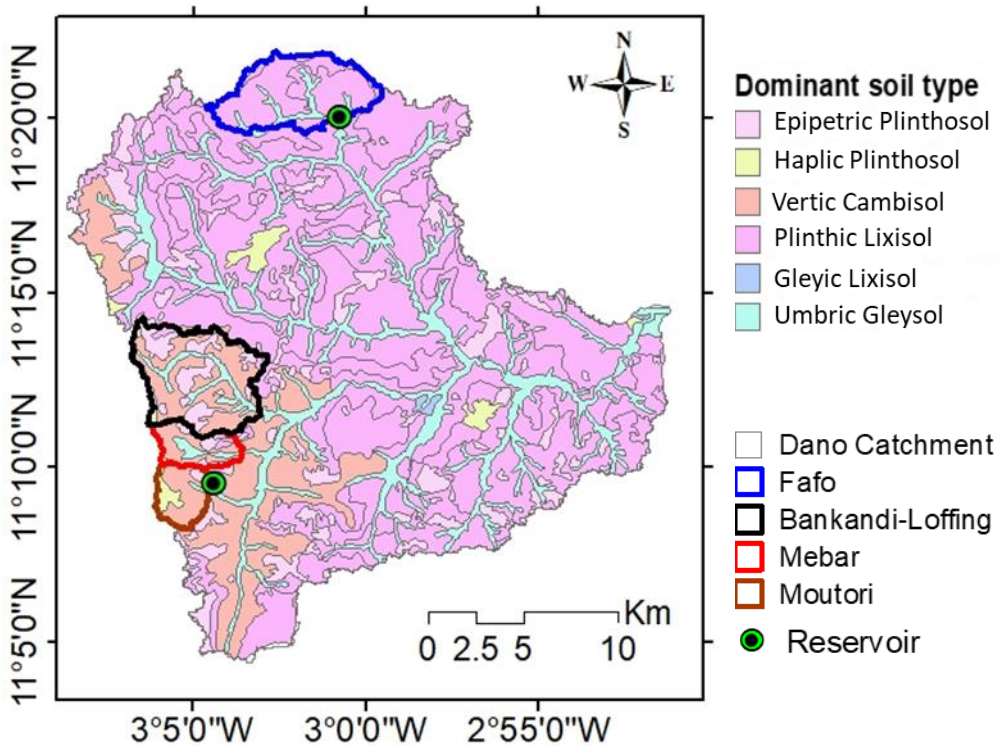

Fig. 2-5. Soil map of the Dano catchment (conversion from the CPCS map provided by BUNASOL to the WRB system).

2.6 Land use and land cover (LULC)

The LULC map of 2013 (Fig. 2-6) was created based on three satellite products, namely RapidEye, TerraSAR-X, and Landsat (Forkuor and Thiel, 2013). The overall accuracy and kappa coefficient (Congalton, 1991) were 78.4% and 0.75 respectively.

Savanna (named mixed vegetation) is made of shrubs, trees, and herbs. It is the major land cover type in the area of Moutori (64% of catchment area), Mebar (41%), and Bankandi-Loffing (40%). In contrast, Fafo is mainly covered by forest (27%) while Mebar has the least forest coverage (7%). Millet (*Pennisetum glaucum*), sorghum (*Sorghum bicolor*) (named cereals on the LULC map), and maize (*Zea mays*) are the main food crops whereas cotton (*Gossypium hirsutum*) is the main cash crop. Rice is usually cultivated in areas with high water availability like in inland valleys or irrigated fields in reservoir-based catchments. Reservoirs allow for rice cropping in both rainy and dry seasons. On the land use map, the water bodies, which correspond to reservoirs in Fafo and Moutori, can be observed. About 56% of the area of Fafo and 51% of Mebar are under cultivation. The grasslands which are observed in Bankandi-Loffing and Mebar are used for grazing cattle.

(a)

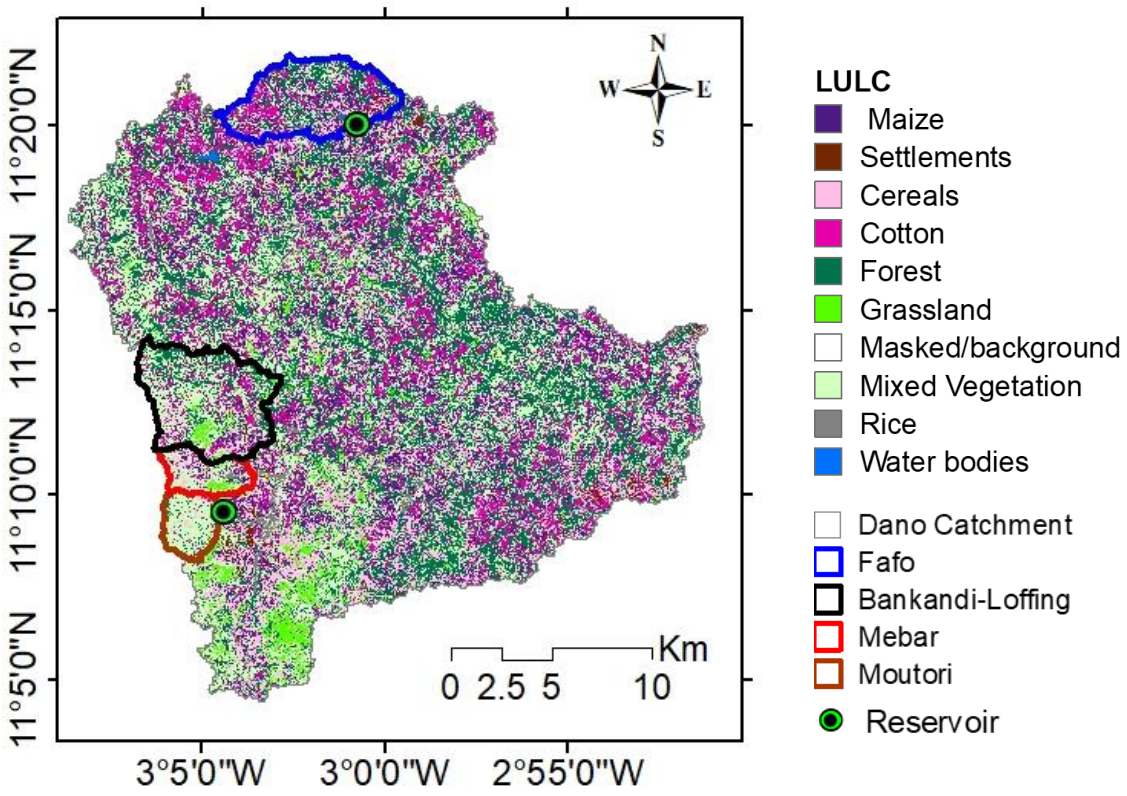

(b)

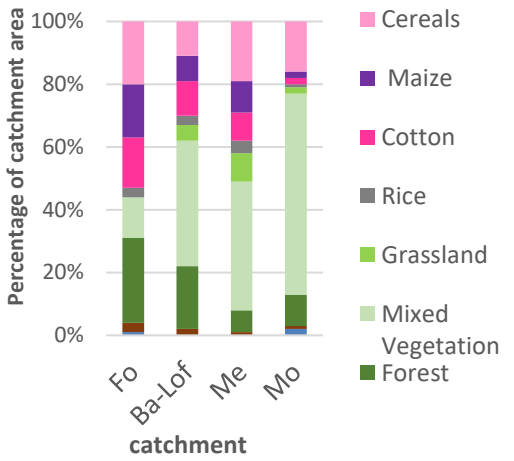

(c)

	Percentage of catchment area (%)			
LULC	**Fo**	**Ba-Lof**	**Me**	**Mo**
Cereals	20	11	19	16
Maize	17	8	10	2
Cotton	16	11	9	2
Rice	3	3	4	1
Grassland	0	5	9	2
Mixed Vegetation	13	40	41	64
Forest	27	20	7	10
Settlements	3	2	1	1
Water bodies	1	0	0	2

Fo: Fafo; **Ba-Lof**: Bankandi-Loffing; **Me**: Mebar; **Mo**: Moutori

Fig. 2-6. Landuse and land cover (LULC) map of the year 2013 for Dano with the percentage of each LULC per selected catchment (Data set: Forkuor, 2014).

2.7 Groundwater use in agriculture

Agriculture is mainly rainfed in the Dano catchment except for rice cultivation which is mostly irrigated. Two small reservoirs are in Moutori and Fafo, whereas Bankandi-Loffing has an improved management of discharge which is diverted to the fields using small concrete flumes (Fig. 2-7). Because of high water availability, rice production is practiced at these three locations. In Fafo, the reservoir water is sufficient for irrigation in both the rainy and the dry seasons, whereas in Moutori the reservoir water is insufficient. Therefore, farmers decide to use it only in the dry season. The Moutori reservoir with its storage capacity of 360,000 m^3 is comparable in size with the Fafo reservoir (storage capacity of 480,000 m^3) but the Fafo catchment (24 km^2) is three times larger than that of Moutori. The comparison of the two catchments equipped with reservoirs proved a significant difference in terms of land use. In Moutori, savanna (or mixed vegetation) is largely dominant (64% of catchment area) whereas, in Fafo, forest has the highest share (27% of the catchment area) with savanna having only 13% of the catchment area. Moreover, more than half of the Fafo catchment is under cultivation (56% cropland) whereas in Moutori only 23% is cropland (see Fig. 2-6). This can contribute to higher infiltration and evapotranspiration in Moutori compared to Fafo, consequently, less surface water is provided to the reservoir in Moutori compared to Fafo. Concerning soils, Lixisols, the dominant soil type in Fafo, have finer material (33% clay and 57% silt) than Cambisol in Moutori (28% clay and 46% silt). The irrigated land in Moutori (20 ha) is slightly larger than the irrigated land in Fafo (15 ha), thus irrigation water demand in Moutori is higher compared to Fafo (Schmengler, 2011). The combined effect of soil properties, LULC, and the catchment sizes is the reason for the lower volume of water in the Moutori reservoir compared to Fafo. Hence, Moutori farmers opt not to practice supplementary irrigation in the rainy season using reservoir water. Instead, the reservoir water is exclusively kept for the dry season.

Fig. 2-7. Concrete flume (showed by the red arrow) for field water management in the Bankandi-Loffing catchment.

In the last few years, the shallow groundwater has been used for vegetable cultivation. Shallow alluvial aquifers are often found in lowlands with depth to groundwater much less than 10 m. A survey conducted in order to investigate the current use of the shallow groundwater for agriculture sampled 50 wells of two types in Moutori, Loffing, and Mebar. The sample was composed of basic or unimproved wells and improved wells. The basic wells are characterized by shallow depths and a missing concrete structure stabilizing the edges while improved wells are equipped with a concrete tube and are deeper than the basic wells (Fig. 2-8).

Basic well (*December 23rd 2016*)

Improved well (*December 24th 2016*)

Fig. 2-8. Pictures of the two types of investigated wells in Dano.

The average depth of improved wells is approximately 7 m whereas it is only 1.8 m for basic wells. The depth distribution of 41 basic wells in Moutori, Mebar and Bankandi-Loffing catchments shows depths ranging from 0.5 to 2 m with the majority

(56%) being 1 to 1.5 m deep and only 7% deeper than1.5 m. Moreover, at the time of the survey in late December 2016, two months after the end of rainy season, for 98% of the basic wells the groundwater table was less than 1 m below the ground level with 51% of the values ranging from 0.5 to 1 m. Most of the shallow wells are not deeper than 1.5 m, thus the available water depth in the wells is only 0.5 to 1 m with a high probability of drying out before the end of the dry season in March-April. Few shallow wells and most of the deep wells are permanent, especially during the wet years.

The sizes of the farms are rather small, ranging from 0.03 to 0.18 ha with an average size of 0.1 ha for the area equipped with improved wells. The field size range was 0.01 to 0.12 ha with an average of 0.06 ha for the area with the basic wells. The total cultivated area using basic wells (0.84 ha) is only slightly larger than the total area relying on improved wells (0.57 ha). A comparison with the total area under cultivation using surface water (20 ha for the Moutori reservoir) shows that the total area under cultivation using the shallow aquifer in the investigated area is far smaller (1.41 ha) than the area using surface water. The distribution of field sizes (Fig. 2-9) using both improved and basic wells for irrigation shows that 66% of the fields are smaller or equal to 0.1 ha.

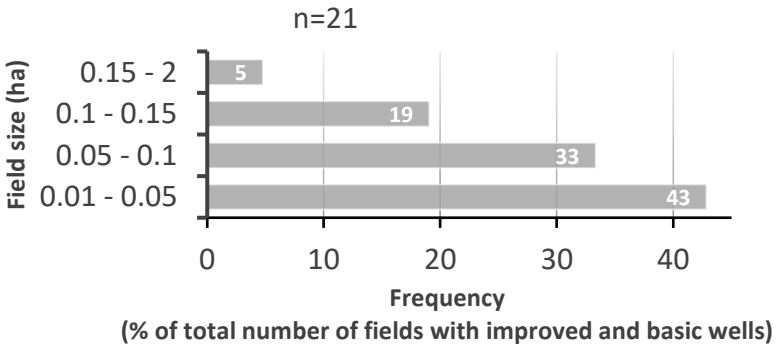

Fig. 2-9. Size of irrigated fields.

On average, the improved and basic wells have been used for irrigation for 9 and 7 years respectively, mainly once every three days (43% of the cases) or daily (36% of the cases), although two irrigations per day are sometimes also applied. The main crops are vegetables (Fig. 2-10) but in addition fruits like banana and papaya are also irrigated at some locations. The most frequent vegetables are tomato, onion, and cabbage followed by eggplant and okra.

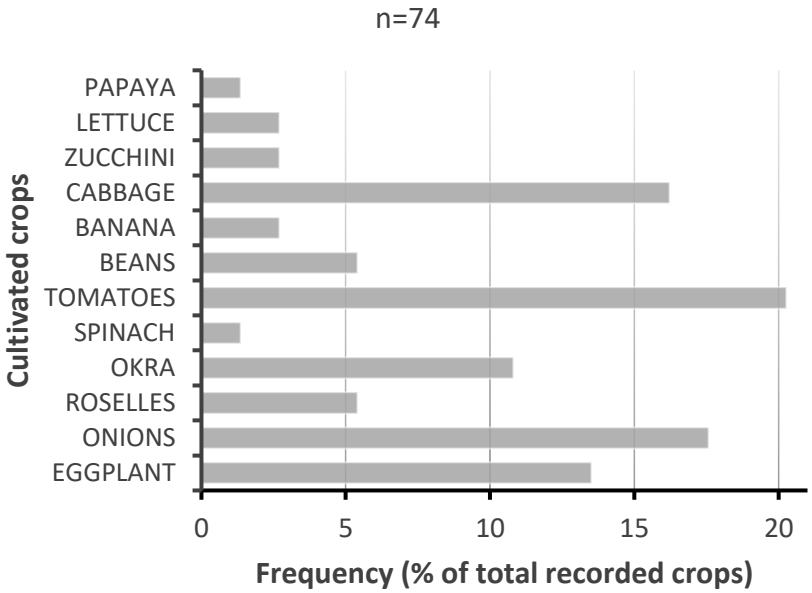

Fig. 2-10. Crops irrigated using shallow aquifer.

The growing period in the dry season is between October-November to April-May. It is important to point out that supplementary irrigation is not practiced using groundwater during the rainy season for annual crops and vegetables, even when farmers experience dry spells. Chapter 5 will investigate the potential of the shallow aquifer to support supplementary irrigation as an adaptation strategy to cope with climate variabilities.

3 THE HYDROLOGICAL MODEL WASIM

3.1 Introduction

WaSiM (Water balance Simulation Model) is a grid-based hydrological model which is deterministic and mainly physically-based (Schulla, 2015). In this study, WaSiM (version 9.10.01) was applied to simulate hydrological processes and the impact of climate and land use change on water resources in two inland valley catchments (Bankandi-Loffing and Mebar) in the Dano catchment.

In the data limited environment of Dano, data driven models (conceptual or empirical) might not represent the hydrological processes well. A recent instrumentation in the catchment under the scope of this study helped to collect high resolution hydrological and soil data. Therefore, a physically-based model can be applied (Devia et al., 2015). WaSiM has been successfully applied in the West African region (Cornelissen, 2016; Kasei, 2010) and in the Dano catchment (Yira, 2016). Moreover, WaSiM is an open source software and is sufficiently documented thus can be employed by anyone without cost in the West African region. A grid-based model can be applied because the catchments are small. The aforementioned reasons motivated the selection of WaSiM to model hydrological processes in the study area.

3.2 Numerical representation of hydrological processes

3.2.1 Evapotranspiration

Evapotranspiration is one of the most important hydrological processes in the West African region (Idrissou et al., 2015; Oguntunde et al., 2018). The annual potential evapotranspiration (ETp) exceeds 2000 mm and is approximately twice as much as rainfall in the region (Cornelissen et al., 2013; Yira et al., 2016). Therefore, the climate system is water limited not energy limited. Two evapotranspiration methods were applied in this study: Penman-Monteith method and Hamon method. The latter was used when only air temperature was available for ETp estimation.

Penman-Monteith ETp

The Penman-Monteith (Monteith, 1975) approach was applied to compute the ETp when the required climate variables (air temperature, relative humidity, global radiation, and wind speed) were available (Allen et al., 2006; Cai et al., 2007; Chiew et al., 1995; Gavilán et al., 2007).

The potential transpiration from plant leaves (TP), the evaporation from the bare soil (EP), and the interception evaporation (EIP) are separately estimated in WaSiM. The potential evapotranspiration is expressed by equation (3-1).

$$\lambda E = \frac{3.6\ \frac{\Delta}{\gamma_p}\ (R_n - G) + \frac{\rho\ C_p}{\gamma_p\ r_a}(e_s - e)\ t_i}{\frac{\Delta}{\gamma_p} + 1 + \frac{r_s}{r_a}} \quad (3\text{-}1)$$

With:

λ	latent vaporization heat, $\lambda = (2500.8 - 2.372\ T)$	[kJ kg^{-1}]
T	Temperature	[°C]
E	latent heat flux	[mm m^{-2}]
Δ	slope of the saturated vapor pressure curve	[hPa K^{-1}]
R_n	net radiation	[Wh m^{-2}]
G	soil heat flux	[Wh m^{-2}]
ρ	density of dry air	[kg m^{-3}]
C_p	specific heat capacity of dry air at constant pressure	[kJ kg^{-1} K^{-1}]
e_s	saturation vapor pressure at the temperature T	[hPa]
e	actual vapor pressure (observed)	[hPa]
t_i	number of seconds within a time step	[s]
γ_p	psychometric constant	[hPa K^{-1}]
r_s	bulk surface resistance	[s m^{-1}]
r_a	bulk aerodynamic resistance	[s m^{-1}]

The bright day potential transpiration (TP_{day}) and night potential transpiration (TP_{night}) are estimated by replacing bulk surface resistance (r_s) by the bright day surface resistance ($r_{s.day}$) and the night surface resistance ($r_{s.night}$), respectively. Equation (3-2) calculates $r_{s.day}$ and equation (3-3) calculates $r_{s.night}$.

$$r_s = r_{s.day} = \frac{1}{\left(\frac{1-A}{r_{sc}}\right)} \quad (3\text{-}2)$$

$$r_s = r_{s.night} = \frac{1}{\left(\frac{LAI * vcf}{2500}\right)} \quad (3\text{-}3)$$

Where: $A = f^{LAI*vcf}$ (f ~ 0.6-0.7); r_{sc}=canopy surface resistance; LAI= leaf area index; and vcf=vegetation cover fraction.

The potential evaporation from the soil (EP) employs evaporation surface resistance (r_{se}) as bulk surface resistance and the potential interception evaporation (EIP) is computed using the interception surface resistance (r_{si}) in place of r_s in the equation (3-1). Moreover, for bare soil (vcf=0 or LAI=0), the r_s is set to 2500

s m^{-1} whereas, r_s is set to null value for an opened water in order to allow maximum evaporation.

When the model is run at a daily time resolution, TP, EP, and EIP are automatically subdivided into day and night calculations of evapotranspiration. The equations (3-4) and (3-5) describe TP_{day} and TP_{night} respectively.

$$TP_{day} = \frac{\Delta_{day}\left(R_{n.day} - G\right) + \rho\, c_p\left(e_{s.day} - e_m\right)}{\Delta_{day} + \gamma_p\left(1 + \frac{r_{s.day}}{r_a}\right)}\, d \qquad (3\text{-}4)$$

$$TP_{night} = \frac{\Delta_{night}\left(R_{n.night} - G\right) + \rho\, c_p\left(e_{s.night} - e_m\right)}{\Delta_{night} + \gamma_p\left(1 + \frac{r_{s.night}}{r_a}\right)}\, (24 - d) \qquad (3\text{-}5)$$

With:

$\Delta_{day}; \Delta_{night}$	Slope of the saturated vapor pressure curve for temperatures at day (T_{day}) at and night (T_{night})	[hPa K^{-1}]
$R_{n.day}$; $R_{n.night}$	Net radiation for day and night	[Wh m^{-2}]
$e_{s.day}$; $e_{s.night}$	Saturation vapor pressure as function of T_{day} and T_{night}	[hPa]
e_m	Mean daily saturation vapor pressure	[hPa]
$r_{s.day}$; $r_{s.night}$	Surface resistance of the vegetation for bright day and for the night after equations (3-2) and (3-3)	[s m^{-1}]
d	Relative duration of bright day	[-]

The other ETp components (EP and EIP) were calculated using the same equations (3-4) and (3-5) with r_s replaced by r_{se} for EP_{day}, EP_{night} and by r_{si} for EIP_{day}, and EIP_{night} (for more detail, see Schulla, 2015)

Hamon ETp

The Hamon method only uses temperature for ETp estimation (Hamon, 1963; Lu et al., 2005). This approach was needed when assessing the hydrological impact of climate change as other required climate variables (solar radiation, wind speed, air humidity) were not available for the Penman-Monteith ETp calculation. The equation (3-6) presents the Hamon ETp computation.

$$ETp = 0.1651\, f_i\, \frac{h_d}{12}\, \frac{216.7\, e_s}{T + 273.3} \qquad (3\text{-}6)$$

With: fi: empirical factor; h_d: the day length [h]; e_s: the saturated vapor pressure at the temperature T [hPa]; and T: temperature [°C].

The monthly empirical factor (f_i) varies with the region. Therefore, the factor was first optimized for the study area during 2014-2016 in order to obtain good agreement between Hamon and Penman-Monteith ETp. The optimized *fi* was then applied to the hydrological impact assessment period (1971-2030).

Actual evapotranspiration (ETa)

The estimation of ETa depends on the actual soil water content. Equation (3-7) shows four different ranges of soil water content and the corresponding ETa calculations. Moreover, the reductions of transpiration resulting from water and oxygen stresses were considered as illustrated by Fig. 3-1 (Feddes and Zaradny, 1978; Schulla, 2015).

$$\begin{aligned} ETa &= 0 && if\ \ \theta(\psi) \le \theta_{wp} \\ ETa &= ETp\ \frac{\theta(\psi) - \theta_{wp}}{\theta_{\psi g} - \theta_{wp}} && if\ \ \theta_{wp} < \theta(\psi) \le \theta_{\psi g} \\ ETa &= ETp && if\ \ \theta_{\psi g} < \theta(\psi) \le\ \eta\theta_{sat} \\ ETa &= ETp\ \frac{\theta_{sat} - \theta(\psi)}{\theta_{sat} - \eta\theta_{sat}} && if\ \ \eta\theta_{sat} < \theta(\psi) \le \theta_{sat} \end{aligned} \qquad (3\text{-}7)$$

With: $\theta(\psi)$: the soil water at the actual suction ψ; $\eta\theta_{sat}$: the maximum relative water content without partial or total anaerobic conditions; θ_{wp}: the soil water at the permanent wilting point; $\theta_{\psi g}$: the soil water at a given suction ψg determines the beginning of water stress; and θ_{sat}: the soil water at saturation.

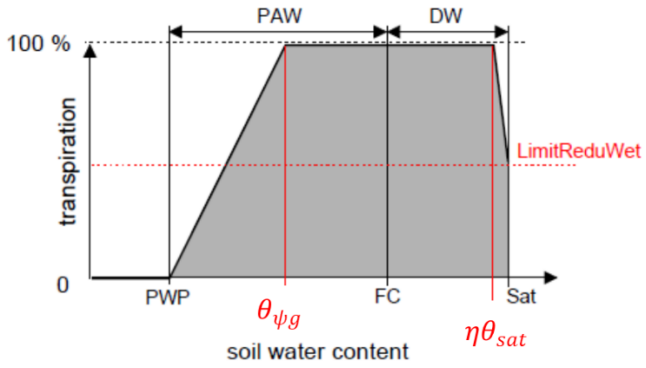

Fig. 3-1. Variation of transpiration with soil water content (Schulla 2015). PAW: plant avalaible water; DW: drainable water; PWP: permanent wilting point; FC: field capacity; Sat: saturation; LimitReduWet: limite of transpiration reduction due to anaerobic conditions.

3.2.2 Interception evaporation

A bucket approach was used for the interception evaporation modeling. The maximum interception storage (SI_{max}) was computed using equation (3-8).

$$SI_{max} = vcf\ LAI\ h_{SI} \tag{3-8}$$

Where SI_{max}: maximum interception storage capacity [mm]; vcf: vegetation cover fraction; LAI: leave area index; and h_{SI}: maximum height of water at the leaf surface.

From equation (3-8), it is clear that no interception is computed for a bare soil (vcf=0 and/or LAI=0). During precipitation, interception storage must be filled before throughfall can be generated and the primary source of ETa extraction is interception storage. It is only when the interception storage is empty that the water can be evaporated from the soil.

3.2.3 Unsaturated zone model and runoff generation

Fig. 3-2 describes how WaSiM computes surface flow or overland flow (QD), interflow (QI), and base flow (QB) from grid cell level to the river that will transport water to the outlet of the catchment.

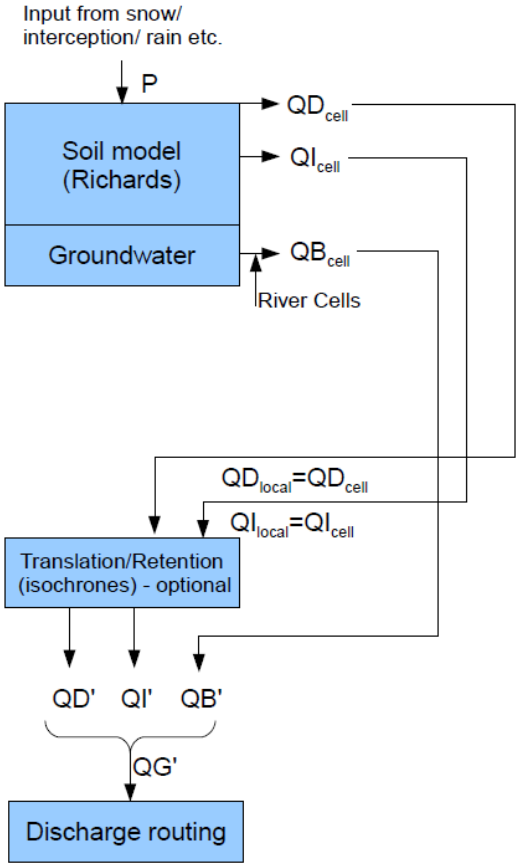

Fig. 3-2. Flow chart of soil and routing modeling (Schulla 2015).

Vertical fluxes after Richards equation

Vertical water fluxes or infiltration in the soil were modeled using the Richards equation (Richards, 1931; Richards and Weaver, 1944). The Richards equation gives one-dimensional description of vertical water fluxes through unsaturated zone and is derived from the continuity equation (3-9). The discrete form between two soil layers of the Richards equation is presented by equation (3-10). This form is needed in order to use the finite difference method for the numerical solution of the differential equation. The van Genuchten equations (3-11) and (3-12) are then employed to solve the Richards equation (van Genuchten, 1980). The van Genuchten parameters (α, n, and m) and some of the required soil hydraulic properties such as saturated hydraulic conductivity, saturated soil water content and residual soil water content for the soil model were estimated by field measurements or pedotransfer functions (Brakensiek and Rawls, 1994; Cosby et al., 1984; Patil and Singh, 2016; Rawls and Brakensiek, 1985; Saxton et al., 1986; Saxton and Rawls, 2006; Schaap et al., 2001; Vereecken et al., 1990).

$$\frac{\partial \theta}{\partial t} = \frac{\partial q}{\partial z} = \frac{\partial}{\partial z}\left(-K(\theta) * \frac{\partial \psi(\theta)}{\partial z}\right) \quad (3\text{-}9)$$

$$q = k_{eff}\ \frac{h(\theta_u) - h(\theta_l)}{0.5\ (d_u + d_l)} \quad (3\text{-}10)$$

$$\theta = \theta_r + (\theta_s - \theta_r) * \left(\frac{1}{1 + (\psi\alpha)^n}\right)^m \quad (3\text{-}11)$$

$$\frac{K\ (\theta)}{K_s} = \left(\frac{\theta - \theta_r}{\theta_s - \theta_r}\right)^{1/2} * \left(1 - \left(1 - \left(\frac{\theta - \theta_r}{\theta_s - \theta_r}\right)^{1/m}\right)^m\right)^2 \quad (3\text{-}12)$$

θ	Actual soil water	[-]
t	Time	[s]
q	Specific flux	[m s^{-1}]
z	Vertical coordinate	[m];
K	Actual soil hydraulic conductivity	[m s^{-1}]
θ_s	Saturation soil water content	[-]
θ_r	Residual soil water content	[-]
ψ	Suction	[m]
k_{eff}	effective hydraulic conductivity	[m s^{-1}]
h	Hydraulic head	[m]
u	Upper discrete layer	[-]
l	Lower discrete layer	[-]
d	Thickness of considered layer	[m]
α	Empirical parameter	[m^{-1}]
n	Empirical parameter	[-]
m	Empirical parameter (m=1-1/n)	[-]
K_s	Saturated hydraulic conductivity of the soil	[m s^{-1}]

Each soil horizon was divided into 16 numerical layers with variable thickness of the layers. The parameterization of the soil model also includes among other parameters the precipitation capacity for triggering macropore runoff, macropore capacity, macropore reduction with depth, and reduction of the hydraulic conductivity with depth. Default values were used for all the macropore parameters (more detailed description of unsaturated zone model can be found in Schulla 2015).

Surface flow

Two main processes contribute to surface flow or overland flow generation: Infiltration excess and saturation excess. The infiltration excess occurs when rainfall intensity is higher than soil infiltration rate. In this case, the unsaturated zone still exists below the soil surface while surface flow is occurring. This is the typical surface runoff

in arid and semi-arid areas where groundwater table is relatively deep. On the other hand, the saturated excess runoff occurs when rainfall fails to infiltrate as result of the saturation in the soil due to groundwater table rise. This can also generate return flow as the subsurface water resurfaces at the slopes. According to Beven (1989), such a return flow is primarily expected to be pre-event water.

The infiltration excess surface flow (QD) for an actual time step t is computed in WaSiM by equation (3-13).

$$QD\ (t) = P(t) + q_{in}(t) - I_a(t) \qquad (3\text{-}13)$$

Where *QD* is surface flow [mm]; P is precipitation in the actual time step; q_{in} is inflow from in the last time step [mm]; and I_a is the actual infiltration for the time step [mm]. The actual infiltration rate is the infiltration calculated using the Richards equation.

Saturation excess runoff is generated in WaSiM groundwater model when the groundwater table is higher than ground surface.

Interflow

Interflow is defined by Beven (1989) as "the near surface flow of water within the soil profile resulting in seepage to the stream channel within the time frame of a storm hydrograph". *Translatory flow*, *macropore flow*, and *groundwater ridging* are the mechanisms that contribute to interflow generation.

The *translatory flow* is the interflow which stems from the displacement of water already stored in the soil mantle before a rainfall event (Hewlett and Hibbert, 1967). This usually happens when the soil is within field capacity or saturated. It can occur in the Dano catchment around September, at the mid-rainy season.

Macropore flow or non-capillary flow occurs through preferential pathways including root channels, wormholes, and soil cracks. Fig. 3-3 presents soil cracks in Dano during a dry season. The cracks occur in high clay content soils in the dry season. Therefore, their influence on water fluxes might be important at the beginning of rainy season.

Fig. 3-3. Photo of soil cracks in the Moutori catchment on October 29th 2014 (beginning of the dry season).

Groundwater ridging mechanism of interflow is characterized by a large increase of hydraulic head of the groundwater during a storm followed by a significant release of water into the streams. It is caused by a quick conversion of near-surface capillary fringe into phreatic water (Sklash and Farvolden, 1979).

In WaSiM, interflow is generated from a given soil layer if the suction in the layer is lower than 338 hPa (3.45 m H_2O) and the local slope angle (β) is 0° < β ≤ 45°. If β=0 there will be water logging. The maximum interflow ($q_{ifl.max}$) also called the drainable water content of an actual soil layer is computed by equation (3-14) and the actual interflow q_{ifl} by equation (3-15).

$$q_{ifl.max} = \left(\theta(\psi) - \theta_{\psi=3.45}\right) \frac{\Delta z}{\Delta t} \qquad (3\text{-}14)$$

$$q_{ifl} = k_s\, \theta(\psi)\, \Delta z\, d_r \tan\beta \qquad (3\text{-}15)$$

Where θ(ψ) is actual soil water content at a given suction ψ [$m^3\ m^{-3}$]; Δz is layer thickness [m]; Δt is duration of a time step [s]; k_s is saturated hydraulic conductivity [$m\ s^{-1}$]; d_r, drainage density in [m^{-1}].

3.2.4 Groundwater model

Groundwater elevation

The water content in a layer for hydrostatic equilibrium with the groundwater table is calculated by equation (3-16) and the interpolated groundwater table considering that it flows in a single layer is presented in equation (3-17).

$$\theta_{GW,min} = \theta_r + (\theta_s - \theta_r) \left(\frac{1}{1 + (0.5\ d\ \alpha)^n}\right)^m \quad (3\text{-}16)$$

$$h_{GW} = h_{geo} + d\ (\theta_i - \theta_{GW,min})\ (\theta_s - \theta_{GW,min}) \quad (3\text{-}17)$$

With:

$\theta_{GW, min}$	Water content at hydrostatic equilibrium	[-]
θ_s	Saturated water content of the layer	[-]
θ_r	Residual water content of the layer	[-]
θ_i	Actual water content in a given layer i	[-]
α	van Genuchten parameter	[m^{-1}]
m, n	van Genuchten parameters	[-]
d	Thickness of the layer	[m]
h_{gw}	Groundwater level	[m]
h_{geo}	Geodesic altitude of the lower limit of the lowest partly saturated layer	[m]

When the groundwater table drops to the next lower layer, the water content at the equilibrium is recalculated. If the groundwater table rises to the next upper layer, the last water content of the previous layer accounts in the groundwater table interpolation.

Base flow

A conceptual approach for the base flow calculation (equation (3-18) was applied. The parameters Q_0 and k_b were calibrated.

$$Q_b = Q_0\ K_s\ e^{(h_{GW} - h_{geo,0})/k_b} \quad (3\text{-}18)$$

With:

Q_b	Base flow	[m s^{-1}]
Q_0	Maximum base flow if the soil is saturated	[-]
K_s	Saturated hydraulic conductivity	[m s^{-1}]
h_{GW}	Groundwater table	[m a.s.l]
$h_{geo, 0}$	Geodesic altitude of the first soil layer (upper limit surface)	[m a.s.l]
k_b	Recession factor for base flow	[m]

3.2.5 Discharge routing model

The discharge routing is based on a kinematic wave approach which considers different water levels in a channel and the corresponding flow velocities. A single linear

storage is then utilized to account for the effects of diffusion and inertia. The three main steps in discharge routing include: translation, storage, and superposition of the discharge from different sub-catchments.

The translation of the discharge in the channel is assumed to be stationary. The calculated flow velocity depends on channel properties such as slope, roughness, width, and depth. The spectrum of flow velocities is computed during the initialization of the model and stored in flow time table. The Manning-Strickler equation (3-19) is utilized to estimate the flow time.

$$v = M\ {R_h}^{2/3}\ I^{1/2} \tag{3-19}$$

Where *v*: flow velocity [m s^{-1}]; M: roughness parameter [$m^{1/3}$ s^{-1}]; R_h: hydraulic radius [m]; and *I*: slope in the direction flow [m m^{-1}].

The wave flattening is done by the retention and diffusion of flow. The retention employs a single linear reservoir approach between the main channel flow and the flood plain flow. The resulting total retention constitutes an inflow to the next routing channel.

Finally, the superposition of the discharge from different sub-catchments can be done by conveying discharge from the headwater sub-catchments to the intermediary ones and then to the outlet of the catchment. The upstream sub-catchment flows are considered as inflow to the lower sub-catchments.

3.3 Model calibration and validation

The Bankandi-Loffing and Mebar catchments were calibrated in years 2014-2015 and validated in 2016 at hourly time step. The optimized parameters include LULC parameters such as r_{sc} (canopy surface resistance) and r_{se} (evaporation surface resistance). Monthly values of r_{sc} and r_{se} were calibrated for each land use type as effective values have to be used and no field measurements were available.

In fact, surface resistance varies in the course of the day and between seasons (Beven, 1979; Lecina et al., 2003; Steduto and Hsiao, 1998; Todorovic, 1999). The variation in the day of surface resistance is characterized by a minimum r_{sc} around mid-day (Allen et al., 2006). This is the time of the day with maximum plant transpiration as plant leaf stomata are largely opened and plant water conductance is at its highest level of the day. Moreover, surface resistance increases with any environmental stress including water stress (Lecina et al., 2003). The most important weather parameters which influence surface resistance include intensity of solar radiation, air temperature, and vapor pressure deficit (Alves and Pereira, 2000).

The other land use parameters such as albedo, LAI, root depth were interpolated from previous studies (Bronstert, 2001; Charles-Dominique et al., 2009; Hansen, 1993; Kelley, n.d.; Kiniry et al., 2005; O'Siullivan, 2008).

Three horizons per soil type were considered and their saturated hydraulic conductivity (Ks) and the reduction of hydraulic conductivity with depth (Kr) were calibrated.

The following groundwater parameters were additionally calibrated: saturated hydraulic conductivity (Kx, Ky), coefficient of storage (So), leakage factor which control the exfiltration (base flow) from the groundwater to the river network (l_k). When the conceptual base flow was applied, the parameters determining maximum base flow if the soil is saturated (Q_0) and the recession factor for base flow (k_b) were optimized.

Finally, catchment characteristic parameters such as drainage density (dr) for interflow, storage coefficient for surface runoff (k_D) and storage coefficient for interflow (k_H) were also calibrated (more detail description of the parameterization of WaSiM can be seen in Schulla, 2015).

The selection of the calibrated parameters and their range were based on the insights from Yira (2016) who studied their sensitivity and determined the most sensitive parameters for the area. The Latin Hypercube sampling was applied in order to ensure a fully stratified sampling of each parameter (Mckay et al., 1979; Schmalz and Fohrer, 2009). The Simulation Environment for uncertainty and sensitivity analysis (SimLab 2.2; European Commission, 2016) software were utilized for the sampling and 200 parameter sets were generated for each model.

3.4 Model performance estimation

A multi-criteria approach was applied for model performance estimation in order to account for the deficiency of single criterion approach (Weglarczyk, 1998). The objective functions include the Nash-Sutcliffe Efficiency (NSE) (Nash and Sutcliffe, 1970), the Kling-Gupta Efficiency (KGE) (Gupta et al., 2009; Kling et al., 2012), the coefficient of determination (R^2) (Benesty et al., 2009), and the percent bias (Pbias) (Moriasi et al., 2007).

NSE, KGE, R^2, and Pbias were computed by equation (3-20), (3-21), (3-22), and (3-23) respectively.

$$NSE = 1 - \frac{\sum_{t=1}^{n}\left(X_{s,t} - X_{o,t}\right)^2}{\sum_{t=1}^{n}\left(X_{o,t} - \mu_o\right)^2} \quad (3\text{-}20)$$

$$KGE = 1 - \sqrt{(R-1)^2 + (\beta-1)^2 + (\gamma-1)^2}$$

$$\beta = \frac{\mu_s}{\mu_o} \quad (3\text{-}21)$$

$$\gamma = \frac{CV_s}{CV_o} = \frac{\sigma_s/\mu_s}{\sigma_o/\mu_o}$$

$$R^2 = \left[\frac{\sum_{t=1}^{n}\left(X_{s,t} - \mu_s\right)\left(X_{o,t} - \mu_o\right)}{\sqrt{\sum_{t=1}^{n}\left(X_{s,t} - \mu_s\right)^2 \sum_{t=1}^{n}\left(X_{o,t} - \mu_o\right)^2}}\right]^2 \quad (3\text{-}22)$$

$$Pbias = \frac{\sum_{t=1}^{n}\left(X_{s,t} - X_{o,t}\right)}{\sum_{t=1}^{n}\left(X_{o,t}\right)} * 100 \quad (3\text{-}23)$$

Where n is total number of time steps, $X_{s,t}$ is simulated discharge at a time t; $X_{o,t}$ is observed discharge at a time t, μ_s is mean of the simulated discharges; μ_o is mean of observed discharge; CV_s is coefficient of variation of the simulated discharge; CV_o is coefficient of variation of observed discharge; σ_s is standard deviation of simulated discharge; and σ_o is standard deviation of observed discharge.

The optimization of the model is towards the maximizing each of the first three objective functions (R^2, NSE, and KGE) with perfect model yielding in a unity value for each of them. R^2 ranges from 0 to 1 whereas NSE and KGE range from -∞ to 1. Concerning Pbias, the optimal value is zero and it ranges from -∞ to +100%. The positive Pbias is equivalent to overestimation and the negative value is underestimation of the discharge by the model. A model starts being satisfactory from NSE> 0.5 and Pbias ≤ ±25 for monthly time step (Moriasi et al., 2007). A lower satisfactory limit of 0.5 was also considered for KGE.

The most optimal parameter set is assumed to be the one with the highest KGE. This is due to the fact that not only KGE incorporates R^2 in its equation, but also accounts for both conditional and unconditional biases (Gupta et al., 2009; Murphy, 1988). According to equation (3-21), maximizing each of the components of KGE will result to maximizing KGE (Kling et al., 2012).

R^2 was not chosen to select the optimal simulation as it measures only the concentration of points around an imaginary line in a graph simulated against observed discharge. R^2 does not measure the concentration of points around 1:1 line (R^2 is susceptible for systematic errors). The use of only R^2 for model performance estimation might be misleading (Weglarczyk, 1998).

Although NSE is the most employed dimensionless objective function in hydrological modeling, it has been criticized for using mean observed discharge as baseline. This might lead to overestimation of model performance when a significant seasonal variation of runoff is observed (Gupta et al., 2009).

4 INSTRUMENTATION AND DATA AVAILABILTIY

4.1 Introduction

Hydrological data is limited in the Dano catchment. Historical stream, soil water, and piezometric data do not exist for the selected catchments. The only weather station with a satisfactory data set for four decades is located in Boromo (70km north of Dano catchment). The available weather stations in the vicinity of the selected catchments have only been operating since June 2012 (Yira, 2016). Basic characteristics of the aquifers can hardly be found (Eguavoen and McCartney, 2013). Therefore, for this study, an intensive catchment instrumentation was designed and carried out in four selected small catchments of the Dano catchment. Time series of data including weather (rainfall, air temperature, relative humidity, solar ration, and wind speed), discharge, and piezometric data were collected for three consecutive years (2014-2016). Spatially distributed data such as the land use and land cover, the dominant soil types, and the digital elevation model were obtained within the WASCAL (West African Service Center on Climate change and Adapted Land use, www.wascal.org) project. The thickness of sub-surface weathered layer and groundwater table depths at the moment of the installation of some local borehole were analyzed to gain knowledge on the local aquifer. Furthermore, a geo-electrical tomographic survey and a slug test were conducted to determine the spatial distribution of the aquifer and its hydraulic conductivity.

This chapter thoroughly presents the instrumentation conducted under the scope of this study for the selected catchments and the subsequent data collected in the field. Fig. 4-1 and Fig. 4-2 illustrate the spatial distribution of the instrumentation in the field.

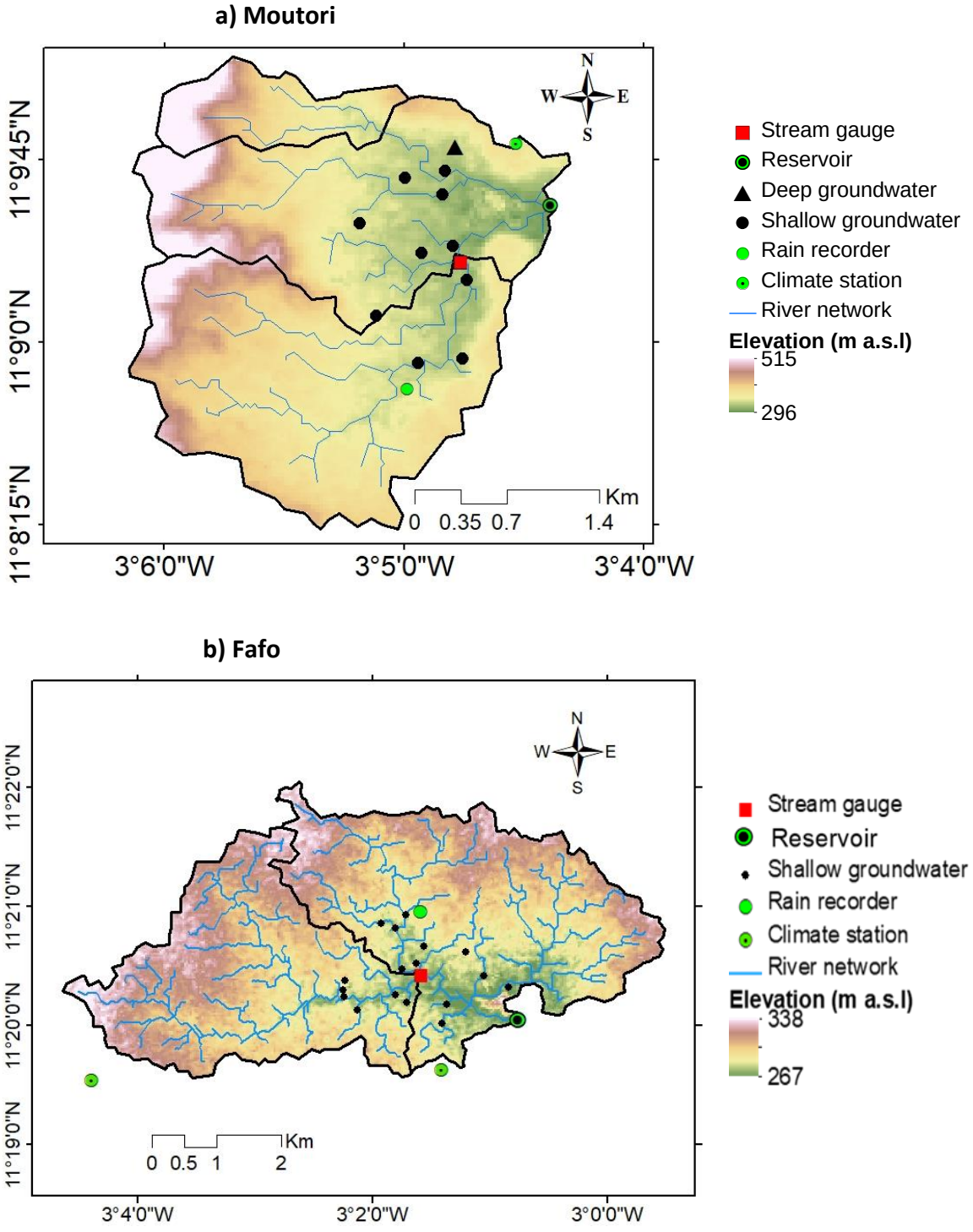

Fig. 4-1. Elevation and instrumentation of the catchments equipped with reservoirs.

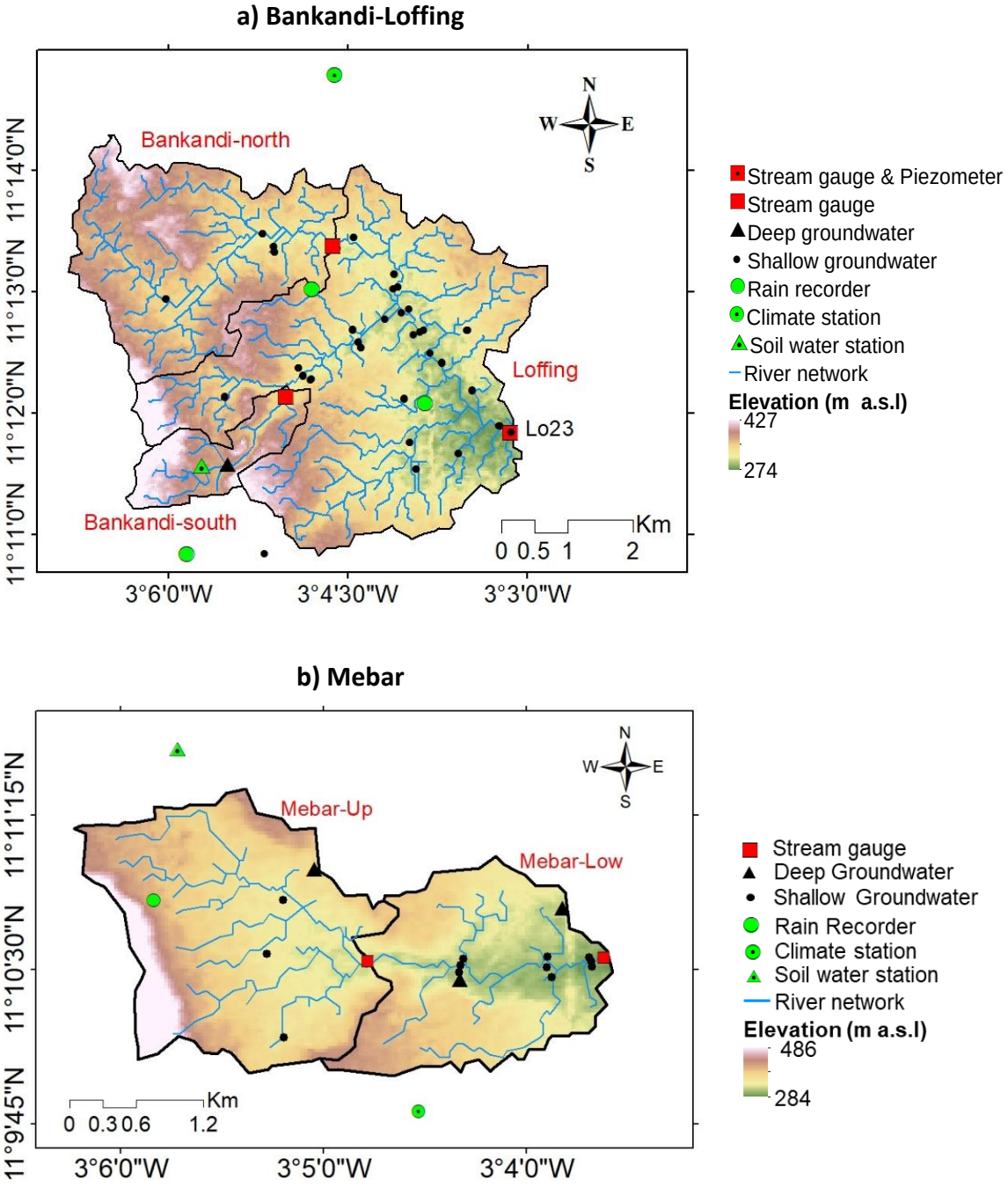

Fig. 4-2. Elevation and instrumentation of the catchments without reservoirs.

a) Piezometer in shallow aquifer

b) Deep well

c) Stream gauge

d) Stream gauging

e) Climate station

f) Rainfall recorder

Fig. 4-3. Piezometric, stream and weather instruments

a) Mobile soil moisture-meter

b) Soil moisture station

c) DGPS

d) Geo-electrical survey

Fig. 4-4. Soil water measurements, topographic and geo-electrical surveys (the DGPS pictures after Astech® ProMark® manual 2011).

4.2 Time series data

4.2.1 Piezometric data

In order to investigate the hydrological processes, this study required the installation of a dense monitoring network in four small catchments in Dano (Fig. 4-1 and Fig. 4-2). In total, 64 piezometers (Fig. 4-3a) were installed in the shallow aquifer and the groundwater level was manually measured using a level tape at weekly time steps. In addition to manual measurements, one site was equipped with a pressure sensor and logger recording the groundwater level every 6 hours.

The relationship between deep and shallow aquifers (< 5 m deep) was determined by selecting 3 local deeper wells (6 to 25 m deep, Fig. 4-3b shows an example of a well located in deep aquifer) for monitoring the groundwater table. They underwent weekly manual measurements using groundwater tape.

4.2.2 Discharge data

The discharge was monitored at seven stream gauge stations. They include six station equipped with simple pressure sensors and one station with both pressure and

electrical conductivity sensors. In Bankandi-Loffing, two gauges (Bankandi-north and Bankandi-south) were installed in the upstream area and one gauge (Loffing) at the outlet. In the Mebar, one gauge at upstream area and one at the outlet were installed. However, only the latter gauge operated well. The former gauge malfunctioned (see Fig. 4-2 for the locations of the stream stations). One gauge was installed in each of the Fafo and Moutori catchments. The water pressure sensors were installed in vertical pipes (Fig. 4-3c) to avoid water level fluctuations due to waves and turbulences during high flood events.

For each stream station, a rating curve which establishes a relationship between water level and discharge was developed using measured discharges acquired during 2014 and 2015. The discharge measurements were carried out using an Acoustic Digital Current meter (ADC) of OTT Hydromet (2007). The discharge measurement method consists of dividing the stream cross section in to several flow segments (Fig. 4-3d). For each flow segment, the velocity was measured using an ultrasonic sensor and the water depth using pressure sensor. The total discharge is the sum of the flow at all the flow segments like suggested by European standard EN ISO 748 (ISO, 2007). The discharge values were measured not only just after every rainfall that induces a significant flood but also regularly during dry seasons in order to account for high and low flows. For some stream stations, the low flow rating curve is significantly different to the high flow rating curve. Therefore, both low flow and high flow rating curves were developed for those stations. This was necessary to take into account the change of cross section shape with depth. In addition to the measured discharge, the Manning approach was utilized to calculate discharge (equation (4-1) for gauging stations with a limited number of measured discharges. This was the case of Mebar, Moutori, and Bankandi-south gauges. At the Bankandi-south, Manning calculated discharges were exclusively used in developing the rating curve due to a very few measured discharge values. The flows at this station are fast and stop immediately after a rainfall. I frequently arrived for discharge measurement at the station when the flows were already over.

$$Q = A_w \frac{1}{n} \left(\frac{A_w}{P_w}\right)^{2/3} S^{1/2} \qquad (4\text{-}1)$$

Where Q is the discharge, A_w is the cross sectional area of flow, n is the Manning roughness coefficient, P_w is the wetted perimeter, and S is the average slope of the river bed. The stream cross section area, the wetted perimeter, and the slope of river bed were assessed though leveling using a DGPS (Fig. 4-4c) (Ashtech, 2011). The

roughness coefficient for each cross section was estimated by calibrating the Manning equation employing the highest measured discharge as ground truth.

All stream gauges operated at 5 min time step. This high resolution is needed because the small catchments are quick-flow dominant catchments, especially following high intensive rainfall events. Fig. 4-5 presents stream flow data availability for the three year field observation. Stream flow was not measured during the dry season (November to May) because these intermittent streams were dry (Raghunath, 2006). The measurements started with a short delay in July-August 2014 instead of June (beginning of the raining season). The delay was due to the installations of field equipment. In 2016, the gaps in the rainy season were mainly caused by the malfunctioned and vandalized stream stations.

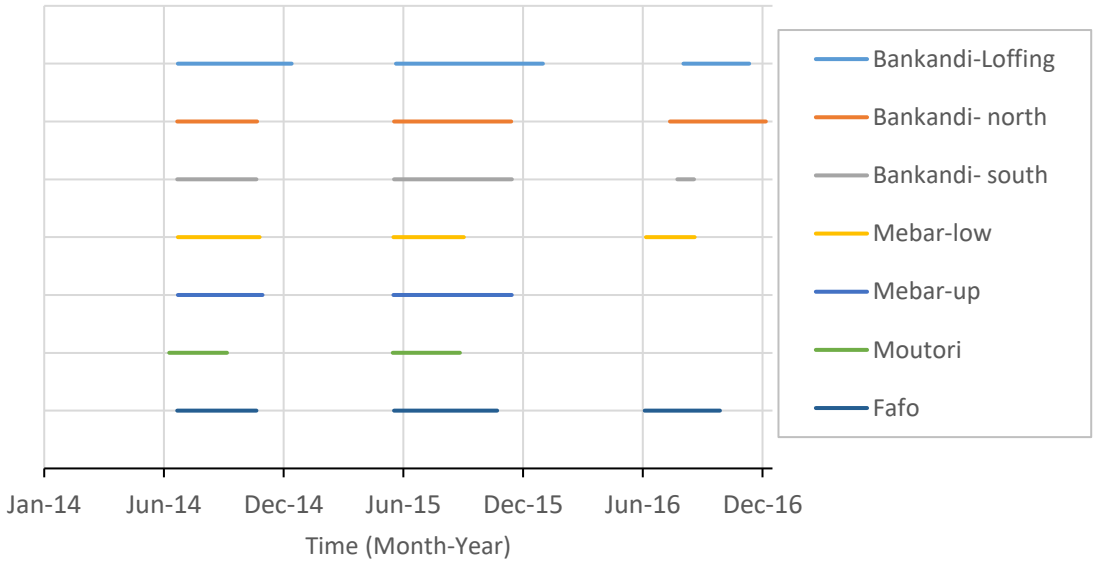

Fig. 4-5. Discharge data availability with stream station: no flow in dry season (November-May).

4.2.3 Climate data

Four climate stations (Fig. 4-3e) were installed since June 2012 in the investigated catchments and at their vicinities as part of the WASCAL project (Yira, 2016). The recorded climate variables include rainfall, air temperature, relative air humidity, global radiation, and wind speed. However, a high spatial variability of rainfall which was estimated to 30-40% was observed in the region (Sivakumar, 1989). Thus, five additional rainfall recorders (Fig. 4-3f) were uniformly installed in the catchments allowing a representative spatial coverage of rainfall measurements in the study area

(ten rain gauges for a total area of 65km²). The WMO (World Meteorological Organization) recommends a minimum network density of 575 km² per station for interior plains (WMO, 2008). The resolutions of rainfall measurement were 0.2 mm rainfall for rain recorders and 0.1 mm for the climate stations. The temporal resolution was 5-10 min for the climate stations and the rain recorders.

4.2.4 Soil water data

Soil moisture was manually measured weekly using a mobile Frequency Domain Reflectometry (FDR) sensor (Fig. 4-4a) at 64 points and for three different depths: topsoil (upper 5 cm), 30 cm and 50 cm. At each point, soil moisture at 30 and 50 cm depths were measured through two access holes (6-7 cm in diameter). Each measurement was repeated three times and the average value was saved. The soil moisture sensor (ML2x Theta Probe) was calibrated according to the method described by the manufacturer (Delta-T Device Ltd 1999). The deviation of the sensor measurements compared to the gravimetric method (considered as a reference) was approximately ± 7%.

Additionally, a soil moisture station (see Fig. 4-4b), was installed in a Plinthosol at Bankandi-south (Yira, 2016). It is equipped with a data logger which continuously records at a temporal resolution of 30 min. Three FDR sensors (EcoTech Umwelt-Meßsysteme GmbH) were used at the first three soil horizons.

The soil measurement points were classified into two groups. The first group of measurements are located in uplands and slopes and the second group includes measurements in lowlands or valley bottoms. The first group of points mainly belongs to plintosols or Cambisols whereas the second group is characterized by Gleysols.

4.3 Digital elevation model (DEM)

The SRTM (Shuttle Radar Topography Mission) of the USGS (United States Geological Survey) dataset with 30m resolution (NASA, 2014) was used to delineate the investigated catchments and to derive topographic based grid data including slope, flow direction and accumulation, aspect, and stream network. The topographic analysis program TANALYS (Schulla, 2015) was used to generate those topographic grid data.

4.4 Characterization of the aquifer

Crystalline rocks (migmatites, granites, shists) are dominant in the study area therefore aquifers can only located in weathered rocks, in faults, and fractures (Singhal and Gupta, 2010). The sub-surface investigation applied two sorts of methods including direct methods and indirect methods. The direct methods include among others, logs

analyses, pumping test and slugs test. The indirect methods mainly use geo-physical methods.

In this section, data collected during the installation of many wells and boreholes (log, groundwater table, pumping rate etc.) are analyzed. The wells and borehole were installed in the local aquifer for drinking water. The criteria considered when defining a *successful well / borehole* include the yield (0.2 to 1 liter per second in rural domestic use with a hand pump in West Africa), water quality, and the cost of the construction of the well (Houston, 1992; Singhal and Gupta, 2013). For a low permeable crystalline-rock aquifer, the siting of well or borehole is important for the well or borehole to penetrate into water-bearing formation (weathered profile, fracture etc.) which increases the probability of successful well or borehole. Furthermore, a slug test was applied on the shallow groundwater to estimate its hydraulic conductivity. Finally, the method of geo-electrical resistivity survey was conducted during this study to gain more insight on the groundwater.

4.4.1 Borehole general information

This section explores available groundwater data collected during the installation of wells or boreholes by the Department of water resources of Burkina Faso (DGRE, www.mea.bf). The aim is to gain insights on groundwater characteristics.

The analyses considered 104 boreholes and wells located in the Dano catchment. All the wells and boreholes are intended for rural domestic needs. 87% of the wells and boreholes were declared successful (water yields are equal or greater than 0.2 l s^{-1} and water quality is fit for human consumption). The depths of the wells and boreholes range from 31 to 96 m. Thus, the investigated wells and boreholes are sufficiently deep to reach the saprolite and a part of the underlain igneous basement rock. The saprolite horizon thickness ranges from 14 to 51 m and the average saprolite thickness is 28 m. The thickness of the remained wells and boreholes (51 to 99 m) and their saprolite (5 to 48 m) are not significantly different from the successful wells and boreholes. This seems to suggest that the success of a well or borehole does not depend only on the depth and the thickness of the saprolite layer. Saprolites which are located at a steep slope with low storage coefficient and high hydraulic conductivity might lose water in favor of the valleys bottoms. Singhal and Gupta (2013) when studying fractured rocks, found out that wells / borehole located in valley bottoms produce greater yields than those located on steep slopes. This can be attributed to the usual groundwater flow from uplands to valleys bottoms. Moreover, the aquifers are usually thicker at the valley bottoms compared to the uplands due to sedimentation processes in the valley bottoms. Additionally, the water contained in the alluvial layers contributes in

deepening the weathering of the underlain bedrock and faults or and fractures located in valley bottoms.

The depth to groundwater table ranges from 2 to 31 m and the average groundwater table depth was 12 m. The yields of the wells and boreholes were 0.4 to 18 m^3 h^{-1} during pumping tests and the subsequent induced drawdown was 2 to 22 m with a mean drawdown of 10 m.

The analyses of the data collected during the installation of wells and boreholes provided valuable information on the local aquifer thickness at the surroundings of the studied catchments. Furthermore, insights in the productivity of the wells and boreholes were gained. However, the information is retrieved on the point scale and the hydraulic conductivity of the aquifer was not available. Therefore, a slug test and a geo-electrical tomography surveys were conducted in the studied catchments in order to improve the knowledge on the aquifer.

4.4.2 Slug test of the shallow aquifer

The slug test method after Bouwer and Rice (Bouwer, 1989; Bouwer and Rice, 1976) was used to estimate saturated hydraulic conductivity (K_s) of the unconfined aquifer of Dano catchment. It consisted of quickly raising water level from the equilibrium in a piezometer by adding some water. The subsequent rate of fall of groundwater table was measured using a water pressure sensor which records the water level at 2 min time step. The investigated piezometers were partial penetrating and partial screened with gravel pack in an unconfined aquifer (Fig. 4-6).

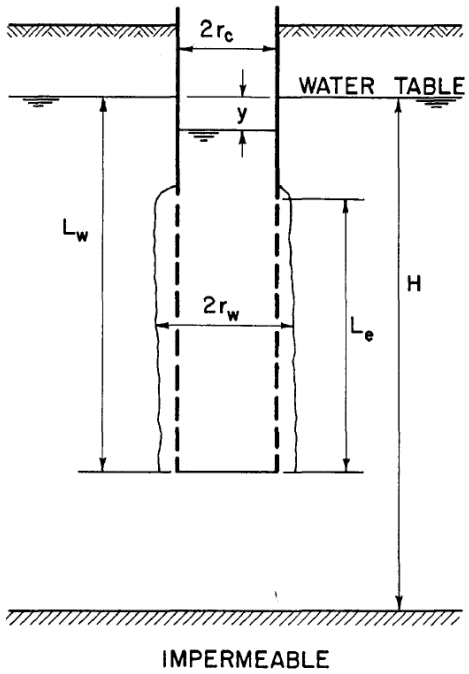

Fig. 4-6. Schematic presentation of the investigated piezometer (Bouwer, 1989). r_c: radius of the investigated well; *y*: difference between groundwater level in well at a given time and the static groundwater table outside the well; L_w: groundwater level in the aquifer with the bottom of the well as reference point; *H*: groundwater level in the aquifer with the impermeable substratum of the aquifer as reference point; r_w: radius of the gravel pack; and L_e: length of the screened tube.

The equation (4-2) presents the computation of the hydraulic conductivity (K_s).

$$K_s = \frac{r_c^2 \, ln(R_e/r_w)}{2L_e} \, \frac{1}{t} \, ln\frac{y_0}{y} \tag{4-2}$$

With: *y*: difference between groundwater level in well at a given time *t* and the static groundwater table outside the well, y_0: y at time t=0; R_e: effective radial distance over which y is dissipated can be expressed by the equation (4-3).

$$ln\frac{R_e}{r_w} = \left[\frac{1.1}{\ln\left(\frac{L_w}{r_w}\right)} + \frac{A + B \, ln[(H - L_w)/r_w]}{L_e/r_w}\right]^{-1} \tag{4-3}$$

The geometric characteristics (r_c, r_w, L_e, L_w, and H) were described by the Fig. 4-6 and y_0 is the value of y at the time t=0. The dimensionless parameters A and B of the equation (4-3) were estimated using Fig. 4-7.

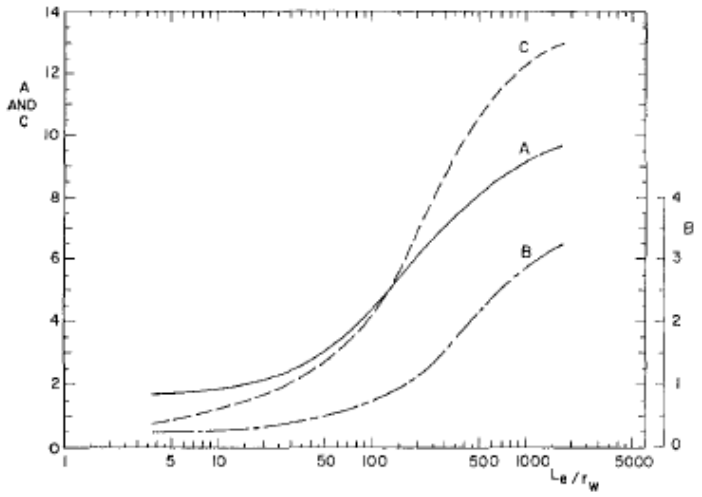

Fig. 4-7. Dimensionless parameters A and B as a function of L_e/r_w. C is used only for full penetrating well (Bouwer, 1989).

From equation (4-2), it appears that ln(y) versus t is a straight line and the slope (b) is expressed by the equation (4-4).

$$b = \frac{2L_e\, K_s}{r_c{}^2 \ln(\frac{R_e}{r_w})} \tag{4-4}$$

The slope b is graphically determined by fitting ln(y) versus t in a semi-logarithm plot. K_s was calculated using equation (4-5) after graphically estimation of R_e using Fig. 4-7.

$$K_s = \frac{r_c^2 \ln\left(\frac{R_e}{r_w}\right)}{2L_e}\, b \tag{4-5}$$

The slug test survey was carried out on 36 piezometers in all the four catchments (Bankandi-Loffing, Mebar, Moutori, and Fafo). The results were utilized for the parameterization of WaSiM.

4.4.3 Geo-electrical tomography

Understanding the sub-surface geology is a key for a successful surface and groundwater availability study. Under the conditions of limited groundwater data availability, a geo-electrical resistivity survey is a relatively easy approach for characterizing the geometry of an aquifer. The geo-electrical resistivity method is often used to assess some of the most important geological and hydrological parameters such as rock or soil type, their degree of water saturation and the pore water solute content (Koch et al., 2009). For instance, Archie's law establishes the relationship between the resistivity of a porous rocks and the porosity and the resistivity of pore water (Loke, 2001). However, due to the wide range of resistivity corresponding to a rock or soil type, the use of absolute resistivity to characterize the sub-surface may be associated with significant uncertainties. Moreover, Archie's Law can only be applied to porous materials with no significant amount of mineralogical clay, mineral ore, or graphite. Therefore, instead of the absolute resistivity, the relative resistivity was used in this study by comparing the measured resistivity of an area to the resistivity of surrounding hydrogeological structures.

The overriding goal of the electrical resistivity survey was to characterize the geological structure of the sub-surface. The information is important for building a robust hydrological model.

A SYSCAL Pro *switch*-48 resistivity-meter (IRIS-Instruments, 2016) was used for field investigation (see Fig. 4-4d). The instrument is equipped with 48 electrodes with 5 m spacing (Fig. 4-8). Two measurement approaches were used including Schlumberger array or pole-pole array (Fig. 4-8).

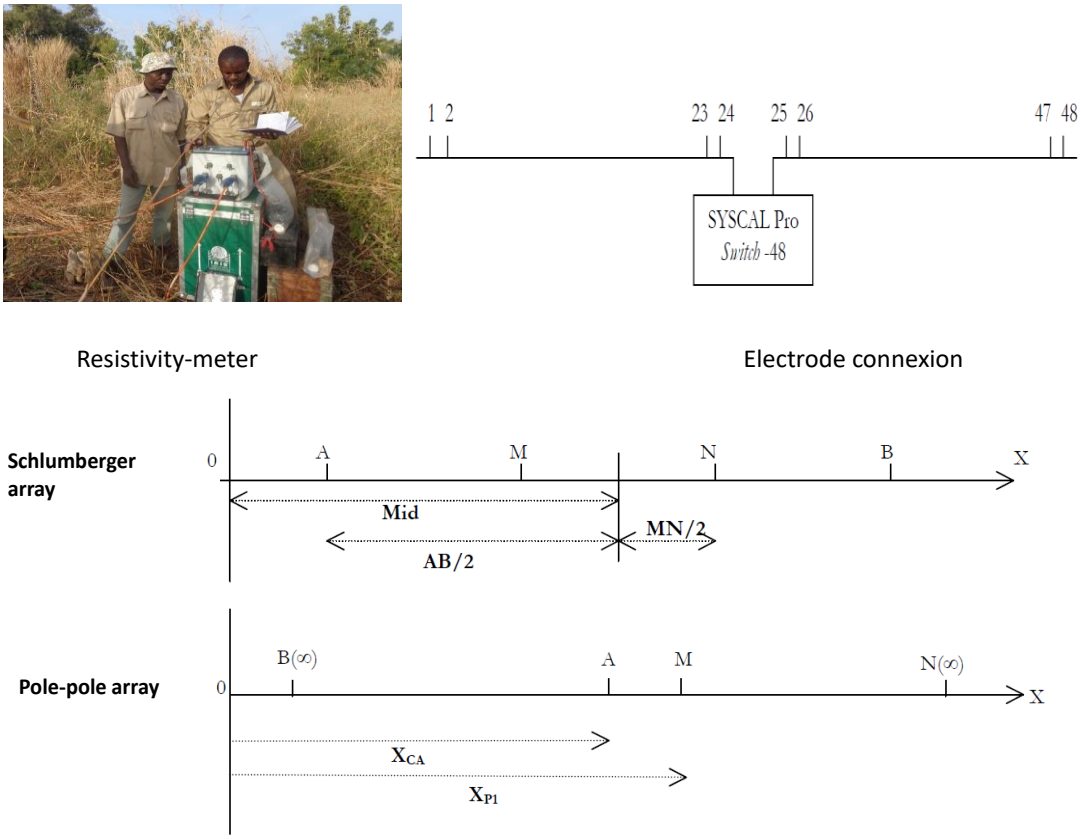

Fig. 4-8. Field setup of the SYSCAL Pro *switch-48*. A and B: current electrodes; M and N: potential electrodes; X : linear axe where the point A, B, M, and N can be located; AB: distance between point A and B; MN: distance between M and N; X_{CA}: cordinate of A on the axe X; and X_{P1}: cordinate of M on the axe X

The measurement principle is based on the application of a potential (V) on the electrodes MN and the resulting current (I) is measured at the electrodes AB. The apparent resistivity (ρ_a) is calculated by equation (4-6).

$$\rho_a = K \frac{V}{I} \tag{4-6}$$

The value of the constant K depends on the measurement array. Hence, for Schlumberger array, K was calculated by the equation (4-7) and for pole-pole array K is calculated by the equation (4-8).

$$K = \frac{\pi(a^2 - b^2)}{2b} \quad (4\text{-}7)$$

$$K = \frac{2\pi}{(1/AM)} \quad (4\text{-}8)$$

Where a=AB/2; b=MN/2; and a>b (see Fig. 4-8). The Schlumberger electrode array explored a maximum depth of 52 m whereas the pole-pole reached more than twice the maximum depth of the Schlumberger array (130 m). The pole-pole array was applied only at locations where there was a need to explore deeper because it is a labor and time consuming method. The field measurements were processed using a 2-D resistivity inversion software called RES2DINV (Geotomo Software, 2010).

The measurements were carried out in collaboration with the National Department of Mining and Geology of Burkina Faso (BUMIGEB). They provided the measurement equipment and the technical support.

5 CHARACTERIZATION OF SURFACE AND GROUNDWATER RESOURCES IN FOUR INLAND VALLEY CATCHMENTS IN DANO

5.1 Introduction

The Dano catchment, located in south-east Burkina Faso, is one of the three focal catchments of the WASCAL project (West African Science Service Center on Climate Change and Adapted Land Use, www.wascal.org). The catchment is located in a region where approximately 57% of the population live under the poverty line (Coulombe et al., 2000). Nearly 90% of the labor force of the area work in agriculture (INSD, 2014). Therefore, many development projects intend to reduce poverty through improvements of the agricultural system especially in inland valleys (Sparacino, 2011). Yet, these projects were often purely based on surface runoff by building either small dams or flumes for canalizing directly water into fields. Although valley bottoms of inland valleys are flooded in the rainy season (Windmeijer and Andriesse, 1993), they dry out in the dry season when water gets scarce with no possibility to irrigate and to grow any crops with surface water without a reservoir. Since 1970s and 1980s, approximately 1700 small reservoirs were constructed in Burkina Faso as response to droughts and in order to alleviate the high water demand for agriculture in rural areas (Venot and Cecchi, 2011). Two reservoirs were constructed in the Dano catchment. One of the reservoirs frequently experiences complete depletion before the end of the dry season. This can be attributed not only to high water demand for food production for a fast growing human population but also to high evapotranspiration losses and insufficient rainfall (Mishra and Singh, 2010).

Using the shallow aquifer for irrigation is an option which is already practiced by some farmers for irrigating vegetables. However, shallow wells are at risk to dry out very fast or before the end of the dry season due to very little knowledge on the appropriate locations to install wells and the depth needed to obtain sustainable water productivity. Increasing the use of shallow groundwater is hindered by the fact that basic information on the groundwater in the catchment is lacking (Eguavoen and McCartney, 2013). Especially information on the extent of the aquifer, its spatial distribution and recharge are not available.

Moreover, the irregular behavior of rainfall regime in the region (Ibrahim et al., 2013b) lead to severe yield losses as agricultural systems are mainly rainfed and dry spells occur in the rainy season at periods when crops need water the most (Traore et al., 2013). This implies a need for supplementary irrigation in the rainy season.

Given the limited adaptive capacity of smallholder farmers and the fact that they are highly vulnerable to climate variability and climate change (Makate et al., 2017; Traore et al., 2015), the aim of this research is (i) to understand the underlying

hydrological processes, (ii) to investigate not only the surface water resources but also the groundwater availability and the linkage in order to support strategies for better utilization of water at the local scale for small irrigation schemes, and (iii) to better understand hydrological processes which control the surface and groundwater availability in the area.

Due to the local scale and the intention to provide reliable information to farmers, this research uses data collected at very high spatial and temporal resolutions. The data were analyzed using fundamental hydrological tools in order to set the base for further investigations with hydrological modeling and water management strategies.

5.2 Material and methods

5.2.1 Total runoff coefficient

Annual total runoff was estimated by runoff coefficient (Cr) which is the ratio of the total runoff (Q) by the rainfall (P) (5-1). Because intermittent flows characterize the investigated catchments, most of the flows are concentrated in the rainy season. Thus, the analyses focused on rainy seasons.

$$Cr = \frac{Q}{P} * 100 \quad (5\text{-}1)$$

With Q: seasonal total runoff; P: seasonal precipitation [mm], and Cr: runoff coefficient [%].

5.2.2 Flow duration curve

The flow duration curve (FDC) was used to compare the four investigated catchments in the Dano catchment. For a given period, FDC can be defined a cumulative frequency curve which presents the percentage of time steps where discharges were equaled or exceeded (Searcy, 1959). The runoff is plotted versus the time exceedance probability in percent (Vogel and Fennessey, 1995). The variation of FDC provides information on catchment hydrological processes including its hydrogeologic characteristics (Peters and Driscoll, 1987).

FDC was developed for the years 2014 and 2015 at a five minute time step. Periods of no-flow were excluded from the analysis as suggested by Croker et al. (2003). FDC was computed for the Bankandi-Loffing catchment using measured total runoff from a gauging station of headwater sub-catchment (Bankandi-north) and the outlet stream gauge. For each of Mebar and Fafo catchments, the stream gauge at their outlet were employed (Mebar-low and Fafo stream gauges, respectively).

5.2.3 Analytical runoff component estimation

Total runoff was decomposed into its components using the measured water electric conductivity and the hydrograph.

The electric conductivity-based estimation is utilizing the mass balance of water and solutes method (Stewart, 2015). In this case, the solutes are ions which naturally dissolve in stream water. The quick or fast flow (Q_r) (surface runoff plus interflow) was estimated for each time step based on the variation of the electric conductivity of the stream discharge (C_d), total discharge (Q_d), electric conductivity of base flow (C_b), and electric conductivity of rainfall (C_p) using equation (5-2) (Giertz et al., 2006). The electric conductivity-based method was applied only at the outlet of Bankandi-Loffing. It is the only gauging station which was equipped with electric conductivity measurement at a five minute time step.

Fig. 5-1 presents a schematic description of the main hydrological processes contributing to the variation of the electric conductivity of the stream.

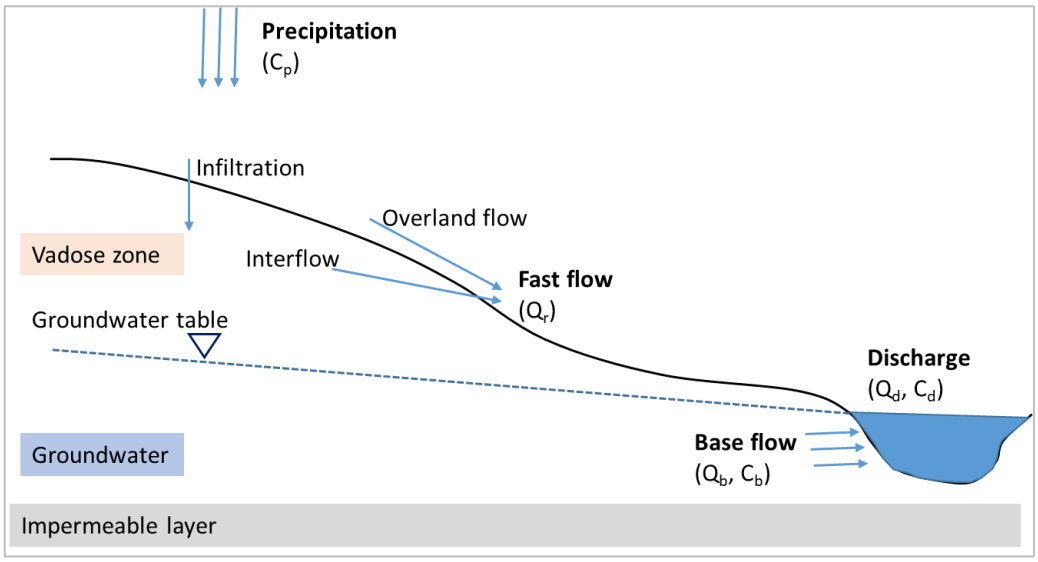

Fig. 5-1. Schematic representation of the main hydrological processes contributing to the electric conductivity of discharge water.

$$Q_r = (C_d - C_b).\frac{Q_d}{(C_p - C_b)} \qquad (5\text{-}2)$$

The electric conductivity of the groundwater (C_b) is considered to be constant during the event therefore the pre-event mean value (120 µS cm^{-1}) measured in the piezometer Lo23 located at the outlet of Bankandi-Loffing catchment was used for the calculations (see Fig. 4-2 for the location of the piezometer Lo23). Regarding the rainfall electric conductivity (C_p), the average measured electric conductivity of rainfall (19 µS cm^{-1}) in the Nakambé basin (north of Burkina Faso) was utilized (Maïga-Yaleu, 2014).

Base flow was calculated by the difference between the total runoff and the fast flow, therefore only these two runoff components can be determined by the electric conductivity method.

Unlike the electric conductivity method, a hydrograph analysis allowed the estimation of three components of total runoff, namely surface runoff or overland flow, interflow, and base flow.

The hydrograph in

Fig. 5-2 shows two distinct peaks for one rainfall event, therefore the decomposition of the hydrograph is based on the assumption that the first peak (A) mainly consisted of surface runoff and the second peak (B) was essentially induced by interflow. The end of interflow was determined by plotting the recession limb of peak B with logarithmic scale for the Y-axis and linear scale for the X-axis. This is an adaptation of the method of Roche (Cosandey and Robinson, 2007). The breaks of the curve allow the separation of fast flow (surface runoff plus interflow) from base flow. An average base flow was used for the duration of the stormflow.

Fig. 5-2 shows that the stormflow starts at t_0, the interflow starts at t_1 and ends at t_2, and the stormflow ends at t_3. The volume of base flow (V_{base}) in equation (5-3) is computed using the average base flow rate (Q_{base}), and the time step duration (T_{step} =5 min). The volume of overland flow (V_s) and the interflow volume (V_i) were calculated using equations (5-4) and (5-5), with Q_i being the discharge at the time step i.

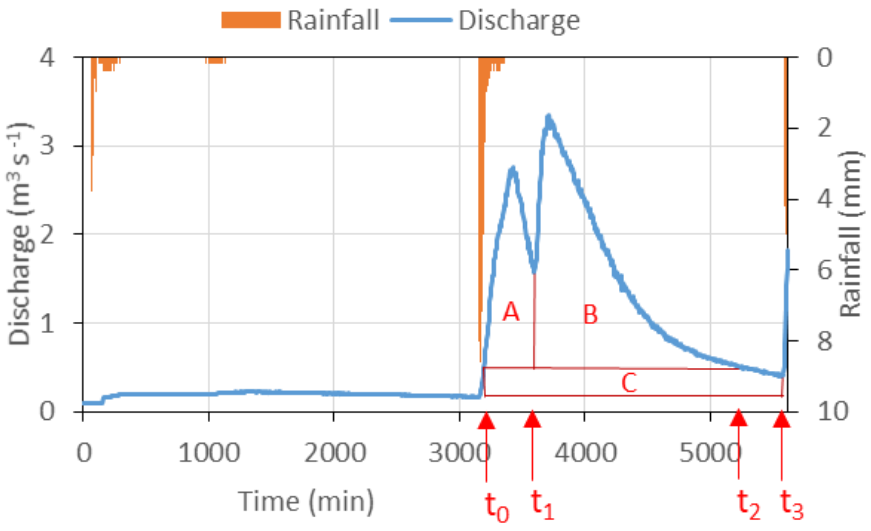

Fig. 5-2. Decomposition of the hydrograph at 5min time steps on September 1-5, 2015 at the main outlet of Bankandi-Loffing. A is surface runoff, B is interflow, and C is baseflow of the stormflow.

$$V_{Base} = \sum_{i=t_0}^{t_3} (Q_{base} * t_{step}) \quad (5\text{-}3)$$

$$V_s = \sum_{i=t_0}^{t_1} [(Q_i - Q_{base}) * t_{step}] \quad (5\text{-}4)$$

$$V_i = \sum_{i=t_1}^{t_2} [(Q_i - Q_{base}) * t_{step}] \quad (5\text{-}5)$$

5.2.4 Groundwater recession

Groundwater recession was estimated using base flow recession curve (Fig. 5-3) and the rate of groundwater level drop in dry seasons. The late base flow recession was separated from the early one in order to reduce the influence of quick flow on the characteristics of the base flow recession curve (Stewart, 2015).

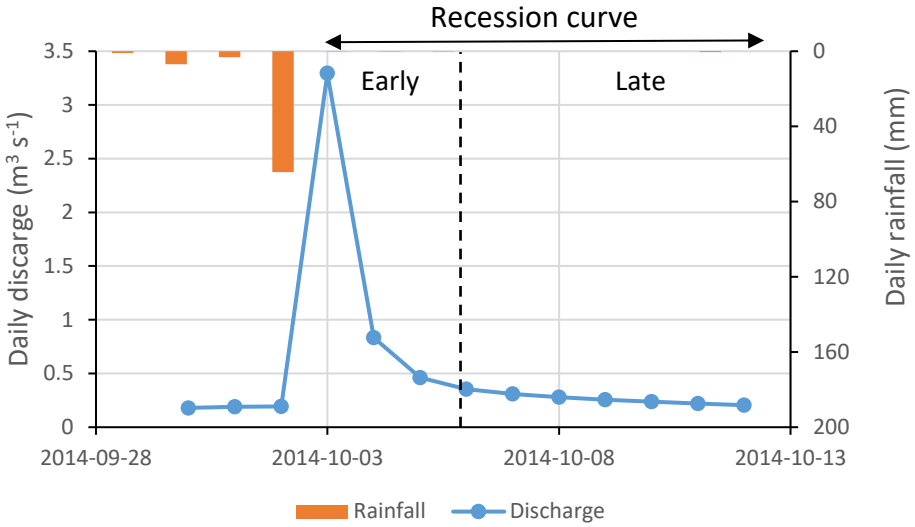

Fig. 5-3. Base flow recession curve at the outlet of Bankandi-Loffing.

An exponential recession of base flow was applied (Chapman, 1999; Stella, 2013; Tallaksen, 1995; Wittenberg, 1994) using equation (5-6).

$$q_t = q_0 * e^{-\frac{t}{\tau}} \quad (5\text{-}6)$$

Where: q_t is the discharge at time t; q_0 is the initial discharge at time t=0; and τ is the turnover time of base flow.

If logarithm is applied to the two sides of the equation (5-6), the equation will result to a linear equation with -1/τ as slope (a) thus the turnover (replacement) time of base flow (τ) is expressed by equation (5-7).

$$\tau = -\frac{1}{a} \quad (5\text{-}7)$$

5.2.5 Soil water characteristics

Soil moisture was measured at three different depths of 64 different locations in the four investigated catchments (see chapter 4 for a detailed description). The measurement points were classified into two groups. The first group is made of measurements performed at uplands and slopes and the second group encompases points located in lowlands or valley bottoms. Plinthosols and Cambisols are the dominant soil types at uplands and slopes whereas Gleysols dominate valleys bottoms. The physical properties of those soil categories are presented in the Table 5-1. Soil hydraulic conductivity (Ks), soil water at saturation (θs), residual soil water (θr), van

Genuchten parametrs (α and n) were estimated by pedo-transfer functions (Brakensiek and Rawls, 1994; Cosby et al., 1984; Patil and Singh, 2016; Rawls and Brakensiek, 1985; Saxton et al., 1986; Saxton and Rawls, 2006; Schaap et al., 2001; van Genuchten, 1980; Vereecken et al., 1990).

Table 5-1. Mean physical characteristics of Cambisols, Gleysols and Plintosols in Dano (Yira 2016).

	Horizon depth (cm)	Sand (%)	Silt (%)	Clay (%)	BD (g cm^{-3})	Ks (cm d^{-1})	θs (vol. %)	θr (vol. %)	α (m^{-1})	n (-)
Cambisols	0-16	25	45	30	1.3	953	46	10	3.5	1.3
	16-42	25	42	33	1.4	420	44	10	3.1	1.3
	42-86	18	54	28	1.5	278	43	10	2.1	1.3
Gleysols	0-18	26	55	19	1.4	545	42	6	2.7	1.3
	18-42	18	51	31	1.5	192	41	7	1.1	1.2
	42-86	18	50	32	1.6	163	40	3	0.5	1.2
Plinthosols	0-15	34	46	20	1.5	958	36	8	2.8	1.3
	15-42	23	42	35	1.6	778	34	9	1.3	1.2
	42-86	20	36	44	1.6	700	35	8	1.1	1.2

BD: Bulk density; **Ks**: saturated hydraulic conductivity; **θs**: saturated soil moisture; **θr**: residual soil moisture; **α** and **n**: van Genuchten parameters.

Soil moisture at the field capacity was computed using the van Genuchten retention curve (Cong et al., 2014; van Genuchten, 1980). Equation (5-8) presents the calculation of soil moisture at field capacity.

$$\theta_{fc} = \left[\left(-\alpha\psi_{fc}\right)^{n} + 1\right]^{-m}(\theta_s - \theta_r) + \theta_r \qquad (5\text{-}8)$$

Where θ_{fc} is soil water at field capacity [vol. %]; ψ_{fc} is the corresponding matric potential [m of water column]; θs and θr are saturated and residual soil moisture respectively [vol. %]; α [m^{-1}], n [-], and m [-] are van Genuchten parameters with m=1-1/n. ψ_{fc} was assumed to be equal to -33 kPa or -3.4 m of watercolumn (Assouline and Or, 2014; Colman, 1947; Richards and Weaver, 1944).

Equation (5-8) was applied for soil water at the permanent wilting point (θ_{PWP}) computation. This was done after replacing the matric potential at the field capacity (ψ_{fc}) by the matric potential at the permanent wilting point (ψ_{PWP}) which is -1500 kPa or -153 m of water column (Kirkham, 2014).

The plant-available water (PAW) was estimated by the difference between soil water at the field capacity and soil water at the permanent wilting point when the groundwater table is below the rooting zone (Blume et al., 2016).

5.3 Results and discussion

5.3.1 Runoff characteristics

Rating curves

The univariate quadratic polynomial equations were used for interpolating the stage-discharge curves (Fig. 5-4 to Fig. 5-7). Power-law equations were sometimes utilized for very low stages (Fig. 5-4-a and Fig. 5-4-b). The coefficient of determination between measured stage and measured discharge range from 0.84 to 0.99. R^2 obtained from the Manning method is higher compared to R^2 of the measured method. This corresponds to very good interpolation performance of rating curves. However, the water level corresponding maximum measured discharge is approximately 0.85 to 0.88 m. An extrapolation beyond maximum measured discharge was done for some gauging stations. Therefore, uncertainties of measured discharge increase when the recorded stage greater than 0.8 m (Leonard et al., 2000; Tomkins, 2014). It is recommended not to extrapolate a stage higher than 1.5 time the height of the highest measured discharge (ISO 1100-2, 2010). Overbank flows often occur during high flood events leading to relatively high uncertainties in observed discharge. The uncertainties might also originate from the number of gauged points, the function used for interpolation (power or polynomial equation type), the stage-of-zero flow used, and the discharge measurement during gauging (Birgand et al., 2013).

Concerning the Manning method, the major uncertainty stem from the roughness coefficient. It varies significantly from the bottom of the stream cross section to the banks and is influenced in terms of magnitude over time by vegetation growth at the gauging station, sedimentation, and erosion of the stream bed.

a) Outlet Loffing

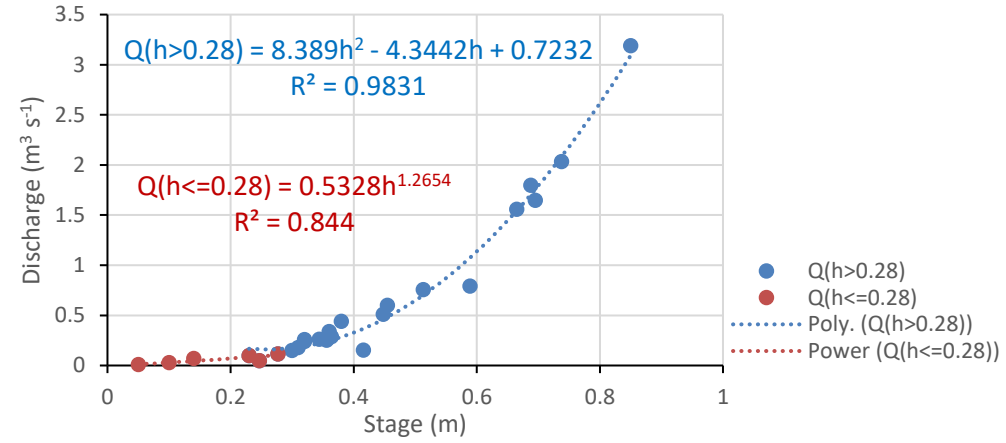

b) Bankandi-north

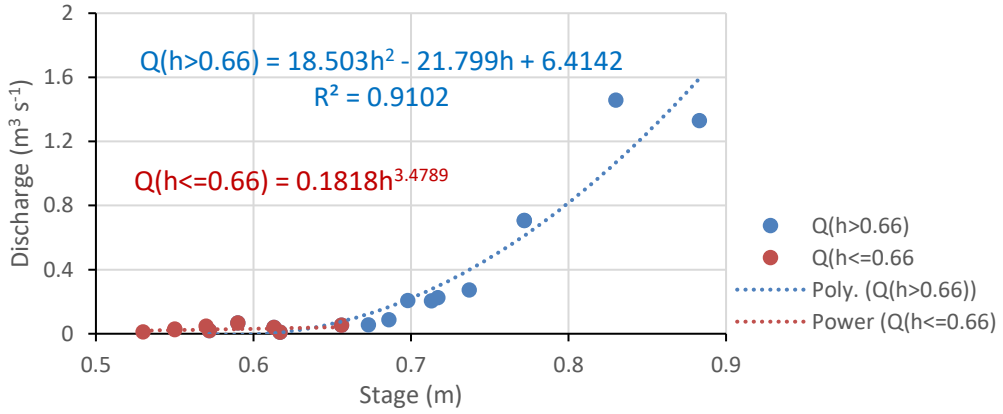

c) Bankandi-south

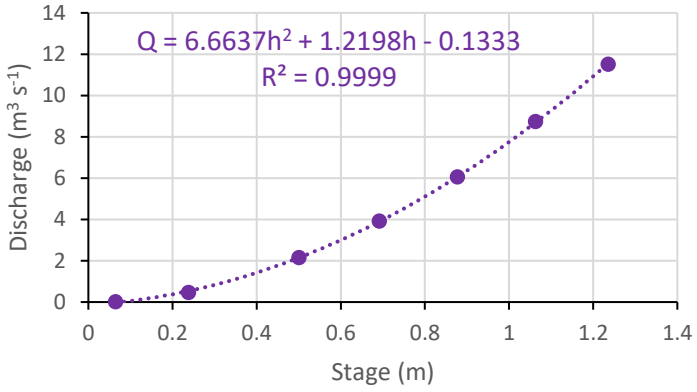

Fig. 5-4. Rating curves in the Bankandi-Loffing catchment (Q: measured discharge, h: stage, R^2: coefficient of determination).

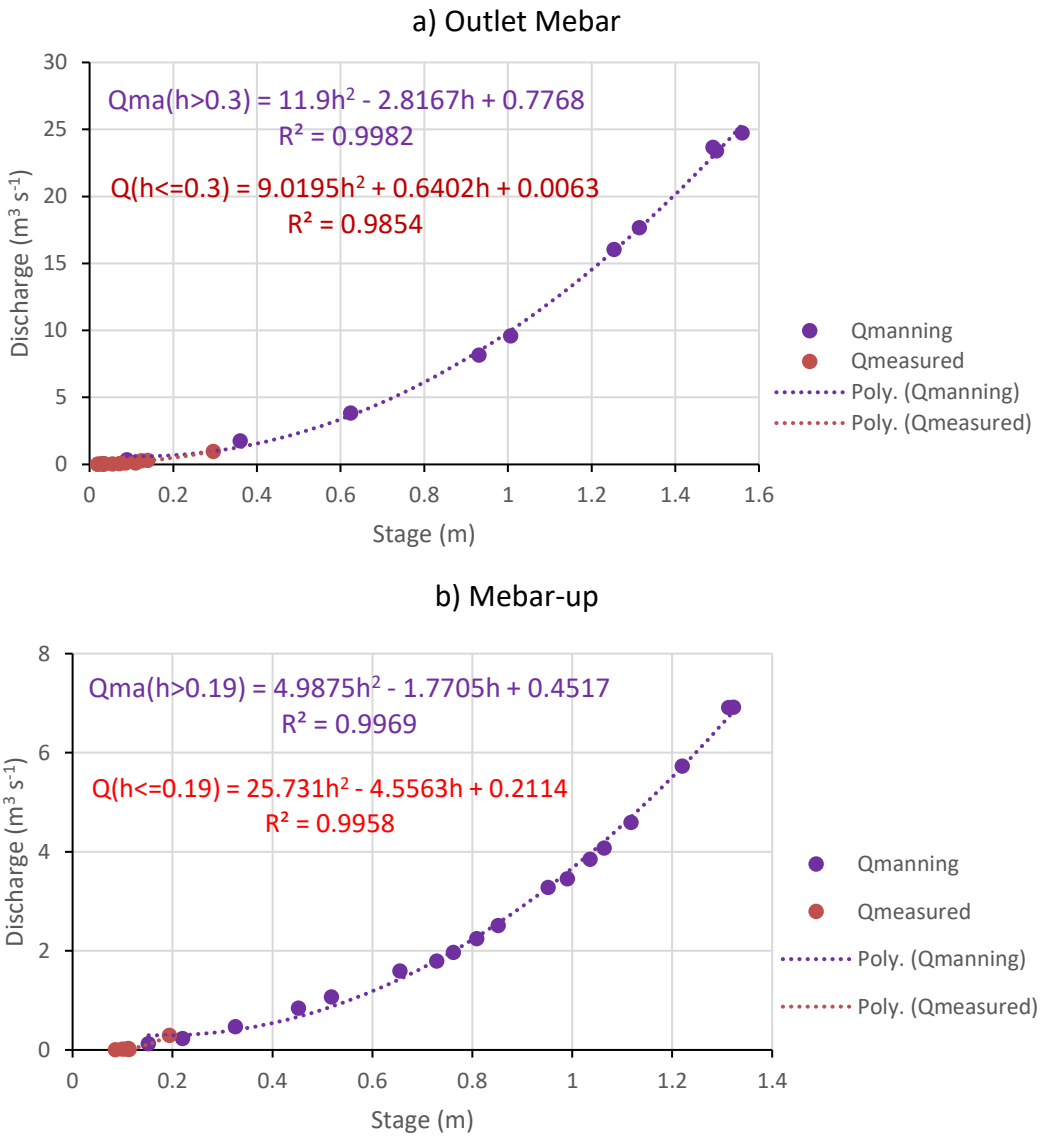

Fig. 5-5. Rating curves of the Mebar stream gauges (Qma: Manning calculated discharge, Q: measured discharge, h: stage, R^2: coefficient of determination).

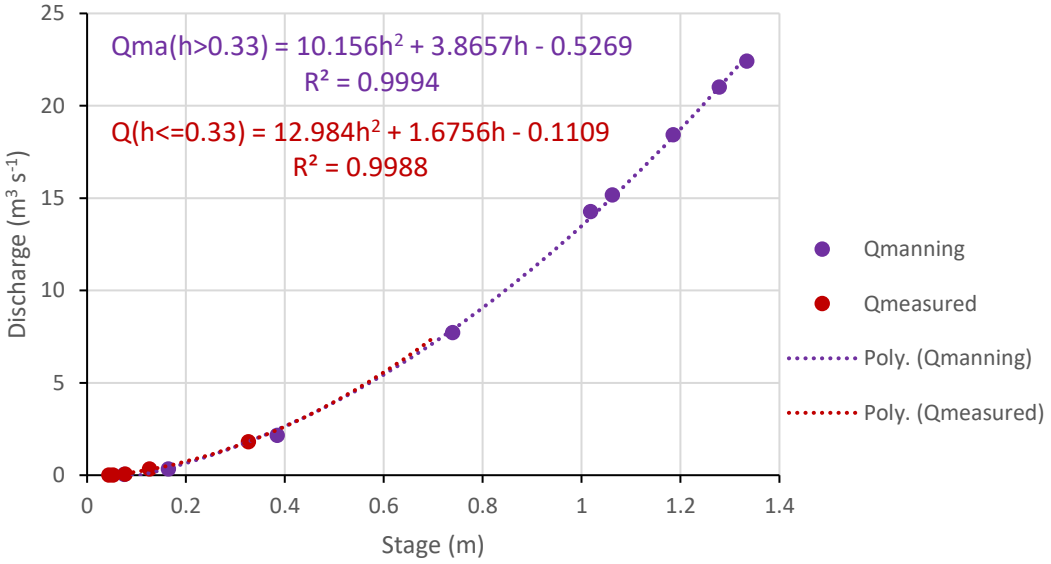

Fig. 5-6. Rating curve of the Moutori stream gauge (Qma: Manning calculated discharge, Q: measured discharge, R^2: coefficient of determination).

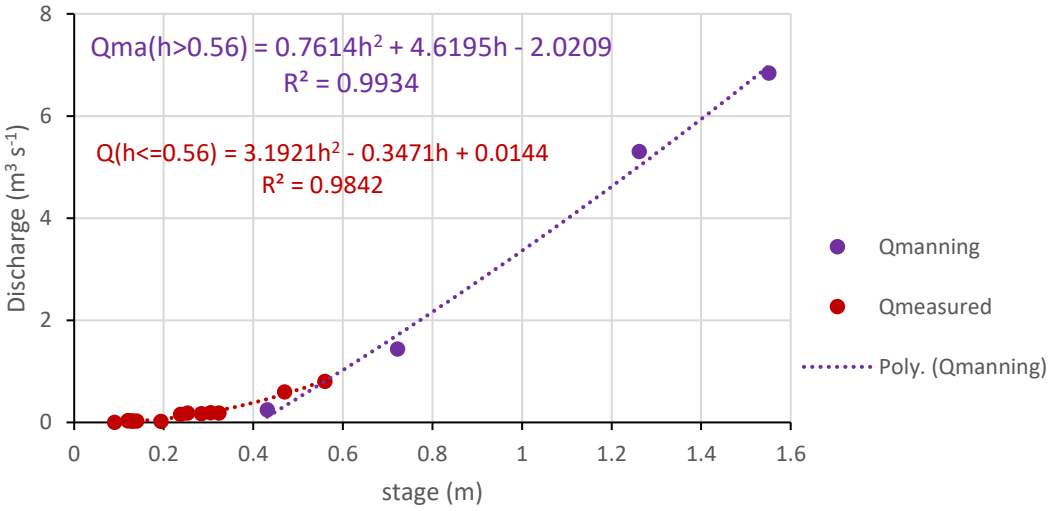

Fig. 5-7. Rating curve of Fafo stream gauge (Qma: Manning calculated discharge, Q: measured discharge, R^2: coefficient of determination).

Hydrographs

The observation of flows at high temporal resolution at a few gauging stations (Fig. 5-8, Fig. 5-9, and Fig. 5-10) shows no flow in the dry seasons (October to May). At the upstream gauging stations such as Bankandi-south and Mebar-up, flows occur only during rain events (Fig. 5-9 and Fig. 5-10) whereas at the Loffing gauging station which is located at the outlet of Bankandi-Loffing, base flow sustains flows over a large period

of rainy seasons. At Bankandi-south and Mebar-up, rainfall is the only source of flows. Base flow does not contribute to the flows due to the fact that the groundwater table is always below the streambed. On the other hand in Loffing, groundwater table is above streambed during rainy season. Therefore, base flow and rainfall are the sources of flows. Based on the classification of Buttle et al. (2012), the flows at Bankandi-south and Mebar-up can be qualified as ephemeral streams while the flows at Loffing are intermittent seasonal stream.

All the investigated streams fall into the temporary stream category as variable periods of no-flows can be observed. In contrast to temporary streams, perennial streams flow continuously during a hydrologic year and receive flows from temporary streams (Nadeau and Rains, 2007).

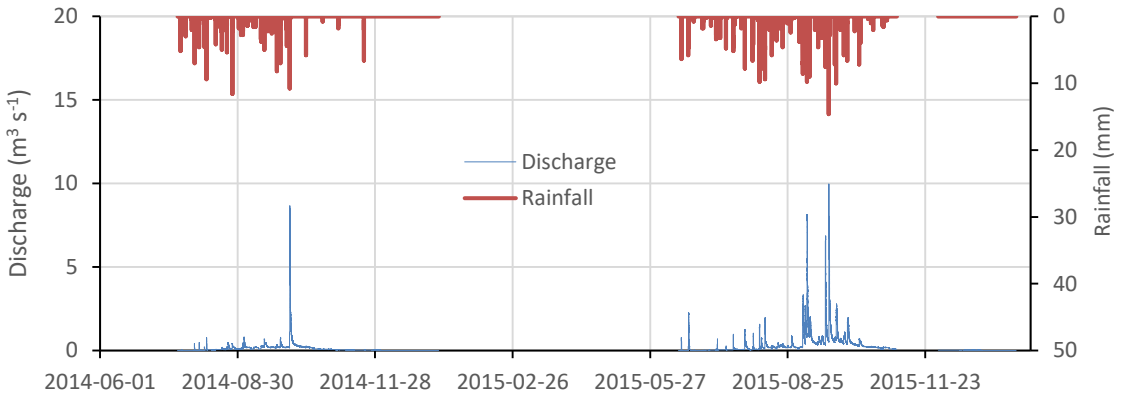

Fig. 5-8. Hyetograph-hydrograph at the Loffing gauging station, outlet of the Bankandi-Loffing catchment in 2014 and 2015 at 5 min time resolution.

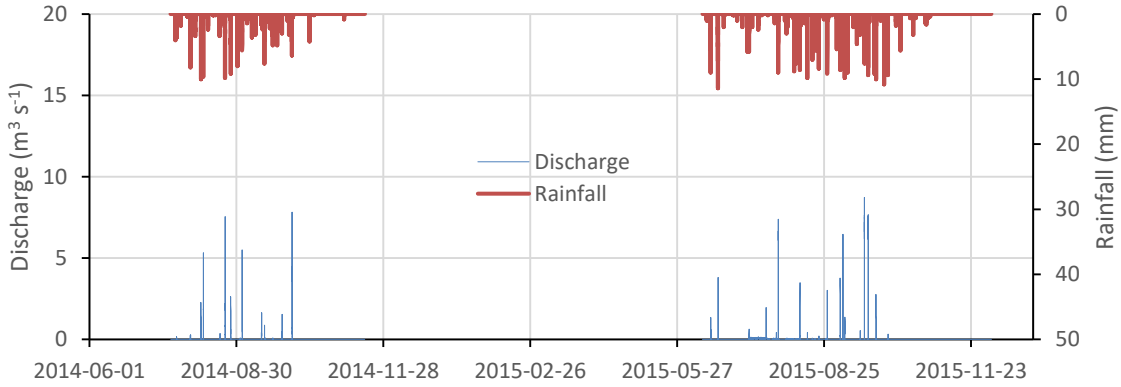

Fig. 5-9. Hyetograph-hydrograph at the Bankandi-south gauging station in 2014 and 2015 at 5 min time resolution.

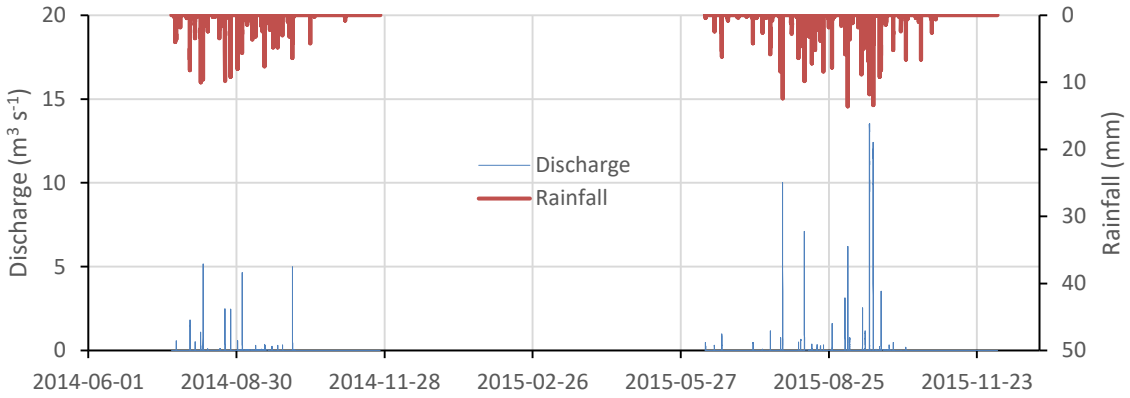

Fig. 5-10. Hyetograph-hydrograph at the Mebar-up gauging station in 2014 and 2015 at 5 min time resolution.

Runoff coefficient

Table 5-2 summarizes some hydrological characteristics of the investigated catchments for the years 2014 and 2015 (see Fig. 4-1 and Fig. 4-2 for the locations of the catchments and their corresponding stream gauges).

Table 5-2. Seasonal total runoff coefficients of the investigated sub-catchments for the observed periods (see Fig. 4-1 and Fig. 4-2 for the locations of the discharge stations).

Discharge station	Year	Area (km²)	P(mm)	Q(mm)	Cr (%)
Loffing	2014	30.23	680	54	8
	2015		778	149	19
Bankandi- north	2014	9.28	507	32	6
	2015		931	127	14
Bankandi- south	2014	2.32	656	53	8
	2015		1079	100	9
Mebar-low	2014	7.85	656	48	7
	2015		915	246	27
Mebar-up	2014	4.66	656	30	4
	2015		1043	66	6
Fafo	2014	11.32	554	75	14
	2015		1014	152	15

P: Seasonal rainfall; **Q**: Total discharge; **Cr**: Total runoff coefficient

The overall spatially weighted average runoff coefficient for the two seasons is 13%. Using hydrological modelling, Yira et al. (2016) obtained a similar result (13.2%) in Batiara-1 which is a sub-catchment located in the southern Dano catchment. The

discharge stations of Moutori, Mebar (up and low), Bankandi (north and south), and Loffing are located upstream of Batiara-1.

Although in the year 2015 precipitation was 163 mm higher than in 2014, the exceedance probability curves of rainfall (Fig. 5-11) present a slight difference of P_{10} (rainfall that is equaled or exceeded for 10% of the hourly time step, computed from non-zero flow data) between the years 2015 (8.8 mm h^{-1}) and 2014 (6.5 mm h^{-1}). Consequently, runoff coefficients in 2015 were higher than in 2014 in most of the sub-catchments. The average runoff coefficient almost doubled from 8% in 2014 to 15% in 2015.

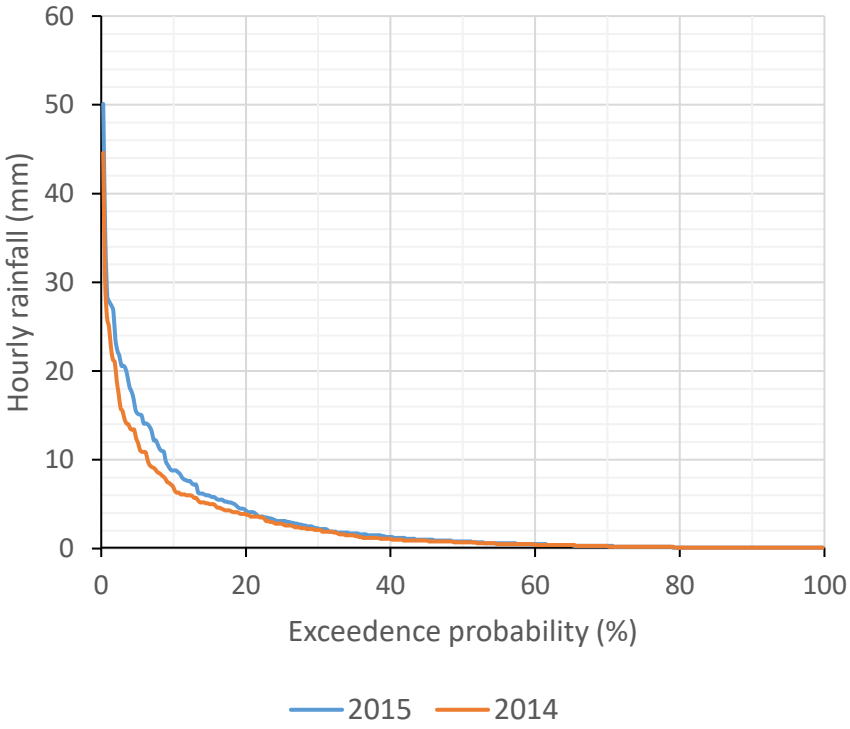

Fig. 5-11. Exceedance probability of hourly rainfall in 2014 and 2015 (zero flow values excluded).

The highest runoff coefficients were observed at Loffing and Mebar-Low gauging stations due to base flow contributions. The runoff coefficients of upstream sub-catchments are low because the contribution of base flow to discharge is negligible. In those upstream sub-catchments, my hypothesis is that rainfall is quickly lost through infiltration to the groundwater which is deeper at these sites. The groundwater then flows to the downstream sub-catchments, where it contributes to total stream flow. This hypothesis is based on the fact that the difference in evapotranspiration between the upstream and downstream sub-catchments is not significant (Yira et al., 2016).

Flow duration curves (FDC)

Throughout this chapter, Q_n will refer to a runoff which is equal or exceeds n% of the time steps. Fig. 5-12 shows a similar Q_{10} for all the sub-catchments (approximately 0.02 mm, time step of analysis = 5 min), which means similar sub-catchment behavior for high flow events. In contrast to the high flows, the sub-catchments differ in terms of low flows. The lower the flows, the higher the differences. However, Loffing and Mebar-Low remain similar for the low flow with Q_{90} being equal to 0.003 mm whereas 0.0008 mm is observed in Bankandi-North and 0.0003 mm in Fafo. These differences may be mainly explained by the contribution of the groundwater to the streamflow. Therefore, soil and LULC, which control the infiltration, are the key factors to the deeper understanding of the differences in one hand and groundwater hydraulic conductivities and the hydraulic gradients are the main parameters controlling groundwater flow (Darcy, 1856). Moreover, the slope can contribute to an extent the differences of behavior. For instance, approximately 16% of the area of Bankandi-south is covered by a slope which is equal or higher than 10% whereas only 3% of the area of the Loffing and Bankandi-north are equal or higher than 10% slope (Fig. 5-13).

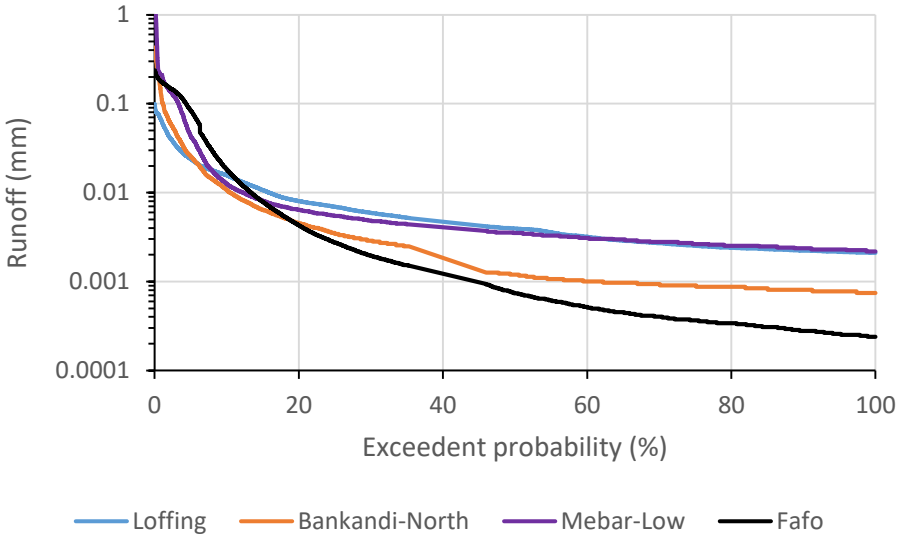

Fig. 5-12. Flow duration curves at 5 minute time step for 4 discharge stations in 2014 and 2015 (see Fig. 4-1 and Fig. 4-2 for the locations of the discharge stations).

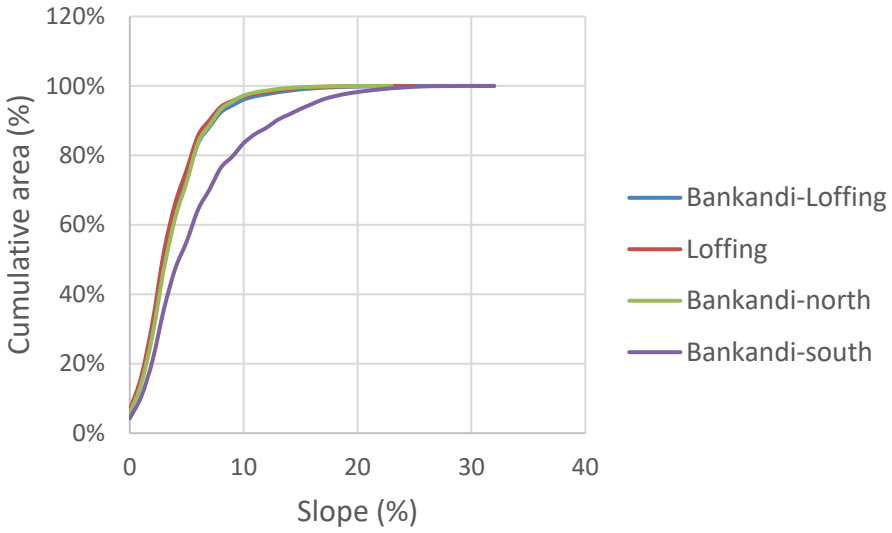

Fig. 5-13. Slope distribution in the Bankandi-Loffing catchment

Runoff components by stream electrical conductivity analysis

The observed electric conductivity (EC) and discharge at the outlet of Bankandi-Loffing (see Fig. 4-2-a for the location of the discharge station) are correlated which is shown for the event of September 20 to 23, 2015 in Fig. 5-14-a (coefficient of determination (R^2) was 0.63). Therefore, EC was used to determine runoff components and especially runoff discharge or fast flow (overland flow plus interflow) and the base flow. The result of application of the equation (5-2) is presented in the Fig. 5-14-b.

The total rainfall for the event (Fig. 5-14) was 75.6 mm during 135 min (2.25 h). The recorded maximum rainfall intensity during the event was 14.6 mm per 5 min (equivalent to 175.2 mm h^{-1}). The mean rainfall intensity of the event which was 33.6 mm h^{-1} shows it was a very heavy rainfall event (Llasat, 2001). The event generated a total runoff coefficient of 20% compare to the rainfall. The decomposition of runoff shows that runoff discharge (64% of total runoff) contitutes the major part of the total runoff and base flow represents 36% of the total runoff of the event (Fig. 5-14-b).

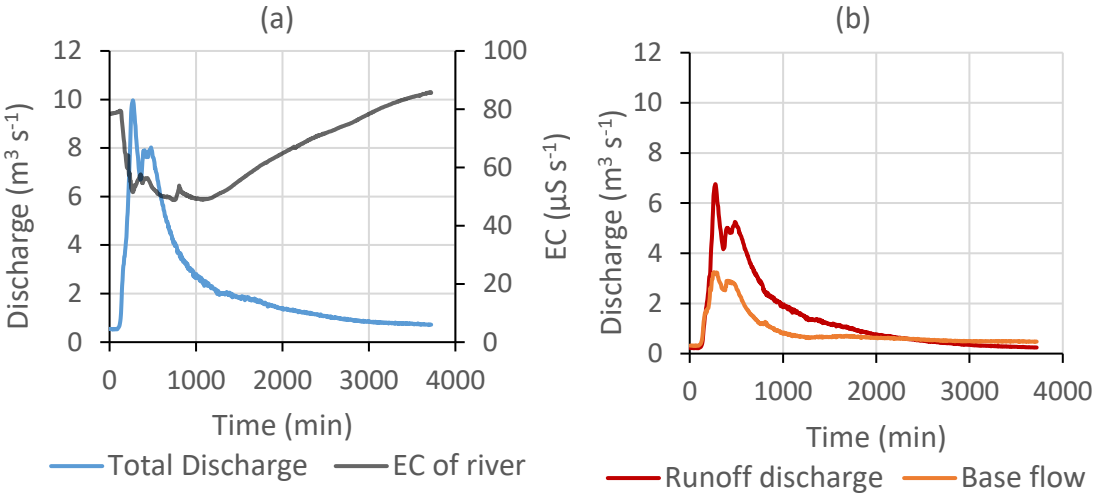

Fig. 5-14. Base flow separation using EC at the main outlet of Bankandi-Loffing station: A- comparison between measured EC and the hydrograph; B- runoff discharge and base flow assessment based on the event recorded for the period of September 20 to 23, 2015.

Runoff components by hydrograph analysis

Table 5-3 summarizes the results of hydrograph-based runoff partitioning. It shows that the interflow is the most important component of total discharge in the majority of the sub-catchments except in Mebar-up where surface flow prevailed compared to other runoff components. Furthermore, it is important to notice the absence of base flow for some ephemeral streams (Moutori, Mebar-up) due to the greater depth of the shallow groundwater.

Although the temporal resolution of the discharge data was high, all flood events do not isolate the two peaks (surface flow and interflow). Most of the well-separated peaks occurred in September, in the middle of the rainy season. This is the time of the season when the soil is almost at its field capacity or saturated and the shallow aquifer close to its highest level below the ground. Therefore, the surface runoff might mainly occur by saturation excess. Regarding the interflow, *groundwater ridging* and the *translatory flow* might account as the major mechanism of rapid sub-surface flow around the middle of the rainy season due to the soil water at the field capacity or wetter (Beven, 1989).

Table 5-3. Total runoff decomposition by the hydrograph analysis.

	Event	P (mm)	I_p (mm h^{-1})	Q_t (mm)	C_r (%)	Runoff components (% of total runoff)		
						Q_s	Q_i	Q_b
Loffing	20-21/09/2015	70	31	11	16	19	39	42
Bankandi-N	6-7/09/2015	75	12	18	24	20	64	16
Bankandi-S	03/10/2014	45	9	14	31	16	75	9
Mebar-up	18/09/2015	99	23	32	32	54	46	0
Moutori	01/09/2014	26	6	8	31	0	100	0
Fafo	1-2/08/2014	28	6	9	32	6	89	6

P: rainfall; **I_p**: Rain Intensity; **Q_t**: Total runoff; **C_r**: Total runoff coefficient; **Q_s**: surface runoff; **Q_i**: interflow; **Q_b**: base flow, Bankandi-N: Bankandi-north, Bankandi-S: Bankandi-south.

By assuming the surface runoff calculated by the EC-based method is equal to the sum of surface flow and interflow, the comparison of the partitioning methods showed only a slight difference. The EC-based partitioning gave a runoff discharge of 64% of total runoff and base flow of 36%, whereas with hydrograph-based partitioning, they were 58%, and 42% respectively.

High disparities in the results of runoff partitioning between the events were observed. This may be attributed to the pre-event hydraulic conditions and in some extent to the variation of rainfall intensity. In fact, rainfall intensity for the investigated events ranges from 6 to 31 mm h^{-1}.

5.3.2 Groundwater dynamics

Temporal variation of groundwater table at the outlet of Bankandi-Loffing

In order to understand the shallow groundwater reaction in both rainy and dryness, the shallow groundwater level was recorded at a 6 h time steps during 2014 to 2016 at the outlet of the Bankandi-Loffing catchment. Fig. 5-15 depicts the shallow groundwater level at the piezometer Lo23 and the rainfall accounting for recharge (see Fig. 4-2-a for the location of the piezometer in Bankandi-Loffing catchment).

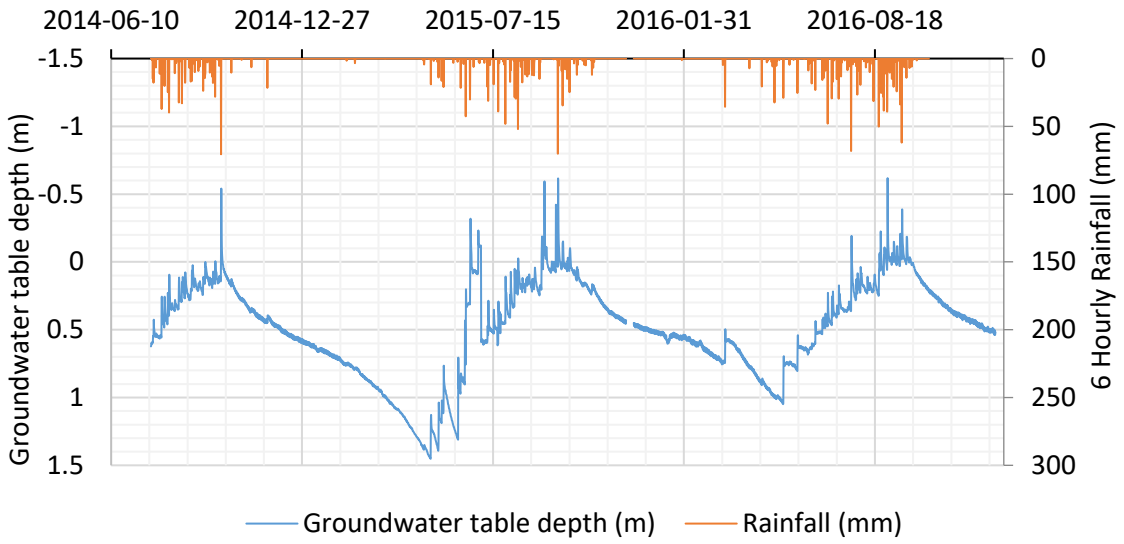

Fig. 5-15. Temporal variation of groundwater table depth at the piezometer Lo23 (see Fig. 4-2 for the location of the piezometer in the Bankandi-Loffing catchment).

Fig. 5-15 shows that the shallow groundwater reacts almost simultaneously to rainfall and increases to its highest level in October whereas, in the dry season, groundwater levels drop steadily reaching its lowest value in mid – May which is 1.45 and 1.05m below surface in 2014 and 2015 respectively. This suggests a shallow groundwater which can be easily accessible by traditional means of digging including pickaxe, shovel, and hoe instead of heavy digging machines. Therefore low financial investment is needed for digging wells. However, further investigation of groundwater productivity through pumping tests is needed to determine the full potential of the groundwater in the area for irrigation.

Hydraulic interrelation between shallow aquifer and streamflow

The groundwater-streamflow relationship is important to understand water fluxes between the two systems. Therefore, water levels in the streambed and water levels in the Piezometer Lo23 located 5 m away from the riverbed at the outlet of Bankandi-Loffing are compared for the years 2014 and 2015. The stream level minus groundwater level is presented in the Fig. 5-16.

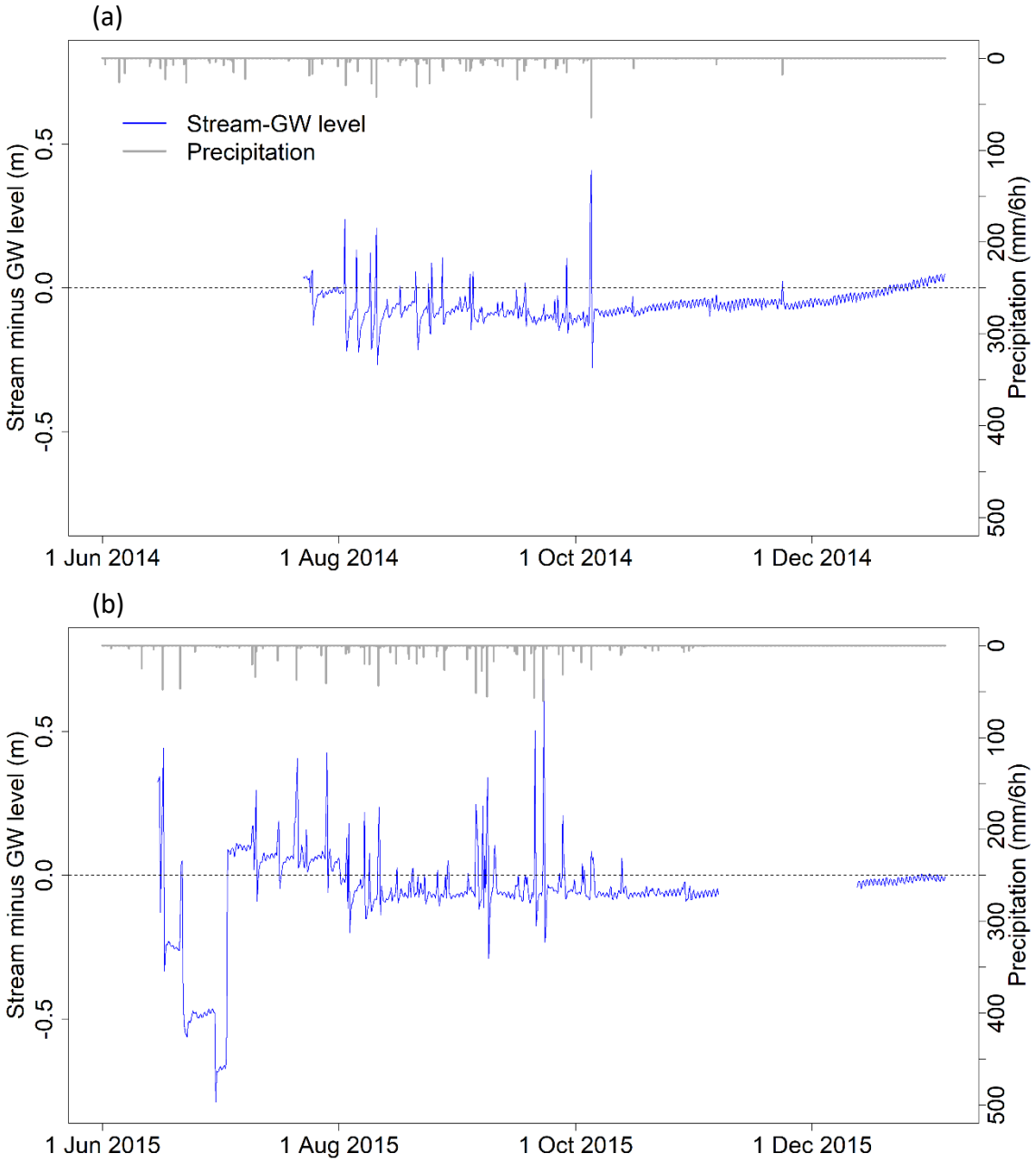

Fig. 5-16. Difference between stream level and groundwater (GW) level at the outlet of the Bankandi-Loffing catchment during 2014 (a) and 2015 (b). (Time resolution: 6 h; the dashed line shows stream-grounwater equilibrium level).

Exfiltration from the shallow groundwater to the stream is driven by a hydraulic gradient from groundwater to the stream. Fig. 5-16 shows that exfiltration occurs most of the observation period whereas infiltration from the stream occurs mainly during flood events. Longer infiltration period was noted in 2015 compared to 2014. This may be mainly explained by the difference in rainfall between the two years. The rise of the curve from October (beginning of dry season) may be attributed to

groundwater level decrease which leads to base flow reduction. Base flow continues to decrease until it completely stops when groundwater drops below the streambed from December and the stream dries out.

Groundwater recession

Table 5-4 shows a variable turnover of the base flow which is influenced by the inter-annual variability of rainfall in the area during the observation period. The base flow turnover was short (11 days) for the rather dry year 2014 but much longer for wetter years 2015 and 2016. This suggests that in the absence of rainfall, base flow may last 11 to 44 days before groundwater level drops below streambed and the stream dries out. It is important to recall that the Bankandi-Loffing is a headwater catchment with an intermittent stream.

Table 5-4. Characteristics of base flow recession curve at the outlet of Bankandi-Loffing.

Flood event date	**q_0 (mm d^{-1})**	**a**	**τ (d)**
October 6-12, 2014	1.0195	-0.0887	11
December 2-31, 2015	0.0717	-0.0356	28
October 11, to November 25, 2016	0.1436	-0.0226	44

***q_0**: initial discharge; **a**: slope of the late recession curve; **τ**: turnover time of groundwater storage.*

A longer observation of groundwater depletion in piezometers for approximately 6 months with no significant rainfall is presented in Fig. 5-17. A gradual depletion of groundwater table was observed during the dry season even after stream flows cease. This means a considerable part of groundwater is discharge by groundwater flow below stream bed. It is important to note higher depletion rate in early dry season (19 mm d^{-1}) compared to late dry season (9 mm d^{-1}). The difference is mainly due to a higher groundwater hydraulic gradient at early dry season compared to late dry season between the upstream and downstream areas.

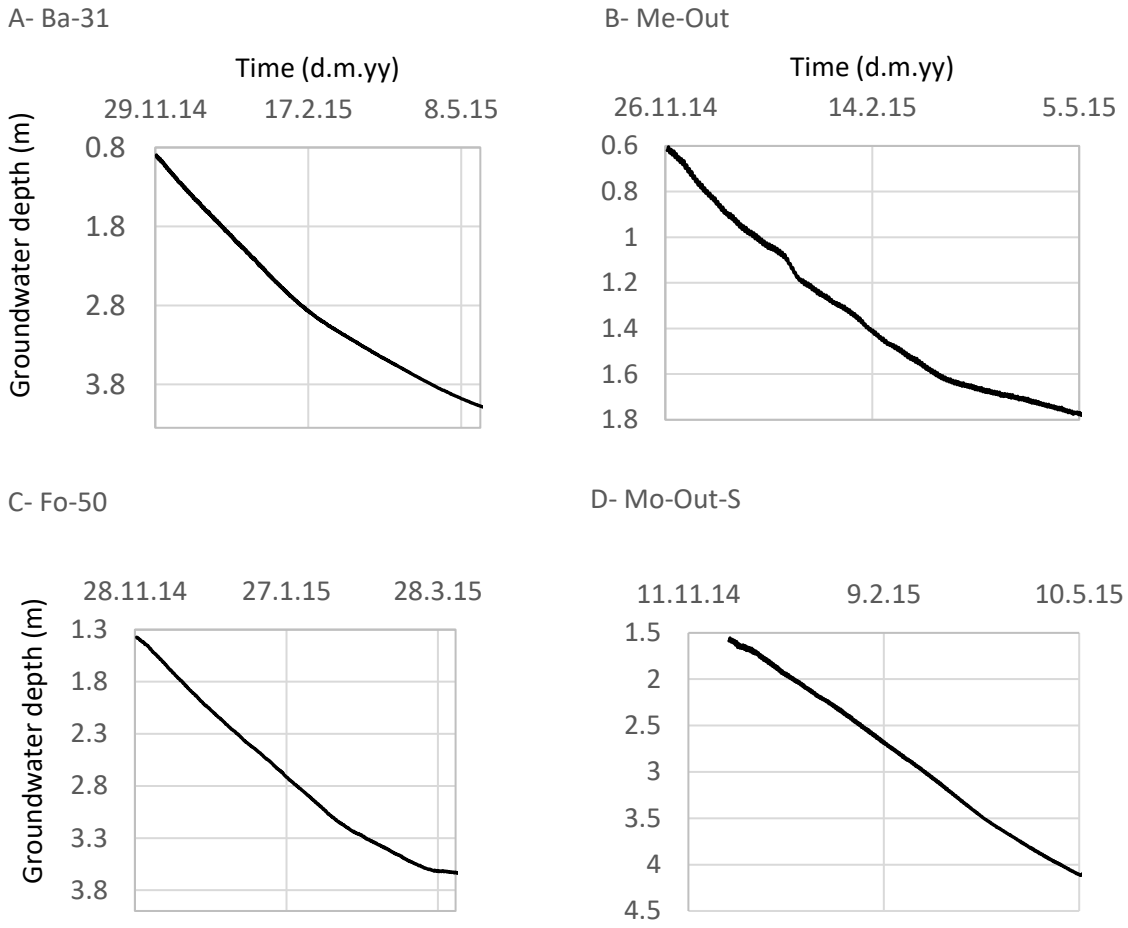

Fig. 5-17. Groundwater depletion in the dry season for 4 piezometers (depths are below ground surface)

Shallow groundwater table spatial and temporal distribution

The spatial distribution of the groundwater level is depicted in Fig. 5-18, contrasting the groundwater levels in October 2015 (end of the rainy season) versus May 2015 (end of dry season).

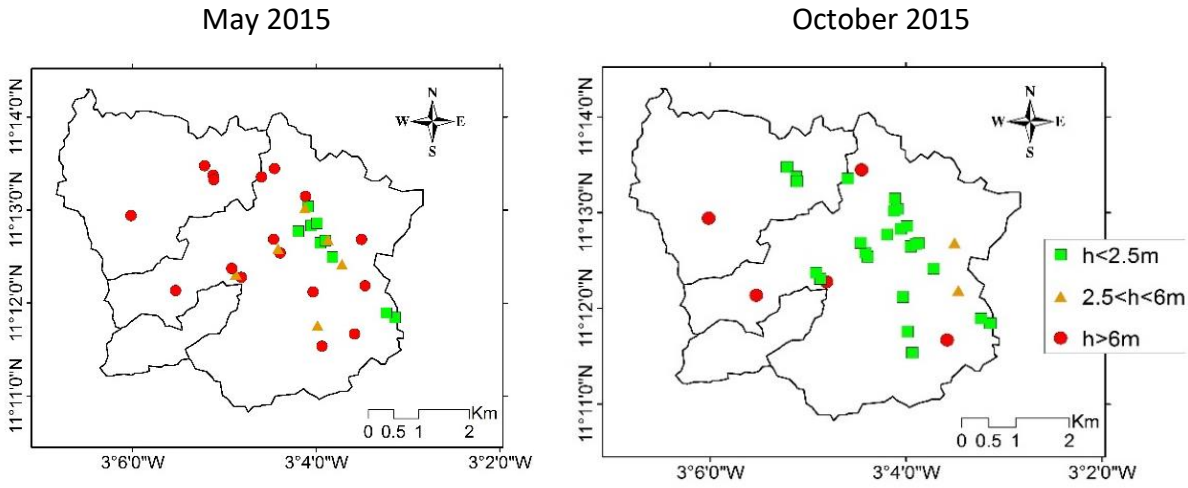

Fig. 5-18. Spatial distribution of the depth to groundwater table in Bankandi-Loffing in May and October 2015.

In October, the observed groundwater level is less than 2.5 m below the ground surface (indicated by spots in green) at most of the observation sites. Red dots indicate that the groundwater is absent at the investigation depth (first 6 m). Dominating green spots indicate rather shallow groundwater in October due to recharge during the rainy season.

In May, the green and orange dots indicate sites with permanent groundwater whereas red dots are locations with temporal or absent shallow groundwater at the first 6m. The spatial distribution of sites with perennial shallow groundwater (green spots) follows a spatial pattern as these sites are concentrated in the depression parts or the inland valleys of the catchments (see Fig. 4-2 for the topography of the catchment).

The shallow groundwater table suggests that it is reachable by basic tools and therefore not much investment is needed to exploit the shallow groundwater in the inland valleys. However, its productivity needs to be assessed by pumping tests in order to determine the quantity of water it can realistically provide.

Deep groundwater table spatial and temporal distribution

Three wells under use by local people for domestic water supply in Mebar, Moutori, and Bankandi were selected to monitor the deep groundwater table dynamics compared to the shallow aquifer previously analyzed in this chapter (Fig. 5-15 and Fig. 5-18). The monitoring was implemented from 2014 to 2016. The total depths of the wells are approximately 6m in Mebar, 16m in Moutori, and 25m in Bankandi-Loffing. Like the shallow aquifer, the monthly groundwater table level observation (Fig. 5-19)

shows a peak level at the end of September whereas the lowest levels were observed from May to June.

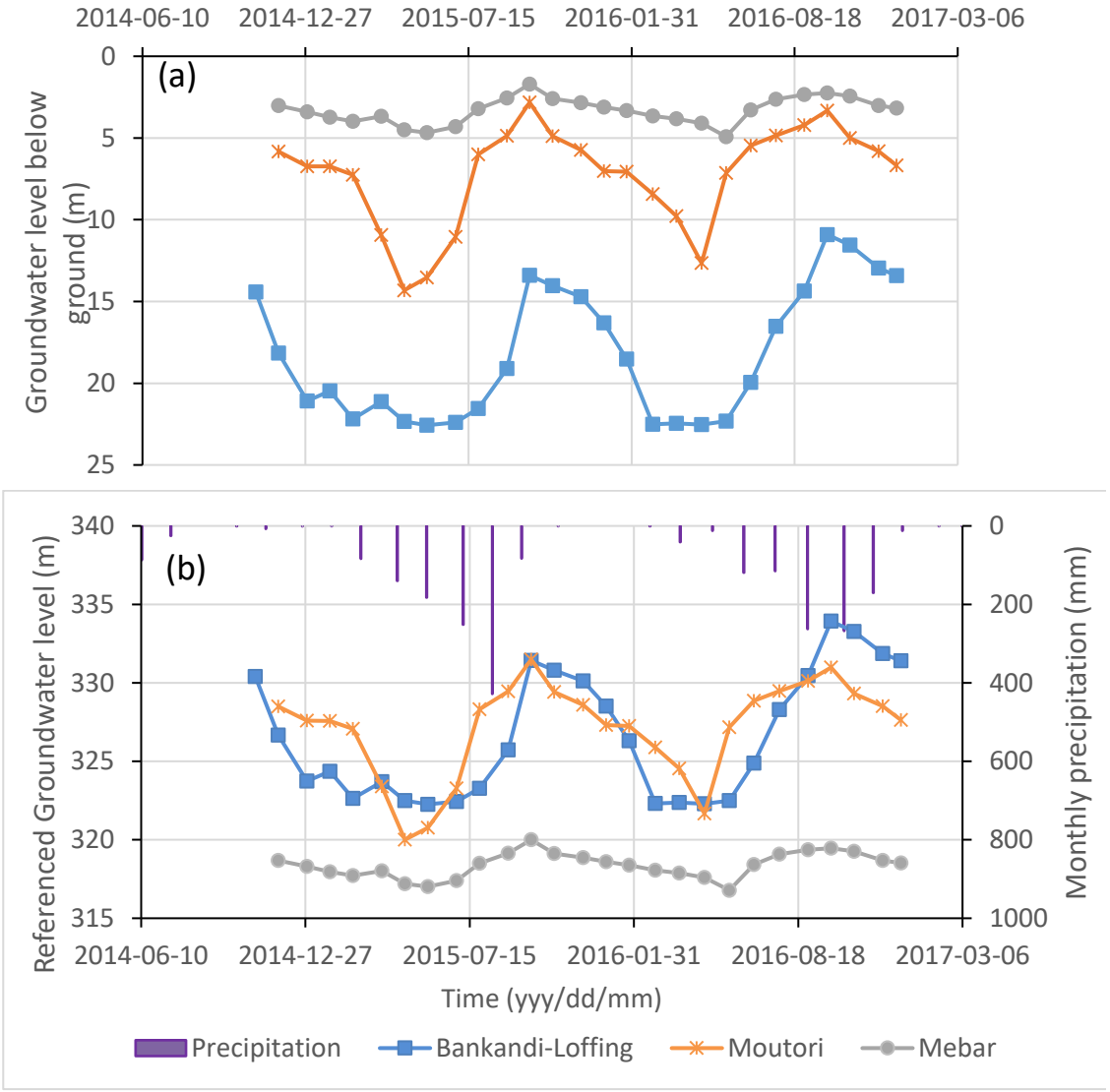

Fig. 5-19. Monthly groundwater table fluctuation in the Bankandi-Loffing, Moutori, and Mebar catchments from 2014 to 2016. (a) level below ground, (b) referenced groundwater level (Fig. 5-20 shows the location of the wells).

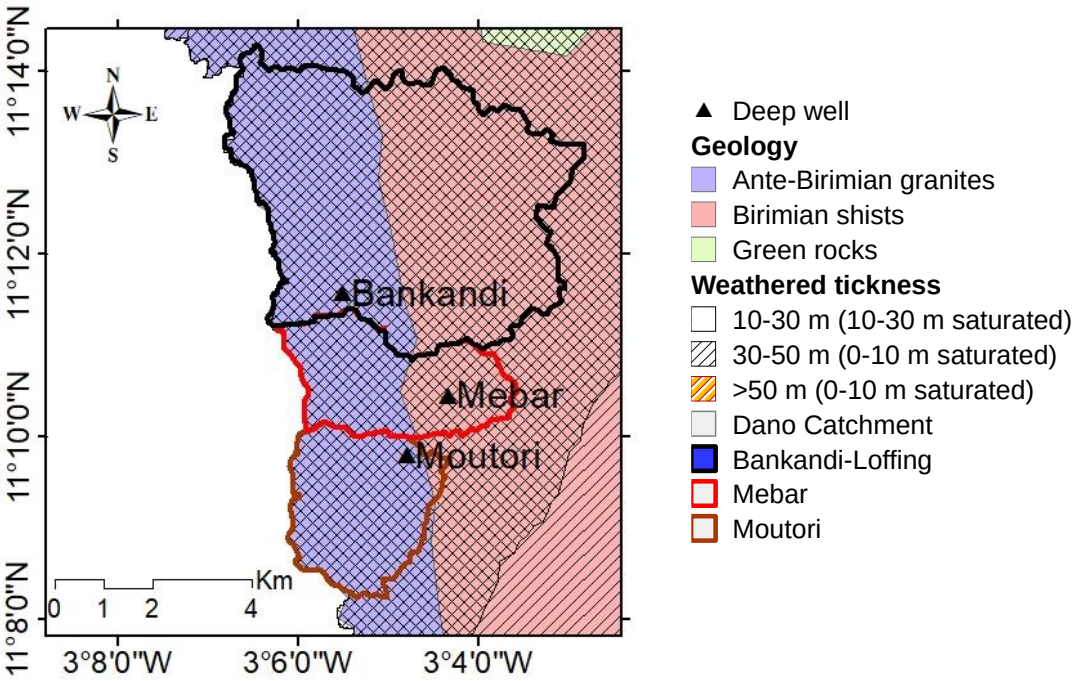

Fig. 5-20. Location of the three monitoring wells on a geological map.

The similarity between groundwater level in Bankandi-Loffing and Moutori (Fig. 5-19) might be attributed to the fact that both wells are located at the upstream area in the same geological formation (Ante-Birimian granites) (Fig. 5-20). Moreover, the referenced groundwater level depicted in Fig. 5-19-b shows a higher level in Bankandi and Moutori compared to Mebar for the observation period. This seems to infer that groundwater flow occurs in the same direction as streamflow; that is west-east.

The groundwater recession rate in the dry season decreased from west to east (68 mm d^{-1} in Bankandi, 31 mm d^{-1} in Moutori and 8 mm d^{-1} in Mebar). This may be due to the direction of groundwater flow (west-east). The large lateral inflow of groundwater in the dry season sustained the flow and reduced the groundwater recession in downstream area.

Electrical resistivity tomography of some transects

Transects (Fig. 5-21 and Fig. 5-22) are centered to valley bottom in order to account for the sub-surface of inland valleys and pass near some piezometers which were installed in the shallow aquifer. The measurements were contrasted between the upstream and downstream area of the catchment.

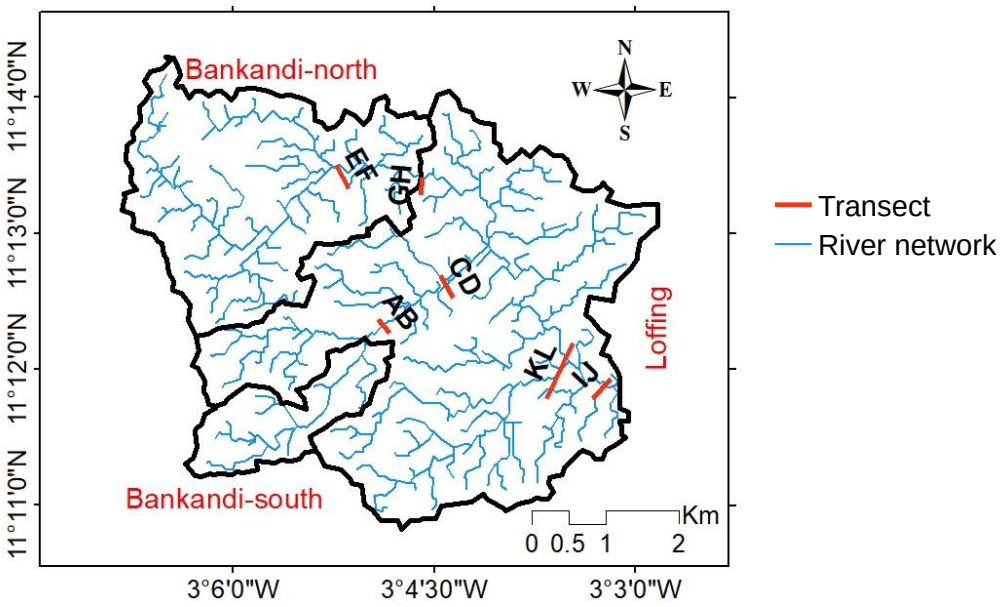

Fig. 5-21 Locations of the transects AB, CD, EF, GH, IJ, and KL in Bankandi-Loffing.

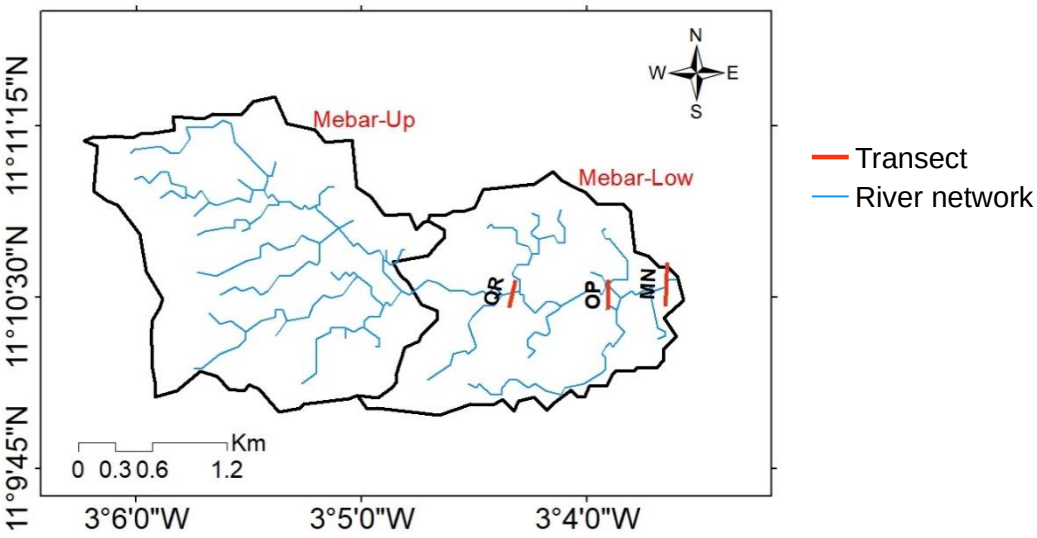

Fig. 5-22. Locations of the transects MN, OP, and QR in Mebar.

The two-dimensional resistivity profiles or the electrical resistivity tomographies (ERT) (Fig. 5-23, Fig. 5-24, Fig. 5-25, and Fig. 5-26) show heterogeneous distribution of electrical resistivity. The highest resistivities can be observed at the bottoms and the edges of the ERTs whereas the lowest resistivities are located at the centers. This may be attributed to relatively low water content of the deep geological formations. Low resistivity at ERT bottoms might indicate the aquifer basement rock which is less weathered hence less permeable. The edges of the ERTs which describe slope and uplands of inland valleys have less water content due to flow of groundwater

from uplands to valley bottoms. Sometimes, narrow bands of relatively high resistivities cover some low resistivity areas (e.g.: transect CD Fig. 5-23; transect EF, GH Fig. 5-24; transect QR, MN Fig. 5-26). This may be attributed to laterite rocks which result from clay induration due to severe superficial weathering followed by selective leaching and concentration of oxidized iron (Fe^{3+}) (Giorgis et al., 2014). The laterite rocks are most of the time impermeable.

The low resistivity observed at the centers of the ERTs might be associated with a significant amount of groundwater. When these formation are permeable, they may constitute good aquifers. However, if they have high clay content, they may shows low electrical resistivity but low permeability. Consequently, they will not be aquifers easy to use. These formation are 20 to 30 m thick in the investigated catchments. This information is valuable for the configuration of the geometry of the aquifer in WaSiM. Nevertheless, the information from these ERTs analyses should be used with precautions because topography is not included to the analyses. Slight deviations might occur from uplands to lowlands for each transect. The deviations might be negligible due to short transects (240 to 950 m) in a relatively flat area.

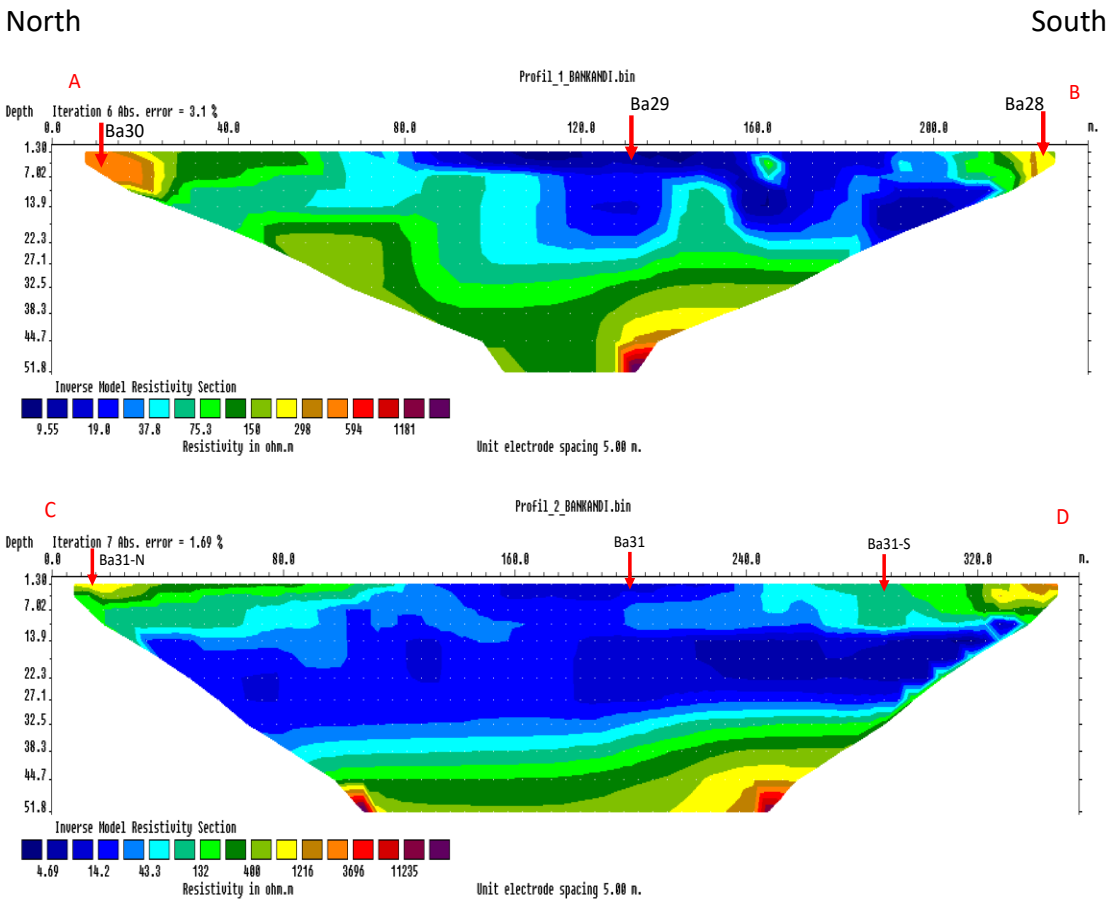

Fig. 5-23. Electrical resistivity tomographies of transects AB and CD located at the center of Bankandi-Loffing (the red arrows indicate the position of some monitored piezometers; see Fig. 5-21 for the locations of the transects).

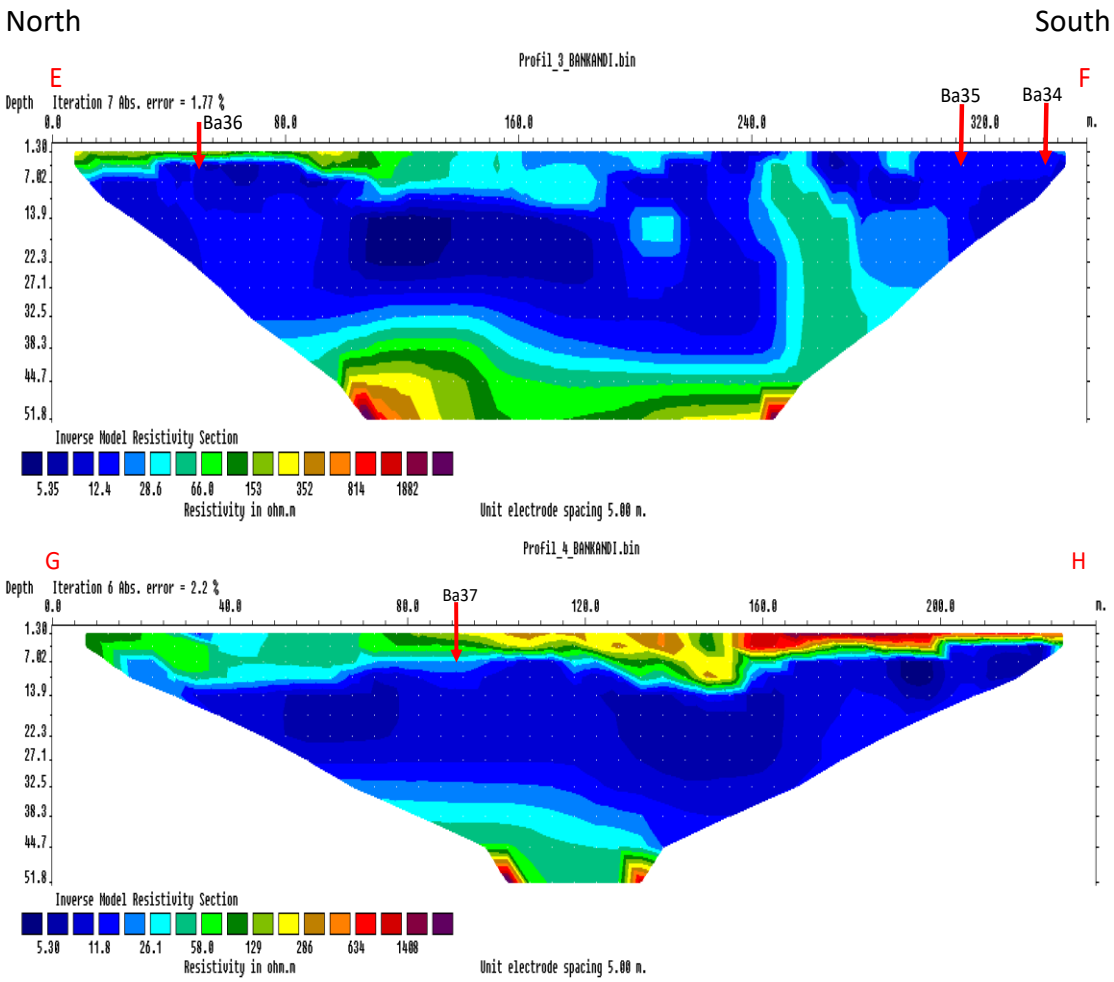

Fig. 5-24. Electrical resistivity tomographies of transects EF and GH located at northern area of Bankandi-Loffing (the red arrows indicate the position of some monitored piezometers; see Fig. 5-21 for the locations of the transects).

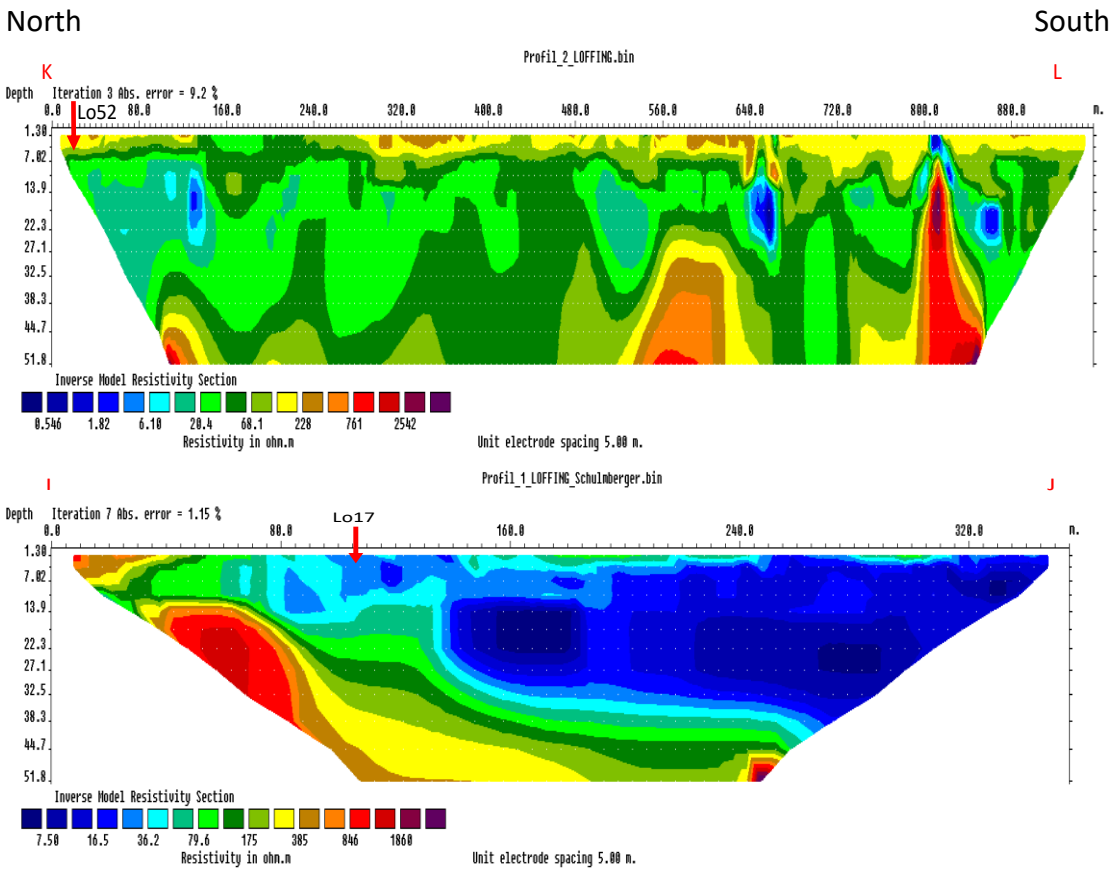

Fig. 5-25. Electrical resistivity tomographies of transects KL and IJ located at downstream area of Bankandi-Loffing (the red arrows indicate the position of some monitored piezometers; see Fig. 5-21 for the locations of the transects).

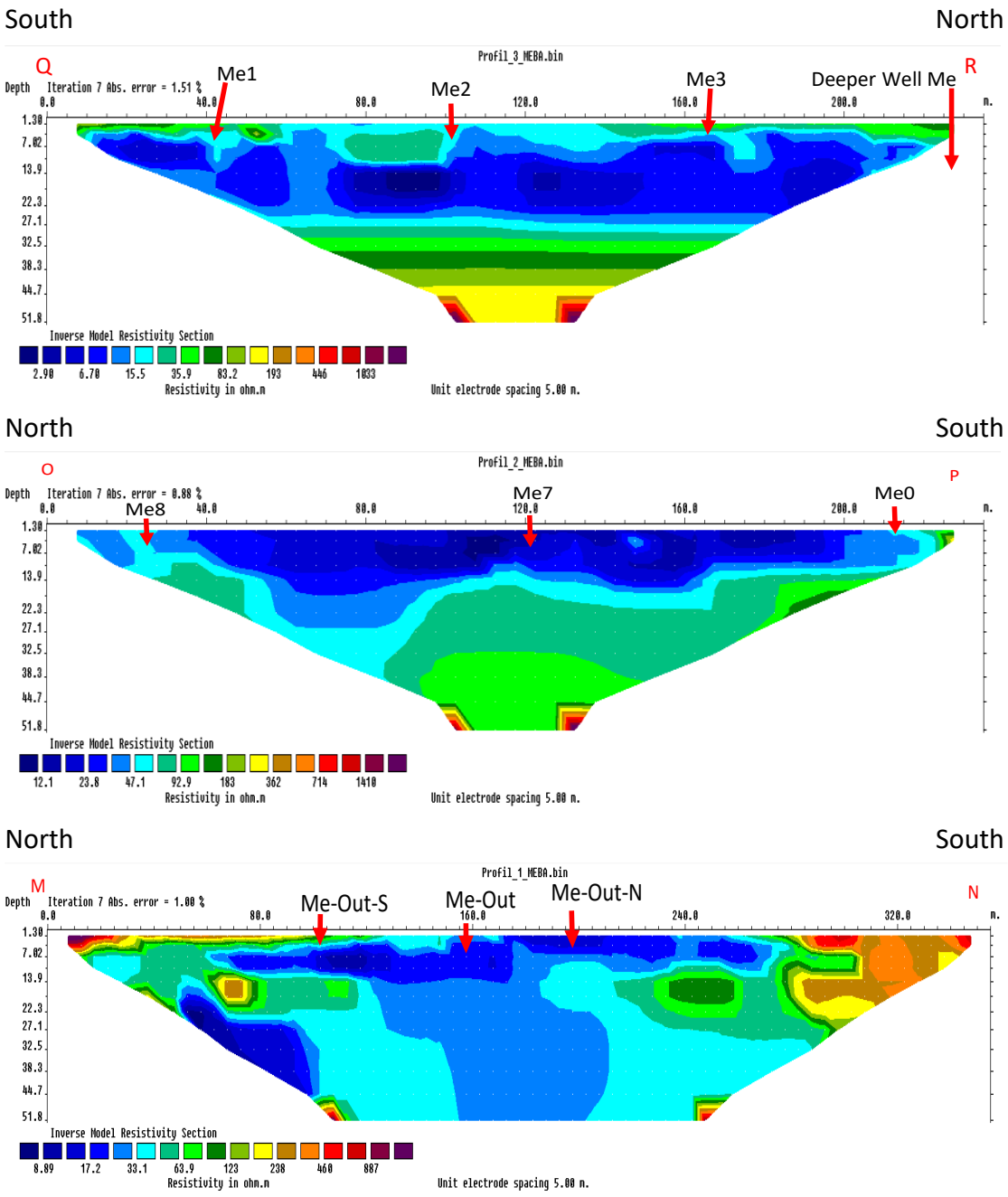

Fig. 5-26. Electrical resistivity tomographies of transects QR, OP, and MN located at Mebar (the red arrows indicate the position of some monitored piezometers; see Fig. 5-22 for the locations of the transects).

Slug test results

Hydraulic conductivity (Ks) is one of the most important characteristics of an aquifer (Hwang et al., 2017). It measures the transmission of water through porous formations. Ks of the shallow aquifer is unknown for the study area. A Slug test has been undertaken in order to estimate Ks. The result (Table 5-5) shows a large range of Ks

variability in the area (10^{-8} to 10^{-5} m s^{-1}). The variation may be explained by the variation of the geological formations which vary from alluvium in the valley bottoms to saprolites in the slope and uplands. The saprolites are very permeable when the coarse materials that they are made of are not cemented by fine materials (clay and silt).

The valley bottoms tend to have alluvial materials on the top of saprolites. Therefore, the recharge of the weathered saprolite aquifer and the underlying migmatitic or granitic aquifer mainly depends on the hydraulic conductivity of the alluvial materials. This process is well described in a similar catchment in the northern Benin (Fass, 2004). The alluvium of the valley bottoms can be constitute of sand or sandy loam and permeable. Nevertheless, if they are made of silt of clay, their permeability is reduced.

The measured Ks obtained is similar to the Ks of a fractured igneous and metamorphic rock (Şen, 2015). However, a precaution is needed when using slug test data because they correspond to Ks at the vicinity of the investigated wells.

Table 5-5. Statistics of measured saturated hydraulic conductivity using slug test in 36 piezometers.

	Ks (m s^{-1})	Ks (cm d^{-1})
Minimum	$1.0\ 10^{-8}$	0.1
Maximum	$1.2\ 10^{-5}$	103.2
Mean	$1.6\ 10^{-6}$	13.8
Percentile 25%	$1.3\ 10^{-7}$	1.1
Median	$8.7\ 10^{-7}$	7.5
Percentile 75%	$1.6\ 10^{-6}$	14.1

5.3.3 Measured soil water

Weekly variations of soil moisture

The calculation of soil water at field capacity and at permanent wilting point and plant available water (Table 5-6) show that Plinthosols is the least plant available water soil with clay to clay loam texture. It is followed by Cambisols (clay loam soil) and Gleysols (silt clay loam). Hence, the plant available water decreases from water valley bottom dominated by Gleysols to uplands where Plinthosols are the main soil type.

Table 5-6. characteristics of dominant soil types and their soil available water.

	Horizon depth (cm)	**Texture**	θ_s	θ_r	θ_{fc}	θ_{PWP}	**PAW**
			(vol. %)				
Cambiosol	0-16	Clay loam	46	10	27	15	12
	16-42	Clay loam	44	10	27	15	11
	42-86	Silty clay Loam	43	10	28	16	12
Gleysol	0-18	Silt Loam	42	6	24	12	12
	18-42	Silty clay Loam	41	7	32	19	13
	42-72	Silty clay Loam	40	3	34	19	15
Plinthosol	0-15	Loam	36	8	22	13	10
	15-42	Clay loam	34	9	27	18	9
	42-86	Clay	35	8	28	18	10

θ_s: soil water at saturation; θ_r: residual soil water; θ_{fc}: soil water at field capacity; θ_{PWP}: soil water at the permanent wilting point; **PAW**: plant available water.

Weekly soil moisture measurements at 3 different depths and 64 points for a total study area of 53 km² at uplands and valley bottoms were conducted in the rainy seasons from 2014 to 2016. The results presented in Fig. 5-27 show a general higher soil moisture at the valleys bottoms compared to uplands. Moreover, soil moisture increase with depth in both uplands and valley bottoms.

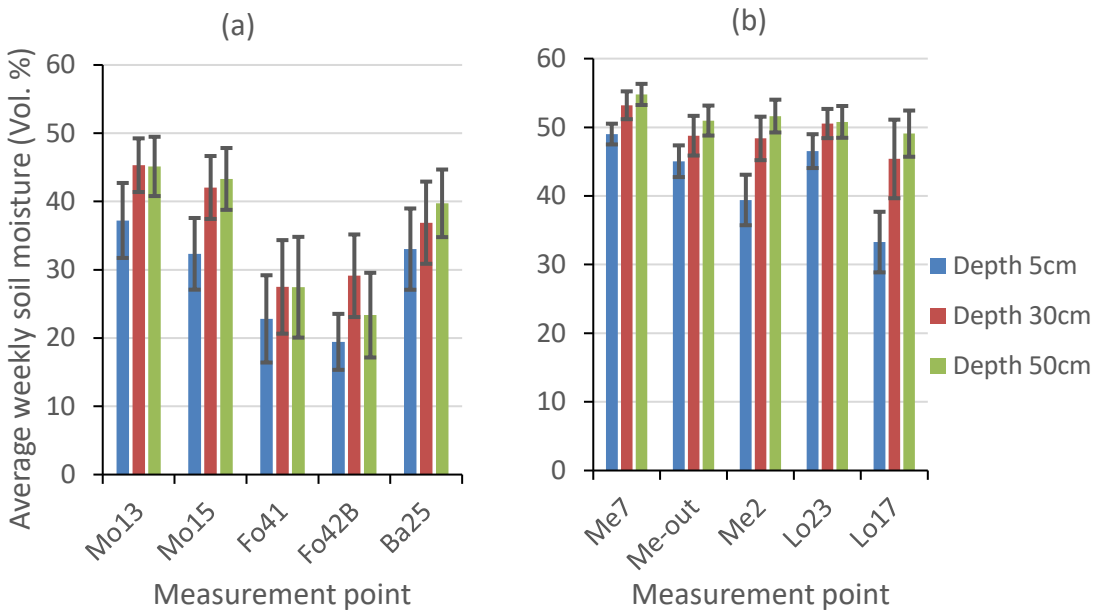

Fig. 5-27. Average weekly soil moisture at upland (a) and lowland (b) for the rainy season 2014 – 2016 at 3 different depths (Mo, Me, Ba, Lo, and Fo refer to Moutori, Mebar, Bankandi, Loffing, and Fafo respectively; error bar are standard deviation of each series).

Daily variation of soil water

Soil moisture was continuously measured (30 min resolution) in the Bankandi-south sub-catchment and in three different horizons of a Cambisol profile. FDR sensors were installed at 10 cm depth in the 1st horizon, 40 cm in the 2nd horizon, and 70 cm depth in the 3rd horizon (see Yira, 2016 for more detailed description of the installation). The 1st horizon has a loamy texture and is made of 33% sand, 45% silt, and 22% clay. The 2nd and the 3rd horizon have clay loamy texture with 22% sand, 40% silt and 37% clay soil fraction for the second horizon and 24% sand, 39% silt, and 37%clay for the third horizon (Yira, 2016).

The temporal variation of soil moisture in the year 2014 (Fig. 5-28) shows lower soil moisture in the first horizon compared the third horizon. This may be partly attributed to the higher proportion of sand and lower proportion of clay in the first horizon (33% sand and 22% silt) compared to the third horizon (24% sand and 37% silt). In fact, soil specific surface area increases when fine particle proportion increase or coarse particle proportion decreases (Ersahin et al., 2006). Hence, an increase in soil specific surface area leads to an increase of soil water holding capacity.

Higher variabilities of soil moisture is observed at the top soil compared to soil moil moisture in the third horizon (Fig. 5-28). Yira (2016) observed a similar result in the experimental site of Tambiri (south-east of the Dano catchment) in 2013. He suggested

this to be attributed to the water retention of the first horizon and the travelling time of the wetting front in the horizon. In some extent, this may also be explained by the fact that the top horizon is the primary source of evaporation and transpiration.

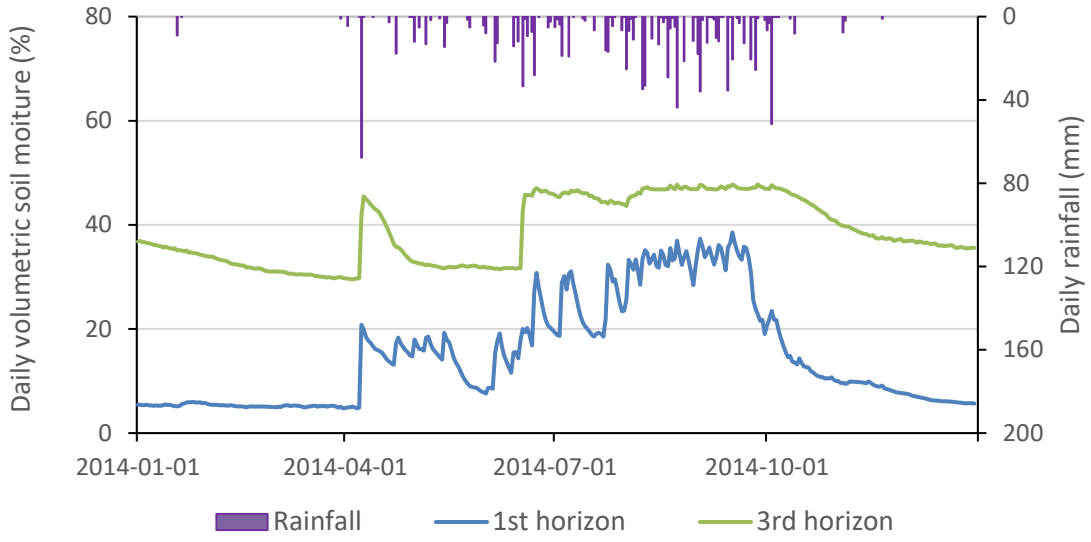

Fig. 5-28. Temporal dynamic of soil moisture at the first three horizons in the Bankandi-south sub-catchment (see Fig. 4-2-a for the location of the station).

5.4 Conclusion

This chapter used several fundamental hydrological methods to analyze data from an intensive instrumentation and monitoring campaign during 2014 and 2015 in order to provide information for a better understanding of hydrological processes which control the water availability for small-scale farmers.

A high interannual variability is observed with rainfall being 163 mm higher in 2015 than in 2014 and runoff coefficients doubling from 8% in 2014 to 15% in 2015. Flow duration curves suggest a similar behavior for the investigated catchments during intense storm events whereas a significant contrast is observed for low flow. In general, the hydrograph-based runoff partitioning shows that interflow is the main component of streamflow.

The observation of shallow and deep groundwater reveals that the recharge occurs from June to October and then depletion follows steadily in the dry season. The general groundwater flow is the same as the streamflow, which is from west to east. In the valley bottoms, the shallow groundwater table remained shallower than 1.5m throughout the year even during the drier year of 2014. The turnover (replacement) of the shallow groundwater varies from 11 to 44 days. Moreover, the spatial distribution of shallow groundwater suggests permanent groundwater availability in the valley

bottom and ephemeral availability at uplands. The geo-electrical tomography and slug test show a heterogeneous aquifer. A further investigation of the shallow groundwater productivity is needed in order to fully assess its potential to support climate change adaptation strategies for smaller scale farmers in Dano.

The plant available water decreases from the valley bottoms to uplands and the mean soil moisture in valley bottoms was significantly higher than the soil moisture at the uplands with soil moisture increasing with depth in the uplands and valley bottoms.

Finally, an integration of the findings into a physical-based and deterministic hydrological model will allow a deeper understanding of hydrological processes in the area.

6 MODELING WATER RESOURCES IN TWO INLAND VALLEY CATCHMENTS IN DANO, BURKINA FASO

6.1 Introduction

Water resources availability for smallholder farmer in West Africa is a major concern for poverty alleviation and economic development as the majority of the population practices rainfed agriculture (Denis et al., 2012). West Africa is one of the regions which are mostly affected by climate variability and climate change (Descroix et al., 2009; Frappart et al., 2009; Ibrahim et al., 2013a; Lebel et al., 2009; Lebel and Ali, 2009; Mougin et al., 2009; Niang et al., 2014; Oguntunde et al., 2017). This is not only because of the particularity of the West African monsoon but also due to the limited capacity to adapt to climate variability and climate change. The region has experienced repetitive droughts during the last four decades which can be associated to climate change (Cornforth, 2011; Kasei et al., 2010; Klein et al., 2015; Lebel et al., 2009).

Although very strong rainfall events (rainfall >30 mm day^{-1}) are rare according to Salih et al. (2018), they account for nearly 50% of the annual rainfall. These strong rainfall events have been disastrous to rainfed agriculture with crop yield loss, soil fertility loss due to surface soil erosion, and other natural hazards including flooding (Braman et al., 2013; Di Baldassarre et al., 2010; Kundzewicz et al., 2013; Nka et al., 2015; Tschakert et al., 2010).

Smallholder farmers in West Africa are the major actors in agriculture and food production (Moyo, 2016) and are, as seen, confronted with many challenges. Moreover, the region has suffered from many policy failures related to “structural adjustment programs” and the liberalization (privatization) of agriculture sector, imposed on developing countries by World Bank and International Monetary Funds (IMF). This led to an aggravation of the social and economic conditions of poor smallholder farmers (Amanor, 2012, 2009; Hounkonnou et al., 2012). Against this background, efficient water and land management is the key for improving the livelihoods and food security of the population.

Taking this into account, the area selected for this study is located in rural south-western Burkina Faso, where 60% of the population are endemically poor smallholder farmers (Coulombe et al., 2000; INSD, 2014). Due to relatively higher water availability in inland valleys, there has been a considerable shift of agriculture from uplands to valley bottoms. Inland valleys are estimated to cover 22-52 million ha in West Africa (Windmeijer and Andriesse, 1993) and approximately 1200 ha in the study area (see chapter 2).

For a meaningful policy design and implementation of an effective water management strategy, it is important to understand the underlying hydrological processes.

Hydrological modeling is usually applied to understand hydrological processes and predict water resources. Several studies used the semi-distributed SWAT (Soil & Water Assessment Tool) model (Arnold et al., 1998) at the West African sub-continental scale and the major river basin scale (e.g. Volta, Niger, Senegal river basins) (Akpoti et al., 2016; Obuobie and Diekkrüger, 2008; Poméon et al., 2018b; Schuol et al., 2008; Schuol and Abbaspour, 2007, 2006). The spatially explicit grid-based mesoscale Hydrological Model (mHM) (Kumar et al., 2013; Samaniego et al., 2010) was also successfully applied by Poméon et al. (2018) at that scale.

However, physically-based models such as MIKE SHE (Ma et al., 2016; Zhou et al., 2013) are rarely utilized in the region because they necessitate the knowledge of physical parameters and the region is a very sparse data environment (Devia et al., 2015). Andersen et al. (2001) used MIKE SHE model to represent hydrological processes and to estimate the water balance of the Senegal River basin. Physically-based models are suitable for hydrological processes modeling and for mitigating the problem of identifiability and equifinality (Beven, 2006; Beven and Freer, 2001; Ebel and Loague, 2006; Savenije, 2001; Vrugt et al., 2009). The problem of identifiability and equifinality is related to uncertainties in hydrological models due to the fact that several parameter sets can produce acceptable matching between observed and modelled variable. The problem is more pronounced with relatively high number of parameters. Nevertheless, due to the data scarcity and the necessity to accurately represent hydrological processes, a model based on both conceptual and physical formulations should be applied.

The Water balance Simulation Model (WaSiM) is a grid-based and mainly physically-based hydrological model (Schulla, 2015). It utilizes the Richards and Weaver (1944) equation for soil hydrological modeling and the van Genuchten (1980) approach for the parameterization of soil hydraulic parameters. The parameterization of the soil model using the van Genuchten equation reduces the number of parameters to be calibrated and thereby the problem of identifiability (Samaniego et al., 2010). WaSiM was previously applied at the mesoscale for modeling the Volta River basin (Kasei, 2010). It has also been used at a smaller scale in the Dano catchment (Yira, 2016). Therefore, WaSiM was selected for the modeling of rural small scale agriculture catchments in Dano.

The objective of this study is to model surface and groundwater resources in order to support adaptation strategies and planning of water management at the local scale for small holder farming systems. This study especially addresses the following

research questions: (1) Can WaSiM be applied at the local scale for hydrological processes representation and water balance estimation? (2) What are the main hydrological processes controlling water resources availability in inland valleys? (3) Can the parameters established for one catchment be transferred to another catchment?

6.2 Materials and methods

Bankandi-Loffing and Mebar are two small rural adjacent catchments located in the Dano catchment in south-western Burkina Faso. The Bankandi-Loffing and Mebar catchments are 30 and 8 km² large, respectively, and Bankandi-Loffing is divided into three sub-catchments including Bankandi-south (2 km²) and Bankandi-north (9 km²) at the upstream area and Loffing (19 km²) at the downstream area. The catchments are located in a Sudan Sahelian climate (Schmengler, 2011). Due to the geomorphology of the area land in the Bankandi-Loffing catchment is flat with several inland valleys which can easily be flooded during the rainy season. On the other hand, in the Mebar catchment, the slopes are steeper, the times of concentration are shorter and inland valley bottoms cover a smaller area of the catchment. The vegetation is mainly of savanna type in both of the catchments and the geology of the area is made of crystalline rocks and the aquifer develops in faults, fractures, saprolites, and alluvial materials (see chapter 2 for more details concerning location and description).

While at the mesoscale remote sensing climate data can be used for hydrological modeling, at the local scales such as the Dano catchment this is hardly possible because the spatial resolution of remote sensing data products is too coarse for small scale studies as they range from 0.03° to 1° with an average resolution of 0.275°(Li et al., 2009; Poméon et al., 2017; Xu et al., 2014). Therefore, I undertook an intensive instrumentation of the catchments by installing and operating an observation network constituting of, among others, stream gauges, piezometers, rainfall recorders and weather stations (see chapter 4 for more detail on the instrumentation). Three year time series data (2014-2016) were collected. A digital elevation model (DEM) in 30 m resolution was obtained from NASA (2014), a soil map from Hounkpatin (2017), soil characteristics from Yira (2016), and a land use and land cover map from Forkuor (2014). The Bankandi-Loffing and Mebar catchments were modeled using WaSiM. The model was calibrated for two years (2014-2015) and validated during the year 2016 at hourly time step. A warmup period of six years was applied by repeating the climate variables of 2013 (rainfall, air temperature, air humidity, global radiation, wind speed). This was necessary in order to stabilize the model and to obtain initial model state near to the observed initial hydrological conditions. The Penman-Monteith approach (Brutsaert, 1982; Monteith, 1975) was used for estimating evapotranspiration and the groundwater

conceptual model was applied (see chapter 3 for methods, and chapter 4 for the field observation network).

6.3 Results and discussion

6.3.1 Calibration and validation of Bankandi-Loffing model

Model performance

WaSiM performed very well as shown by the objective functions (Table 6-1) (see chapter 3 for the description of objective functions). The Nash-Sutcliffe efficiency (NSE) (Nash and Sutcliffe, 1970), the Kling-Gupta efficiency (KGE) (Gupta et al., 2009; Kling et al., 2012), and the coefficient of determination (R^2) are larger than 0.5 in most of the cases in the calibration and the validation periods. In general, the model performed as well at the upstream area (Bankandi-north) as at the overall catchment (Bankandi-Loffing). The R^2 ranges from 0.47 to 0.95, NSE from 0.40 to 0.95, and KGE from 0.57 to 0.84, at the outlet and at the Bankandi-north stream station and for calibration and validation periods. The slight decrease of the model performance might be attributed to overcalibration as the best simulation is selected based on the highest value of the objective functions (Harmel et al., 2010). Pbias is lower than 30% for all the cases indicating a slight overestimation of the discharge by the model.

Table 6-1. Model performance for daily simulated values for the upstream area Bankandi-north (BaN) and the outlet of Bankandi-Loffing (BaLof) catchment.

	Calibration (2014-2015)		***Validation (2016)***	
	BaLof	**BaN**	**BaLof**	**BaN**
R^2	0.91	0.95	0.82	0.47
NSE	0.88	0.95	0.77	0.40
KGE	0.82	0.84	0.57	0.68
Pbias (%)	15.9	12.4	29.4	1.6

BaLof: Overall catchment of Bankandi-Loffing; **BaN**: Bankandi-north**;**
R^2: Coefficient of determination; **NSE**: Nash-Sutcliffe Efficiency; **KGE**: Kling-Gupta Efficiency.

In addition to the assessed numerical model performance, the visual performance of the model, which is illustrated by the hydrographs in Fig. 6-1 and Fig. 6-2, showed very good results for the upstream area and the overall catchment. Temporal dynamics as well as most of the high and low flows were well simulated in the calibration and validation periods. However, as already shown previously in the numerical performance analyses, the model performed better in the calibration period compared to the validation period especially at the Bankandi-north station. Some peaks

were not well captured by the model at that station. This is partly due to the quality of the observed discharge data as a sensor dysfunction was noted in the period.

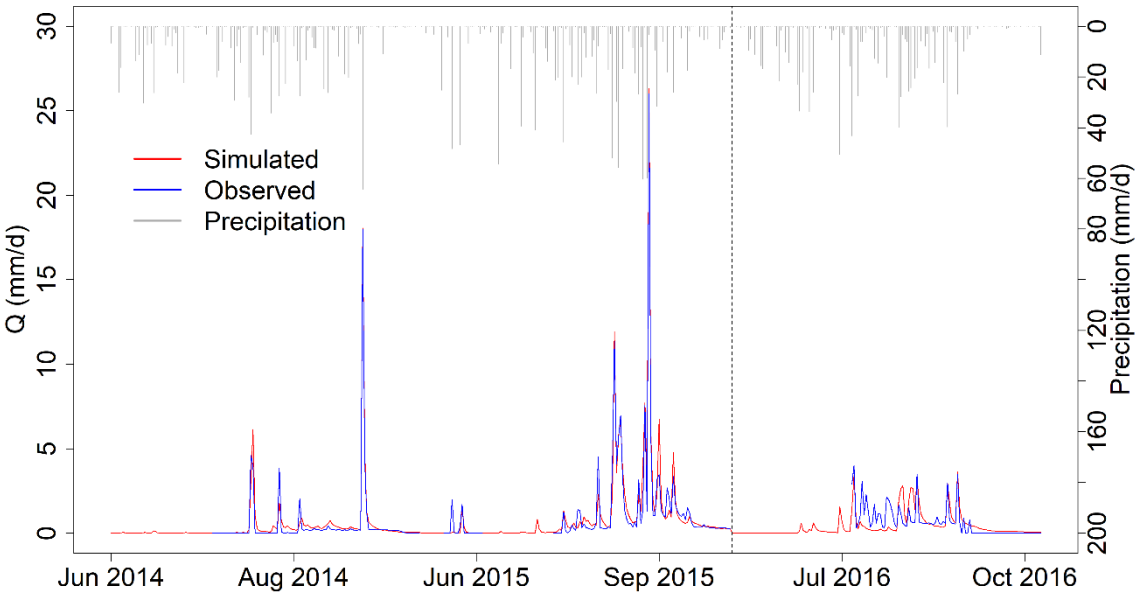

Fig. 6-1. Comparison of simulated and observed hydrographs for the upstream sub-catchment (Bankandi-north). The vertical dash line separates the calibration period from the validation period.

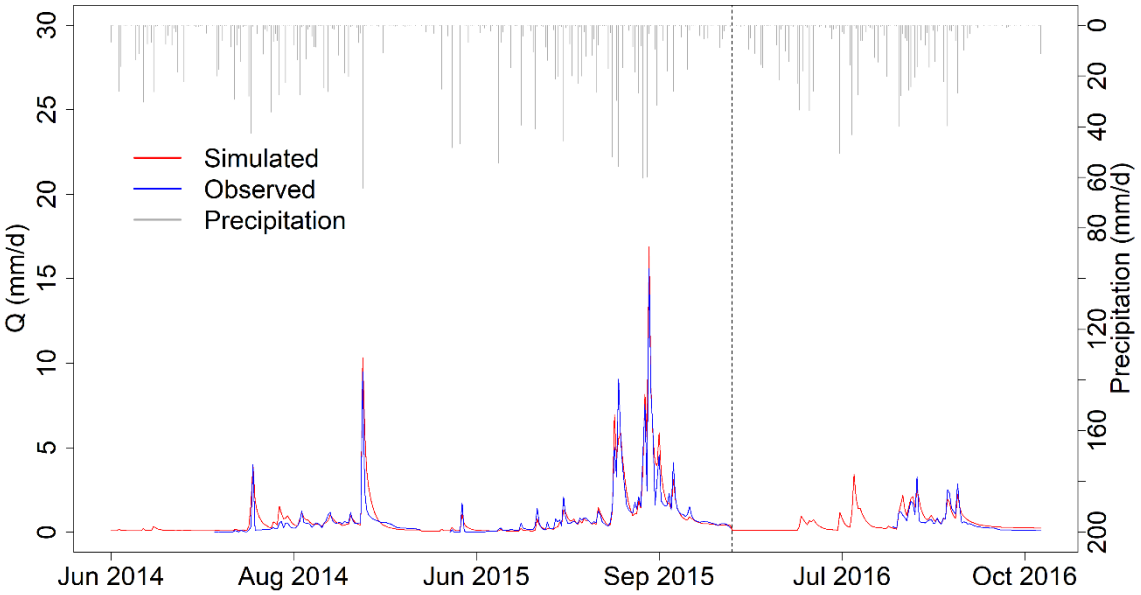

Fig. 6-2. Comparison of simulated and observed hydrographs for the outlet (Bankandi-Loffing). The vertical dash line separates the calibration period from the validation period.

The comparison of the simulated and observed top soil (10 cm depth) moisture during the year 2014 showed a good agreement (Fig. 6-3). It should be noted that the model was not calibrated for soil moisture as most of the soil parameters were measured in the field or laboratory. Each of the calculated objective functions (R^2, NSE, and KGE) were higher than 0.5. The graphical comparison shows good agreement between the simulated and observed soil moisture and the model simulated the initial soil moisture well. This indicated that the applied six year warmup period was sufficient to stabilize the model. Although some discrepancies can be observed in the rainy season and the dry season, on the whole, the temporal dynamics were well captured. A good top soil modeling is important for runoff generation and partitioning between different soil layers and the aquifer.

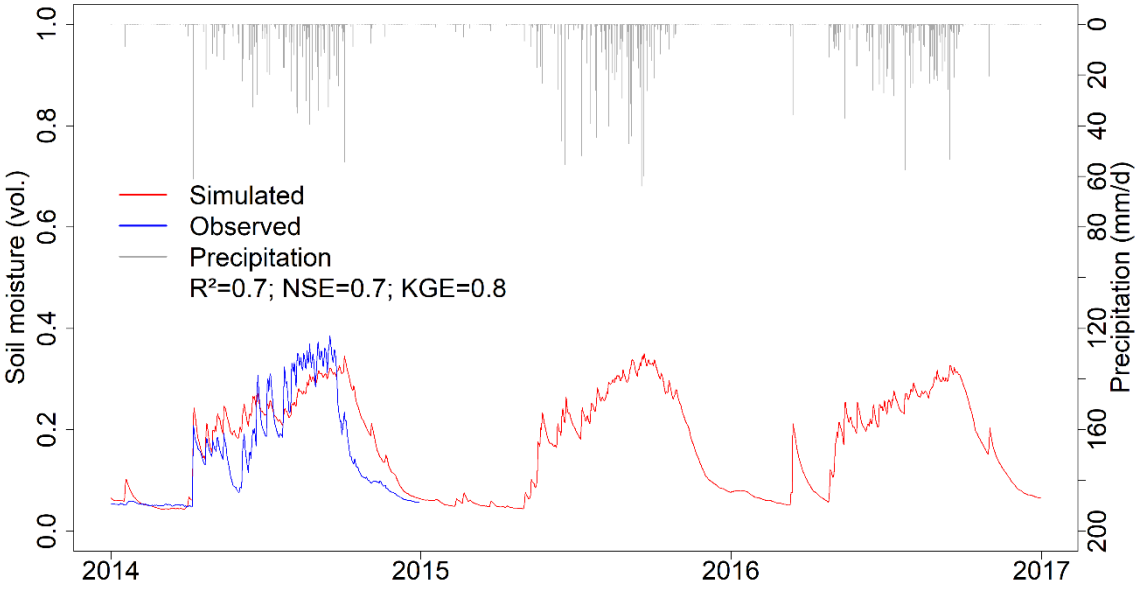

Fig. 6-3. Comparison of daily average simulated top soil water and observed soil moisture at Bankandi-south (measured soil moisture data at 10 cm depth were only available for the year 2014 at the soil moisture station).

In addition to the soil moisture, the model was validated by comparing the average simulated monthly groundwater level at the outlet sub-catchment (Loffing) with the observed groundwater level at a piezometer located at the outlet of the catchment. The comparison was done after subtracting the elevation difference between the piezometer and the Loffing sub-catchment from the areal simulated groundwater level. Fig. 6-4 suggests a short delay of some simulated groundwater level peaks compared to observed peaks. This led to unsatisfactory results with regards to R^2 and NSE. However, in general, the temporal dynamics and the amplitudes of variations were acceptable with KGE 0.5.

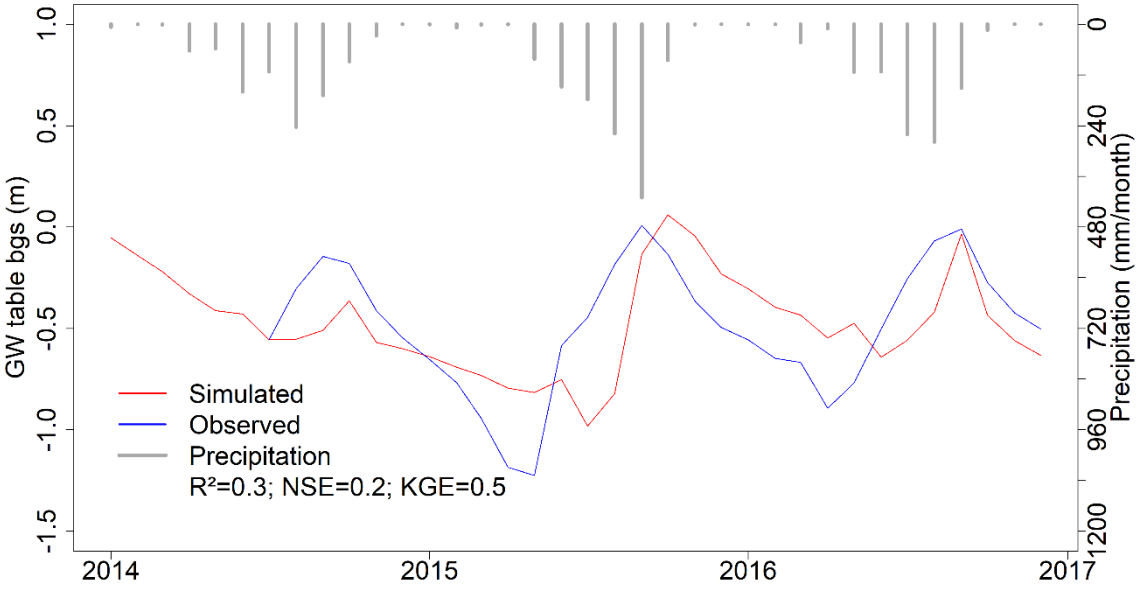

Fig. 6-4. Comparison of monthly areal average of simulated groundwater table below ground surface (bgs) at the downstream sub-catchment (Loffing) and the observed groundwater level at a piezometer located at the outlet of the catchment.

Water balance

A considerable inter-annual variation of rainfall was observed during the three year period of monitoring (Table 6-2). The difference in annual rainfall between the years 2014 and 2015 was 223 mm (21% of the mean annual rainfall).

The actual evapotranspiration (ETa) represents 45% of the potential evapotranspiration (ETp). This indicates a water limited and not an energy limited catchment. During dry years (2014 and 2016), decreases of soil water storage are observed whereas in the wet year 2015, an increase of soil water storage is noted. This is shown by negative change in storages (delta S) in former years and positive delta S in the latter year (Table 6-2). The succession of dry and wet years resulted in a more or less stable system from 2014 to 2016 with a relatively low annual mean delta S for the overall Bankandi-Loffing catchment (delta S= -12 mm). This means that water stored in the soil and aquifers during wetter years is lost through evapotranspiration and groundwater flow during dry years. Therefore, consecutive dry years similar to the year 2014 will not only jeopardize the livelihoods of the majority of the farmers who practice rainfed agriculture but also will affect the general hydrological processes and water resources.

Table 6-2. Average annual water balance in mm at the Bankandi-Loffing catchment for years 2014-2016.

		P	ETp	ETa	EIa	Ea	Ta	E/Ta	Qt	Qs	Qi	Qb	Sim.Cr (%)	Obs.Cr (%)	Delta S
2014	**BaS**	969	2077	906	60	699	147	5	106	33	67	5	11	-	-43
	BaN	925	1985	932	59	712	162	4	65	32	25	8	7	6	-72
	Lof	968	1941	868	57	675	136	5	130	38	17	75	13	-	-30
	BaLof	955	1965	890	58	688	145	5	108	36	23	49	11	8	-43
2015	**BaS**	1116	2158	898	56	676	165	4	195	72	108	15	17	-	23
	BaN	1172	2044	930	60	696	174	4	161	76	59	26	14	14	81
	Lof	1189	2012	880	57	674	148	5	224	83	34	107	19	-	85
	BaLof	1178	2033	897	58	681	157	4	203	80	47	75	17	19	78
Calibration (2014-2015)	**BaS**	1042	2118	902	58	688	156	4	150	52	88	10	14	-	-10
	BaN	1048	2014	931	60	704	168	4	113	54	42	17	11	10	4
	Lof	1078	1976	874	57	674	142	5	177	60	26	91	16	-	28
	BaLof	1066	1999	894	58	684	151	5	156	58	35	62	15	14	18
Validation (2016)	**BaS**	933	2053	939	62	709	168	4	67	14	47	6	7	-	-73
	BaN	980	2119	997	66	755	176	4	73	24	31	18	7	17	-90
	Lof	1019	1992	927	61	712	154	5	154	29	18	106	15	-	-62
	BaLof	1001	2036	949	63	725	162	4	122	26	24	71	12	14	-70
Annual mean (2014-2016)	**BaS**	1006	2096	914	59	695	160	4	123	40	74	9	12	-	-31
	BaN	1026	2049	953	62	721	171	4	100	44	38	17	10	12	-27
	Lof	1059	1982	892	58	687	146	5	169	50	23	96	16	-	-2
	BaLof	1045	2011	912	60	698	155	5	144	47	31	65	14	14	-12

BaLof: *Overall catchment of Bankandi-Loffing (30km²);* ***BaN****: Bankandi-north (9km²);* ***BaS****: Bankandi-south (2km²);* ***Lof:*** *Loffing (19km²);* ***P****: precipitation;* ***ETp****: potential evapotranspiration;* ***ETa****: total actual evapotranspiration;* ***EIa****: actual interception evaporation;* ***Ea****: actual evaporation from bare soil and open water surfaces;* ***Ta****: actual transpiration;* ***E****: total actual evaporation (Ea + EIa) ;* ***Qt****: total runoff; Q****s****: surface runoff;* ***Qi****: interflow;* ***Qb****: base flow;* ***Sim.Cr****: simulated total runoff coefficient;* ***Obs.Cr****: observed total runoff coefficient;* ***Delta S****: change in storage.*

At the catchment scale of Bankandi-Loffing, the evaporation was five times as high as the transpiration. This can be explained by the long dry season of 7 to 8 months per year, in which most farmers cease activities, the herbaceous vegetation dries out completely, and most of trees lose their leaves in savanna areas. This leads to a significant reduction of transpiration by plants. However, a relatively higher coverage of permanent plants (forest) in the Bankandi-north sub-catchment compared to Bankandi-south and Loffing sub-catchment (see chapter 2 for the land use land cover map) can partially explain the significant difference of transpiration between the former and the latter sub-catchments.

The observed variability in annual rainfall led to a more pronounced variation of the observed runoff volume. For instance, the variation of rainfall from 2014 to 2015 was 21% of the mean annual rainfall but the increase in total runoff was approximately four times the increase in rainfall (approximately 88% of the mean runoff). The mean total runoff coefficient at the outlet was 14% of mean annual rainfall but there was a significant contrast between upstream sub-catchments (Bankandi-south and Bankandi-north) and the downstream sub-catchments (Loffing). The highest runoff coefficient was obtained at the downstream sub-catchment due to a high contribution of base flow to streamflow. The high contribution of base flow can be explained by the shallowness of the groundwater table at this sub-catchment compared to the upland sub-catchments (see chapter 5 for the observed groundwater table).

Table 6-2 also indicates that interflow is the main runoff component in Bankandi-south sub-catchment and represents 60% of the total runoff. It is noteworthy that interflow decreases from the upstream sub-catchments to the downstream. Yira et al. (2016) obtained 56% on average between 2011 and 2014 and 59% in 2014 while modeling a 6.5-times larger catchment than Bankandi-Loffing. In a similar catchment in northern Benin simulated for the period 1998-2004 by Cornelissen et al. (2013), the interflow was 65% of the total runoff using the UHP-HRU model and 38% using WaSiM. Based on field experiments the authors conclude that UHP-HRU has a better representation of the hydrological dynamics of the catchment. Moreover, in the Volta basin, Kasei (2010) found 68% interflow at the northern area and 60% at the southern area where the Dano catchment is located. However, interflow is not the dominant runoff component in the other Bankandi-Loffing sub-catchments. For instance, in Bankandi-north, surface flow is the most dominating component of runoff (44% of total runoff) and in the Loffing sub-catchment and the overall Bankandi-Loffing catchment, base flow largely dominates streamflow (57% and 45% of total runoff, respectively). An increase of base flow was noted from upstream to downstream section. The comparison between observed base flow (see chapter 5) estimated using analytical hydrograph decomposition and the simulated base flow shows close similarities. For instance, the

observed base flow at Bankandi-south, Bankandi-north, and Bankandi-Loffing represent 9%, 16%, and 42% of the total runoff, respectively, and the simulated base flow is 7%, 17%, and 45% for the respective sub-catchments. The difference between these findings and the previously cited studies is due to the fact that a considerable part of the downstream area of the investigated catchment is occupied by valley bottoms of inland valleys. The proximity of aquifer level to the ground surface allows for a significant contribution of base flow in valley bottoms.

It is also important to recall that the partitioning of runoff into its components is not only influenced by rainfall intensity and physical properties of soil and slope but also by hydrological conditions of the catchment before flood events (Beven, 1989). Furthermore, macropore density and distribution drive runoff component generation in West African savanna. For instance, Giertz et al. (2005) reported 219 bio-pores per m² in a savanna plot of a catchment in northern Benin whereas only 60 bio-pores were counted in cultivated field. With the conversion of savanna to croplands in the Dano catchment (Op de Hipt, 2017; Yira et al., 2016), the current pattern of runoff components is likely to change in favor of surface flow. This might lead to significant soil fertility loss due to high soil erosion (Op de Hipt et al., 2017). Therefore, an improvement of the current traditional water and soil management should be planned.

6.3.2 Transfer of Bankandi-Loffing parameters to Mebar model without recalibration

The parameter set which gave the highest objective functions during calibration and validation of the Bankandi-Loffing model was directly applied to the Mebar model without recalibration and the calculated model performance (Table 6-3) shows very good results during years 2014-2015. The Mebar model performed even better than Bankandi-Loffing during the period 2014-2015. R^2, NSE, and KGE were approximately 0.3 higher in Mebar than in Bankandi-Loffing.

However, in 2016, the Mebar model resulted in lower R^2 and NSE than the Bankandi-Loffing model but the values of the objective functions remain higher or equal to 0.6. In contrast to R^2 and NSE, the Pbias significantly improved in Mebar model (12%) compared to Bankandi-Loffing (29%) in 2016. On the basis of KGE, the performance difference between the non-recalibrated Mebar model (KGE 0.59) and the Bankandi-Loffing model (KGE 0.57) is negligible during 2016.

Moreover, the hydrograph (Fig. 6-5) shows that the non-recalibrated Mebar model has fallen slightly short in matching some peaks but in general the performance is good.

Table 6-3. Non-recalibrated Mebar model performance in the period 2014-2015 and 2016.

	2014-2015	2016
R^2	0.93	0.65
NSE	0.92	0.64
KGE	0.84	0.59
Pbias (%)	0.9	11.9

R^2: Coefficient of determination; **NSE**: Nash-Sutcliffe Efficiency; **KGE**: Kling-Gupta Efficiency.

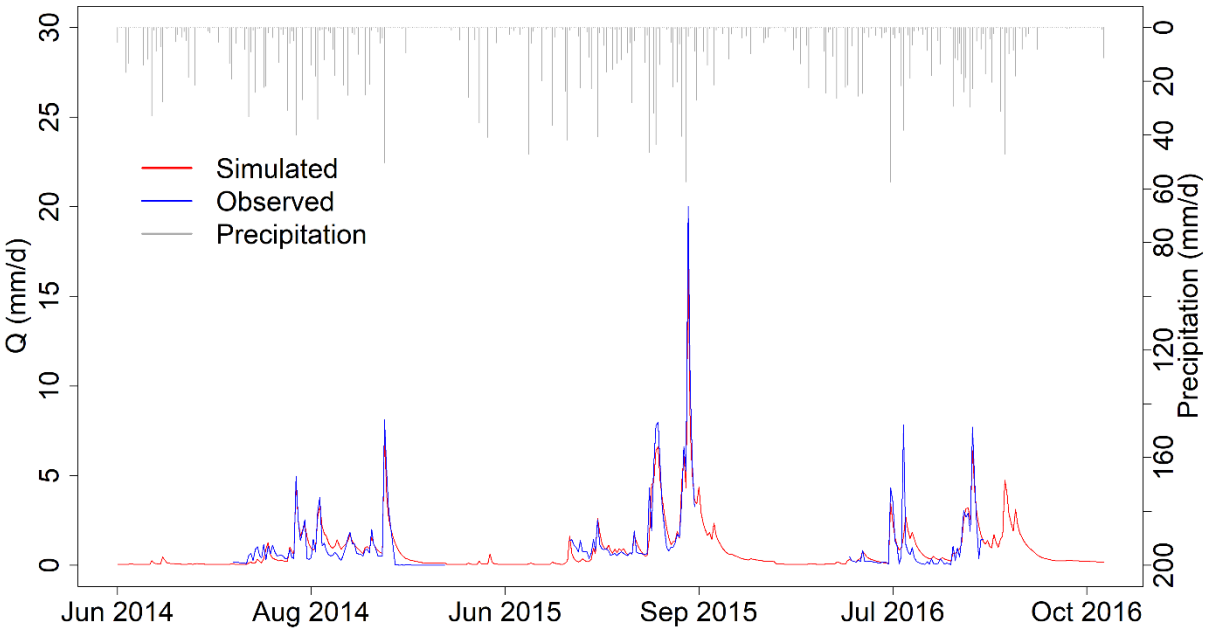

Fig. 6-5. Comparison of simulated Mebar hydrograph using the parameters from the best Bankandi-Loffing simulation and the observed hydrograph from 2014 to 2016.

The numerical and graphical Mebar model performances show good results in both periods 2014-2015 and 2016. Therefore, the transfer of the parameters from the Bankandi-Loffing model to Mebar can be considered as a success. However, it is important to note that the calibration and validation period of the initial Bankandi-Loffing model and the transfer period of for Mebar are identical (2014-2016). The period is characterized by two dry years separated by a wet year. These findings therefore need to be tested for longer time periods and in different climate conditions in order to fully evaluate the robustness of the model in transferring parameters from one catchment to another.

6.3.3 Recalibration and validation of the Mebar model

The Mebar model was calibrated for 2014-2015 and validated for 2016 in order to establish a reference Mebar model for evaluating the quality of the parameter transfer. The summary (Table 6-4) indicates an improvement of model performance with the recalibration. Each objective function (R^2, NSE, and KGE) is greater than 0.9 in calibration period and 0.7 in validation year. The increase of R^2 and NSE (0.02 in calibration period and 0.06 in validation period) with the recalibration is lower than the increase of KGE (0.11 in calibration and 0.12 in validation periods) during both the calibration and the validation periods. This may be explained by the combined effect of the increase of R^2 and NSE. KGE is a function of correlation coefficient which is the square root of R^2, the bias ratio and the variability ratio which can be estimated in NSE (Kling et al., 2012).

The comparison of the simulated hydrograph and measured hydrograph (Fig. 6-6) shows good agreement between the hydrographs and is consistent with the numeric model performance assessment.

Table 6-4. Mebar model performance for the calibration and validation periods

	Calibration (2014-2015)	**Validation (2016)**
R^2	0.95	0.71
NSE	0.95	0.70
KGE	0.96	0.70
Pbias (%)	1.9	11.5

R^2: Coefficient of determination; **NSE**: Nash-Sutcliffe Efficiency; **KGE**: Kling-Gupta Efficiency.

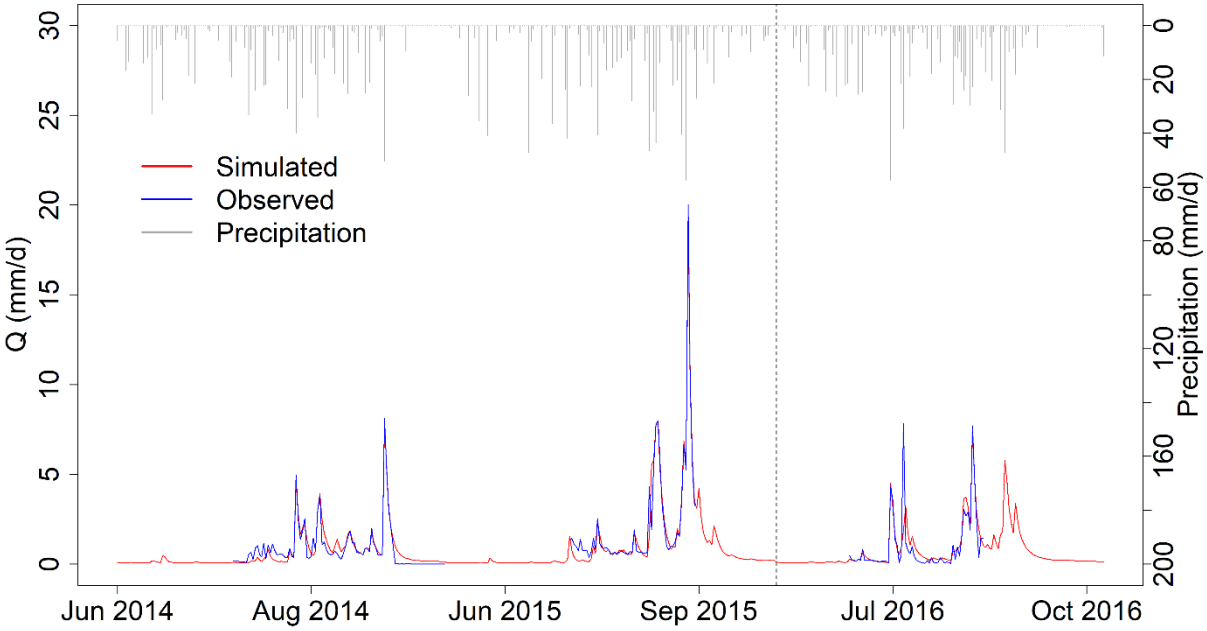

Fig. 6-6. Comparison of simulated and observed hydrographs at the Mebar catchment during the calibration period 2014-2015 and the validation year 2016. The vertical dash line separates the calibration period from the validation period.

The water balance of the best simulation of the Mebar model (Table 6-5) shows many similarities with Bankandi-Loffing. The actual evapotranspiration (ETa) is 85% of rainfall, physical evaporation accounts for 79% of ETa, and only 45% of the potential evapotranspiration (ETp) could actually evaporate in form of ETa given the water limited conditions of the area.

In contrast to Bankandi-Loffing, instead of base flow, interflow is the main component of runoff in Mebar (39% of total runoff) and is followed by surface flow (32% of total runoff). The contrast between Mebar and Bankandi-Loffing can be partly explained by to the difference in slopes and land use. A large area of the Mebar catchment is located between the Ioba Mountains and is mostly covered by uplands while the Bankandi-Loffing catchment is characterized by flat land and valley bottoms of the inland valleys. The estimated mean slope is 5.1% with a standard deviation of 4.6% in the Mebar catchment whereas the mean slope is 4.1% with standard deviation of 3.1% in the Bankandi-Loffing catchment. Concerning land use, croplands occupy a larger area in Mebar (42%) than in Bankandi-Loffing (33%) (See chapter 2 and 4 for topography and land use land cover of the catchments). The slope and land use may be responsible for the higher contribution of both surface runoff and interflow in Mebar compared to Bankandi-Loffing.

Table 6-5. Water balance components in mm per year of the Mebar model for the calibration and validation periods.

	Calibration (2014-2015)	Validation (2016)	Mean (2014-2016)
P	1008	1024	1013
ETp	1924	1848	1898
ETa	848	875	857
EIa	58	62	59
Ea	672	694	679
Ta	118	119	119
Qt	146	141	144
Qs	48	40	46
Qi	58	54	56
Qb	40	48	43
Sim. Cr (%)	14	14	14
Delta S	14	8	12

***P:** precipitation; **ETp**: potential evapotranspiration; **ETa**: total actual evapotranspiration; **EIa**: actual interception evaporation; **Ea**: actual evaporation from bare soil and open water surfaces; **Ta**: actual transpiration; **Qt**: total runoff; **Qs**: surface runoff; **Qi**: interflow; **Qb**: base flow; **Sim.Cr**: simulated total runoff coefficient; **Delta S**: change in storage.*

6.3.4 Water balance summary in Bankandi-Loffing and Mebar

The comparison of the mean annual water balance for Bankandi-Loffing (BaLof), Mebar before (Meb_0) and after (Meb) recalibration (Fig. 6-7) shows only 3% lower rainfall in Mebar models (Meb_0 and Meb) compared to Bankandi-Loffing and no rainfall rate difference between Meb_0 and Meb was noted. This could in part explain the similar simulated total runoff for the three models. However, significant differences were noted between the simulated runoff components for the three models and the variations of runoff components between the models do not indicate any trend.

Furthermore, the potential evapotranspiration (ETp) does not seem to continuously decrease between the models but the total actual evapotranspiration (ETa) and the actual transpiration (Ta) do. If only Meb_0 and Meb were examined, it is clear that the recalibration led to reductions ETp, ETa, and Ta while actual evaporation (Ea) increased. This behavior seems to be caused by the increase of the mean canopy surface resistance (r_{sc}) from 64 to 73 s m^{-1} and the evaporation surface resistance (r_{se}) increase from 50 to 52 s m^{-1} due to land use land cover differences.

Fig. 6-8 presents monthly temporal variations of the water balance components. For very intense rainfall conditions such as the conditions in September 2015, the peak of surface runoff is higher than interflow. Conversely, under moderate rainfall conditions like in September 2014 and September 2016, the peak of surface

runoff is lower than interflow. However, the peaks of base flow stay lower than the surface runoff and interflow but are sustained for longer time compared to surface runoff and interflow. As for the transpiration, their rates were only considerable during rainy seasons (June to October). This is consistent with the field observations which present much reduced plant activities in dry seasons due to water unavailability. The herbaceous vegetation completely dies out and most of trees loss their leaves, therefore, most of the ability to transpire.

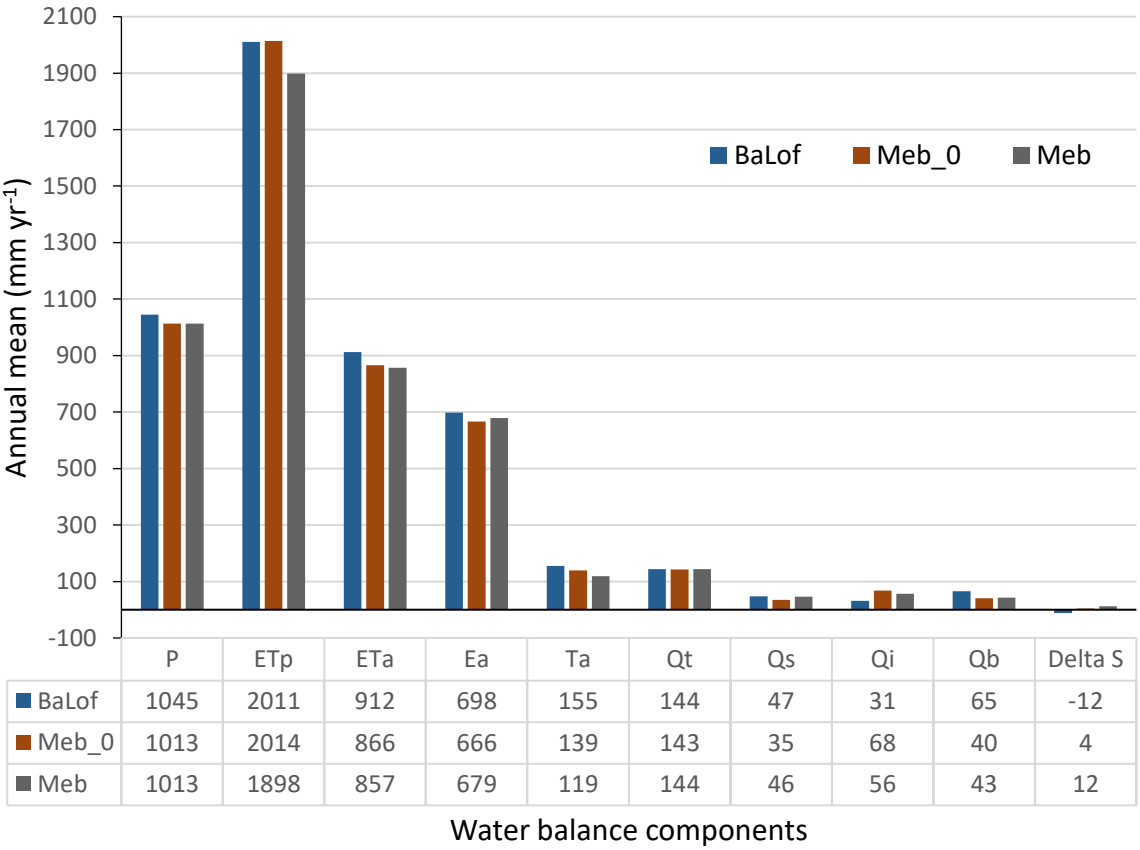

	P	ETp	ETa	Ea	Ta	Qt	Qs	Qi	Qb	Delta S
BaLof	1045	2011	912	698	155	144	47	31	65	-12
Meb_0	1013	2014	866	666	139	143	35	68	40	4
Meb	1013	1898	857	679	119	144	46	56	43	12

Fig. 6-7. Annual mean water balance for Bankandi-Loffing (BaLof), Mebar before recalibration (Meb_0), and after recalibration (Meb) for the period 2014-2016. P: precipitation; ETp: potential evapotranspiration; ETa: total actual evapotranspiration; Ea: actual evaporation from bare soil and open water surfaces; Ta: actual transpiration; Qt: total runoff; Qs: surface runoff; Qi: interflow; Qb: base flow; Delta S: change in storage.

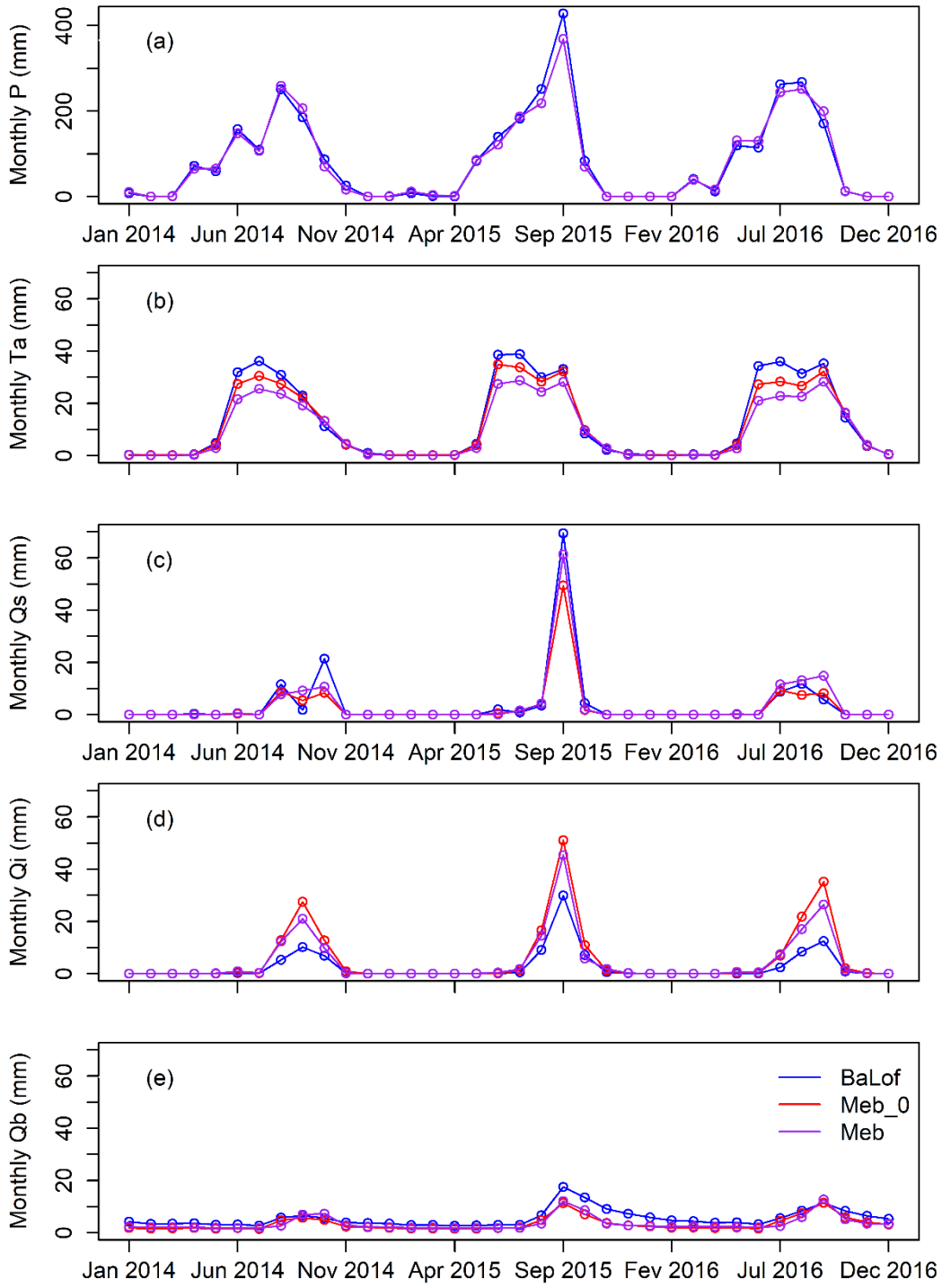

Fig. 6-8. Temporal variation of some water balance components in Bankandi-Loffing (*BaLof*), Mebar before recalibration (*Meb_0*), and Mebar after recalibration (*Meb*) from 2014 to 2016. *(a)*: precipitation (*P*), *(b)*: actual transpiration (*Ta*), *(c)*: surface runoff (*Qs*), *(d)*: interflow (*Qi*), *(e)*: base flow (*Qb*).

6.4 Conclusion

The instrumentation of the catchments and the available spatial distributed data (soil, LULC, topography, etc.) allowed to obtain sufficient high quality hydrological and meteorological data for a successful calibration and validation of the WaSiM hydrological model. The four applied objective functions (R^2, NSE, KGE, and Pbias) suggest that WaSiM performed well in modeling the discharge from small scale rural inland valley catchments (Bankandi-Loffing and Mebar). The soil moisture and groundwater table depth were also well modeled and the initial soil moisture conditions were well reproduced by the model.

The analysis of the water balance indicates that evapotranspiration is quantitatively the most important hydrological process in the area and the physical evaporation largely dominates evapotranspiration. The average annual loss of 688 mm (approximately 67% of annual rainfall) due to evaporation does not contribute to biomass production. Therefore, evaporation reduction techniques such as agroforestry or mulching should be implemented as part of an effort for better management of soil and scarce water resources. Moreover, 14% of annual rainfall run out of the catchment as total runoff without being used. Therefore, soil water management techniques could be setup in order to slow down the surface flow and thereby increase the infiltration and soil water availability while keeping the impact on downstream in an acceptable range. The success of the implementation of the water resources management depend on the level of involvement of stakeholders.

Interflow dominates runoff in the Mebar catchment and upstream area of Bankandi-Loffing whereas base flow is the major runoff components in downstream area of Bankandi-Loffing which has large area of inland valley bottoms. Due to the trend of conversion of savanna into croplands as a result of population growth, surface flow will presumably increase, leading to an increase of soil erosion. Consequently, adaptation strategies should be planned accordingly. Supplementing the current erosion technique (stone-belt) with agroforestry and/or mulching might be considered.

The transfer of parameters from Bankandi-Loffing model to Mebar shows good results. However, considering that this investigation occurred for the same time period and the study period is relatively short, the robustness of the model should be tested for longer period in different climate and catchment conditions.

7 MODELING THE IMPACT OF CLIMATE AND LAND USE / LAND COVER CHANGE ON WATER AVAILABILITY IN AN INLAND VALLEY CATCHMENT IN DANO, BURKINA FASO

7.1 Introduction

A sustainable water and land resource management is crucial for poverty reduction, food security, and ecosystem preservation in West Africa, where the majority of the population earn their livelihood from rainfed agriculture (AGRA, 2014; FAO, 2014; Hollinger and Staatz, 2015; Jalloh et al., 2013). Agriculture contributes approximately 25% of the gross domestic product (GDP) of West Africa and account for more than quarter of the region's GDP growth (African Development Bank, 2019). Smallholder farming is a mainstay of the economy and the main source of food production in the region (Denis et al., 2012).

The region experienced high variability of rainfall during the last five decades and is expected to be the most impacted worldwide by climate change in the twenty first century (Descroix et al., 2009; Frappart et al., 2009; Ibrahim et al., 2013a; Lebel et al., 2009; Lebel and Ali, 2009; Mougin et al., 2009; Niang et al., 2014; Oguntunde et al., 2017). Regional climate models (RCMs) have been increasingly utilized to assess hydrological impacts of climate change because they are applied at a relatively high spatial resolution (0.11° to 0.44°) (Gutiérrez et al., 2019). Therefore, they better represent the variations of land surface, vegetation, topography, and coast line compared to global climate models (GCMs) (Gbobaniyi et al., 2014). Hence, RCMs use physically-based modeling for downscaling. Consequently, the coherence between climate variables, especially precipitation and temperature can be conserved (Gutiérrez et al., 2019; Muerth et al., 2012).

The Coordinated Regional Climate Downscaling Experiment (CORDEX-Africa, www.cordex.org) project used a dynamical downscaling method to simulate relatively high spatial resolution climate variables for the African domain (Dosio et al., 2015; Gbobaniyi et al., 2014; Kim et al., 2014; Stanzel et al., 2018; Yira et al., 2017). The dynamical downscaling method consist of using GCM data as the initial and lateral boundary conditions for the RCMs (Xu et al., 2019).

In the hydrological impact assessment studies, simulated climate variables from one or several climate models are often employed to force one or several hydrological models (Chawla and Mujumdar, 2015; Chegwidden et al., 2019; Feng et al., 2019; Zhang et al., 2018).

RCM data are frequently associated with systematic error when compared to historical observation data (Moghim and Bras, 2017; Shrestha et al., 2017; Teng et al., 2015; Teutschbein and Seibert, 2012). The uncertainty in climate simulations is directly

translated to the output of hydrological models (Kling et al., 2012). Thus, these data are difficult to use in climate impact studies without a bias correction (Teutschbein and Seibert, 2012).

Several post-processing bias correction methods of RCM data were proposed (Maraun et al., 2017; Smitha et al., 2018). Most of the bias correction methods are based on the assumption that the bias distribution in the historical period does not change in the future. Fundamentally, the hypothesis cannot be verified but can only be falsified (Popper, 2002). Moreover, bias correction methods have been criticized for violating some RCM assumptions by altering the physical relationship between climate variables including the relationship between precipitation and temperature (Addor et al., 2016; Ehret et al., 2012; Maraun, 2016; Maraun et al., 2017). Although Maraun et al. (2017) fiercely criticized bias correction, they do not suggest dismissal of bias correction in impact assessment studies. They highly recommend a good understanding of the sources of climate model bias and the selection of a bias correction method accordingly. For more transparency on the uncertainty induced by bias correction, some authors recommended to report both bias corrected and non-bias corrected results (Ehret et al., 2012).

Post-processing bias corrections are not the only source of uncertainties in hydrological impact assessments. Uncertainties exist at each step of the assessment chain (Muerth et al., 2012). In the European domain, it has been demonstrated that GCMs are the major source of uncertainty compared to RCMs and other sources of uncertainties (Déqué et al., 2007; Muerth et al., 2012). Findings in North America seem to indicate that the largest uncertainty originates from climate internal variability (Braun et al., 2012; Music and Caya, 2009). The regional climate internal variability is the variability induced by changing only initial conditions of a RCM. The climate internal variability is more pronounced when precipitation is the most influencing factor over a water limited environment (Chegwidden et al., 2019).

In order to account for the large uncertainties in climate projections, it has been recommended to apply multiple model and multiple run ensemble approaches (Bormann et al., 2009; Laux et al., 2017; Stanzel et al., 2018).

The selection of the type of hydrological model (conceptual vs physically-based) is not exempt from uncertainty. Thus, In addition to climate model ensembles, the use of hydrological model ensembles has been suggested (Block et al., 2009).

Land use change has been proven to significantly influence the hydrology of the region. Therefore, hydrological impact assessment study might not be realistic if land use change impact is not included into the analyses (Giertz et al., 2005; Yira et al., 2016).

Many hydrological impact studies have been conducted in the region. Aich et al. (2014) compared the impact of climate change on streamflow in four major river basins in several African regions. Kasei (2010) analyzed climate change in the Volta River basin (400,000 km²) and Bossa et al. (2014) in the Ouémé River basin (49,256 km²), Benin. However, few studies investigated hydrological impacts at the local scale in the region (Cornelissen et al., 2013; Op de Hipt et al., 2018; Yira et al., 2017). Local studies that combine impacts of climate and land use change on hydrology with a focus on inland valleys are very rare in the West African region (Op de Hipt et al., 2019).

The objective of this study was to look into the impact of climate and land use change on water resources in an inland valley in the Dano catchment in order to support informed decision making for smallholder farmers who are the most vulnerable to climate change. A separated and combined effect of climate and land use changes were scrutinized and the implications of the future changes on the adaptation strategies were discussed.

7.2 Material and methods

7.2.1 Climate model ensembles

The impact of climate change on water resources in an inland valley catchment (Bankandi-Loffing, 30 km², south-western Burkina Faso) was assessed using climate data of the CORDEX-Africa. A more detailed description of the Bankandi-Loffing catchment can be found in chapter 2. A climate ensemble constituted of five RCM-GCMS was applied for the impact assessment (Table 7-1). The ensemble was obtained from three RCMs which use four global climate models (GCMs) as boundary conditions. An ensemble of several RCM-GCMs was necessary in order to account for the uncertainties associated to climate models (Déqué et al., 2017; IPCC, 2014). Five RCM-GCMs were applied in the present study for data availability reason. An insight into the regional scale by Laux et al. (2017) recommend an ensemble of more than ten RCM-GCMs for precipitation related impact studies. Each RCM-GCM data comprises precipitation and air temperature for a reference period (1971-2000) and a predicted period (2021-2050). According to Vautard et al. (2014), the selected reference period corresponds to 0.46°C air temperature increase compared to pre-industrial period (1881-1910). For the predicted period, two greenhouse gas emission scenarios were considered, namely the representative concentration pathway (RCP) 4.5 and 8.5 (Moss et al., 2010). Daily temperature and precipitation of the RCM-GCMs were available at a 0.44° spatial resolution. Temperature and precipitation were extracted from 3x2 nodes and the average values were applied to the calibrated WaSiM model. Some authors utilized 3x3, 5x5, or 7x7 nodes for a better coverage of spatial variabilities (Mercogliano et al., 2014; Villani et al., 2014). Bias corrected temperature using the delta change approach

(Haddeland et al., 2012) and precipitation using non-parametric quantile mapping (Gudmundsson et al., 2012) were employed to force the hydrological model. The non-bias corrected results are not presented here because they had already been considered in previous researches in the study area (Op de Hipt et al., 2018; Yira et al., 2017).

The decision to use only bias corrected climate variables is motivated by the fact that bias correction reduces inconsistencies and deviations. It restores the timing of rainy seasons and considerably minimizes inter-node deviations (Yira et al., 2017). This subsequently leads to a more realistic seasonal distribution of precipitation and air temperature. Therefore, bias correction makes climate variables suitable for hydrological impact assessment of climate change (Johnson and Sharma, 2015; Muerth et al., 2012; Op de Hipt et al., 2018; Portoghese et al., 2011; Teutschbein and Seibert, 2012; Vrac et al., 2012; Yira et al., 2017).

Table 7-1. RCM-GCM products and the research centers of their production.

RCM-GCM label	RCM	Driving GCM	RCM center / Institute	Country of RCM center / Institute	Acronym (Yira et al. 2017)
M1	CCLM48	CNRM-CM5	CCLMcom	Germany	CCLM-CNRM
M2	CCLM48	EC-EARTH	CCLMcom	Germany	CCLM-EARTH
M3	CCLM48	ESM-LR	CCLMcom	Germany	CCLM-ESM
M4	HIRHAM5	NorESM1-M	DMI	Denmark	HIRHAM-NorESM
M5	RACMO22	EC-EARTH	KNMI	Netherlands	RACMO-EARTH

RCM: Regional Climate model; GCM: Global Climate Model; **CCLM**: Climate Limited Modelling Community; **DMI**: Danish Meteorological Institute; **KNMI**: Royal Netherlands Meteorological Institute.

7.2.2 Land use land cover (LULC) prediction

The future LULC maps (LULC-2019, LULC-2025, and LULC-2030) were developed by Op de Hipt (2017) based on historical maps (LULC-2000 and LULC-2013) using the Land Change Modeler (LCM) (Clark Labs, 2016). LCM is an empirically driven processing software which follows three steps. The first step is the past land cover analysis. The second step is the modelling of transition potentials. For this step, LCM uses a multi-layer neural network (Chan et al., 2001) to model the potential for land transition from one land use class to another. The method considers multiple variables including slopes, distance to roads, previously deforested areas, and settlements. The calibrated transition potential model is then used for future scenario predictions. Finally, the last step consists of using historical rates of change and the transition potential model to determine changes of land use per pixel and time step. At this step, a stochastic

Markov chain technique (Wilson and Weng, 2011) was applied to simulate the probability of LULC and the future LULC map is generated.

Fig. 7-1 shows a gradual conversion of savanna to cropland and settlement. The average annual reduction rate of savanna was 1.1% of the catchment area and the highest conversion rate occurred from 2007 to 2013 (3.3% of the catchment area per year). The trend of savanna conversion was previously reported in Yira et al. (2016). They analyzed the impact of LULC change on hydrological processes in the catchment including evapotranspiration and the soil infiltration. The modification of evapotranspiration could be attributed to the change in vegetation characteristics such as albedo, which modifies evapotranspiration by defining net solar radiation (Monteith, 1975). In addition to albedo, canopy surface resistance, leave area index, and root depth could be modified by LULC change and consequently could lead to a variation of evapotranspiration.

However, LULC change influences infiltration rates by modifying macropore distribution in the soil. In a similar catchment in northern Benin, Giertz et al. (2005) demonstrated a significant decrease of the number of macropores from savanna to cropland. Macropore distribution could affect interflow and base flow.

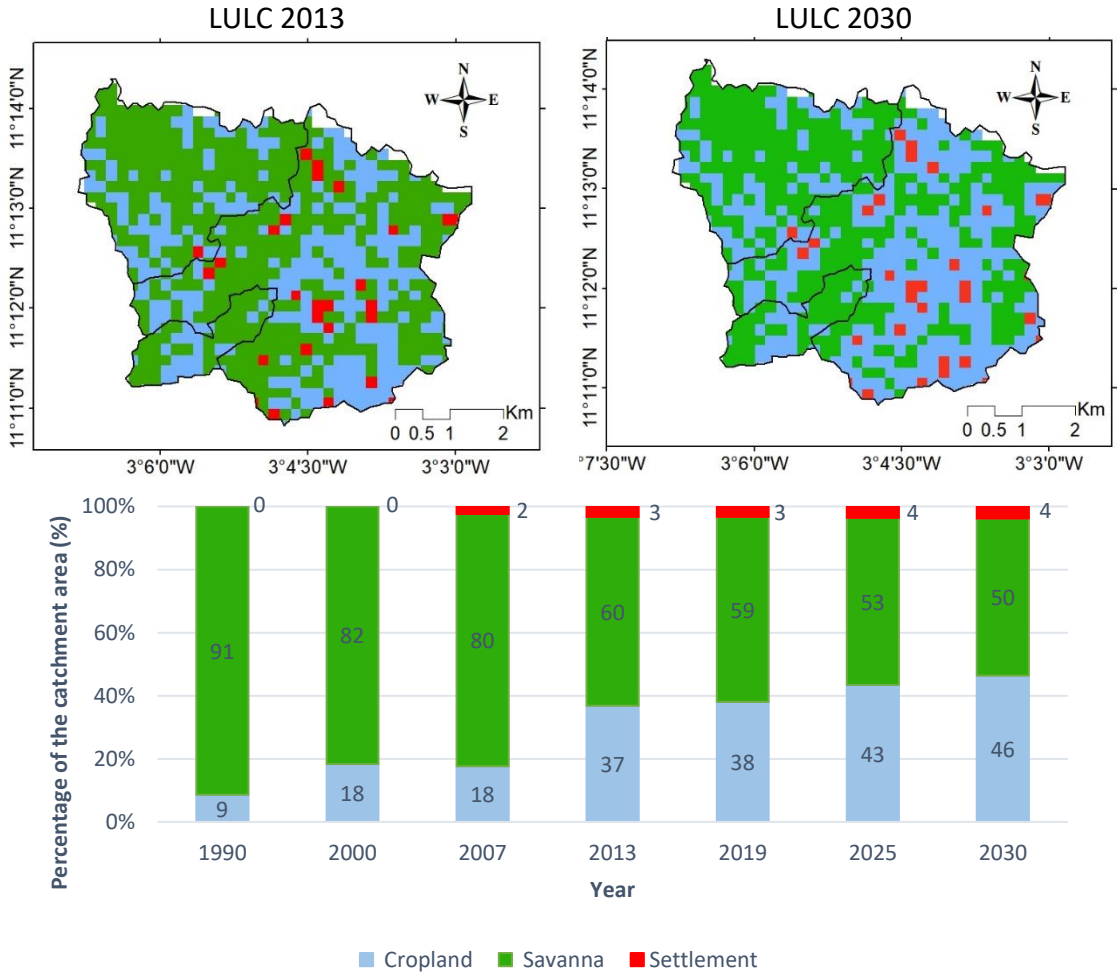

Fig. 7-1. Spatial and temporal variation of historical land use and Land cover (LULC 1990, 2000, 2007, and 2013) and the predicted future LULC (years 2019, 2025, and 2030) at a spatial resolution 200 m. (Dataset: Op de Hipt, 2017).

On the question of drivers of land use change, many studies suggest that population growth (3% per year) is the main driver of savanna conversion to cropland (CILSS, 2016; Codjoe, 2004; Op de Hipt et al., 2019; Ouedraogo et al., 2010; Paré et al., 2008; Yira et al., 2016). This is needed to satisfy the considerable increase of food demand in the region. Moreover, the evolution of the farming systems suggests that the development of cotton cultivation has significantly contributed to the savanna conversion (Op de Hipt et al., 2019; Yira et al., 2016). The production of cotton increased from 75,476 t in 1990 to 280,000 t in 2013 (270% increase) at the country level (FAO, 2019).

Other drivers of natural vegetation conversion into croplands include bushfire, mining, wood harvesting, and climate variability, among others (Zoungrana et al., 2015). The conversion is frequently associated with the vulnerability of soil to erosion and soil

fertility losses. This in return exacerbates more natural ecosystem conversion to agriculture. Hounkpatin et al. (2018) estimated soil organic carbon loss in the Dano catchment of up to 24 t C ha^{-1} (ton carbon per hectare) at the top 10 cm and 49 t C ha^{-1} at the upper 30 cm.

7.2.3 Calibration and validation of the hydrological model

To study impacts of climate change on hydrology, a calibrated hydrological model is often forced by RCM-GCM climate variables including precipitation and temperature (Chegwidden et al., 2019; Chen et al., 2019; Fazeli Farsani et al., 2019; Feng et al., 2019; Nilawar and Waikar, 2019; Oeurng et al., 2019). The Bankandi-Loffing catchment was initially calibrated and validated at an hourly time step using the Penman-Monteith approach (Monteith, 1975) for evapotranspiration estimation (see chapter 6 for the calibration and validation of the Bankandi-Loffing model). As the temperature is the only climate variable available at a daily time step for evapotranspiration approximation, the model was recalibrated at a daily time step using the Hamon method to estimate evapotranspiration for the climate impact assessment (Federer and Lash, 1983; Hamon, 1963; Rao et al., 2011; Schulla, 2015). The recalibration of the model was solely based on the optimization of the Hamon monthly correction factor which depends on season and location. The model was calibrated during 2014-2015 and validated in 2016 using LULC-2013 as a reference and the annual water balance was estimated.

7.2.4 Climate and land use scenarios

Climate and land use scenarios were implemented according to Table 7-2. For each of the five RCM-GCMs, the bias corrected precipitation and temperature were utilized as input for the recalibrated hydrological model. The hydrological model was separately run for each of the three components of a RCM-GCM (reference period, RCP 4.5, and RCP 8.5) for 30 years. The reference period (1971-2000) and the predicted period (2021-2050) were preceded by the same warmup period of 6 years. The water balance of each RCM-GCM for RCP 4.5 and RCP 8.5 were compared to their counterpart reference periods. An equal duration (30 years) of predicted and reference periods were used and the predicted periods were compared to the reference period in order to cancel out systematic bias related to the hydrological model and the climate models. The systematic error is assumed to be constant between the reference period and the predicted period (Chaix et al., 2018). The identical warmup period was used to avoid variation in the initial conditions of the hydrological model.

The predicted RCM-GCMs were compared to their counterpart modelled past and not observed historical data because the bias correction is not perfect. Therefore,

comparing predicted modelled data with observed data will add a new layer of uncertainty to the impact assessment.

The LULC-2013 was considered as the reference LULC and was used during the reference period and the predicted periods, except while assessing the combined climate and land use change impact. During the assessment of combined climate and land use change impact, LULC-2013 was replaced by LULC-2030 for the predicted future climate scenarios (Table 7-2).

Table 7-2. Model setup for hydrological impact assessment of climate and land use.

	Reference		**Prediction**	
Scenario	*LULC*	*Historical RCM-GCM*	*LULC*	*RCM-GCM (RCP 4.5 and 8.5)*
1	2013	1971-2000	2013	2021-2050
2	2013	1971-2000	2030	2021-2050

LULC: land use and land cover; **RCM**: regional climate model, **GCM**: global climate model; **RCP**: representative concentration pathway

7.3 Results and discussion

7.3.1 Hydrological model performance and water balance

The simulated hydrograph (Fig. 7-2) and the model performance statistics (Table 7-3) show a good performance of the hydrological model at daily time step using the Hamon method for the evapotranspiration estimation. There is a good agreement between simulated and observed total runoff in terms of timing and magnitude. Most of the peak flows were well captured. However, some extreme events were not well captured. This can be attributed to the uncertainty increase with the size of the flood due to overbank flows.

The Kling-Gupta efficiency (KGE) (Gupta et al., 2009; Kling et al., 2012) was approximately 0.7 for the calibration and validation periods. The Nash-Sutcliffe efficiency (NSE) (Nash and Sutcliffe, 1970) (≥ 0.5) and percent bias (24% for calibration period and 21% for validation) were satisfactory (Moriasi et al., 2007; Van Liew et al., 2007).

The annual average change in storage was negative during the simulation period (delta S = -30 mm). This is partly attributed not only to the short simulation period but also mainly to high inter-annual variability of rainfall during the observation period (2014-2016). The annual rainfall in the year 2015 was 21% higher than the year 2014 and 16% higher than the year 2016. Therefore, the simulation period cannot be qualified as a stationary period and the equilibrium of the water balance was not reached. In the dry years, the water deficit is compensated by the soil moisture originating from the shallow groundwater of inland valley bottoms. In the valley bottoms, the groundwater

table is near the ground surface and consequently, contributes significantly to soil moisture through capillary rise.

In general, the water balance is in the range of previous studies in the region (Cornelissen et al., 2013; Yira et al., 2017, 2016). Given that the impact assessment is done by relative change in water balance between the predicted period and the reference period, the systematic error will be cancelled out (Habel, 2010).

Table 7-3. Mean annual water balance and the model performance.

	Calibration (2014-2015)	**Validation (2016)**	**Annual mean (2014-2016)**
P (mm)	1067	1001	1045
ETa (mm)	982	954	973
Qt (mm)	96	113	102
Qs (mm)	39	46	41
Qi (mm)	40	43	41
Qb (mm)	18	23	19
Delta S (mm)	-11	-66	-30
R^2	0.59	0.71	-
NSE	0.57	0.48	-
KGE	0.66	0.73	-
Pbias (%)	-23.70	21.20	-

***P**: precipitation; **ETa**: total actual evapotranspiration; **Qt**: total runoff; **Qs**: surface runoff; **Qi**: interflow; **Qb**: base flow; **Delta S**: change in storage; **R^2**: Coefficient of determination; **NSE**: Nash Sutcliffe Efficiency; **KGE**: Kling-Gupta Efficiency.*

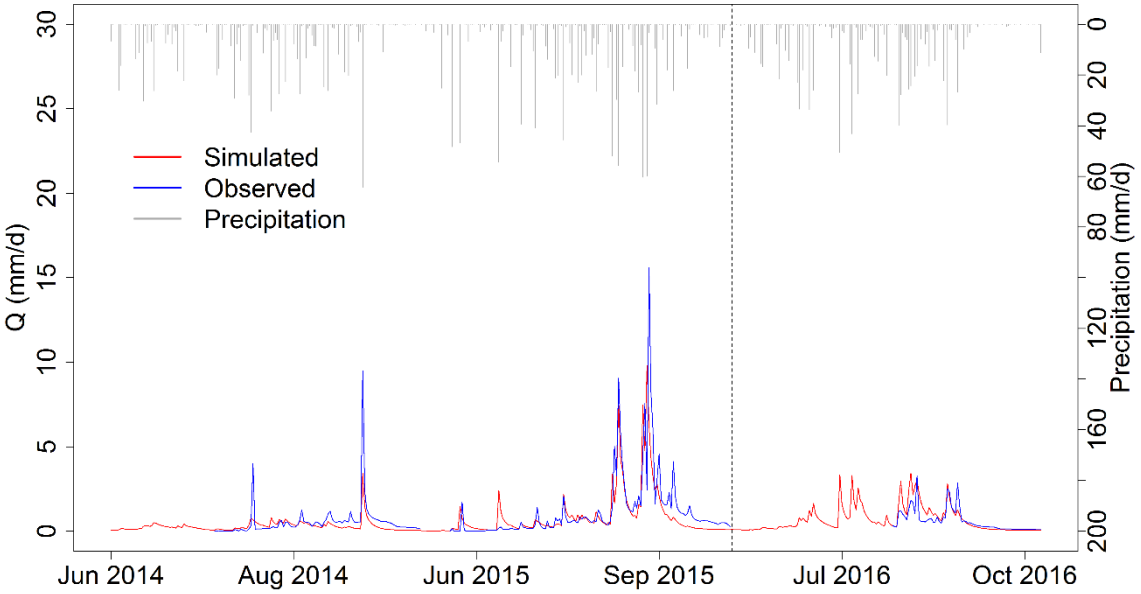

Fig. 7-2. Comparison of simulated discharge using Hamon ETp and observed discharge at the outlet of Bankandi-Loffing catchment. The vertical dashed line separates the calibration (2014-2015) period from the validation (2016) period.

7.3.2 Sensitivity of the hydrological model to LULC change

Four historical LULCs (LU-1990, LU-2000, LU-2007, and LU-2013) and three predicted future LULCs (LU-2019, LU-2025, and LU-2030) were utilized to run the calibrated hydrological model for three years (2014-2016). The annual mean water balance results (Table 7-4) demonstrate a linear decrease of the actual evapotranspiration (ETa) while the total runoff increases with conversion of savanna to croplands. The savanna area decrease is highly correlated to the change in mean annual ETa and more than 96% of the variation of the annual ETa can be attributed to the decrease in savanna area (Pearson correlation coefficient R^2= 0.96, p-value= 0.0001). The relative decrease of ETa from LU-2013 to LU-2030 is -5%, whereas the relative increase of the total runoff is +27%. This seems to suggest that runoff is nearly six times more sensitive to savanna conversion than ETa. Moreover, the increase in the total runoff is primarily driven by the increase in the surface runoff (R^2=0.996, p-value < 0.0001). This could contribute to a soil erosion increase and a soil fertility loss for agriculture (Op de Hipt, 2017).

Table 7-4. Mean annual water balance for each land use land cover for the period 2014-2016.

	Land use and land cover						
	LU-1990	**LU-2000**	**LU-2007**	**LU-2013**	**LU-2019**	**LU-2025**	**LU-2030**
P (mm)	1045	1045	1045	1045	1045	1045	1045
ETa (mm)	1039	1011	1014	973	950	934	924
Qt (mm)	44	69	71	102	119	133	140
Qs (mm)	16	28	27	41	51	58	62
Qi (mm)	24	27	29	41	43	45	45
Qb (mm)	4	14	14	19	25	30	33

LU: *land use and land cover;* ***P****: precipitation;* ***ETa****: total actual evapotranspiration;* ***Qt****: total runoff; Q****s****: surface runoff;* ***Qi****: interflow;* ***Qb****: base flow;* ***Cr****: simulated total runoff coefficient.*

The variation of average monthly ETa (Fig. 7-3-e) suggests that the largest differences between the land use scenarios occur at the beginning (May, June, and July) and the end of the rainy season (October). The magnitude of monthly ETa in September is approximately the same for all the land use scenarios. This can be explained by the fact that there is sufficient water to satisfy the monthly potential evapotranspiration in September. The total runoff (Fig. 7-3-a), surface runoff (Fig. 7-3-b), and base flow (Fig. 7-3-d) clearly show September as the month of the highest contrast between the scenarios while August recorded the maximum variance for interflow (Fig. 7-3-c).

Many authors have documented the conversion of savanna to cropland in the region and a subsequent increase in runoff (Descroix et al., 2018; Mahé et al., 2010, 2005; Op de Hipt et al., 2019; Paré et al., 2008; Stéphenne and Lambin, 2001; Yira et al., 2016; Zoungrana et al., 2015). Mahé et al. (2005)reported 30% decline of natural vegetation and 23% croplands increase from 1965 to 1995 in the Nakambe River basin in the central-northern Burkina Faso. They attributed the subsequent increase in runoff to the decrease of soil water holding capacity (WHC). In a similar climatic zone in northern Benin, Giertz et al., (2005) found that the infiltration rate of natural savanna is significantly higher than in croplands. Therefore, croplands tend to produce more runoff than savanna areas.

It is noteworthy that the evapotranspiration considerably influenced the outcome of the resulting water balance in this study. None of soil parameters were modified. Thus, the change in water balance cannot be attributed to a change in infiltration. As the Hamon method of evapotranspiration was applied instead of the Penman-Monteith method, parameters such as albedo and canopy surface resistance could not explain the variation of the actual evapotranspiration either (Hamon, 1963; Monteith, 1975). The major parameter in this study which influences the change of the water balance with land use change is root depth. The root depth varies throughout the

year from 0.2 to 1.8 m under natural savanna. Most of cropland are bare soil (root depth 0 m) during dry season (January to May). In the cropping period (June to October), the root depth ranges from 0.01 to 0.53 m. The following parameters can contribute to a lesser extent: the specific thickness of water layer on the leaves (interception parameter, *IntercepCap*), the root distribution (*RootDistr*), the vegetation cover fraction (*VCF*), and the leave area index (*LAI*). This is supported by Leemhuis et al. (2007) and Beck et al. (2013) in their studies in tropical regions in Indonesia and Puerto-Rico, respectively. Hence, evapotranspiration reduction as a result of natural savanna conversion to cropland favors infiltration excess runoff. Furthermore, it is important to note that rainfall characteristics (intensity, distribution in time) play a crucial role in runoff generation (Niehoff et al., 2002; Zhou et al., 2019).

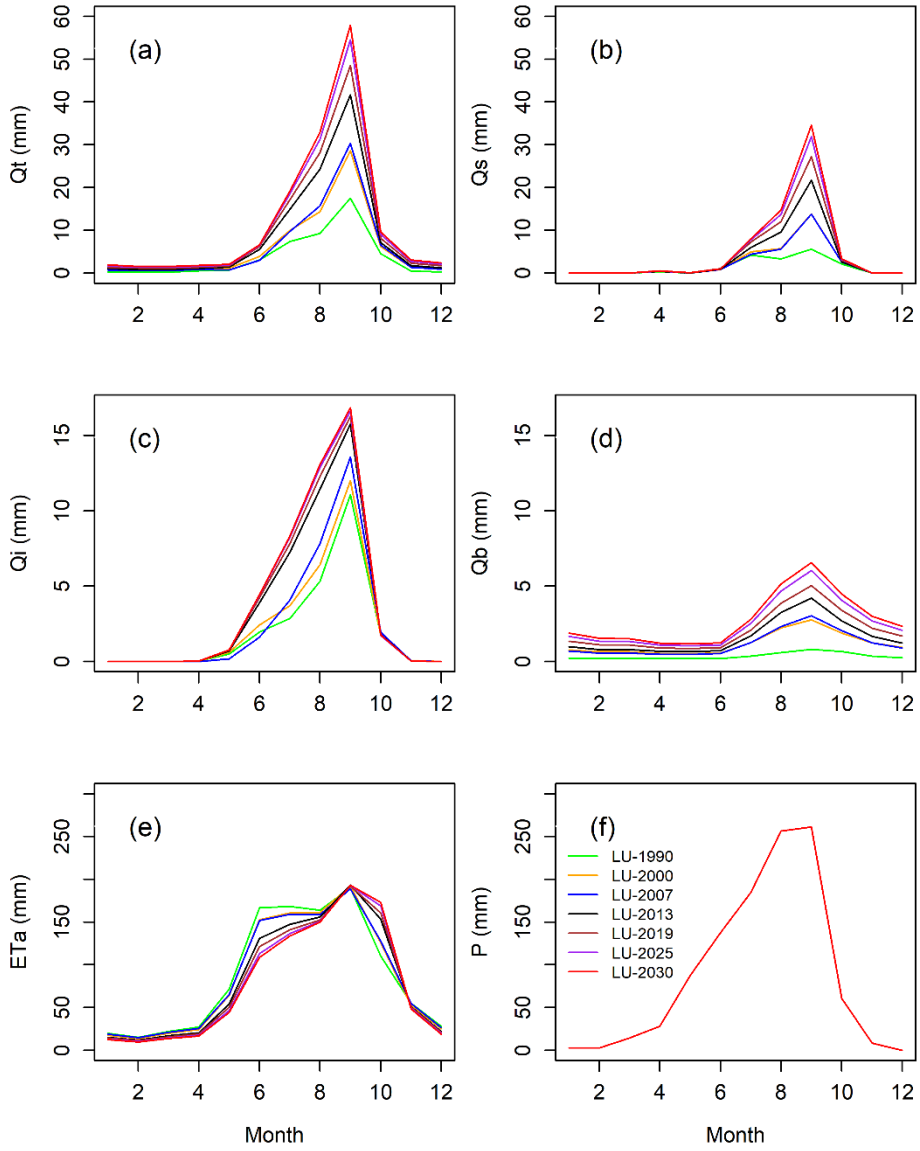

Fig. 7-3. Mean monthly water balance variation with land use land cover change for the period 2014-2016. Land use (LU) for the years 2019, 2025, and 2030 are modeled land use and land cover. (a): total runoff (Qt); (b): surface runoff (Qs); (c): interflow (Qi); (d): base flow (Qb); (e): actual evapotranspiration (ETa); (f): rainfall (P);. The same meteorological data set for all land use scenarios was used.

7.3.3 Climate change impact on hydrology

Fig. 7-4 illustrates the input climate model data (precipitation and air temperature) and the output main water balance components (total runoff, surface runoff, interflow, base flow, and actual evapotranspiration) for the reference period (1971-2000). The comparison between the five RCM-GCMs using the nonparametric, pairwise, and corrected Wilcoxon test shows no significant difference for the reference

climate input data of most of the RCM-GCMs. This suggests that most of the RCM-GCMs belongs to the same population and have a similar distribution for the reference period. However, significant difference was obtained for actual evapotranspiration between RACMO-EARTH and each of the following models: CCLM-CNRM (p-value=0.0197), CCLM-ESM (p-value=0.0164), and HIRHAM-NorESM (P-value=0.0426). A similar result was observed for base flow with a significant difference between RACMO-EARTH and CCLM-CNRM (p-value=0.0309) and between RACMO-EARTH and CCLM-ESM (p-value=0.0426). It is important to note that a significant difference for base flow occurred although there was no significant difference for the total runoff. This is due to the low contribution of base flow to runoff.

The relative change in temperature and precipitation and the implication for water balance components is shown in Fig. 7-5. All the models revealed an increase in temperature compared to the reference period (Fig. 7-5-g). The increase in temperature is higher for the RCP 8.5 than RCP 4.5. This is because the greenhouse forcing of RCP 8.5 (>1,370 ppm CO_2 equivalent) is higher than the greenhouse forcing of RCP 4.5 (~650 ppm CO_2 equivalent) (Moss et al., 2010). The annual increase in temperature ranges from 1 to 2°C until 2030. The highest increases in temperature were predicted by CCLM-EARTH and CCLM-ESM. The predicted temperature is consistent with the decision adopted by the Conference of the Parties at its twenty-first session in Paris (COP 21). The Paris agreement urgently recommended that parties limit the temperature increase to well below 2°C compared to the pre-industrial level (Déqué et al., 2017; Diedhiou et al., 2018; UN-FCCC, 2016).

Although the investigated climate models unanimously simulate an increase in temperature, they diverge on precipitation signals (Fig. 7-5-f) and the uncertainties are high among the ensemble members. CCLM-EARTH and CCLM-ESM which predict the highest increases in temperature project negative precipitation signals while the other models (CCLM-CNRM, HIRHAM-NorESM, and RACMO-EARTH) simulated positive signals. For the models which predicted positive precipitation signals, the increase in annual precipitation is higher under high greenhouse gas forcing (RCP 8.5) than the moderate greenhouse gas forcing (RCP 4.5). However, for the models which predicted negative precipitation signals, there was no clear trend of precipitation signals as function of greenhouse gas concentration. The climate models predict precipitation increases from 3% (predicted by HIRHAM-NorESM under RCP 4.5) to 18% (predicted by CCLM-CNRM/RCP 8.5) and the decreases range from -10 to -5%. Yira et al. (2017) obtained +1 to +18% increase and -9 to -6% decrease in precipitation in a 6.5 times larger catchment in Dano compared to the Bankandi-Loffing catchment. Op de Hipt et al. (2018) found +6 to +19% increase and -11 to -4% decrease in the Dano catchment (4

times larger than the Bankandi-Loffing catchment). It is noteworthy that the selected climate models do not present opposite signals between RCP 4.5 and RCP 8.5.

Furthermore, the models with higher increase in temperature project lower increase in mean annual precipitation whereas the models with lower increase in temperature show higher increase in mean annual precipitation. This seems to contradict the Clausius-Clapeyron relation (Pall et al., 2007). According to the Clausius-Clapeyron equation, rainfall intensity increases with green-house gas under constant moisture availability at global or regional scale. Annual comparison of rainfall in this study might be the reason for the differences. Additionally, at local scale, air moisture might significantly vary. Importantly, the distribution of daily rainfall shows an increase of the 95^{th} percentile for most of the models. The daily rainfall 95^{th} percentile increases in a range of 2% to 24% compared to the reference period for all the models. This is applicable to the negative and positive precipitation signal models. The increase of intense rainy days is associated with a decrease of rainy days for most of the climate models. This is consistent with previous studies in the region which demonstrated not only the increase rainfall intensity and the decrease of rainy days but also a delay of rainy season onset (Ibrahim et al., 2013a).

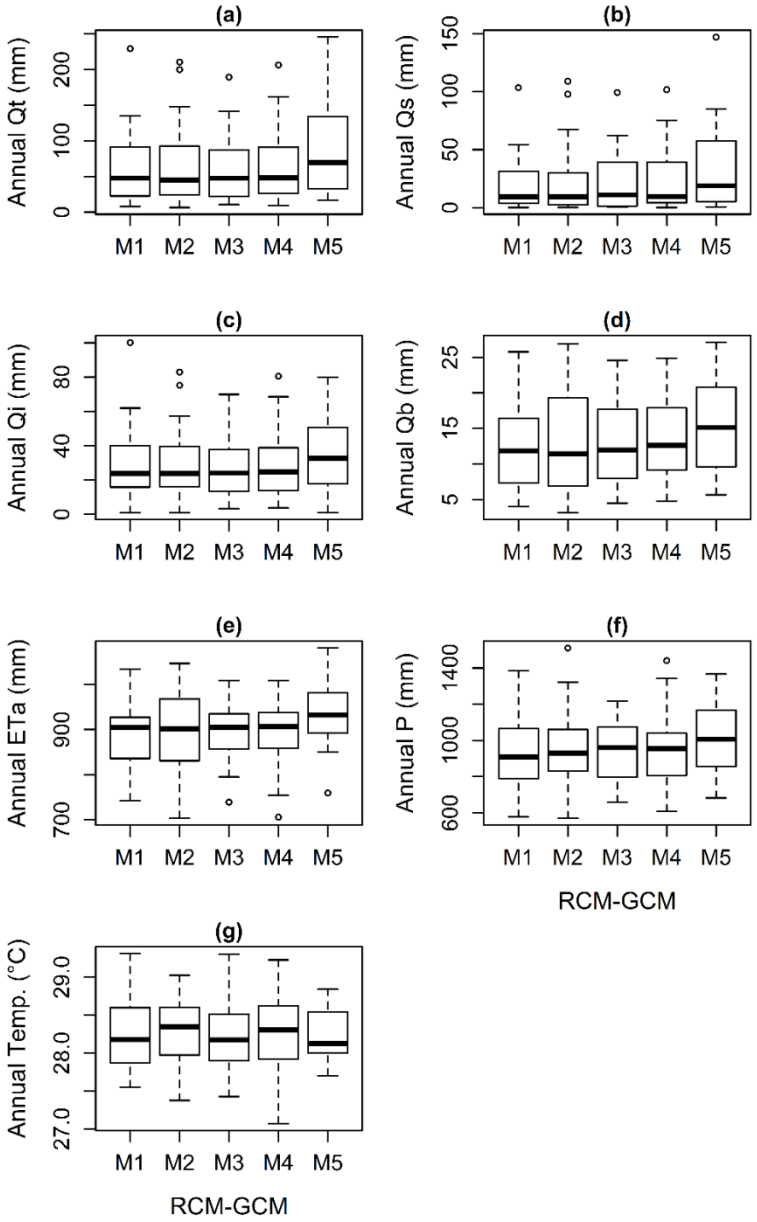

Fig. 7-4. Annual water balance distribution during the reference period (1971-2000) for the five RCM-GCMs using LULC 2013. *M1*: CCLM-CNRM; *M2*: CCLM-EARTH*; M3*: CCLM-ESM; *M4*: HIRHAM-NorESM; and *M5*: RACMO-EARTH; Temp.: air temperature (2 m height); P: precipitation; Qt: total runoff; Qs: surface runoff; Qb: base flow; ETa: actual evapotranspiration.

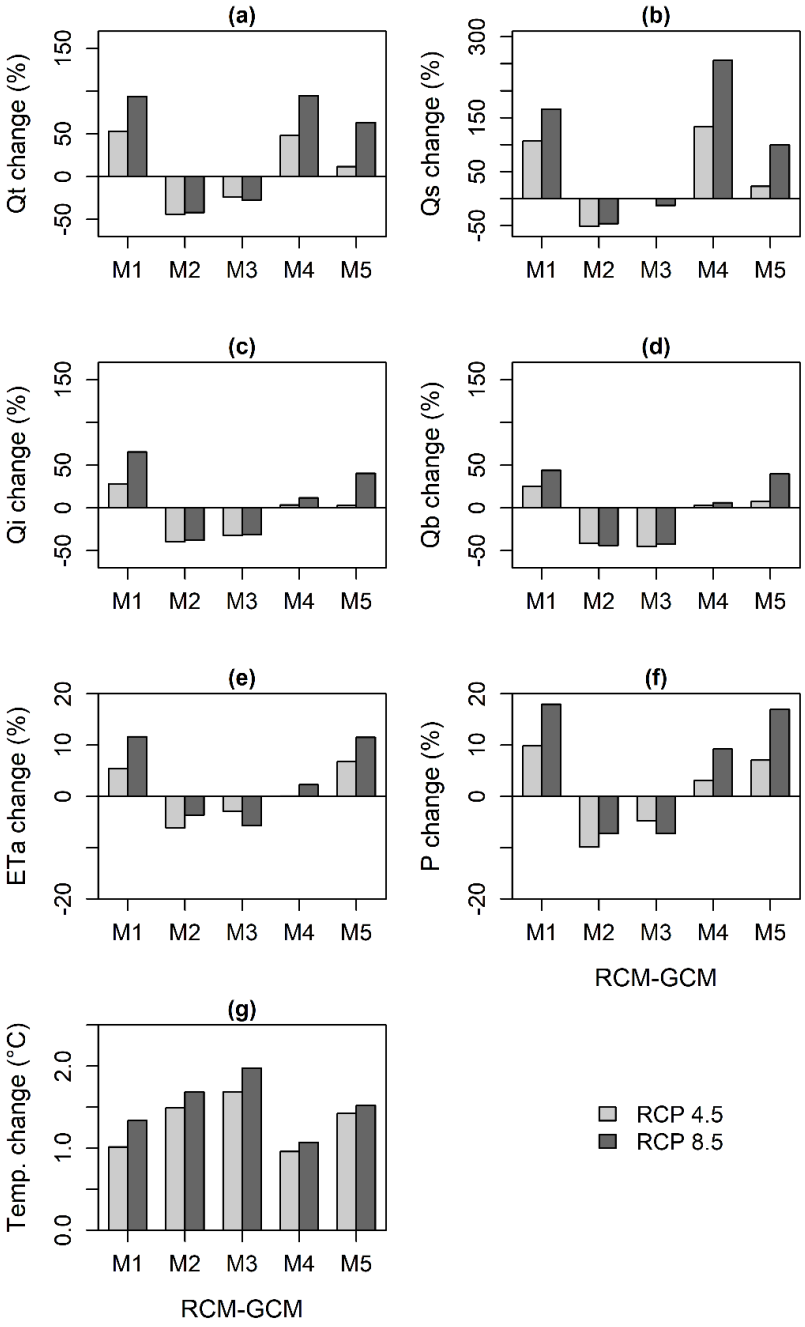

Fig. 7-5. Annual change for the period 2021-2050 of air temperature (Temp.) and precipitation (P) and the subsequent change of actual evapotranspiration (ETa), total runoff (Qt), surface runoff (Qs), interflow (Qi), and base flow (Qb) compared to the period 1971-2000 (LU-2013 was employed for both reference and prediction periods). *M1*: CCLM-CNRM; *M2*: CCLM-EARTH*; M3*: CCLM-ESM; *M4*: HIRHAM-NorESM; and *M5*: RACMO-EARTH.

The direction of change in the estimated water balance components (Fig. 7-5-a to Fig. 7-5-e) are superimposed by precipitation signals. CCLM-EARTH and CCLM-

ESM show a negative change while the other models predict positive change. This seems to suggest that the predicted water balance is mainly influenced by precipitation in the study area. This is consistent with Yira et al. (2017), who suggested that could be attributed to water limited conditions of the area. Evidence from a similar catchment in California simulated using the SWAT model is also in line with these findings (Arnold et al., 1998; Ficklin et al., 2010). However, insight from Op de Hipt et al. (2018) seems to indicate that potential evapotranspiration is more influential to runoff than rainfall. They attributed the divergent finding to the structural difference between the hydrological models SHETRAN (see https://research.ncl.ac.uk/shetran/ for the description) and WASIM (Schulla, 2015).

The annual actual evapotranspiration (ETa) (Fig. 7-5-e) varies from 0% (no change) predicted by HIRHAM-NorESM/RCP 4.5 to +12% projected by CCLM-CNRM/RCP 8.5. CCLM-EARTH/RCP 4.5 projected the lowest ETa decrease (-6%). In contrast with ETa, the total runoff (Fig. 7-5-a) exhibits a much higher increase (+12% to +95%) and decrease (-44% to -24%). The total runoff decrease is expected to be an order of magnitude less than the increase but still more prominent than the decrease of ETa.

A more detailed analysis of the runoff components clearly demonstrates that surface runoff (Fig. 7-5-b) is expected to have a major change. The maximum surface runoff change is predicted by HIRHAM/RCP 8.5 (+256%) followed by CCLM-CNRM/RCP8.5 (+166%). Moreover, a considerable increase in surface runoff was noted under RCP 4.5, such as +133% increase projected by HIRHAM-NorESM and +106% by CCLM-CNRM. However, CCLM-EARTH predicted a decrease of -51% and -46% under RCP 4.5 and RCP 8.5, respectively and CCLM-ESM projected negligible change in surface runoff under RCP 4.5 and only -12% decrease under RCP 8.5. If the increase of surface runoff, such as predicted by CCLM-CNRM and HIRHAM-NorESM occurred, it would be detrimental for soil in terms of erosion and fertility loss (Op de Hipt, 2017; Op de Hipt et al., 2019, 2018; Yira, 2016; Yira et al., 2016).

7.3.4 Predicted dry spell change

Daily bias corrected modelled rainfall data were utilized to analyze dry spells of >5 days and >10 days in wet seasons (June to October) by comparing the predicted period (2021 to 2030) with the reference period (1971 to 2000). The threshold of a rainy day was assumed to be 0.1 mm.

Fig. 7-6 depicts a variable relative change of dry spells for the five climate models under RCP 4.5 and RCP 8.5. Some models predict increase in dry spells. The increase of dry spells ranges from 12% to 96% for >5 day dry spells and 12% to 125% for >10 day dry spells compared to the reference period. Nonetheless, other models project a decrease of dry spells which range from -10% to -44% for >5 day dry spells and -2% to

-44% for >10 day dry spells. The models CCLM-EARTH and CCLM-ESM predict a decrease in annual rainfall (Fig. 7-5-f). However, CCLM-EARTH shows a decrease in dry spells whereas CCLM-ESM predicts an increase in dry spells. This seems to suggest that the decrease in annual rainfall is mainly due to increase in dry spells for CCLM-ESM. This in line with Kendon et al. (2019) who found the decrease of precipitations to be due to decrease in rainfall occurrence in the West African region. As for CCLM-EARTH, the decrease in annual rainfall might be due to its projection of light rainfall. However, some models have been reported to show increase in rainfall intensity in the region (Han et al., 2019).

In general, the change in >10 day dry spells are expected to be higher than the change in >5 day dry spells. In a similar study in East Africa, it has be found that maize experiences at least one >10 day dry spells in 74% to 80% of the season (Barron et al., 2003). The occurrence of dry spells during flowering and grain filling stages might lead to yield reduction or crop failure (Laux et al., 2009, 2008).

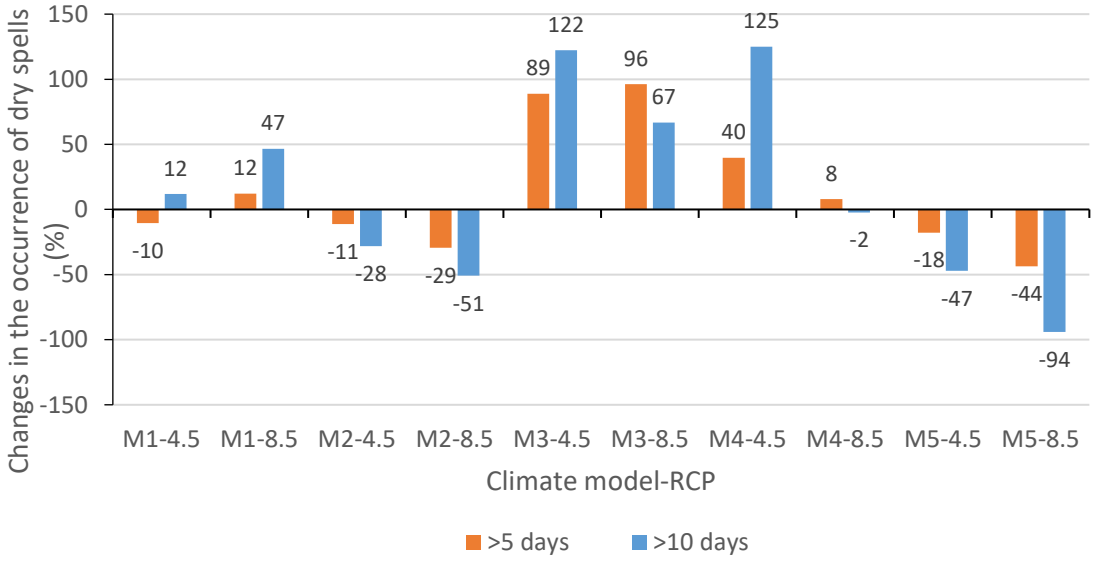

Fig. 7-6. Relative changes of >5 day and >10 day dry spells of the predicted period (2021 to 2030) compared to the reference period (1971 to 2000). *M1*: CCLM-CNRM; *M2*: CCLM-EARTH*; M3*: CCLM-ESM; *M4*: HIRHAM-NorESM; and *M5*: RACMO-EARTH. Bias corrected data were utilized. The threshold of a rainy day is 0.1 mm. the analysis was performed in the rainy season (June to October).

7.3.5 Climate and land use change impact on hydrology

The results of the combined impact of climate and land use change on hydrology is depicted in Fig. 7-7. The land use change exacerbates the increase of runoff

due to climate change (Fig. 7-7-a). Under the effect of land use 2030, CCLM-CNRM, HIRHAM-NorESM, and RACMO-EARTH project a total runoff increase range of +52% to +158% compared to the reference period. The maximum increase was predicted by CCLM-CNRM/RCP 8.5 whereas the lowest increase was observed with RACMO-EARTH/RCP 4.5. Total runoff has increased by a factor of 1.4 to 4.5 times compared to the climate change impact only scenario depending on the ensemble member.

Nevertheless, the models CCLM-EARTH and CCLM-ESM predicted a total runoff decrease range of -29% to -11%. In this case, the highest and the lowest decrease are observed under RCP 4.5 forcing. Land use change reduces the impact of climate change for these climate models (CCLM-EARTH and CCLM-ESM) by a factor of 0.5 to 0.7 compared to the climate change impact only scenario.

A comparison with the previous scenario (climate change impact only) clearly reveals that 27% to 78% of total runoff change can be attributed to land use change. Consequently, the impact of Land use change on the total runoff varies significantly with the climate model. The maximum land use change contribution is predicted under RACMO-EARTH/RCP 4.5 forcing whereas the minimum land use change impact contribution is projected under HIRHAM-NorESM/RCP 8.5. Thus, the projected land use impact indicates that land use change impact on total runoff is not negligible and cannot be ignored when studying future climate impact on hydrology in the area.

The runoff component analyses (Fig. 7-7-b, Fig. 7-7-c, and Fig. 7-7-d) shows that the major driver of runoff change is surface runoff (Fig. 7-7-b). Nearly fourfold increase in surface runoff is expected under RCP 8.5 for CCLM-CNRM (+281%) and HIRHAM-NorESM (+305%). Surface runoff is projected to approximately triple under RACMO-EARTH/RCP 8.5 (+186%), CCLM-CNRM/RCP 4.5 (+185%), and HIRHAM-NorESM/RCP 4.5 (+173%). This could subsequently intensify soil erosion with disastrous loss in soil fertility if no mitigation strategies are put in place.

It is interesting to note a significant increase of base flow with land use change from 3% to 44% in the first scenario (Fig. 7-5-d) to 67% to 141% (Fig. 7-7-d) in the second scenario compared to the reference period. The contribution of the land use change to base flow increase is therefore estimated to 69-96% of the combined land use and climate change. This seems to suggest that land use change is the major driver of base flow change in the catchment. No direct relationship exists between base flow and land use parameters. The increase of the base flow with land use change can be attributed to the surplus water from the ETa decrease from the first scenario (0% to 12% compared to the reference period; Fig. 7-5-e) to the second scenario (-3% to 7% compared to the reference period; Fig. 7-7-e). This may be attributed to the fact that root depth is greater in savanna (0.2 to 1.8 m used for WaSiM parameterization) than in croplands (0 to 0.61 m used for WaSiM parameterization).

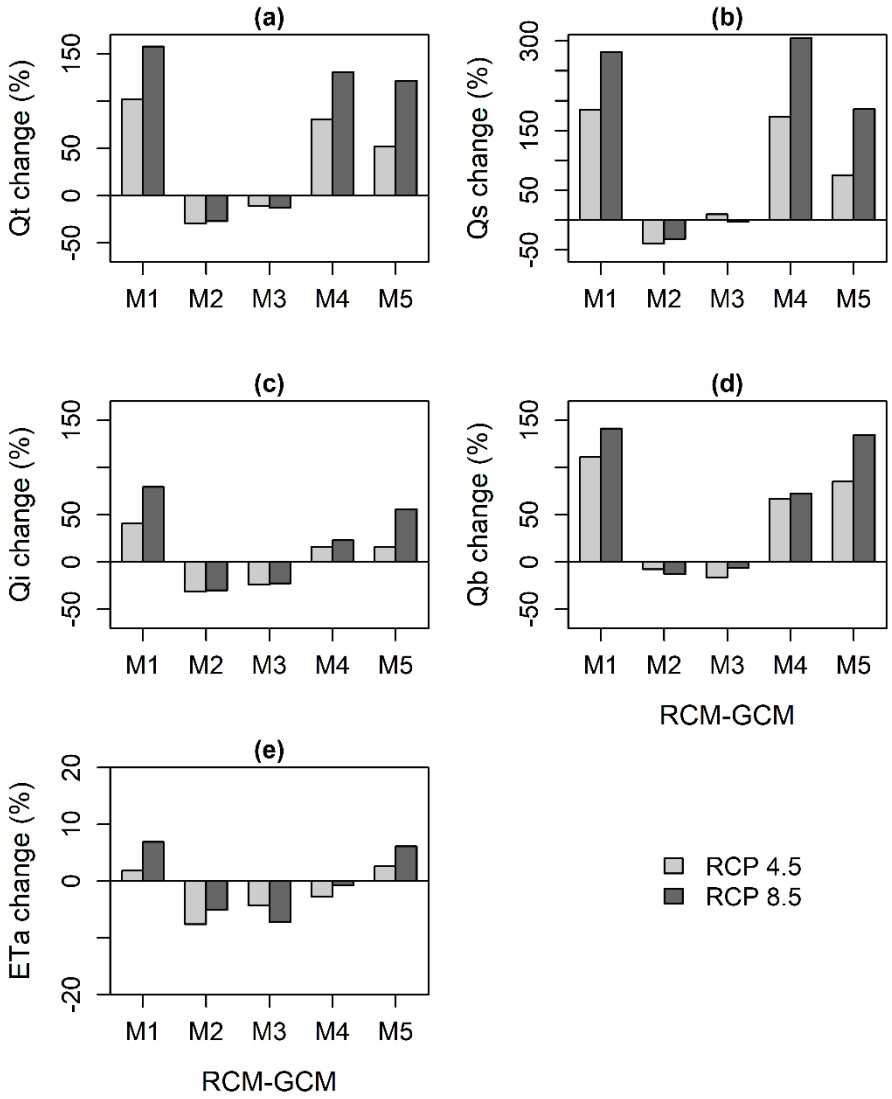

Fig. 7-7. Annual change for the period 2021-2050 (LULC 2030) of total runoff (Qt), surface runoff (Qs), interflow (Qi), base flow (Qb), and actual evapotranspiration (ETa) compared to the period 1971-2000 (LULC 2013). *M1*: CCLM-CNRM; *M2*: CCLM-EARTH*; M3*: CCLM-ESM; *M4*: HIRHAM-NorESM; and *M5*: RACMO-EARTH.

The monthly signal variations of the input climate variables (Fig. 7-8) and the subsequent simulated water balance before and after the application of land use change (Fig. 7-9) was presented in order to look into seasonal variations of the water balance (in mm).

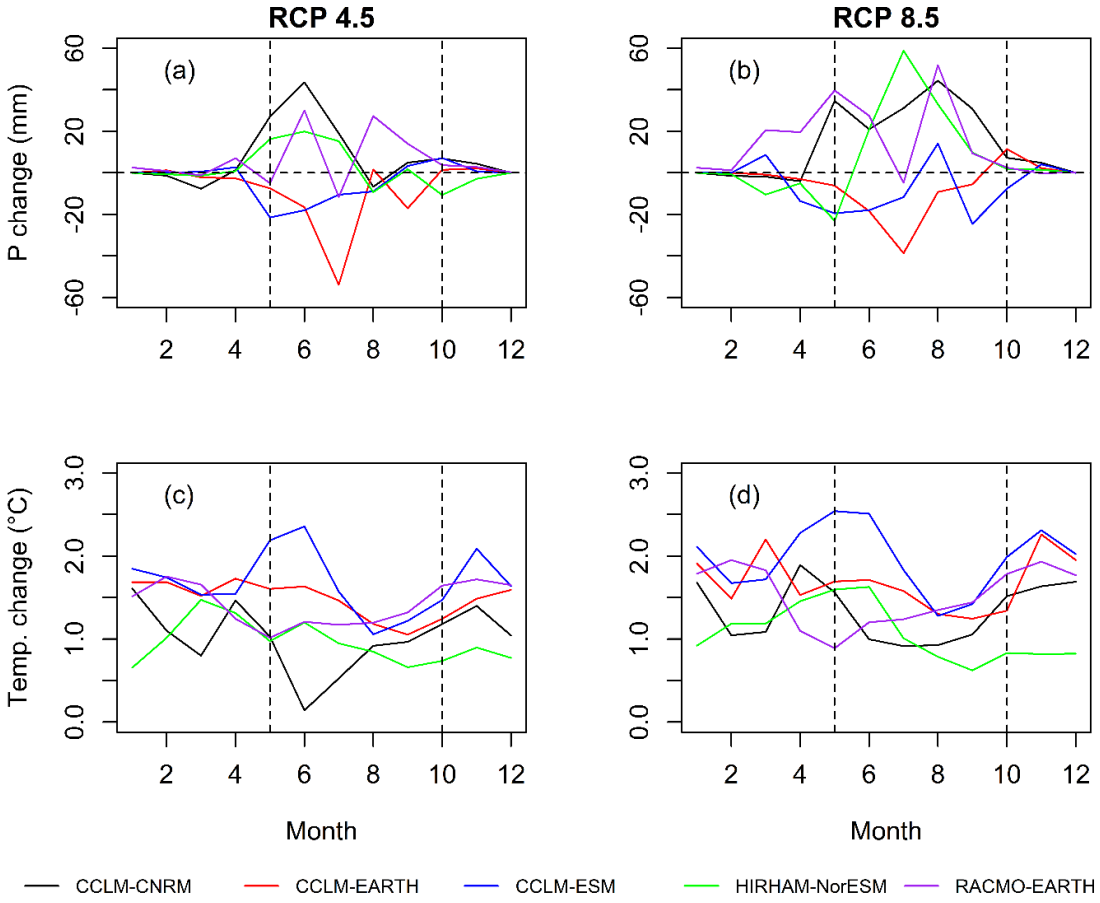

Fig. 7-8. Monthly change of precipitation (a) and (b) and air temperature (c) and (d) for five RCM-GCMs (CCLM-CNRM; CCLM-EARTH; CCLM-ESM; HIRHAM-NorESM; RACMO-EARTH). The predicted period (2021-2050) for each representative concentration pathway (RCP 4.5 and RCP 8.5) was compared to reference period (1971-2000). P: precipitation, Temp.: air temperature at 2 m height, vertical dashed lines mark the beginning and the end of rainy season.

Fig. 7-8-a and Fig. 7-8-b suggest that the peak rainfall changes occur in June under RCP 4.5 for CCLM-CNRM, HIRHAM-NorESM, and RACMO-EARTH whereas the peaks are expected two months later (in August) under RCP 8.5 for CCLM-CNRM and RACMO-EARTH. The peak magnitude of rainfall change increases from RCP 4.5 to RCP 8.5 for CCLM-CNRM, HIRHAM-NorESM, and RACMO-EARTH (positive precipitation signal models) decreases from RCP 4.5 to RCP 8.5 for CCLM-EARTH (negative precipitation signal model).

The simulated monthly change in total runoff is depicted by Fig. 7-9-a1 to Fig. 7-9-a4. Like rainfall, the extreme changes of total runoff under RCP 8.5 forcing are delayed compared to RCP 4.5 forcing. For instance, the extreme changes of total

discharge are expected in July under RCP 4.5 forcing whereas they are expected in August under RCP 8.5 for CCLM-CNRM, HIRHAM-NorESM, and CCLM-EARTH. A similar prediction is obtained for surface runoff (Fig. 7-9-b1 to b4) and interflow (Fig. 7-9-c1 to c4). Yet, base flow peak changes are projected to occur in August irrespective of greenhouse gas forcing.

For ETa, no general trend seems to be observed in terms of the time of occurrence of the peaks for the first scenario (Fig. 7-9-e1 and Fig. 7-9-e2). However, under the second scenario (Fig. 7-9-e3 and Fig. 7-9-e4), ETa change appears to increase gradually during the rainy season from June to October.

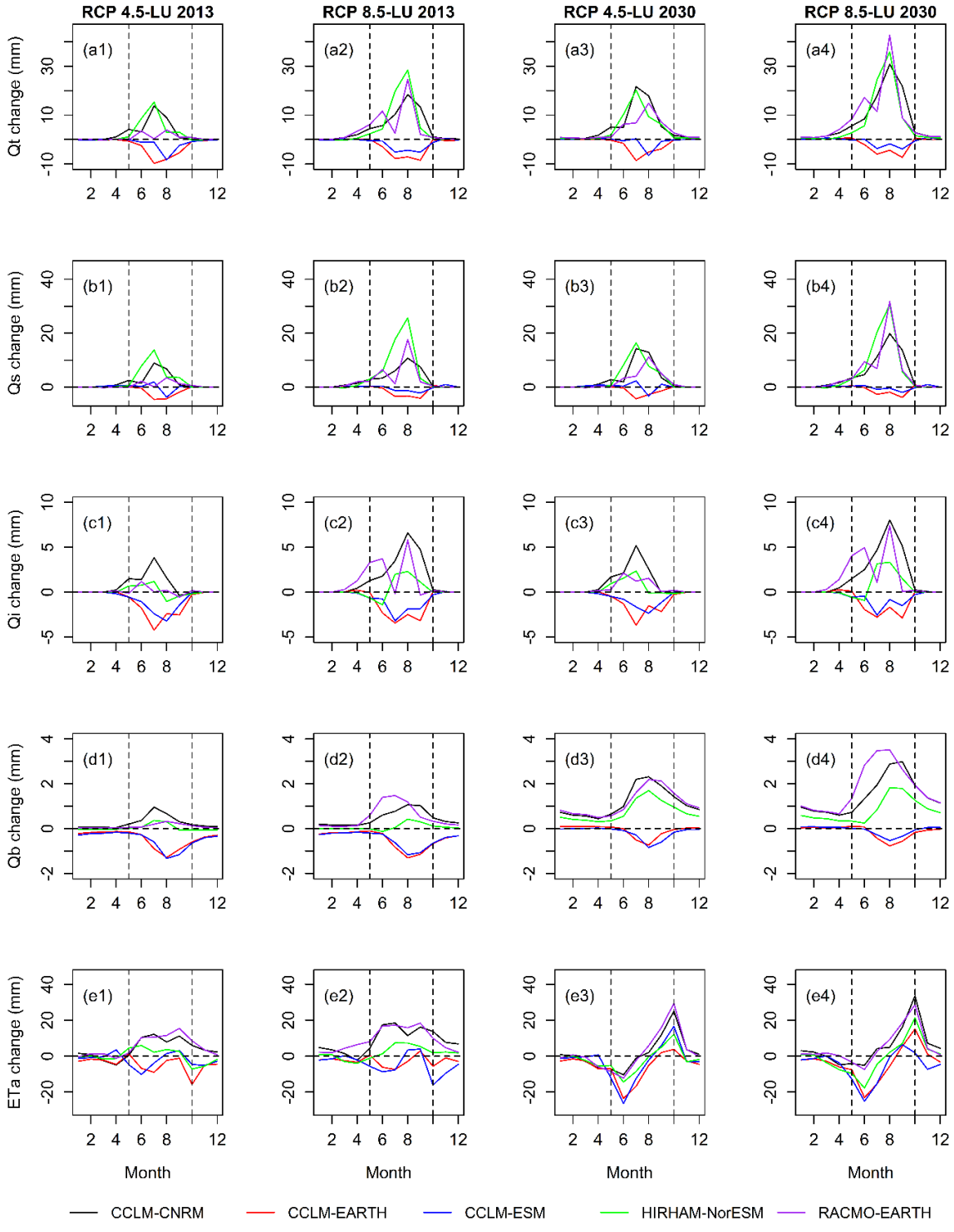

Fig. 7-9. Monthly change of predicted (2021-2050) total runoff (Qt), surface runoff (Qs), interflow (Qi), base flow (Qb), and actual evapotranspiration (ETa) compared to reference period (1971-2000). RCP: representative concentration pathway; LU: land use. The vertical dashed lines show the beginning and the end of rainy season.

7.3.6 Implications of the future uncertainty for adaptation strategies

In order to develop water management strategies to support decision making, the output of the hydrological impact assessment is frequently utilized as an input to water management models. The uncertainty in the future hydrology exacerbates the already difficult water resource management in the region.

The projected increase of annual rainfall will not be harmful for agriculture if the increase in rainfall is not characterized by increase in rainfall intensity and the rainfall is evenly distributed in time. In this case, increasing reservoir storage can help to achieve food security for the growing population in the region. However, problems might arise if the increase in rainfall is characterized by an increase in rainfall intensity and the reduction in rainy days. In this case, there will be an increase in soil erosion with soil fertility loss. Furthermore, farmers might not be able to grow current crops because of too short rainy seasons. In this scenario, it is crucial to develop and implement techniques for mitigating erosion processes including e.g. stone belts and afforestation. As for the shortening of the rainy seasons, development and application of short-term crop species would be needed. Evidence from previous studies showed a shift of the onset of the rainy season. Systems of seasonal forecasts and information propagation need to be improved and accessible to farmers before the onset of the rainy season (Waongo, 2015).

A decrease in annual rainfall can be characterized by frequent long dry spells (see Fig. 7-6). In this case, a substantial increase in surface and subsurface storage will be essential to supplement water deficits. The water storage development would have to take into account the downstream water needs including ecosystem needs. Moreover, techniques for decreasing evaporation and increasing the soil water holding capacity (WHC) (Descroix et al., 2018) will be necessary. The situation can be aggravated if the decrease in rainfall is associated with an increase in rainfall intensity and decrease in rainy days. In this case, adaptation strategies will need to address not only the unavailability of water but also soil erosion. Although there has been failure in the management of some inland valleys in the area (Yacouba et al., 2018), inland valleys can be still utilized as a mitigation option for smallholder farmers as their valley bottoms are relatively wetter than the uplands. However, the management of inland valleys needs to be improved in order to fully benefit from their water availability potential. In the worst case scenario, water exchange between regions would have to be envisaged. For instance, some water from the Congo River basin could be channelized to regions which experience more atrocious droughts. The Congo River is the second largest river in the world in terms of the discharge with a mean monthly discharge of 24,700 to 75,500 m s^{-1} from 1903 to 1996 (Coynel et al., 2005). It is important to note that water transfer

between regions is not only costly but also might be associated with negative ecological impacts.

All these propositions are mainly curative approaches of dealing with climate change impacts. It is certainty better if preventive mitigation strategies can also be put in place such as decelerating global warming by reducing greenhouse gas emissions. It is also vital to protect and/or restore ecosystems including rivers, lakes, oceans, and forests that we crucially depend on. These ecosystems sequestrate a significant amount of carbon and therefore contribute to the stability of the climate systems (Baldocchi and Penuelas, 2019; Hessen et al., 2004; Lal, 2004).

7.4 Conclusion

Hydrological impacts of climate and land use change were investigated at a local scale in the Dano catchment using five RCM-GCMs under RCP 4.5 and RCP 8.5 greenhouse gas forcings. After calibration and validation of WaSiM, bias corrected simulated daily rainfall and temperature were applied to force the hydrological model for the reference period (1971-2000) and the future period (2021-2050).

The calibration (2014-2015) and validation (2016) of WaSiM show good agreement in terms of hydrographs and objective functions between the observed and the simulated discharge. KGE equals to approximately 0.7, NSE > 0.5 and Pbias ranges between 21% and 24%.

The sensitivity of the hydrological model to land use change was investigated using four historical LULC from 1990 to 2013 and three predicted future LULC from 2019 to 2030. The results show an increase of runoff with time as the conversion of the savanna to croplands occurs.

The impact of climate change on streamflow was assessed by comparing the predicted period with the reference period. The results suggest a large spread for the future change of runoff in response to the non-agreement between the RCM-GCM simulations. Three models project an increase of the total runoff from +12% to +95% and ETa from 0 to 12% whereas two models predict a decrease of total runoff from -44% to -24% and ETa from -3% to -6%. Surface runoff is projected to record the highest relative change compared to the other runoff components.

The combined climate and land use change was estimated using LULC-2013 in the reference period and the LULC-2030 as future land use. The results indicate that land use change exacerbates the increase of total runoff (+52% to +158% compared to reference period) predicted by three RCM-GCMs, and reduces the decrease of total runoff (-29% to -11% compared to reference period) predicted by the other two models.

By comparing the two scenarios it can be concluded that the contribution of land use change impact on hydrology is not negligible and varies significantly with the climate model (27% to 78% of the combined climate and land use change).

The spread of the future predictions does not lead to one direction to follow for the development of climate adaptation strategies. However, the selected model ensemble allows to explore both directions of change (increase or decrease of water resource). Given the uncertainty of the future projections and the adverse impacts that might rise from the implementation of some adaptation strategies, it is clearly better to opt for preventive measures.

The results of this study can be used as input to water management models in order to derive strategies to cope with present and future water scarcities for smallholder farming in the investigated area.

8 OVERALL CONCLUSION

This study ultimately aims at supporting strategies for efficient management of water resources at local scale for smallholder farming systems. Hence, improving the adaptation capacities of smallholder farmers to cope with climate variabilities, reduce poverty, attain food security, and preserve ecosystems.

To achieve these goals, an intensive instrumentation has been undertaken and operationalized due to the lack of in situ observation systems. The data include climate parameters, stream flow, soil water, and shallow and deep groundwater. A slug test, a geo-electrical resistivity survey, and the groundwater use in agriculture were investigated. These data were completed by soil, LULC, historical, and modeled future climate data.

The hydrological processes were described using fundamental hydrological methods and a physically-based and spatially distributed hydrological model (WaSiM).

An ensemble of five RCMs, which were forced under RCP 4.5 and RCP 8.5 scenarios, four historical LULC, and three predicted LULC data set were utilized to assess the impact of climate change and LULCC on water resources.

The conclusion of each of these studies were presented in detail in the conclusion of chapter 5, 6, and 7. The following lines summarize these conclusions with regard to the research questions presented in chapter 1.

1) To what extent can an intensive instrumentation combined with fundamental hydrological methods effectively improve the understanding of hydrological processes in four inland valley catchments?

The instrumentation helped to achieve high temporal and spatial resolution of time series data which includes discharge, meteorological, piezometric, and soil moisture data for three consecutive years (2014 to 2016). The field surveys provided the required spatially distributed data for physically-based and spatially distributed modeling.

The observed hydrographs and flow duration curves of the observed runoff data show headwater sub-catchments that are fast flowing with reduced total runoff due to a limited contribution of base flow, whereas in the downstream sub-catchments, flows are sustained by base flow and consequently yield in higher annual total runoff coefficients. The decomposition of the total runoff into runoff components using water electrical conductivity and hydrographs shows that interflow is the major contributor of the runoff.

The groundwater table remains shallower than 1.5 m throughout the year. A permanent groundwater availability is observed at the valley bottoms of inland valleys

whereas ephemeral availability is observed in uplands. A further investigation of the shallow groundwater productivity is needed in order to fully assess its potential to support climate change adaptation strategies for small scale farmers in Dano.

2) How can a physically-based and a spatially distributed hydrological model be applied in a data limited environment to improve the understanding of hydrological processes in an inland valley catchment?

WaSiM has been calibrated for two years (2014 to 2015) and validated in 2016 using multi-criteria approach (the coefficient of determination, R^2; the Nash-Sutcliffe efficiency, NSE; the Kling-Gupta efficiency, KGE; and the percent bias, Pbias) were applied for model performance evaluation. The Bankandi-Loffing catchment was considered for this experiment.

The four applied objective functions (R^2, NSE, KGE, and Pbias) suggest, that WaSiM performed well in modeling the discharge of a small scale rural inland valley catchment (Bankandi-Loffing). The R^2 ranges from 0.47 to 0.95, NSE from 0.40 to 0.95, and KGE from 0.57 to 0.84. The soil moisture and groundwater table depth were also modeled well and the initial soil moisture conditions were adequately reproduced by the model. The numerical performance for soil moisture modeling is 0.70 for R^2 and NSE and 0.80 for KGE. As for the groundwater table modeling, the results are 0.30, 0.20, and 0.5 for R^2, NSE, and KGE, respectively.

The analysis of the water balance indicates that evapotranspiration is quantitatively the most important hydrological process in the area and the physical evaporation largely dominates evapotranspiration. Moreover, 14% of annual rainfall run out of the catchment as total runoff without being used.

Interflow dominates runoff in the headwater sub-catchment whereas base flow is the major runoff component in the downstream containing the inland valley bottoms. Surface flow will presumably increase, leading to an increase of soil erosion due to the trend of conversion of savanna into croplands as a result of population growth. Consequently, adaptation strategies should be planned accordingly. Supplementing the current erosion technique (stone-belt) with agroforestry and/or mulching might be considered.

3) How will be the performance of WaSiM if the resulting parameter set from calibration and validation of a catchment is applied without recalibration to another catchment in the study area?

The transfer of parameters from the Bankandi-Loffing WaSiM model to Mebar shows good results. The simulated discharge matches well the observed discharge. The

model score 0.93, 0.92, and 0.84 for R^2, NSE, and KGE, respectively in the year 2014 to 2015 and R^2: 0.65, NSE: 0.64, and KGE: 0.59 in the year 2016. However, considering that this investigation occurred for the same time period in the same climate zone (Sudan Sahelian climate zone) and the short duration of the study (three years), the robustness of the model should be tested for a longer period in different climate and catchment conditions.

4) What is the impact of climate change and LULCC on water resources in an inland valley catchment? What are the implications of climate change on adaptation strategies?

The sensitivity of the hydrological model to LULCC was investigated using four historical LULC maps from 1990 to 2013 and three predicted future LULC maps from 2019 to 2030. The results show an increase of surface runoff (overland flow) with time as the conversion of the savanna to croplands occurs.

The impact of climate change on streamflow was assessed by comparing the predicted period with the reference period. The results suggest a large uncertainty for the future changes of runoff in response to the large uncertainty in the RCMs' simulations. Three models project an increase of the total runoff from +12% to +95% and the actual evapotranspiration from 0 to 12% whereas two models predict a decrease of total runoff from -44% to -24% and the actual evapotranspiration from -3 to -6%. Surface runoff is projected to record the highest relative change compared to the other runoff components (interflow and base flow).

The combination of climate change and LULCC uses LULC-2013 in the reference period and LULC-2030 for the future. The results indicate that LULCC exacerbates the increase of total runoff (increase range: +52% to +158% compared to the reference period) predicted by three RCMs, and reduces the decrease of total runoff (decrease range: -29% to -11% compared to the reference period) predicted by the other two models. This may lead to adverse impact on the ecosystems of the area, soil erosion, and water scarcity in the study area.

The uncertainty of the future predictions does not lead to one direction to follow for the development of climate adaptation strategies. However, the selected climate model ensemble allows exploring both directions of change (increase or decrease of water resources).

Given the uncertainty of the future projections and the adverse impacts that might arise for the implementation of adaptation strategies, it is clearly more preferable to opt for preventive measures structured in adaptive management approach.

9 REFERENCES

Abe, S.S., Buri, M.M., Issaka, R.N., Kiepe, P., Wakatsuki, T., 2010. Soil fertility potential for rice production in West African lowlands. Japan Agric. Res. Q. 44, 343–355. doi:10.6090/jarq.44.343

Addor, N., Rohrer, M., Furrer, R., Seibert, J., 2016. Propagation of biases in climate models from the synoptic to the regional scale: Implications for bias adjustment. J. Geophys. Res. 121, 2075–2089. doi:10.1002/2015JD024040

African Development Bank, 2019. West Africa Economic Outlook. Abidjan, Côte d'Ivoire; https://www.afdb.org/fileadmin/uploads/afdb/Documents/Publications/2019AEO/REO_2019_-_West_africa.pdf.

AGRA, - Alliance for Green Revolution in Africa, 2014. Africa agriculture status report 2016 - Progress towards Agricultural Transformation in Africa. Nairobi, Kenya. doi:10.1007/s10040-019-01977-2

Aich, V., Liersch, S., Vetter, T., Huang, S., Tecklenburg, J., Hoffmann, P., Koch, H., Fournet, S., Krysanova, V., Müller, E.N., Hattermann, F.F., 2014. Comparing impacts of climate change on streamflow in four large African river basins. Hydrol. Earth Syst. Sci. 18, 1305–1321. doi:10.5194/hess-18-1305-2014

Akpoti, K., Antiwi, O.E., Kabo-Bah, A.T., 2016. Impacts of Rainfall Variability , Land Use and Land Cover Change on Stream Flow of the Black Volta. Hydrology 2, 1–24. doi:10.3390/hydrology3030026

Ali, A., Lebel, T., 2009. The Sahelian standardized rainfall index revisited. Int. J. Climatol. 26, 1705–1714.

Allen, R.G., Pruitt, W.O., Wright, J.L., Howell, T.A., Ventura, F., Snyder, R., Itenfisu, D., Steduto, P., Berengena, J., Yrisarry, J.B., Smith, M., Pereira, L.S., Raes, D., Perrier, A., Alves, I., Walter, I., Elliott, R., 2006. A recommendation on standardized surface resistance for hourly calculation of reference ETo by the FAO56 Penman-Monteith method. Agric. Water Manag. 81, 1–22. doi:10.1016/j.agwat.2005.03.007

Alves, I., Pereira, S.L., 2000. Modelling surface resistance from climatic variables? Agric. Water Manag. 42, 371–385. doi:10.1016/S0378-3774(99)00041-4

Amanor, K.S., 2012. Global resource grabs , agribusiness concentration and the smallholder : two West African case studies. J. Peasant Stud. 39, 731–749. doi:10.1080/03066150.2012.676543

Amanor, K.S., 2009. Global Food Chains , African Smallholders and World Bank Governance. J. Agrar. Chang. 9, 247–262.

Andersen, J., Refsgaard, J.C., Jensen, K.H., 2001. Distributed hydrological modelling of the Senegal River Basin — model construction and validation. J. Hydrol. 247, 200–214. doi:10.1016/S0022-1694(01)00384-5

Andriesse, W., Fresco, L.O., Van Duivenbooden, N., Windmeijer, P.N., 1994. Multi-scale characterization of inland valley agro-ecosystems in West Africa. Netherlands J. Agric. Sci. 42, 159–179.

Arnold, J.G., Srinivasan, R., Muttiah, R.S., Williams, J.R., 1998. Large area hydrologic modeling and assessment; Part I: Model development. J. Am. Water Resour. Assoc. 34, 73–89. doi:10.1111/j.1752-1688.1998.tb05961.x

Ashtech, 2011. ProMark ™ Field Software: Getting started guide [WWW Document].

URL https://ashgps.com/mirror/master/ProMark 100-200/Manuals/PMF_GSG_C_en.pdf (accessed 9.12.18).

Assouline, S., Or, D., 2014. The concept of field capacity revisited: Defining intrinsic static and dynamic criteria for soil internal drainage dynamics. Water Resour. Res. 50, 4787–4802. doi:10.1002/2014WR015475

Baldocchi, D., Penuelas, J., 2019. The physics and ecology of mining carbon dioxide from the atmosphere by ecosystems. Glob. Chang. Biol. 25, 1191–1197. doi:10.1111/gcb.14559

Barron, J., Rockström, J., Gichuki, F., Hatibu, N., 2003. Dry spell analysis and maize yields for two semi-arid locations in East Africa. Agric. For. Meteorol. 117, 23–37. doi:10.1016/S0168-1923(03)00037-6

Beck, H.E., Bruijnzeel, L.A., M. Van Dijk, A.I.J., McVicar, T.R., Scatena, F.N., Schellekens, J., 2013. The impact of forest regeneration on streamflow in 12 mesoscale humid tropical catchments. Hydrol. Earth Syst. Sci. 17, 2613–2635. doi:10.5194/hess-17-2613-2013

Beguería, S., Vicente-Serrano, S.M., Reig, F., Latorre, B., 2014. Standardized precipitation evapotranspiration index (SPEI) revisited: Parameter fitting, evapotranspiration models, tools, datasets and drought monitoring. Int. J. Climatol. 34, 3001–3023. doi:10.1002/joc.3887

Benesty, J., Chen, J., Huang, Y., Cohen, I., 2009. Pearson Correlation Coefficient, in: Noise Reduction in Speech Processing. Springer Berlin Heidelberg, Berlin, Heidelberg, pp. 1–4. doi:10.1007/978-3-642-00296-0_5

Beven, K., 2006. A manifesto for the equifinality thesis. J. Hydrol. 320, 18–36. doi:10.1016/j.jhydrol.2005.07.007

Beven, K., 1989. Interflow, in: Unsaturated Flow in Hydrologic Modeling Theory and Practice. Kluwer Academic Publishers, Dordrecht / Boston / London, pp. 191–219.

Beven, K., 1979. A sensitivity analysis of the Penman-Monteith actual evapotranspiration estimates 44, 179–190. doi:https://doi.org/10.1016/0022-1694(79)90130-6

Beven, K., Freer, J., 2001. Equifinality, data assimilation, and uncertainty estimation in mechanistic modelling of complex environmental systems using the GLUE methodology. J. Hydrol. 249, 11–29. doi:10.1016/S0022-1694(01)00421-8

Birgand, F., Lellouche, G., Appelboom, T.W., 2013. Measuring flow in non-ideal conditions for short-term projects: Uncertainties associated with the use of stage-discharge rating curves. J. Hydrol. 503, 186–195. doi:10.1016/j.jhydrol.2013.09.007

Block, P.J., Souza Filho, F.A., Sun, L., Kwon, H.H., 2009. A streamflow forecasting framework using multiple climate and hydrological models. J. Am. Water Resour. Assoc. 45, 828–843. doi:10.1111/j.1752-1688.2009.00327.x

Blume, H.-P., Brümmer, G.W., Fleige, H., Horn, R., Kandeler, E., Kögel-Knabner, I., Kretzschmar, R., Stahr, K., Wilke, B.-M., 2016. Soil-plant relations, in: Soil Science. Springer Berlin Heidelberg, Berlin, pp. 409–484. doi:https://doi.org/10.1007/978-3-642-30942-7_9

Bormann, H., Breuer, L., Gräff, T., Huisman, J.A., Croke, B., 2009. Assessing the impact of land use change on hydrology by ensemble modelling (LUCHEM) IV: Model sensitivity to data aggregation and spatial (re-)distribution. Adv. Water Resour. 32,

171–192. doi:10.1016/j.advwatres.2008.01.002

Bossa, A.Y., Diekkrüger, B., Agbossou, E.K., 2014. Scenario-based impacts of land use and climate change on land and water degradation from the meso to regional scale. Water (Switzerland) 6, 3152–3181. doi:10.3390/w6103152

Bouwer, H., 1989. The Bouwer and Rice Slug Test — An Update. Ground Water 27, 304–309. doi:10.1111/j.1745-6584.1989.tb00453.x

Bouwer, H., Rice, R.C., 1976. A slug test for determining hydraulic conductivity of unconfined aquifers with completely or partially penetrating wells. Water Resour. Res. 12, 423–428. doi:https://doi.org/10.1029/WR012i003p00423

Brakensiek, D.L., Rawls, W.J., 1994. Soil containing rock fragments: effects on infiltration. Catena 23, 99–110. doi:10.1016/0341-8162(94)90056-6

Braman, L.M., van Aalst, M.K., Mason, S.J., Suarez, P., Ait-Chellouche, Y., Tall, A., 2013. Climate forecasts in disaster management: Red Cross flood operations in West Africa, 2008. Disasters 37, 144–164. doi:10.1111/j.1467-7717.2012.01297.x

Braun, M., Caya, D., Frigon, A., Slivitzky, M., 2012. Internal variability of the Canadian RCM's hydrological variables at the basin scale in Quebec and Labrador. J. Hydrometeorol. 13, 443–462. doi:10.1175/JHM-D-11-051.1

Bronstert, A., 2001. Quantifizierung des Einflussess der Landnutzung und-bedeckung auf den Hochwasserabfluss in Flussgebieten. Postdam-Institut Klimafolgenforschung e.V; Postsdam, Germany. doi:10.1017/CBO9781107415324.004

Brutsaert, W., 1982. Evaporation to the atmosphere, 1st ed. Kluwer Academic Publishers, Dordrecht / Boston / London. doi:10.1007/978-94-017-1497-6

Buttle, J.M., Boon, S., Peters, D.L., Spence, C., (Ilja) van Meerveld, H.J., Whitfield, P.H., 2012. An Overview of Temporary Stream Hydrology in Canada. Can. Water Resour. J. 37, 279–310. doi:10.4296/cwrj2011-903

Cai, J., Liu, Y., Lei, T., Pereira, L.S., 2007. Estimating reference evapotranspiration with the FAO Penman-Monteith equation using daily weather forecast messages. Agric. For. Meteorol. 145, 22–35. doi:10.1016/j.agrformet.2007.04.012

Carsky, R.J., Walker, P., Hauser, S., Dashiell, K., Dixon, A.G.O., 1993. Response of selected crop associations to groundwater table depth in an inland valley. F. Crop. Res. 34, 1–13. doi:10.1016/0378-4290(93)90106-W

Chaix, J.-F., Henault, J.-M., Garnier, V., 2018. Quality, Uncertainties and Variabilities, in: Balayssac, J.-P., Garnier, V. (Eds.), Non-Destructive Testing and Evaluation of Civil Engineering Structures. Elsevier, pp. 199–229. doi:10.1016/B978-1-78548-229-8.50006-6

Chan, J.C.W., Chan, K.P., Yeh, A.G.O., 2001. Detecting the nature of change in an urban environment: A comparison of machine learning algorithms. Photogramm. Eng. Remote Sensing 67, 213–225.

Chapman, T., 1999. A comparison of algorithms for streamflow recession and baseflow separation. Hydrol. Process. 13, 701–714. doi:10.1002/(SICI)1099-1085(19990415)13:5<701::AID-HYP774>3.0.CO;2-2

Charles-Dominique, T., Mangenet, T., Rey, H., Jourdan, C., Edelin, C., 2009. Architectural analysis of root system of sexually vs. vegetatively propagated yam (Dioscorea rotundata Poir.), a tuber monocot. Plant Soil 317, 61–77. doi:10.1007/s11104-008-9788-9

Chawla, I., Mujumdar, P.P., 2015. Isolating the impacts of land use and climate change on streamflow. Hydrol. Earth Syst. Sci. 19, 3633–3651. doi:10.5194/hess-19-3633-2015

Chegwidden, O.S., Nijssen, B., Rupp, D.E., Arnold, J.R., Clark, M.P., Hamman, J.J., Kao, S.C., Mao, Y., Mizukami, N., Mote, P.W., Pan, M., Pytlak, E., Xiao, M., 2019. How Do Modeling Decisions Affect the Spread Among Hydrologic Climate Change Projections? Exploring a Large Ensemble of Simulations Across a Diversity of Hydroclimates. Earth's Futur. 7, 623–637. doi:10.1029/2018EF001047

Chen, J., Brissette, F.P., Zhang, X.J., Chen, H., Guo, S., Zhao, Y., 2019. Bias correcting climate model multi-member ensembles to assess climate change impacts on hydrology. Clim. Change 153, 361–377. doi:10.1007/s10584-019-02393-x

Chiew, F.H.S., Kamaladasa, N.N., Malano, H.M., McMahon, T.A., 1995. Penman-Monteih, FAO-24 refernce crop evapotranspiration and clas-A pan data in Australia. Agric. Water Manag. 28, 9–21.

CILSS, (Comité Inter-état de Lutte contre la Sécheresse dans le Sahel), 2016. Landscapes of West Africa: A window on a changing world. United States Geological Survey, U.S Geological Survey EROS, 47914252nd St, Garretson, SD 57030, United States.

Clark Labs, 2016. Land Change Modeller (LCM), in: Eastman, J.R. (Ed.), TerrSet . Geospatial Monitoring System. Clark University, Worcester, MA, USA, pp. 206–219.

Codjoe, S.N.A., 2004. Poulation and Land Use /Cover Dynamics in the Volta river basin of Ghana, 1960-2010. Ecology and Development Series N° 15, Center for Development Research (ZEF), Bonn, Germany.

Colman, E.A., 1947. A laboratory procedure for determining the field capacity of soils. Soil Sci. 63, 277–284.

Commune de Dano, 2013. Plan Communal de Développement sectoriel Approvisionnement en Eau Potable et Assainissement de Dano. Dano, Burkina Faso.

Cong, Z., Lü, H., Ni, G., 2014. A simplified dynamic method for field capacity estimation and its parameter analysis. Water Sci. Eng. 7, 351–362. doi:10.3882/j.issn.1674-2370.2014.04.001

Congalton, R.G., 1991. A review of assessing the accuracy of classifications of remotely sensed data. Remote Sens. Environ. 37, 35–46. doi:10.1016/0034-4257(91)90048-B

Cook, K.H., Vizy, E.K., 2006. Coupled model simulations of the West African monsoon system: Twentieth- and twenty-first-century simulations. J. Clim. 19, 3681–3703. doi:10.1175/JCLI3814.1

Cornelissen, T., Diekkrüger, B., Giertz, S., 2013. A comparison of hydrological models for assessing the impact of land use and climate change on discharge in a tropical catchment. J. Hydrol. 498, 221–236. doi:10.1016/j.jhydrol.2013.06.016

Cornelissen, T.D., 2016. 3D-Modeling of unsaturated flow dynamics and patterns: Potentials and limitations at different spatial and temporal scales. (PhD Thesis) University of Bonn, Germany, http://hss.ulb.uni-bonn.de/2016/4396/4396.htm.

Cornforth, R., 2011. Overview of the West African. Weather 67, 59–65.

Cosandey, C., Robinson, M., 2007. Hydrologie continentale. Armand Colin, Paris.

Cosby, B.J., Hornberger, G.M., Clapp, R.B., Ginn, T.R., 1984. A statical exploration of the

relationships of soil moisture characteristics to the physical properties of soils. Water Resour. Res. 20, 682–690.

Coulombe, H., Savadogo, K., Sawadogo, H., Yameogo, A.E., Kone, M., Bonkoungou, M., Sinare, K., Simonpietri, A., Menye, E., Fofack, H., 2000. Profil et évolution de la pauvrété au Burkina Faso. Institut National de la Statistique et de la Démographie (INSD), Ouagadougou.

Coynel, A., Seyler, P., Etcheber, H., Meybeck, M., Orange, D., 2005. Spatial and seasonal dynamics of total suspended sediment and organic carbon species in the Congo River. Global Biogeochem. Cycles 19, 1–17. doi:10.1029/2004GB002335

Croker, K.M., Young, A.R., Zaidman, M.D., Rees, H.G., 2003. Flow duration curve estimation in ephemeral catchments in Portugal. Hydrol. Sci. J. 48, 427–439. doi:10.1623/hysj.48.3.427.45287

Danvi, A., Giertz, S., Zwart, S.J., Diekkrüger, B., 2017. Comparing water quantity and quality in three inland valley watersheds with different levels of agricultural development in central Benin. Agric. Water Manag. 192, 257–270. doi:10.1016/j.agwat.2017.07.017

Darcy, H., 1856. Les Fontaines publiques de la ville de Dijon. Dalmont, Paris.

Delta-T Devices Ltd, 1999. ThetaProbe: Soil moisture sensor, User manual ML2x-UM-1.21 [WWW Document]. URL https://www.upgmbh.com/fileadmin/produkte/support/ML2x_Theta_ProbeUserManual_v1.21.pdf (accessed 2.16.18).

Denis, S., Gapia, M., Pokam, W., Losembe, F., Mfochivé, O., 2012. The link between forest, water and people: an agenda to promote in the context of climate change in Central Africa, in: Bojang, F., Ndeso-Atanga, A. (Eds.), Nature and Faune: Managing Africa´s Water Resources: Integrating Sustainable Use of Land, Forest and Fisheries. FAO, Accra, Ghana, pp. 48–51. doi:http://www.fao.org/africa/publications/nature-and-faune-magazine/

Déqué, M., Calmanti, S., Christensen, O.B., Dell Aquila, A., Maule, C.F., Haensler, A., Nikulin, G., Teichmann, C., 2017. A multi-model climate response over tropical Africa at +2 °C. Clim. Serv. 7, 87–95. doi:10.1016/j.cliser.2016.06.002

Déqué, M., Rowell, D.P., Lüthi, D., Giorgi, F., Christensen, J.H., Rockel, B., Jacob, D., Kjellström, E., De Castro, M., Van Den Hurk, B., 2007. An intercomparison of regional climate simulations for Europe: Assessing uncertainties in model projections. Clim. Change 81, 53–70. doi:10.1007/s10584-006-9228-x

Descroix, L., Guichard, F., Grippa, M., Lambert, L.A., Panthou, G., Mahé, G., Gal, L., Dardel, C., Quantin, G., Kergoat, L., Bouaïta, Y., Hiernaux, P., Théo, V., Pellarin, T., Faty, B., Wilcox, C., Malam Abdou, M., Mamadou, I., Vandervaere, J., Diongue-Niang, A., Ndiaye, O., Sane, Y., Dacosta, H., Goset, M., Cassé, C., Sultan, B., Barry, Aliou, Amogu, O., Nka Nnomo, B., Barry, Alseny, Paturel, J.-E., 2018. Evolution of Surface Hydrology in the Sahelo-Sudanian Strip : An Updated Review. Water 10, 1–37. doi:10.3390/w10060748

Descroix, L., Mahé, G., Lebel, T., Favreau, G., Galle, S., Gautier, E., Olivry, J.-C., Albergel, J., Amogu, O., Cappelaere, B., 2009. Spatio-temporal variability of hydrological regimes around the boundaries between Sahelian and Sudanian areas of West Africa: A synthesis. J. Hydrol. 375, 90–102. doi:10.1016/j.jhydrol.2008.12.012

Devia, G.K., Ganasri, B.P., Dwarakish, G.S., 2015. A Review on Hydrological Models. Aquat. Procedia 4, 1001–1007. doi:10.1016/j.aqpro.2015.02.126

Di Baldassarre, G., Montanari, A., Lins, H., Koutsoyiannis, D., Brandimarte, L., Blschl, G., 2010. Flood fatalities in Africa: From diagnosis to mitigation. Geophys. Res. Lett. 37, 2–6. doi:10.1029/2010GL045467

Diedhiou, A., Bichet, A., Wartenburger, R., Seneviratne, S.I., Rowell, D.P., Sylla, M.B., Diallo, I., Todzo, S., Touré, N.E., Camara, M., Ngatchah, N.B., Kane, N.A., Tall, L., Affholder, F., 2018. Changes in climate extremes over West and Central Africa at 1.5°C and 2°C global warming. Environ. Res. Lett. 13, 1–11. doi:https://doi.org/10.1088/1748-9326/aac3e5

Dosio, A., Panitz, H.-J., Schubert-Frisius, M., Lüthi, D., 2015. Dynamical downscaling of CMIP5 global circulation models over CORDEX - Africa with COSMO - CLM : evaluation over the present climate and analysis of the added value. Clim. Dyn. 44, 2637–2661. doi:https://doi.org/10.1007/s00382-014-2262-x

Ebel, B.A., Loague, K., 2006. Physics-based hydrologic-response simulation: Seeing through the fog of equifinality. Hydrol. Process. 20, 2887–2900. doi:10.1002/hyp.6388

Eguavoen, I., McCartney, M., 2013. Water storage : a contribution to climate change adaptation in Africa. Rural 21 01/2013, 38–41.

Ehret, U., Zehe, E., Wulfmeyer, V., Warrach-Sagi, K., Liebert, J., 2012. HESS Opinions "should we apply bias correction to global and regional climate model data?" Hydrol. Earth Syst. Sci. 16, 3391–3404. doi:10.5194/hess-16-3391-2012

Ersahin, S., Gunal, H., Kutlu, T., Yetgin, B., Coban, S., 2006. Estimating specific surface area and cation exchange capacity in soils using fractal dimension of particle-size distribution. Geoderma 136, 588–597. doi:10.1016/j.geoderma.2006.04.014

European Commission, 2016. SIMLAB and other software [WWW Document]. EU Sci. HUB. URL https://ec.europa.eu/jrc/en/samo/simlab (accessed 11.9.19).

FAO, 2019. Cotton lint production in Burkina Faso (1990-2013) [WWW Document]. Food Agric. Organation United Nations. URL http://www.fao.org/faostat/en/#data/QC (accessed 9.11.19).

FAO, 2014. The FAO Statistical Yearbook 2014: Africa Food and Agriculture. Accra, Ghana.

Fass, T., 2004. Hydrogeologie im Aguima Einzugsgebiet in Benin / Westafrika. (PhD Thesis) University of Bonn, Germany, http://hss.ulb.uni-bonn.de.

Fazeli Farsani, I., Farzaneh, M.R., Besalatpour, A.A., Salehi, M.H., Faramarzi, M., 2019. Assessment of the impact of climate change on spatiotemporal variability of blue and green water resources under CMIP3 and CMIP5 models in a highly mountainous watershed. Theor. Appl. Climatol. 136, 169–184. doi:10.1007/s00704-018-2474-9

Feddes, R.A., Zaradny, H., 1978. Model for simulating soil-water content considering evapotranspiration - Comments. J. Hydrol. 37, 393–397.

Federer, C.A., Lash, D., 1983. BROOK: A hydrologic simulation model for eastern forests. Research Report 19. Durahm, Water Resource Research Center, University of New Hampshire.

Feng, D., Beighley, E., Raoufi, R., Melack, J., Zhao, Y., Iacobellis, S., Cayan, D., 2019.

Propagation of future climate conditions into hydrologic response from coastal southern California watersheds. Clim. Change 153, 199–218. doi:10.1007/s10584-019-02371-3

Ficklin, D.L., Luo, Y., Luedeling, E., Gatzke, S.E., Zhang, M., 2010. Sensitivity of agricultural runoff loads to rising levels of CO2 and climate change in the San Joaquin Valley watershed of California. Environ. Pollut. 158, 223–34. doi:10.1016/j.envpol.2009.07.016

Forkuor, G., 2014. Agricultural Land Use Mapping in West Africa Using Multi-sensor Satellite Imagery. (PhD thesis) Julius-Maximilians-Universität Würzburg, https://opus.bibliothek.uni-wuerzburg.de/opus4-wuerzburg/frontdoor/deliver/index/docId/10868/file/Thesis_Gerald_Forkuor_2014.pdf.

Forkuor, G., Thiel, M., 2013. Land Use and Land Cover Maps for Vea, Dano and Dassari.

Frappart, F., Hiernaux, P., Guichard, F., Mougin, E., Kergoat, L., Arjounin, M., Lavenu, F., Koité, M., Paturel, J.-E., Lebel, T., 2009. Rainfall regime across the Sahel band in the Gourma region, Mali. J. Hydrol. 375, 128–142. doi:10.1016/j.jhydrol.2009.03.007

Gavilán, P., Berengena, J., Allen, R.G., 2007. Measuring versus estimating net radiation and soil heat flux: Impact on Penman-Monteith reference ET estimates in semiarid regions. Agric. Water Manag. 89, 275–286. doi:10.1016/j.agwat.2007.01.014

Gbobaniyi, E., Sarr, A., Sylla, B., Diallo, I., Lennard, C., Dosio, A., Dhiédiou, A., Kamga, A., Klutse, N.A.B., Hewitson, B., Nikulin, G., Lamptey, B., 2014. Climatology , annual cycle and interannual variability of precipitation and temperature in CORDEX simulations over West Africa. Int. J. Climatol. 34, 2241–2257. doi:10.1002/joc.3834

Geotomo Software, 2010. RES2DINV ver. 3.59.

Giertz, S., Diekkrüger, B., Steup, G., 2006. Physically-based modelling of hydrological processes in a tropical headwater catchment in Benin (West Africa) – process representation and multi-criteria validation. Hydrol. Earth Syst. Sci. 3, 595–651. doi:10.5194/hessd-3-595-2006

Giertz, S., Junge, B., Diekkrüger, B., 2005. Assessing the effects of land use change on soil physical properties and hydrological processes in the sub-humid tropical environment of West Africa. Phys. Chem. Earth 30, 485–496. doi:10.1016/j.pce.2005.07.003

Giorgis, I., Bonetto, S., Giustetto, R., Lawane, A., Pantet, A., Rossetti, P., Thomassin, J.H., Vinai, R., 2014. The lateritic profile of Balkouin, Burkina Faso: Geochemistry, mineralogy and genesis. J. African Earth Sci. 90, 31–48. doi:10.1016/j.jafrearsci.2013.11.006

Gudmundsson, L., Bremnes, J.B., Haugen, J.E., Engen-Skaugen, T., 2012. Technical Note: Downscaling RCM precipitation to the station scale using statistical transformations – A comparison of methods. Hydrol. Earth Syst. Sci. 16, 3383–3390. doi:10.5194/hess-16-3383-2012

Gupta, H. V., Kling, H., Yilmaz, K.K., Martinez, G.F., 2009. Decomposition of the mean squared error and NSE performance criteria: Implications for improving hydrological modelling. J. Hydrol. 377, 80–91. doi:10.1016/j.jhydrol.2009.08.003

Gutiérrez, J.M., Maraun, D., Widmann, M., Huth, R., Hertig, E., Benestad, R., Roessler, O., Wibig, J., Wilcke, R., Kotlarski, S., San Martín, D., Herrera, S., Bedia, J.,

Casanueva, A., Manzanas, R., Iturbide, M., Vrac, M., Dubrovsky, M., Ribalaygua, J., Pórtoles, J., Räty, O., Räisänen, J., Hingray, B., Raynaud, D., Casado, M.J., Ramos, P., Zerenner, T., Turco, M., Bosshard, T., Štěpánek, P., Bartholy, J., Pongracz, R., Keller, D.E., Fischer, A.M., Cardoso, R.M., Soares, P.M.M., Czernecki, B., Pagé, C., 2019. An intercomparison of a large ensemble of statistical downscaling methods over Europe: Results from the VALUE perfect predictor cross-validation experiment. Int. J. Climatol. 39, 3750–3785. doi:10.1002/joc.5462

Habel, W.R., 2010. Non-Destructive Evaluation of Reinforced Concrete Structures: Volume 2: Non-destructive testing methods. Oxford, Cambridge, New Delhi. doi:10.1533/9781845699604.1.63

Haddeland, I., Heinke, J., Voß, F., Eisner, S., Chen, C., Hagemann, S., Ludwig, F., 2012. Effects of climate model radiation, humidity and wind estimates on hydrological simulations. Hydrol. Earth Syst. Sci. 16, 305–318. doi:10.5194/hess-16-305-2012

Hamon, W.R., 1963. Computation of direct runoff amounts from storm rainfall. Int. Assoc. Sci. Hydrol. 63, 52–62. doi:http://hydrologie.org/redbooks/a063/063006.pdf

Han, F., Cook, K.H., Vizy, E.K., 2019. Changes in intense rainfall events and dry periods across Africa in the twenty-first century. Clim. Dyn. 53, 2757–2777. doi:10.1007/s00382-019-04653-z

Hansen, F. V, 1993. Albedos. Army Research Laaboratory; Adelphi, Maryland, USA.

Harmel, R.D., Smith, P.K., Migliaccio, K.W., 2010. Modifying goodness-of-fit indicators to incorporate both measurement and model uncertainty in model calibration and validation. Am. Soc. Agric. Biol. Eng. 53, 55–63. doi:10.13031/2013.29502

Hayes, M., Svoboda, M., Whilhite, D.A., Vanyarkho, O. V., 1999. Monitoring the 1996 drought using the standardized precipitation index. Bull. Am. Meteorol. Soc. 80, 429–438.

Henry, G., Frost-Killian, S., Master, S., 2004. Africa geologically under exposed [WWW Document]. Min. Rev. Africa. URL https://web.archive.org/web/20081202133720/http://www.miningreview.com/archive/mra_2_2004/54_1.php (accessed 2.16.17).

Hessen, D.O., Agren, G.I., Anderson, T.R., Elser, J.J., de Ruiter, P.C., 2004. Carbon sequestration in ecosystems: the role of stoichiometry. Ecology 85, 1179–1192.

Hewlett, J.D., Hibbert, A.R., 1967. Factors affecting the response of small watershed to precipitation in humid areas, in: Sooper, W.E., Lull, H.W. (Eds.), Forest Hydrology. Pergamon, Oxford, pp. 275–279. doi:10.1177/0309133309338118

Hollinger, F., Staatz, J.M., 2015. Agricultural Growth in West Africa: Market and policy drivers. Food and Agriculture Organization and African Development Bank, Rome, Italy.

Hounkonnou, D., Kossou, D., Kuyper, T.W., Leeuwis, C., Nederlof, E.S., Röling, N., Sakyi-dawson, O., Traoré, M., Huis, A. Van, 2012. An innovation systems approach to institutional change : Smallholder development in West Africa. Agric. Syst. 108, 74–83. doi:10.1016/j.agsy.2012.01.007

Hounkpatin, K.O.L., Welp, G., Akponikpè, P.B.I., Rosendahl, I., Amelung, W., 2018. Carbon losses from prolonged arable cropping of Plinthosols in Southwest Burkina Faso. Soil Tillage Res. 175, 51–61. doi:10.1016/j.still.2017.08.014

Hounkpatin, O.K.L., 2017. Digital soil mapping using survey data and soil organic carbon dynamics in semi-arid Burkina Faso. (PhD Thesis) University of Bonn, Germany, http://hss.ulb.uni-bonn.de/2018/5058/5058.htm.

Houston, J., 1992. Rural water supplies: comparative case histories from Nigeria and Zimbabwe. Geol. Soc. 66, 243–257. doi:https://doi.org/10.1144/GSL.SP.1992.066.01.12

Hwang, H.T., Jeen, S.W., Suleiman, A.A., Lee, K.K., 2017. Comparison of saturated hydraulic conductivity estimated by three different methods. Water (Switzerland) 9, 1–15. doi:10.3390/w9120942

Ibrahim, B., Karambiri, H., Polcher, J., Yacouba, H., Ribstein, P., 2013a. Changes in rainfall regime over Burkina Faso under the climate change conditions simulated by 5 regional climate models. Clim. Dyn. 42, 1363–1381. doi:10.1007/s00382-013-1837-2

Ibrahim, B., Karambiri, H., Polcher, J., Yacouba, H., Ribstein, P., 2013b. Changes in rainfall regime over Burkina Faso under the climate change conditions simulated by 5 regional climate models. Clim. Dyn. 42, 1363–1381. doi:10.1007/s00382-013-1837-2

Idrissou, M., Ngom, D.F., Malou, R., Vayssade, B., Courbis, A.-L., 2015. Water balance simulation for resource evaluation at watershed scale: application to the Nema (Sudano-Sahelian zone, Senegal). Hydrol. Sci. J. 60, 1620–1630. doi:10.1080/02626667.2014.932055

INSD, 2014. Tableau de bord social du Burkina Faso, INSD. Institut National des Statistiques de la Démographie (INSD), Ouagadougou.

IPCC, 2014. Climate Change 2014: Impacts, Adaptation, and Vulnerability. Part B: Regional Aspects. Contribution of Working Group II to the Fifth Assessment Report of the Intergovernmental Panel on Climate Change. Cambridge University Press, Cambridge, United Kingdom and New York, NY, USA. doi:https://www.ipcc.ch/site/assets/uploads/2018/02/WGIIAR5-PartB_FINAL.pdf

IRIS-Instruments, 2016. Syscal Pro switch [WWW Document]. IRIS Instruments. URL http://www.iris-instruments.com/syscal-prosw.html (accessed 2.19.17).

ISO, 2007. ISO 748-Hydrometry - Measurement of liquid flow in opened chanels using current-meters of floats. Geneva.

ISO 1100-2, 2010. Hydrometry — Measurement of liquid flow in open channels — Part 2: Determination of the stage-discharge relationship, 3rd ed. Geneva, Switzerland.

IWACO, B. V., 1993. Carte hydrogeologique de Burkina Faso-Feuille Bobo-Dioulasso.

Jalloh, A., Nelson, G.C., Thomas, T.S., Zougmoré, R., Roy-macauley, H., 2013. West African Agriculture and Climate Change: A Comprehensive Analysis. International Food Policy Research Institute, Washington, DC. doi:http://dx.doi.org/10.2499/9780896292048 Library

Johnson, F., Sharma, A., 2015. What are the impacts of bias correction on future drought projections? J. Hydrol. 525, 472–485. doi:10.1016/j.jhydrol.2015.04.002

Kasei, R., Diekkrüger, B., Leemhuis, C., 2010. Drought frequency in the Volta Basin of West Africa. Sustain. Sci. 5, 89–97. doi:10.1007/s11625-009-0101-5

Kasei, R.A., 2010. Modelling Impacts of Climate Change on Water Resources in the Volta Basin, West Africa. (PhD thesis); University of Bonn, Germany; http://hss.ulb.uni-

bonn.de/2010/1977/1977a.pdf. doi:http://hss.ulb.uni-bonn.de/2010/1977/1977a.pdf

Kelley, J., n.d. Growth and Development, in: Grain Sorghum Production Handbook. Little Rock, Arkansas, USA; https://www.uaex.edu/publications/pdf/mp297/MP297.pdf, pp. 3–5.

Kendon, E.J., Stratton, R.A., Tucker, S., Marsham, J.H., Berthou, S., Rowell, D.P., Senior, C.A., 2019. Enhanced future changes in wet and dry extremes over Africa at convection-permitting scale. Nat. Commun. 10, 1–23. doi:10.1038/s41467-019-09776-9

Kiepe, P., 2006. characterization of three key environments for integrated irrigation-aquaculture and their local names, in: Halwart, M., van Dam, A.A. (Eds.), Integrated Irrigation and Aquaculture in West Africa: Concepts, Practicesand Potential. Rome, FAO 181pp., pp. 1–6.

Kim, J., Waliser, D.E., Mattmann, C.A., Goodale, C.E., Hart, A.F., Zimdars, P.A., Crichton, D.J., Jones, C., Nikulin, G., Hewitson, B., Jack, C., Lennard, C., Favre, A., 2014. Evaluation of the CORDEX-Africa multi-RCM hindcast: Systematic model errors. Clim. Dyn. 42, 1189–1202. doi:10.1007/s00382-013-1751-7

Kiniry, J.R., Simpson, C.E., Schubert, A.M., Reed, J.D., 2005. Peanut leaf area index, light interception, radiation use efficiency, and harvest index at three sites in Texas. F. Crop. Res. 91, 297–306. doi:10.1016/j.fcr.2004.07.021

Kirkham, M.B., 2014. Chapter 10 - Field Capacity, Wilting Point, Available Water, and the Nonlimiting Water Range, in: Kirkham, M.B. (Ed.), Principles of Soil and Plant Water Relations (Second Edition). Academic Press, Boston, pp. 153–170. doi:https://doi.org/10.1016/B978-0-12-420022-7.00010-0

Klein, C., Heinzeller, D., Bliefernicht, J., Kunstmann, H., 2015. Variability of West African monsoon patterns generated by a WRF multi-physics ensemble. Clim. Dyn. 45, 2733–2755. doi:10.1007/s00382-015-2505-5

Kling, H., Fuchs, M., Paulin, M., 2012. Runoff conditions in the upper Danube basin under an ensemble of climate change scenarios. J. Hydrol. 424–425, 264–277. doi:10.1016/j.jhydrol.2012.01.011

Koch, K., Wenniger, J., Uhlenbrook, S., Bonell, M., 2009. Joint interpretation of hydrological and geophysical data: Electrical resistivity tomography results from a process hydrological research site in the Black Forest Mountains, Germany Kristof. Hydrol. Process. 23, 1501–1513. doi:10.1002/hyp.7275

Kumar, R., Samaniego, L., Attinger, S., 2013. Implications of distributed hydrologic model parameterization on water fluxes at multiple scales and locations. Water Resour. Res. 49, 360–379. doi:10.1029/2012WR012195

Kundzewicz, Z.W., Kanae, S., Seneviratne, S.I., Handmer, J., Nicholls, N., Peduzzi, P., Mechler, R., Bouwer, L.M., Arnell, N., Mach, K., Muir-Wood, R., Brakenridge, G.R., Kron, W., Benito, G., Honda, Y., Takahashi, K., Sherstyukov, B., 2013. Flood risk and climate change: global and regional perspectives. Hydrol. Sci. J. 1–28. doi:10.1080/02626667.2013.857411

Lal, R., 2004. Soil carbon sequestration to mitigate climate change. Geoderma 123, 1–22. doi:10.1016/j.geoderma.2004.01.032

Laux, P., Kunstmann, H., Bardossy, A., 2008. Predicting the regional onset of the rainy

season in West Africa. Int. J. Climatol. 28, 329–342. doi:10.1002/joc.1542

Laux, P., Nguyen, P.N.B., Cullmann, J., Van, T.P., Kunstmann, H., 2017. How many RCM ensemble members provide confidence in the impact of land-use land cover change? Int. J. Climatol. 37, 2080–2100. doi:10.1002/joc.4836

Laux, P., Wagner, S., Wagner, A., Jacobeit, J., Bardossy, A., Kunstmann, H., 2009. Modelling daily precipitation features in the Volta Basin of West Africa. Int. J. Climatol. 29, 937–954. doi:10.1002/joc.1852

Le Barbé, L., Lebel, T., Tapsoba, D., 2002. Rainfall variability in West Africa during the years 1950-90. J. Clim. 15, 187–202. doi:10.1175/1520-0442(2002)015<0187:RVIWAD>2.0.CO;2

Lebel, T., Ali, A., 2009. Recent trends in the Central and Western Sahel rainfall regime (1990–2007). J. Hydrol. 375, 52–64. doi:10.1016/j.jhydrol.2008.11.030

Lebel, T., Cappelaere, B., Galle, S., Hanan, N., Kergoat, L., Levis, S., Vieux, B., Descroix, L., Gosset, M., Mougin, E., 2009. AMMA-CATCH studies in the Sahelian region of West-Africa: An overview. J. Hydrol. 375, 3–13. doi:10.1016/j.jhydrol.2009.03.020

Lecina, S., Martínez-Cob, A., Pérez, P.J., Villalobos, F.J., Baselga, J.J., 2003. Fixed versus variable bulk canopy resistance for reference evapotranspiration estimation using the Penman-Monteith equation under semiarid conditions. Agric. Water Manag. 60, 181–198. doi:10.1016/S0378-3774(02)00174-9

Leduc, C., Favreau, G., Schroeter, P., 2001. Long-term rise in a Sahelian water-table: the Continental Terminal in South-West Niger. J. Hydrol. 243, 43–54. doi:10.1016/S0022-1694(00)00403-0

Leemhuis, C., Erasmi, S., Twele, A., Kreilein, H., Oltchev, A., Gerold, G., 2007. Rainforest Conversion in Central Sulawesi, Indonesia: Recent Development and Consequences for River Discharge and Water Resources - An Integrated Remote Sensing and Hydrological Modelling Approach. Erdkunde 61, 284–293.

Leonard, J., Mietton, M., Najib, H., Gourbesville, P., 2000. Rating curve modelling with Manning's equation to manage instability and improve extrapolation. Hydrol. Sci. J. 45, 739–750. doi:10.1080/02626660009492374

Li, Z.L., Tang, R., Wan, Z., Bi, Y., Zhou, C., Tang, B., Yan, G., Zhang, X., 2009. A review of current methodologies for regional Evapotranspiration estimation from remotely sensed data. Sensors 9, 3801–3853. doi:10.3390/s90503801

Llasat, M.C., 2001. An objective classification of rainfall events on the basis of their convective features: Application to rainfall intensity in the Northeast of Spain. Int. J. Climatol. 21, 1385–1400. doi:10.1002/joc.692

Loke, M.H., 2001. Tutorial : 2-D and 3-D electrical imaging surveys [WWW Document]. Stanford Univ. URL https://pangea.stanford.edu/research/groups/sfmf/docs/DCResistivity_Notes.pdf (accessed 2.18.17).

Lu, J., Sun, G., McNulty, S.G., Amatya, D.M., 2005. a Comparison of Six Potential Evapotranspiration Methods for Regional Use in the Southeastern United States. J. Am. Water Resour. Assoc. 41, 621–633. doi:10.1111/j.1752-1688.2005.tb03759.x

Ma, L., He, C., Bian, H., Sheng, L., 2016. MIKE SHE modeling of ecohydrological processes: Merits, applications, and challenges. Ecol. Eng. 96, 137–149. doi:10.1016/j.ecoleng.2016.01.008

Mahé, G., 2009. Surface/groundwater interactions in the Bani and Nakambe rivers, tributaries of the Niger and Volta basins, West Africa. Hydrol. Sci. J. 54, 704–712. doi:10.1623/hysj.54.4.704

Mahé, G., Diello, P., Paturel, J., Barbier, B., Karambirir, H., Dezetter, A., Dieulin, C., Rouché, N., 2010. Baisse des pluies et augmentation des écoulements au Sahel : impact climatique et anthropique sur les écoulements du Nakambe au Burkina Faso. Secheresse 21, 1–6.

Mahé, G., Paturel, J., Servat, E., Conway, D., Dezetter, A., 2005. The impact of land use change on soil water holding capacity and river flow modelling in the Nakambe River, Burkina-Faso. J. Hydrol. 300, 33–43. doi:10.1016/j.jhydrol.2004.04.028

Maidment, R.I., Allan, R.P., Black, E., 2015. in precipitation over Africa. Geophys. Res. Lett. 42, 1–10. doi:10.1002/2015GL065765.Received

Maïga-Yaleu, B.S., 2014. Etude géochimique de l'eau de ruissellement du bassin versant de Tougou (bassin supérieur du Nakanbé) au Nord du Burkina Faso. Université de Ouagadougou.

Makate, C., Makate, M., Mango, N., 2017. Smallholder Farmers' Perceptions on Climate Change and the Use of Sustainable Agricultural Practices in the Chinyanja Triangle, Southern Africa. Soc. Sci. 1–14. doi:10.3390/socsci6010030

Maraun, D., 2016. Bias Correcting Climate Change Simulations - a Critical Review. Curr. Clim. Chang. Reports 2, 211–220. doi:10.1007/s40641-016-0050-x

Maraun, D., Shepherd, T.G., Widmann, M., Zappa, G., Walton, D., Gutiérrez, J.M., Hagemann, S., Richter, I., Soares, P.M.M., Hall, A., Mearns, L.O., 2017. Towards process-informed bias correction of climate change simulations. Nat. Clim. Chang. 7, 764–773. doi:10.1038/nclimate3418

Mckay, M.D., Beckman, R.J., Conover, W.J., 1979. A Comparison of Three Methods for Selecting Values of Input Variables in the Analysis of Output from a Computer Code. Technometrics 21, 239–245. doi:10.1080/00401706.1979.10489755

Mercogliano, P., Montesarchio, M., Rianna, G., Schiano, P., Vezzoli, R., Zollo, A.L., 2014. High resolution climate scenarios on Mediterranean test case areas for the hydro-climate integrated system. C. Res. Pap. 233. doi:http://dx.doi.org/10.2139/ssrn.2539008

Mishra, A.K., Singh, V.P., 2010. A review of drought concepts. J. Hydrol. 391, 202–216. doi:10.1016/j.jhydrol.2010.07.012

Mitsch, W.J., Gosselink, J.G., 2015. Wetlands, 5th ed, Aging. JohnWiley & Sons, Inc, Hoboken, New Jersey. doi:10.1017/CBO9781107415324.004

Moghim, S., Bras, R.L., 2017. Bias correction of climate modeled temperature and precipitation using artificial neural networks. J. Hydrometeorol. 18, 1867–1884. doi:10.1175/JHM-D-16-0247.1

Monteith, H.L., 1975. Vegetation and the Atmosphere, Vol. 1: Principles, 1st ed, Academic Press. Academic Press, London. doi:10.1017/S0014479700008607

Moriasi, D.N., Arnold, J.G., Liew, M.W. Van, Bingner, R.L., Harmel, R.D., Veith, T.L., 2007. Model evalution guide line for systematic qualification of accuracy in watershed simulation. Am. Soc. Agric. Biol. Eng. 50, 885–900.

Moss, R.H., Edmonds, J.A., Hibbard, K.A., Manning, M.R., Rose, S.K., Van Vuuren, D.P., Carter, T.R., Emori, S., Kainuma, M., Kram, T., Meehl, G.A., Mitchell, J.F.B.,

Nakicenovic, N., Riahi, K., Smith, S.J., Stouffer, R.J., Thomson, A.M., Weyant, J.P., Wilbanks, T.J., 2010. The next generation of scenarios for climate change research and assessment. Nature 463, 747–756. doi:10.1038/nature08823

Mougin, E., Hiernaux, P., Kergoat, L., Grippa, M., de Rosnay, P., Timouk, F., Le Dantec, V., Demarez, V., Lavenu, F., Arjounin, M., 2009. The AMMA-CATCH Gourma observatory site in Mali: Relating climatic variations to changes in vegetation, surface hydrology, fluxes and natural resources. J. Hydrol. 375, 14–33. doi:10.1016/j.jhydrol.2009.06.045

Moyo, S., 2016. Family farming in sub-Saharan Africa: its contribution to agriculture, food security and rural development. FAO UNDP 150. doi:http://www.fao.org/3/a-i6056e.pdf

Muerth, M.J., Gauvin St-Denis, B., Ricard, S., Velázquez, J.A., Schmid, J., Minville, M., Caya, D., Chaumont, D., Ludwig, R., Turcotte, R., 2012. On the need for bias correction in regional climate scenarios to assess climate change impacts on river runoff. Hydrol. Earth Syst. Sci. 17, 1189–1204. doi:10.5194/hess-17-1189-2013

Murphy, A.H., 1988. Skill Scores Based on the Mean Square Error and Their Relationships to the Correlation Coefficient. Mon. Weather Rev. doi:10.1175/1520-0493(1988)116<2417:SSBOTM>2.0.CO;2

Music, B., Caya, D., 2009. Investigation of the Sensitivity of Water Cycle Components Simulated by the Canadian Regional Climate Model to the Land Surface Parameterization , the Lateral Boundary Data , and the Internal Variability. J. Hydrometeorol. 10, 3–21. doi:10.1175/2008JHM979.1

Nadeau, T.L., Rains, M.C., 2007. Hydrological connectivity between headwater streams and downstream waters: How science can inform policy. J. Am. Water Resour. Assoc. 43, 118–133. doi:10.1111/j.1752-1688.2007.00010.x

NASA, 2014. Shuttle Radar Topography Mission (SRTM) C-Band data products [WWW Document]. Jet Propuls. Lab. URL https://www2.jpl.nasa.gov/srtm/cbanddataproducts.html (accessed 12.31.14).

Nash, J.E., Sutcliffe, J. V, 1970. River Flow Forecasting Through Conceptual Models Part I-a Discussion of Principles. J. Hydrol. 10, 282–290. doi:10.1016/0022-1694(70)90255-6

Niang, I., Ruppel, O.C., Abdrabo, M.A., Essel, A., Lennard, C., Padgham, J., Urquhart, P., 2014. Africa, in: Barros, V.R., Field, C.B., DOkken, D.J., Mastrandrea, M.D., Mach, K.J., Bilir, T.E., Matterjee, M., Ebi, K.L., O, E.Y., Genova, R.C., Girma, B., Kissel, E.S., Levy, A.N., MAcCracken, S., Mastrandrea, P.R., White, L.L. (Eds.), Climate Change 2014: Impacts, Adaptation and Vulnerability - Contributions of the Working Group II to the Fifth Assessment Report of the Intergovernmental Panel on Climate Change. Cambridge University Press, Cambridge, United Kingdom and New York, NY, USA, pp. 1199–1265. doi:10.1017/CBO9781107415386.002

Nicholson, S.E., 1980. The nature of rainfall fluctuations in subtropical West Africa. Am. Meteorol. Soc. April, 473–487. doi:https://doi.org/10.1175/1520-0493(1980)108<0473:TNORFI>2.0.CO;2

Niehoff, D., Fritsch, U., Bronstert, A., 2002. Land-use impacts on storm-runoff generation : scenarios of land-use change and simulation of hydrological response in a meso-scale catchment in SW-Germany. J. Hydrol. 267, 80–93.

Nilawar, A.P., Waikar, M.L., 2019. Impacts of climate change on streamflow and sediment concentration under RCP 4.5 and 8.5: A case study in Purna river basin, India. Sci. Total Environ. 650, 2685–2696. doi:10.1016/j.scitotenv.2018.09.334

Nka, B.N., Oudin, L., Karambiri, H., Paturel, J.E., Ribstein, P., 2015. Trends in floods in West Africa: Analysis based on 11 catchments in the region. Hydrol. Earth Syst. Sci. 19, 4707–4719. doi:10.5194/hess-19-4707-2015

O'Siullivan, J.N., 2008. Root distribution of yam (Dioscorea alata) determined by strontium tracer. Expl Agric. 44, 223–233. doi:10.1017/S0014479708006169

Obuobie, E., Diekkrüger, B., 2008. Using SWAT to Evaluate Climate Change Impact on Water Resources in the White Volta River Basin, West Africa, in: Tropentag. Hohenheim. http://www.tropentag.de/2008/abstracts/full/496.pdf.

Oeurng, C., Cochrane, T.A., Chung, S., Kondolf, M.G., Piman, T., Arias, M.E., 2019. Assessing climate change impacts on river flows in the Tonle Sap Lake Basin, Cambodia. Water (Switzerland) 11. doi:10.3390/w11030618

Ogban, P.I., Babalola, O., 2003. Soil characteristics and constraints to crop production in inland valley bottoms in southwestern Nigeria. Agric. Water Manag. 61, 13–28. doi:10.1016/S0378-3774(02)00170-1

Oguntunde, P.G., Abiodun, B.J., Lischeid, G., 2017. Impacts of climate change on hydro-meteorological drought over the Volta Basin, West Africa. Glob. Planet. Change 155, 121–132. doi:10.1016/j.gloplacha.2017.07.003

Oguntunde, P.G., Lischeid, G., Abiodun, B.J., 2018. Impacts of climate variability and change on drought characteristics in the Niger River Basin, West Africa. Stoch. Environ. Res. Risk Assess. 32, 1017–1034. doi:10.1007/s00477-017-1484-y

Op de Hipt, F., 2017. Modeling climate and land use change impacts on water resources and soil erosion in the Dano catchment (Burkina Faso, West Africa). (PhD Thesis) University of Bonn, Germany, http://hss.ulb.uni-bonn.de/2018/5030/5030.htm.

Op de Hipt, F., Diekkrüger, B., Steup, G., Yira, Y., Hoffmann, T., Rode, M., 2018. Modeling the impact of climate change on water resources and soil erosion in a tropical catchment in Burkina Faso, West Africa. Catena 163, 63–77. doi:10.1016/j.catena.2017.11.023

Op de Hipt, F., Diekkrüger, B., Steup, G., Yira, Y., Hoffmann, T., Rode, M., 2017. Applying SHETRAN in a tropical west African catchment (Dano, Burkina Faso)-calibration, validation, uncertainty assessment. Water (Switzerland) 9. doi:10.3390/w9020101

Op de Hipt, F., Diekkrüger, B., Steup, G., Yira, Y., Hoffmann, T., Rode, M., Näschen, K., 2019. Modeling the effect of land use and climate change on water resources and soil erosion in a tropical West African catch-ment (Dano, Burkina Faso) using SHETRAN. Sci. Total Environ. 653, 431–445. doi:10.1016/j.scitotenv.2018.10.351

OTT Hydromet, 2007. OTT ADC-Acoustic , digital current meter [WWW Document]. OTT Hydromet. URL http://www.ott.com/download/operating-instructions-acoustic-digital-current-meter-ott-adc/ (accessed 4.20.06).

Ouedraogo, I., Tigabu, M., Savadogo, P., Compaoré, H., Odén, P.C., Ouadba, J.M., 2010. Land cover change and its relation with population dynamics in Burkina Faso, West Africa. L. Degrad. Dev. 21, 453–462. doi:10.1002/ldr.981

Paeth, H., Hall, N.M.J., Gaertner, M.A., Alonso, M.D., Moumouni, S., Polcher, J., Ruti, P.M., Fink, A.H., Gosset, M., Lebel, T., Gaye, A.T., Rowell, D.P., Moufouma-Okia, W.,

Jacob, D., Rockel, B., Giorgi, F., Rummukainen, M., 2011. Progress in regional downscaling of West African precipitation. Atmos. Sci. Lett. 12, 75–82. doi:10.1002/asl.306

Pale, S., Da, D.E.C., 2013. Gestion traditionnelle des ressources en eau en cultures pluviale et maraîchère dans le département de Dano. Université de Ouagadougou.

Pall, P., Allen, M.R., Stone, D.A., 2007. Testing the Clausius – Clapeyron constraint on changes in extreme precipitation under CO 2 warming. Clim. Dyn. 28, 351–363. doi:10.1007/s00382-006-0180-2

Paré, S., Söderberg, U., Sandwall, M., Ouadba, J.M., 2008. Land use analysis from spatial and field data capture in southern Burkina Faso , West Africa. Agric. , Ecosyst. Environ. 127, 277–285. doi:10.1016/j.agee.2008.04.009

Patil, N.G., Singh, S.K., 2016. Pedotransfer Functions for Estimating Soil Hydraulic Properties: A Review. Pedosphere 26, 417–430. doi:10.1016/S1002-0160(15)60054-6

Peters, N.E., Driscoll, C.T., 1987. Hydrogeologic controls of surface-water chemistry in the Adirondack region of New York State. Biogeochemistry 3, 163–180.

Poméon, T., 2019. Evaluating the Contribution of Remote Sensing Data Products for Regional Simulations of Hydrological Processes in West Africa using a Multi-Model Ensemble. (PhD Thesis) University of Bonn, Germany, http://hss.ulb.uni-bonn.de/2019/5421/5421.htm.

Poméon, T., Diekkrüger, B., Kumar, R., 2018a. Computationally Efficient Multivariate Calibration and Validation of a Grid-Based Hydrologic Model in Sparsely Gauged West African River Basins. Water 10, 1–26. doi:10.3390/w10101418

Poméon, T., Diekkrüger, B., Springer, A., Kusche, J., Eicker, A., 2018b. Multi-Objective Validation of SWAT for Sparsely-Gauged West African River Basins—A Remote Sensing Approach. Water 10, 1–22. doi:10.3390/w10040451

Poméon, T., Jackisch, D., Diekkrüger, B., 2017. Evaluating the performance of remotely sensed and reanalysed precipitation data over West Africa using HBV light. J. Hydrol. 547, 222–235. doi:10.1016/j.jhydrol.2017.01.055

Popper, K., 2002. The Logic of Scientific Discovery. Routledge Classic, London, New York. doi:http://strangebeautiful.com/other-texts/popper-logic-scientific-discovery.pdf

Portoghese, I., Bruno, E., Guyennon, N., Iacobellis, V., 2011. Stochastic bias-correction of daily rainfall scenarios for hydrological applications. Nat. Hazards Earth Syst. Sci. 11, 2497–2509. doi:10.5194/nhess-11-2497-2011

Raghunath, H.M., 2006. Hydrology: Principles-Analysis-Design.

Rao, L.Y., Sun, G., Ford, C.R., Vose, J.M., 2011. Modeling potential evapotranspiration of two forested watershed in the southern appalachians. Trans. ASEBE 54, 2067–2078. doi:10.13031/2013.40666

Raunet, M., 1985. Bas-fonds et riziculture en Afrique Approche structurale comparative. l'Agronomie Trop. 40, 181–201.

Rawls, W.J., Brakensiek, D.L., 1985. Prediction of Soil Water Properties for Hydrologic Modelling, in: Jones, E.B., Ward, T.J. (Eds.), Proceedings of a Symposium Watershed Management in the Eighties. Jones, E. B. Ward, T. J., New York, pp. 293–299.

Richards, L.A., 1931. Capillary conduction of liquids through porous mediums. J. Appl. Phys. 1, 318–333. doi:10.1063/1.1745010

Richards, L.A., Weaver, L.R., 1944. Moisture retention by some irrigated soils as related to soil-moisture tension. J. Agric. Res. 69, 215–235.

Salih, A.A.M., Elagib, N.A., Tjernström, M., Zhang, Q., 2018. Characterization of the Sahelian-Sudan rainfall based on observations and regional climate models. Atmos. Res. 202, 205–218. doi:10.1016/j.atmosres.2017.12.001

Samaniego, L., Kumar, R., Attinger, S., 2010. Multiscale parameter regionalization of a grid - based hydrologic model at the mesoscale. Water Resour. Res. 46, 1–25. doi:10.1029/2008WR007327

Savenije, H.H.G., 2001. Equifinality, a blessing in disguise? Hydrol. Process. 15, 2835–2838. doi:10.1002/hyp.494

Saxton, K.E., Rawls, W.J., 2006. Soil Water Characteristic Estimates by Texture and Organic Matter for Hydrologic Solutions. Soil Sci. Soc. Am. J. 70, 1569–1578. doi:10.2136/sssaj2005.0117

Saxton, K.E., Rawls, W.J., Romberger, J.S., Papendick, R.I., 1986. Estimating generalized soil-water characteristics from texture. Soil Sci. Soc. Am. J. 50, 1031–1036. doi:10.2136/sssaj1986.03615995005000040039x

Schaap, M.G., Leij, F.J., van Genuchten, M.T., 2001. ROSETTA: a computer program for estimating soil hydraulic parameters with hierarchical pedotransfer functions. J. Hydrol. 251, 163–176.

Schmalz, B., Fohrer, N., 2009. Comparing model sensitivities of different landscapes using the ecohydrological SWAT model. Adv. Geosci. 21, 91–98. doi:10.5194/adgeo-21-91-2009

Schmengler, A.C., 2011. Modeling soil erosion and reservoir sedimentation at hillslope and catchment scale in semi-arid Burkina Faso. (PhD Thesis) University of Bonn, Germany, http://hss.ulb.uni-bonn.de/diss_online elektronisch publiziert.

Schulla, J., 2015. Model Description WaSiM. Technical report. Hydrology Software Consulting J. Schulla, Zurich; http://www.wasim.ch/downloads/doku/wasim/wasim_2015_en.pdf.

Schuol, J., Abbaspour, K., Srinivasan, R., Yang, H., 2008. Estimation of freshwater availability in the West African sub-continent using the SWAT hydrologic model. J. Hydrol. 352, 30–49. doi:10.1016/j.jhydrol.2007.12.025

Schuol, J., Abbaspour, K.C., 2007. Using monthly weather statistics to generate daily data in a SWAT model application to West Africa. Ecol. Modell. 201, 301–311. doi:10.1016/j.ecolmodel.2006.09.028

Schuol, J., Abbaspour, K.C., 2006. Calibration and uncertainty issues of a hydrological model (SWAT) applied to West Africa. Adv. Geosci. 9, 137–143. doi:hwww.adv-geosci.net/9/137/2006/

Searcy, J.K., 1959. Flow-Duration Curves Flow-Duration Curves. U.S Geol. Surv. Water-Supp, 1–33.

Seiller, G., Anctil, F., Perrin, C., 2012. Multimodel evaluation of twenty lumped hydrological models under contrasted climate conditions. Hydrol. Earth Syst. Sci. 16, 1171–1189. doi:10.5194/hess-16-1171-2012

Şen, Z., 2015. Basic Porous Medium Concepts, Practical and Applied Hydrogeology. Amsterdam, Boston, Waltham, Heidelberg, London, New York, Oxford, Paris, San Diego, San Francisco, Singapore, Sydney, Tokyo. doi:10.1016/b978-0-12-800075-

5.00002-9

Shrestha, M., Acharya, S.C., Shrestha, P.K., 2017. Bias correction of climate models for hydrological modelling – are simple methods still useful? Meteorol. Appl. 24, 531–539. doi:10.1002/met.1655

Singhal, B.B.S., Gupta, R.P., 2013. Applied Hydrogeology of Fractured Rocks, 2nd ed. Springler Netherlands, Dordrecht Heidelberg, London, New York. doi:10.1007/978-90-481-8799-7

Singhal, B.B.S., Gupta, R.P., 2010. Fractures and Discontinuities, in: Applied Hydrogeology of Fractured Rocks. Springer Netherlands, Dordrecht Heidelberg, London, New York, pp. 13–33. doi:10.1007/978-90-481-8799-7

Sivakumar, M.V.K., 1989. Climate vulnerability of sorghum and millet, in: Climate and Food Security. International Rice Research Institute, American Association for the Advancement of Science, Manila, Washington, pp. 188–192.

Sklash, M.G., Farvolden, R.N., 1979. The role of groundwater in storm runoff. J. Hydrol. 43, 45–65. doi:https://doi.org/10.1016/S0167-5648(09)70009-7

Smitha, P.S., Narasimhan, B., Sudheer, K.P., Annamalai, H., 2018. An improved bias correction method of daily rainfall data using a sliding window technique for climate change impact assessment. J. Hydrol. 556, 100–118. doi:10.1016/j.jhydrol.2017.11.010

Sparacino, C., 2011. Oeuvrer pour que les populations rurales pauvres se libèrent de la pauvreté au Burkina Faso [WWW Document]. URL https://www.ifad.org/documents/10180/a1580f09-efbd-4c77-b2b6-6e9f982f906a (accessed 4.2.16).

Stanzel, P., Kling, H., Bauer, H., 2018. Climate change impact on West African rivers under an ensemble of CORDEX climate projections. Clim. Serv. 11, 36–48. doi:10.1016/j.cliser.2018.05.003

Steduto, P., Hsiao, T.C., 1998. Maize canopies under two soil water regimes II. Seasonal trends of evapotranspiration, carbon dioxide assimilation and canopy conductance, and as related to leaf area index. Agric. For. Meteorol. 89, 185–200. doi:10.1016/S0168-1923(97)00084-1

Stella, J.M., 2013. Mathematical model for the prediction of recession curves . Rev. la Asoc. Geol. Argentina 70, 229–237.

Stéphenne, N., Lambin, E.F., 2001. A dynamic simulation model of land-use changes in Sudano-sahelian countries of Africa (SALU). Agric. Ecosyst. Environ. 85, 145–161. doi:https://doi.org/10.1016/S0167-8809(01)00181-5

Stewart, M.K., 2015. Promising new baseflow separation and recession analysis methods applied to streamflow at Glendhu Catchment, New Zealand. Hydrol. Earth Syst. Sci. 19, 2587–2603. doi:10.5194/hess-19-2587-2015

Tallaksen, L.M., 1995. A review of baseflow recession analysis. J. Hydrol. 165, 349–370. doi:10.1016/0022-1694(94)02540-R

Teng, J., Potter, N.J., Chiew, F.H.S., Zhang, L., Wang, B., Vaze, J., Evans, J.P., 2015. How does bias correction of regional climate model precipitation affect modelled runoff? Hydrol. Earth Syst. Sci. 19, 711–728. doi:10.5194/hess-19-711-2015

Teutschbein, C., Seibert, J., 2012. Bias correction of regional climate model simulations for hydrological climate-change impact studies: Review and evaluation of different

methods. J. Hydrol. 456–457, 12–29. doi:10.1016/j.jhydrol.2012.05.052

Todorovic, M., 1999. Single-layer evapotranspiration model with variable canopy resistance. J. Irrig. Drain. Eng. 125, 235–245. doi:https://doi.org/10.1061/(ASCE)0733-9437(1999)125:5(235)

Tomkins, K.M., 2014. Uncertainty in streamflow rating curves: Methods, controls and consequences. Hydrol. Process. 28, 464–481. doi:10.1002/hyp.9567

Traore, B., Corbeels, M., van Wijk, M.T., Rufino, M.C., Giller, K.E., 2013. Effects of climate variability and climate change on crop production in southern Mali. Eur. J. Agron. 49, 115–125. doi:10.1016/j.eja.2013.04.004

Traore, B., Van Wijk, M.T., Descheemaeker, K., Corbeels, M., Rufino, M.C., Giller, K.E., 2015. Climate Variability and Change in Southern Mali: Learning From Farmer Perceptions and on-Farm Trials. Exp. Agric. 51, 615–634. doi:10.1017/S0014479714000507

Tschakert, P., Sagoe, R., Ofori-Darko, G., Codjoe, S.N., 2010. Floods in the Sahel: An analysis of anomalies, memory, and anticipatory learning. Clim. Change 103, 471–502. doi:10.1007/s10584-009-9776-y

UN-FCCC, 2016. Action taken by the Conference of the Parties at its twenty-first session. Paris. doi:https://unfccc.int/resource/docs/2015/cop21/eng/10a01.pdf#page=2

van Genuchten, M.T., 1980. A Closed-form Equation for Predicting the Hydraulic Conductivity of Unsaturated Soils1. Soil Sci. Soc. Am. J. 44, 892. doi:10.2136/sssaj1980.03615995004400050002x

Van Liew, M.W., Veith, T.L., Bosch, D.D., Arnold, J.G., 2007. Suitability of SWAT for the conservation effects assessment project: Comparison on USDA agricultural research service watersheds. J. Hydrol. Eng. 12, 173–189. doi:10.1061/(ASCE)1084-0699(2007)12:2(173)

Vautard, R., Gobiet, A., Sobolowski, S., Kjellström, E., Stegehuis, A., Watkiss, P., Mendlik, T., Landgren, O., Nikulin, G., Teichmann, C., Jacob, D., 2014. The European climate under a 2 °C global warming. Environ. Res. Lett. 9, 11 pp. doi:10.1088/1748-9326/9/3/034006

Velázquez, J.A., Schmid, J., Ricard, S., Muerth, M.J., Gauvin St-Denis, B., Minville, M., Chaumont, D., Caya, D., Ludwig, R., Turcotte, R., 2013. An ensemble approach to assess hydrological models' contribution to uncertainties in the analysis of climate change impact on water resources. Hydrol. Earth Syst. Sci. 17, 565–578. doi:10.5194/hess-17-565-2013

Venot, J.-P., Cecchi, P., 2011. Valeurs d'usage ou performances techniques : comment apprécier le rôle des petits barrages en Afrique subsaharienne ? Cah. Agric. 20, 112–117. doi:10.1684/agr.2010.0457

Vereecken, H., Maes, J., Feyen, J., 1990. Estimating unsaturated hydraulic conductivity from easily measured soil properties. Soil Sci. 149, 1–12. doi:10.1097/00010694-199001000-00001

Vicente-Serrano, S.M., Beguería, S., López-Moreno, J.I., 2010. A multiscalar drought index sensitive to global warming: The standardized precipitation evapotranspiration index. J. Clim. 23, 1696–1718. doi:10.1175/2009JCLI2909.1

Villani, V., Rianna, G., Mercogliano, P., Zollo, A.L., Schiano, P., 2014. Statistical approaches versus weather generator to downscale RCM outputs to point scale: A

comparison of performances. J. Urban Environ. Eng. 8, 142–154. doi:10.4090/juee.2014.v8n2.142154

Vogel, R.M., Fennessey, N.M., 1995. Flow duration curves II: a review of applications in water resources planning. Am. Water Resour. Assoc. 31, 1029–1039. doi:10.1111/j.1752-1688.1995.tb03419.x

Vrac, M., Drobinski, P., Merlo, A., Herrmann, M., Lavaysse, C., Li, L., Somot, S., 2012. Dynamical and statistical downscaling of the French Mediterranean climate: Uncertainty assessment. Nat. Hazards Earth Syst. Sci. 12, 2769–2784. doi:10.5194/nhess-12-2769-2012

Vrugt, J.A., ter Braak, C.J.F., Gupta, H. V., Robinson, B.A., 2009. Equifinality of formal (DREAM) and informal (GLUE) Bayesian approaches in hydrologic modeling? Stoch. Environ. Res. Risk Assess. 23, 1011–1026. doi:10.1007/s00477-008-0274-y

Waongo, M., 2015. Optimizing Planting Dates for Agricultural Decision-Making under Climate Change over Burkina Faso / West Africa. (M.Sc. Thesis), University of Augsburg, Germany, https://opus.bibliothek.uni-augsburg.de/opus4/frontdoor/deliver/index/docId/3280/file/PhD_MWaongo.pdf.

Weglarczyk, S., 1998. The interdependence and applicability of some statistical quality measures for hydrological models. J. Hydrol. 206, 98–103. doi:https://doi.org/10.1016/S0022-1694(98)00094-8

Wilson, C.O., Weng, Q., 2011. Simulating the impacts of future land use and climate changes on surface water quality in the Des Plaines River watershed, Chicago Metropolitan Statistical Area, Illinois. Sci. Total Environ. 409, 4387–4405. doi:10.1016/j.scitotenv.2011.07.001

Windmeijer, P.N., Andriesse, W., 1993. Inland valleys in West Africa: Agro-ecological characerization of rice growing environments. International Institute for Land Reclamation and improvement, Wageningen, the Netherlands.

Wittenberg, H., 1994. Nonlinear analysis of flow recession curves. J. Hydrol. 158, 405–406. doi:10.1016/0022-1694(94)90065-5

WMO, 2008. Guide to Hydrological Practices. Hydrology - From Measurement to Hydrological Information, WMO-No. 16. ed. Word Meteorological Organization, Geneva. doi:http://www.wmo.int/pages/prog/hwrp/publications/guide/english/168_Vol_I_en.pdf

WRB, 2006. World reference base for soil resources-A framework for international classification, correlation and communication. World Soil Resources, Report 103 FAO, Rome, Italy., 2006th ed. FAO, Rome. doi:10.1017/S0014479706394902

Xu, X., Li, J., Tolson, B.A., 2014. Progress in integrating remote sensing data and hydrologic modeling. Prog. Phys. Geogr. 38, 464–498. doi:10.1177/0309133314536583

Xu, Z., Han, Y., Yang, Z., 2019. Dynamical downscaling of regional climate: A review of methods and limitations. Sci. China Earth Sci. 62, 365–375. doi:10.1007/s11430-018-9261-5

Yacouba, Y., Aymar, B., Amadou, K., Louis, F., Georges, S., Thomas, Y., Mouhamed, I., Bruno, L., 2018. Failure of Inland Valleys Development: A Hydrological Diagnosis of the Bankandi Valley in Burkina Faso. Irrig. Drain. Syst. Eng. 07, 1:8.

doi:10.4172/2168-9768.1000217

Yira, Y., 2016. Modeling land use change impacts on water resources in a tropical West African catchment (Dano, Burkina Faso). (PhD Thesis) University of Bonn, Germany, http://hss.ulb.uni-bonn.de/2017/4583/4583.pdf.

Yira, Y., Diekkrüger, B., Steup, G., Bossa, A.Y., 2016. Modeling land use change impacts on water resources in a tropical West African catchment (Dano, Burkina Faso). J. Hydrol. 537, 187–199. doi:10.1016/j.jhydrol.2016.03.052

Yira, Y., Diekkrüger, B., Steup, G., Yaovi Bossa, A., 2017. Impact of climate change on hydrological conditions in a tropical West African catchment using an ensemble of climate simulations. Hydrol. Earth Syst. Sci. 21, 2143–2161. doi:10.5194/hess-21-2143-2017

Yu, M., Li, Q., Hayes, M.J., Svoboda, M.D., Heim, R.R., 2014. Are droughts becoming more frequent or severe in China based on the standardized precipitation evapotranspiration index: 1951-2010? Int. J. Climatol. 34, 545–558. doi:10.1002/joc.3701

Zhang, L., Cheng, L., Chiew, F., Fu, B., 2018. Understanding the impacts of climate and landuse change on water yield. Curr. Opin. Environ. Sustain. 33, 167–174. doi:10.1016/j.cosust.2018.04.017

Zhou, M., Qu, S., Chen, X., Shi, P., Xu, S., Chen, H., Zhou, H., Gou, J., 2019. Impact assessments of rainfall-runoff characteristics response based on land use change via hydrological simulation. Water (Switzerland) 11. doi:10.3390/w11040866

Zhou, X., Helmers, M., Qi, Z., 2013. Modeling of subsurface tile drainage using MIKE SHE. Appl. Eng. Agric. 29, 865–873. doi:10.13031/aea.29.9568

Zoungrana, B.J., Conrad, C., Amekudzi, L.K., Thiel, M., Da, E.D., Forkuor, G., Löw, F., 2015. Multi-Temporal Landsat Images and Ancillary Data for Land Use/Cover Change (LULCC) Detection in the Southwest of Burkina Faso, West Africa. Remote Sens. 7, 12076–12102. doi:https://doi.org/10.3390/rs70912076

10 APPENDICES

Appendix 1: Historical LULC from 1990 to 2013 of Bankandi-Loffing catchment (data set provided by Op de Hipt et al., 2019).

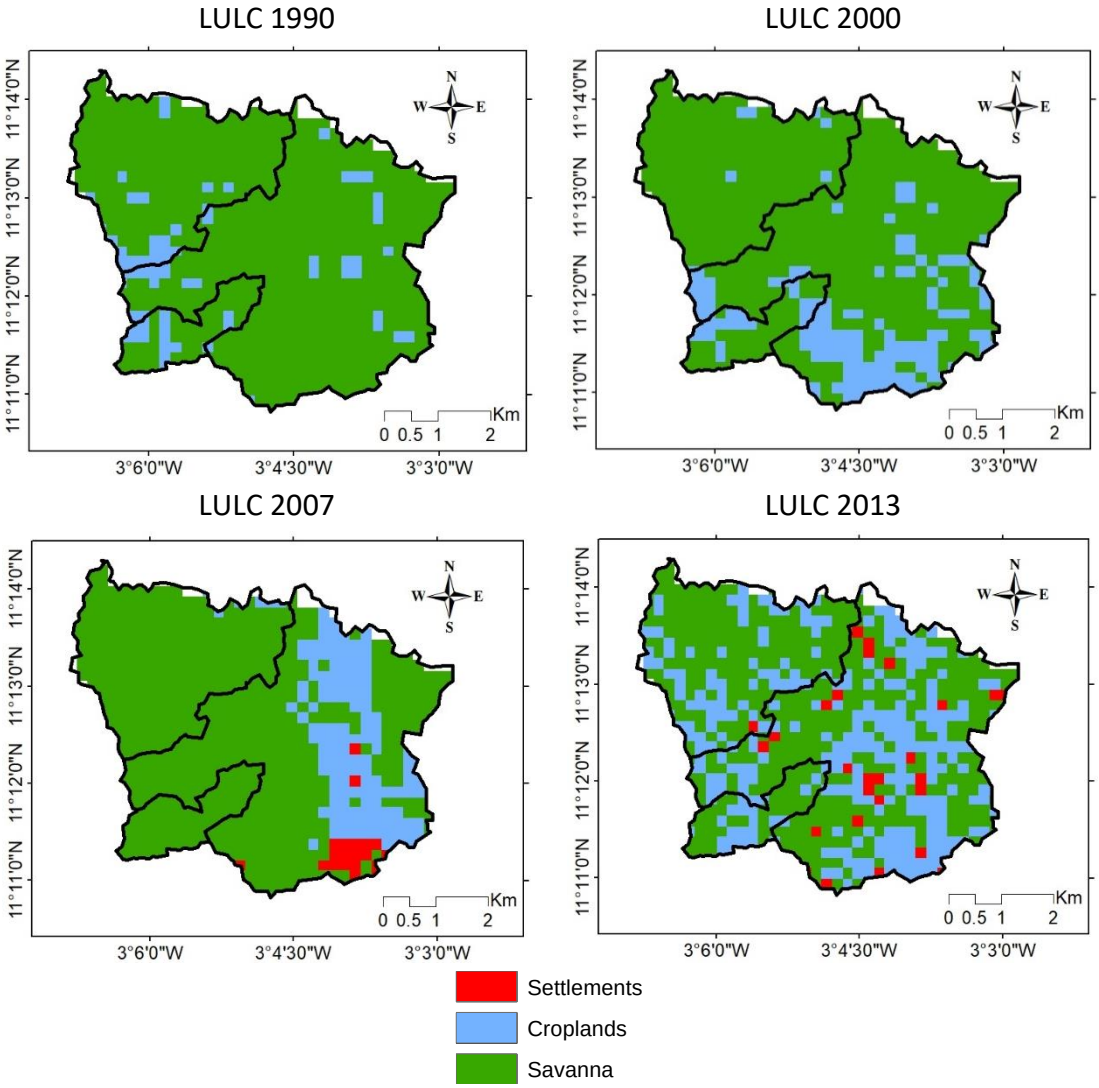

Appendix 2: Predicted LULC from 2019 to 2030 of Bankandi-Loffing catchment (data set provided by Op de Hipt et al., 2019).

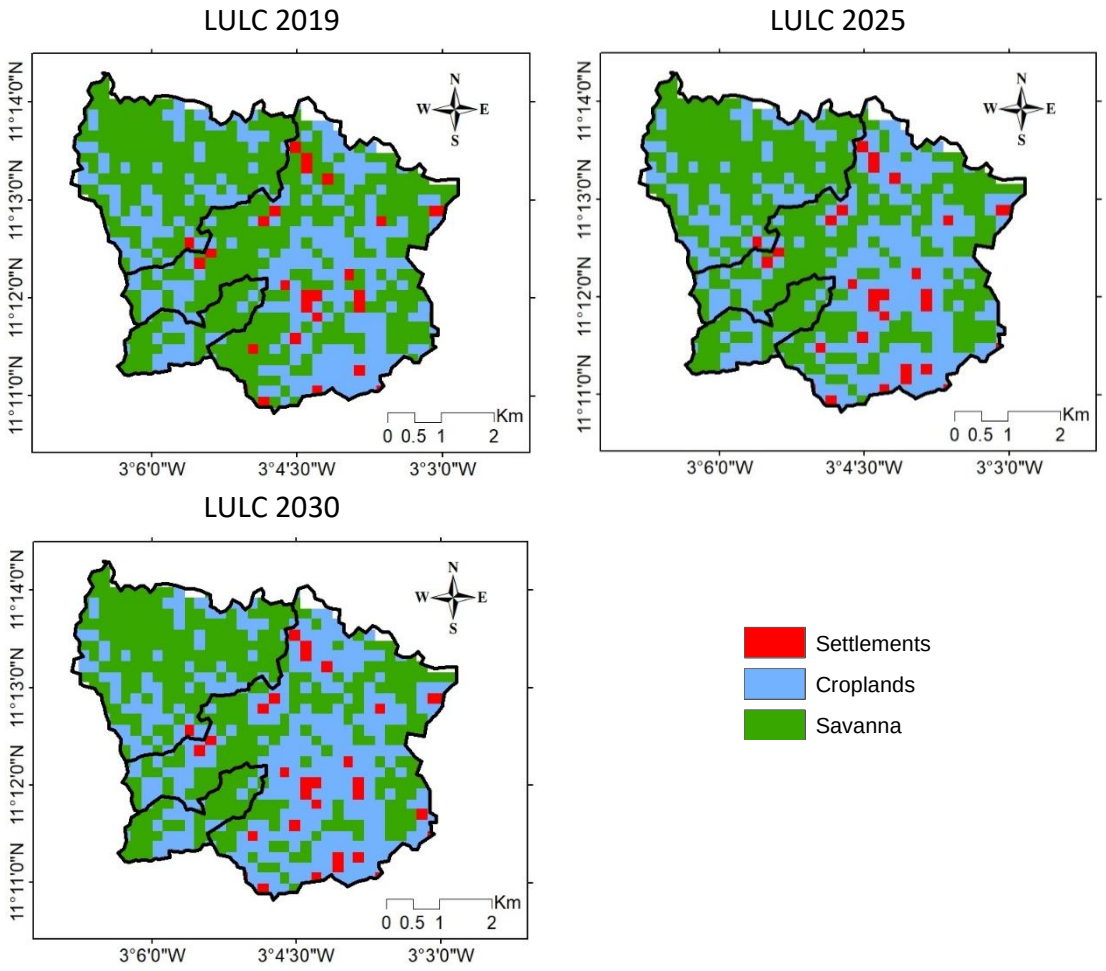

Appendix 3: **Sensitivity of ETp to evaporation surface resistance (r_{se}) and model temporal resolution**

The aim of this sensitivity analyses is to determine the range of r_{se} that yields in realistic ETp in the study area and how the model time resolution influence annual ETp. The Penman-Monteith method was used for an r_{se} range of 50-500 s m^{-1} and 10, 30, 60 min, and 1 day time resolutions. All other parameters including the canopy surface resistance (r_{sc}) and the interception surface resistance (r_{si}), were constant (r_{sc}= 100 s m^{-1} and r_{si}=80 s m^{-1}). The year 2013 LULC with 30 m spatial resolution were utilized and the calculation was applied for the period 2013-2015. A comparison of sub-daily times step (10, 30, 60 min) results were compared to daily time step result using the discrepancy (Δ) calculated in the following equation.

$$\Delta = \frac{\sum ETp_{\Delta t} - \sum ETp_{d}}{\sum ETp_{d}} * 100\%$$

With $ETp._{\Delta}t$, the ETp computed at the time step Δt; and $ETp._{d}$, the evapotranspiration calculated at daily time step.

Table: Variation of ET_p with rse and with daily and hourly time steps of calculations.

r_{se} (s m^{-1})	**Hourly ET_p calculation** (mm yr^{-1})	**Daily ET_p calculation** (mm yr^{-1})	**Variation Delta**
50	2889	2715	6%
100	2612	2443	7%
150	2405	2245	7%
200	2243	2089	7%
225	2173	2023	7%
250	2111	1964	7%
300	2001	1848	8%
350	1908	1764	8%
400	1829	1693	8%
450	1759	1626	8%
500	1698	1568	8%